A Measurement of the CP Violation Parameter $\mathcal{R}e(\epsilon'/\epsilon)$

Victoria Jane Martin

Department of Physics & Astronomy
The University of Edinburgh

Thesis submitted for the degree of Doctor of Philosophy

August 3, 2000

Abstract

The NA48 experiment is a fixed target experiment on the Super Proton Synchrotron accelerator at CERN. The aim of the experiment is to investigate direct **CP** violation in the neutral kaon system by measuring the parameter $\mathcal{R}e(\epsilon'/\epsilon)$ to an accuracy of 2×10^{-4}. In 1998 the NA48 experiment took 14 weeks of data for this measurement.

This thesis describes a method for determining $\mathcal{R}e(\epsilon'/\epsilon)$ and the systematic studies of the measurement. The result of my analysis is:

$$\mathcal{R}e(\epsilon'/\epsilon) = (12.3 \pm 2.8 \pm 3.7) \times 10^{-4}$$

where the first error is statistical and the second error is systematic.

Declaration

This work represents the effort of many members of the NA48 Collaboration at CERN. However, the analysis and final results presented in this thesis are entirely my own.

Acknowledgements

First of all, I would like to thank all my collaborators on the NA48 experiment at CERN. Without your foresight and dedication NA48 would never have been built and would have never taken any data which I could analyse.

To our little $\mathcal{R}e(\epsilon'/\epsilon)$ analysis group at CERN: Harald Fox, Benedetto Gorini and Mayda Velasco, thank-you for the code and the discussions, and for your continued help even after you had finished your theses/got new jobs and were working on new projects. A second thank-you goes to Mayda for being my de-facto supervisor for nearly two years while I was at CERN.

I would like to thank the academic members of the Edinburgh PPE group: Ian Knowles, Steve Playfer, Franz Muheim and Alan Walker – all of whom have supervised or advised me during my PhD. Obviously I can't forget Ken Peach who made a PhD position for me, and appears occasionally to fulfill his rôle as the grand master of my supervision.

To the Edinburgh members of NA48: Helen, Christina and Roberto and to Tim, Manny, Ranpal, Matt and George from Cambridge, thanks for the discussions about epsilon prime, rare kaon decays, and more mundane matters over tea.

Lastly I'd like to thank all my friends and family for trying to distract me from doing work over the last three-and-a-bit years, especially to Mayda (again), Harald and Tim in Geneva and to Jane and David (and Hamish!) and everyone at 64/4 West Mains Road in Edinburgh.

Contents

1 Introduction 1

2 CP Violation and Neutral Kaons 4

2.1 The Discrete Symmetries **C**, **P** and **T** 4

2.2 Introduction to the Kaon System 5

2.2.1 The Neutral Kaons 6

2.3 Particle – Antiparticle Mixing 6

2.3.1 Evolution of the Kaons 7

2.3.2 Constraints from **CPT** Conservation 8

2.3.3 **CP** Conservation 10

2.4 **CP** Violation in $K_L \to \pi\pi$ decays 10

2.5 Classification of **CP** Violation 11

2.6 **CP** Violation in the Standard Model 13

2.6.1 The Unitarity Triangle(s) 15

2.6.2 The Wolfenstein Parameterisation 15

2.6.3 B^0 Physics 16

2.7 Phenomenology of $K \to \pi\pi$ Decays 17

2.7.1 Notation 19

2.8 The $\Delta I = \frac{1}{2}$ Rule 20

2.9 Indirect and Direct **CP** Violation 20

2.9.1 Expressions for ϵ and ϵ' 21
2.9.2 Experimental Measurements of ϵ 23
2.9.3 Interpretation of ϵ 23
2.9.4 Experimental Measurements of ϵ' 24
2.9.5 Interpretation of ϵ' 25
2.10 Theoretical Estimates of $\mathcal{R}e(\epsilon'/\epsilon)$ 25

3 The NA48 Experiment **29**
3.1 Introduction and motivation 29
3.2 Overview 30
3.3 The Simultaneous K_L and K_S Beams 32
3.3.1 The SPS 33
3.3.2 The K_L Beam 33
3.3.3 The Bent Crystal 34
3.3.4 The K_S Beam 35
3.3.5 Beam Monitors 36
3.4 Proton Tagging 37
3.4.1 The Proton Tagger 38
3.5 The Anti-K_S detector 39
3.6 The Decay Region 41
3.7 The Spectrometer 41
3.7.1 The Drift Chambers 41
3.7.2 Performance of the Spectrometer 42
3.7.3 Drift Chamber Readout 42
3.8 The Charged Hodoscope 43
3.9 The Electromagnetic Calorimeter 44
3.9.1 LKR Design Aims 44

3.9.2 Cryogenics and the LKR readout cells 45
3.9.3 Readout of the LKR 47
3.9.4 The Data Concentrator 47
3.9.5 The Performance of the LKR 48
3.9.6 The Neutral Hodoscope 49
3.10 The Hadronic Calorimeter 49
3.11 The Muon Veto 50

4 Triggers and Data Acquisition **51**
4.1 The trigger architecture 51
4.2 The Neutral Trigger System 53
4.2.1 The $\pi^0\pi^0$ Trigger 54
4.2.2 The E_{TOT} signal 56
4.3 The $\pi^+\pi^-$ Trigger 57
4.4 Data Acquisition 58
4.4.1 Subdetector Read Out 59
4.4.2 The PC Farm 59
4.5 The Level 3 Trigger 60
4.5.1 Data Formats and Post-Run Reprocessing 61
4.6 Data Reconstruction 61
4.6.1 Reconstruction of the LKR calorimeter data 61
4.6.2 Reconstruction of the drift chamber data 63
4.6.3 Reconstruction of the Charged Hodoscope Data 64
4.6.4 Reconstruction of the Muon Veto Data 64

5 $\mathcal{R}e(\epsilon'/\epsilon)$ Analysis Strategy **65**
5.1 The Double Ratio 65
5.2 The 1998 Run 67

5.3 K_L Event Weighting 68
5.3.1 Kaon Decay Distribution 69
5.4 Energy Binning 70
5.4.1 Fitting the Double Ratio 71
5.5 Error and Efficiency Formulae 72

6 Event Selection **73**
6.1 Introduction 73
6.1.1 Time Offsets 73
6.2 Proton Tagging 74
6.2.1 Tagging Dilution 74
6.3 Event Selection Criteria 76
6.4 Common Event Selection 77
6.4.1 Kaon Energy Selection 77
6.4.2 Kaon Lifetime Selection 78
6.4.3 Detector Active Volume 80
6.4.4 Centre of Gravity Selection 80
6.4.5 Deadtime Effects 81
6.4.6 Charged Trigger Deadtime 81
6.4.7 Drift Chamber Overflow Conditions 82
6.5 Charged Event Selection 83
6.5.1 Backgrounds 83
6.5.2 Momentum Asymmetry 85
6.5.3 Definition of the Signal Region 86
6.6 Neutral Event Selection 90
6.7 The Raw Double Ratio 92

7 Corrections to the Double Ratio **95**

7.1 Tagging Corrections 95
7.2 Dilution and Tagging Inefficiency in $\pi^+\pi^-$ decays 96
7.3 Tagging Dilution Difference 97
7.3.1 Probability in the Sidebands 97
7.3.2 The calculation of W^{00} 98
7.3.3 Correction to **R** from the Tagging Dilution Difference 98
7.4 Tagging Inefficiency Difference 100
7.5 Trigger Efficiencies 101
7.6 Charged Trigger Efficiency 102
7.6.1 The Pre-Trigger Signals 102
7.6.2 Massbox Inefficiency 104
7.6.3 Charged Trigger Correction 104
7.7 Neutral Trigger Efficiency 104
7.8 Charged Background 105
7.8.1 The Charged Background Fitting Method 106
7.8.2 The Charged Background Counting Method 110
7.8.3 Charged Background Correction to **R** 111
7.9 Beam Scattering 111
7.10 Neutral Background 115
7.11 Accidental Activity 117
7.11.1 Beam Related Activity 117
7.11.2 Noise Effects 118
7.11.3 Correction to **R** for Accidental Activity 119
7.12 Energy Scale 119
7.12.1 AKS Position Fitting 120
7.13 Charged Energy Scale 121
7.14 Neutral Energy Scale 122

7.14.1 Linear Effects 124
7.14.2 Non-Linear Effects 124
7.14.3 Reconstruction Uncertainties 125
7.14.4 Correction to **R** for the Neutral Energy Scale 125
7.15 Acceptance 125
7.15.1 Monte Carlo 126
7.15.2 The Acceptance of the Double Ratio 127
7.15.3 Comparison of Data and Monte Carlo Events 130
7.15.4 Correction to **R** for the Acceptance 131
7.16 The Double Ratio after all Corrections 139

8 Result and Discussion **141**
8.1 The Value of $\mathcal{R}e(\epsilon'/\epsilon)$ 141
8.2 Comparison with other Results 141

A Charged Energy Scale **144**

Bibliography **146**

List of Figures

2.1 Box diagrams for $K^0 \leftrightarrow \overline{K^0}$ mixing 7

2.2 The **CP** violating processes contributing to $K_L \rightarrow \pi\pi$ 11

2.3 The Unitarity Triangle 15

2.4 Current bounds on the Wolfenstein parameters $\overline{\eta}$ and $\overline{\rho}$ 17

2.5 Feynman diagrams for $K \rightarrow \pi\pi$ decays 18

2.6 Penguin diagrams for $\Delta S = 1$ decays 19

2.7 The contributions of the $\langle Q_i \rangle$ to ϵ'/ϵ 26

2.8 Recent theoretical estimates of ϵ'/ϵ 28

3.1 The layout of the NA48 experiment 31

3.2 The NA48 Detector 32

3.3 The defining, cleaning and final collimators in the K_L beam 34

3.4 The bent silicon crystal 36

3.5 The profiles of the K_S and K_L beams 37

3.6 Time difference between the proton tagger and the LKR 38

3.7 The proton tagging detector 39

3.8 The AKS detector 40

3.9 The internal structure of the drift chambers 42

3.10 The charged hodoscope 44

3.11 The internal structure of the LKR 45

3.12 The effect of the accordion geometry 46

3.13 The Data Concentrator algorithm 47

3.14 The Hadronic Calorimeter 49

4.1 The NA48 Level 1 and Level 2 trigger systems 52

4.2 The summing procedure for defining the projective strips of the LKR . 54

4.3 Online plot of a $K^0 \to \pi^0\pi^0 \to 4\gamma$ event 55

4.4 The NA48 data acquisition system 59

5.1 The weighting function for K_L decays 69

6.1 The time difference between the event time and the nearest proton . . 74

6.2 Tagging distributions for $K_L \to \pi^+\pi^-$ and $K_S \to \pi^+\pi^-$ events 75

6.3 The decay vertex for $K^0 \to \pi^+\pi^-$ decays 76

6.4 The z-position of the decay vertex for tagged K_S decays 79

6.5 The centre of gravity distributions for $K^0 \to \pi^+\pi^-$ events 80

6.6 Time of an overflow condition with respect to the event time 82

6.7 The E_{LKR}/p distribution of tracks 84

6.8 The momentum asymmetry for two kaon energy ranges 85

6.9 The definition of the transverse momentum variable p'_T 86

6.10 The p'^2_T distribution for K_L and K_S events 88

6.11 Invariant mass of the $\pi^+\pi^-$ pair 88

6.12 Fits of the $m_{\pi^+\pi^-}$ distribution for two kaon energy ranges 89

6.13 Kaon energy dependence of the resolution of $m_{\pi^+\pi^-}$ 89

6.14 The invariant masses of the photon pairs for $K_S \to \pi^0\pi^0 \to 4\gamma$ 90

6.15 The $R_{ellipse}$ distribution for K_S and K_L events 91

6.16 Numbers of events for the four $\mathcal{R}e(\epsilon'/\epsilon)$ decay modes 93

6.17 The raw double ratio 93

7.1 Time between all protons and the event time for K_L events 99

7.2 The probability of finding protons in the shifted tagging windows . . . 99
7.3 Event time difference for events with a photon conversion 100
7.4 The efficiency of the Level 2 Charged Trigger 103
7.5 The efficiency of the $\pi^0\pi^0$ trigger 104
7.6 Distribution of $\pi^+\pi^-$ events in the $(m_{\pi^+\pi^-}, p_T'^2)$ plane 107
7.7 Distribution of Ke3 and Kμ3 events in the $(m_{\pi^+\pi^-}, p_T'^2)$ plane 107
7.8 The control regions for the charged background fitting method 108
7.9 The control region for the charged background counting method . . . 108
7.10 The distribution of $K_L \to \pi^+\pi^-$ events in $m_{\pi^+\pi^-}$ and $p_T'^2$ 109
7.11 The distribution of Ke3 and Kμ3 events in $m_{\pi^+\pi^-}$ and $p_T'^2$ 109
7.12 The result of the charged background fitting method 110
7.13 Charged background in kaon energy bins 112
7.14 Events from the K_L and K_S beams with $p_T'^2 > 200$ (MeV/c)^2 113
7.15 The radius at the final K_L collimator for scattered events 114
7.16 The lifetime and radial position of the scattered events 114
7.17 Events with $p_T'^2 > 200$ (MeV/c)^2 and no additional activity in the LKR 115
7.18 Background subtracted from the $\pi^0\pi^0$ sample 116
7.19 The z-position of the decay vertex for $K_S \to \pi^0\pi^0$ events 120
7.20 The reconstructed position of the AKS detector using $\pi^+\pi^-$ decays . . 121
7.21 The reconstructed position of the AKS detector using $\pi^0\pi^0$ decays . . 124
7.22 The E_{LKR}/p distribution for electrons 125
7.23 The acceptance of the four $\mathcal{R}e(\epsilon'/\epsilon)$ decay modes 129
7.24 The acceptance of **R** 129
7.25 The kaon energy spectra for data and Monte Carlo events 132
7.26 Ratio of the kaon energy spectra of data and Monte Carlo events . . . 133
7.27 Radius of tracks in the drift chamber for $K_S \to \pi^+\pi^-$ events 134
7.28 Radius of tracks in the drift chamber for $K_L \to \pi^+\pi^-$ events 135

7.29 Radius of clusters in the LKR from $K_S \to \pi^0\pi^0$ events 136

7.30 Radius of clusters in the LKR from $K_L \to \pi^0\pi^0$ events 137

7.31 The distribution of r_{cog} for data and Monte Carlo events 138

7.32 The value of **R** after all corrections 140

8.1 Recent measurements of $\mathcal{R}e(\epsilon'/\epsilon)$ 142

List of Tables

2.1 The main decay modes of K_L and K_S. 6

4.1 Pre-trigger signals sent to the level one trigger supervisor 53

4.2 Online cuts used in the Neutral Trigger for the $\pi^0\pi^0$ trigger 56

4.3 Cuts applied by the Level 2 Charged Trigger 57

6.1 Events lost due to the overflow condition 83

6.2 The numbers of events in each decay modes 92

6.3 Event selection criteria applied to all events. 94

6.4 The criteria used to select $K^0 \to \pi^+\pi^-$ events 94

6.5 The criteria used to select $K^0 \to \pi^0\pi^0$ events 94

7.1 The efficiencies of the Q_X, E_{TOT} and 2track signals 103

7.2 The numbers of events gained and lost in the overlay analysis 119

7.3 Uncertainties on **R** due to the response of the LKR 123

7.4 The acceptance of the four $\mathcal{R}e(\epsilon'/\epsilon)$ decay modes 128

7.5 Summary of all the corrections applied to **R** 139

Chapter 1

Introduction

Symmetries play a very important role in physics. Physicists use symmetries as a mathematical way of describing conserved quantities in nature.

For most people, the definition of which direction is called left and and which is called right seems to be an arbitrary (but conventional) choice. For a physicist this equivalence in the direction of space is due to the conservation of parity symmetry (denoted as **P**) at a macroscopic level. Likewise, the definition of which charge is called positive and which is called negative seems also to be an arbitrary choice. Again physicists interpret this as a conservation of a symmetry, this time charge conjugation symmetry (denoted as **C**).

Even at a microscopic level the conservation of **P** and **C** has been observed. Intermolecular, interatomic and subatomic forces are governed by the electromagnetic interaction. Subnuclear forces, which hold together protons and neutrons inside (stable) atomic nuclei, are governed by the strong interaction. Both the strong and electromagnetic interactions respect the **P** and **C** symmetries. However experiments in nuclear and particle physics have observed that both the **P** and **C** are maximally violated in interactions due to the weak nuclear force.

The **P** and **C** symmetries may be combined to define a new symmetry called **CP**. **CP** symmetry relates particles which are identical in all ways except two: they have opposite electric charge and opposite parity. Parity can be thought of as an internal spatial dimension of the particles. The difference between a particle and its antiparticle is that they have opposite electric charge. Therefore **CP** symmetry relates, at least partially, the properties of matter and antimatter.

CP violation was first observed in the decays of neutral kaons in 1964 by Christenson, Cronin, Fitch and Turlay [20]. In contrast to the violation of the **P** and **C** symmetries, the amount of **CP** violation observed was very small: only 2 parts in 1000.

Returning to the original analogy, the violation of the combined symmetry **CP** may be interpreted as allowing a simultaneous definition of which direction is left *and* which particles have a negative charge. A more physical interpretation is that the weak force, which violates **CP** symmetry, acts differently on matter and antimatter particles which have opposite parity.

Today the Standard Model is the accepted theory of the fundamental particles: quarks and leptons, and the interactions between them: strong, weak and electromagnetic. In 1973 it was shown by Kobayashi and Maskawa that **CP** violation can be incorporated into the theory of electromagnetic and weak interactions that make up part of the Standard Model [45].

CP violation is also an important concept in cosmology. It is one of the three conditions outlined by Andrei Sakharov to account for the observed imbalance of matter and anti-matter in the universe [57]. Therefore **CP** violation, in part, explains the existence of all matter in the universe such as galaxies, stars, planets and even us!

Although **CP** violation is an integral part of the Standard Model, until recently it was one of the model's least tested areas. Currently **CP** violation is the subject of much experimental research throughout the world. Physicists are looking for **CP** violation in the decays of neutral kaons, B^0-mesons and hyperons. There is also on-going work to measure the electric dipole moment of the neutron, which is a **CP** violating quantity.

The analysis in this thesis is concerned with measuring **CP** violation in the neutral kaon system. There are two neutral kaons, one made from a down quark and an anti-strange quark, and the other made from a strange quark and an anti-down quark. The two neutral kaons are the antiparticles of each other.

In the neutral kaon system, **CP** violation is classified into two types: indirect and direct, parameterised by ϵ and ϵ' respectively. Indirect **CP** violation is observed through the asymmetry in the mixing of the two neutral kaons. This was the type of **CP** violation observed by Christenson *et al.* in 1964.

Direct **CP** violation is observed through the asymmetry in the decays of the two neutral kaons. The amount of direct **CP** violation is usually measured in terms of the parameter $\mathcal{R}e(\epsilon'/\epsilon)$, which is actually the real part of the ratio of direct to indirect **CP** violation. The expected value of this parameter is around 1 part in 1000 which means that the amount of direct **CP** violation in the kaon system is actually very small indeed: of the order of one part in a million.

Until recently, physicists were unsure whether there was any direct **CP** violation in the neutral kaon system. Two conflicting results were announced in 1993. One result from the NA31 experiment at CERN showed clear evidence for the existence of direct **CP** violation [9]. The other result from the E731 experiment at FNAL was compatible with no direct **CP** violation [31]. In order to make more precise measurements of

direct **CP** violation, two new experiments were built: NA48 at CERN and KTeV at FNAL.

This thesis presents a measurement of the **CP** violation parameter $\mathcal{R}e(\epsilon'/\epsilon)$ using data taken by the NA48 experiment in 1998. Chapter 2 describes the theory of **CP** in more detail and explains the significance of the parameters ϵ and ϵ'. Chapter 3 describes the NA48 experiment and chapter 4 describes the acquisition and reconstruction of the data from the experiment. Chapter 5 discusses the analysis technique used to measure $\mathcal{R}e(\epsilon'/\epsilon)$ and chapters 6 and 7 present the analysis of the data. Finally the measured value of $\mathcal{R}e(\epsilon'/\epsilon)$ is presented in chapter 8, where it is compared to other recent measurements and predictions.

Chapter 2

CP Violation and Neutral Kaons

This chapter introduces the theoretical background to **CP** violation in the neutral kaon system.

After introducing the discrete symmetries **C**, **P** and **T** and the neutral kaon system, the manifestations of **CP** violation in kaons is investigated. The Standard Model picture of **CP** violation, and the classification of **CP** violation into three types is also discussed.

2.1 The Discrete Symmetries C, P and T

If a symmetry is respected in an interaction it implies that relationships can be defined between different physical processes. If a unitary symmetry is respected in an interaction then this is interpreted as the conservation of a quantum number. In particular, discrete symmetries lead to conserved multiplicative quantum numbers. In particle physics there are three important discrete symmetries: Charge Conjugation, Parity and Time Reversal. A definition of these three symmetries is:

- **C: Charge Conjugation**. Charge conjugation interchanges a particle with its antiparticle. This operation reverses the electric charge, colour, hypercharge, baryon/lepton number of the particle, but leaves the space-time coordinates and momentum unchanged.
- **P: Parity**. Parity consists of inverting the three coordinates in the origin: $\vec{x} \rightarrow \vec{x}' = -\vec{x}$. Momentum is transformed from $\vec{p}$ into $-\vec{p}$. Spin and angular momentum remain unchanged and hence the helicity of objects is transformed from left-handed to right-handed.

- **T: Time Reversal.** Time reversal consists of inverting the direction of time: $t \rightarrow t' = -t$. In a reaction, the direction of momenta and the spins of each particle are reversed, and the initial and final states are swapped. **T** is an anti-unitary symmetry and leads to no conserved quantities.

Assuming only a few basic principles of relativistic quantum field theories, it has been shown by Lüders, Schwinger and Pauli that the combined symmetry **CPT** (in any order) must be conserved [51].

The individual symmetries **C**, **P** and **T** are conserved in electromagnetic and strong interactions. However, as described in the introduction, this is not the case in the weak interaction. Parity and charge conjugation violation were first observed in the same year by Wu and collaborators in β decays of polarised Cobalt-60 nuclei [67]. It was suggested by Landau, also in 1957, that weak interactions should respect the combined symmetry **CP** [46]. In 1964 Christenson, Cronin, Fitch and Turlay unexpectedly observed the decay of the long-lived neutral K meson into a 2π state [20] which, as is discussed later, implies **CP** violation in weak decays.

2.2 Introduction to the Kaon System

Kaons are mesons which contain strange quarks. Kaons, or K-mesons, are predominantly produced in strong interactions. Examples of reactions that produce strange particles, Λ and K, are:

$$\begin{aligned} \pi^- p &\rightarrow \Lambda^0 \mathrm{K}^0 \\ \overline{p} p &\rightarrow \mathrm{K}^+ \pi^- \overline{\mathrm{K}^0} \\ \overline{p} p &\rightarrow \mathrm{K}^0 \overline{\mathrm{K}^0} \\ \overline{p} p &\rightarrow \mathrm{K}^+ \mathrm{K}^- \end{aligned}$$

When they are produced the kaons and the Λ are flavour eigenstates, *i.e.* they have a known quark content:

$$|\mathrm{K}^0\rangle = \bar{\mathrm{s}}\mathrm{d} \qquad |\overline{\mathrm{K}^0}\rangle = \mathrm{s}\bar{\mathrm{d}} \qquad |\mathrm{K}^+\rangle = \bar{\mathrm{s}}\mathrm{u} \qquad |\mathrm{K}^-\rangle = \mathrm{s}\bar{\mathrm{u}} \qquad |\Lambda^0\rangle = \mathrm{sud} \tag{2.1}$$

A value of strangeness, S, can be assigned to each of these states. $\mathrm{S} = +1$ for states containing an $\bar{\mathrm{s}}$ quark, and $\mathrm{S} = -1$ for states containing an s quark. Strangeness is an additive quantum number.

The strong and electromagnetic interactions conserve the value of S. Therefore in the strong interactions above the strange particles must be produced in pairs. The kaons K^0, $\overline{\mathrm{K}^0}$, K^+ and K^- are the lightest strange mesons and therefore decay by the weak interaction, which does not conserve S.

K_L modes	branching ratio	K_S modes	branching ratio
$\pi^{\pm}e^{\mp}\nu_e$	$(38.78 \pm 0.28) \times 10^{-2}$	$\pi^+\pi^-$	$(68.61 \pm 0.28) \times 10^{-2}$
$\pi^{\pm}\mu^{\mp}\nu_\mu$	$(27.18 \pm 0.25) \times 10^{-2}$	$\pi^0\pi^0$	$(31.39 \pm 0.28) \times 10^{-2}$
$\pi^0\pi^0\pi^0$	$(21.13 \pm 0.27) \times 10^{-2}$		
$\pi^+\pi^-\pi^0$	$(12.55 \pm 0.20) \times 10^{-2}$		
$\pi^+\pi^-$	$(2.056 \pm 0.033) \times 10^{-3}$		
$\pi^0\pi^0$	$(0.937 \pm 0.019) \times 10^{-3}$		

Table 2.1: The main decay modes of K_L and K_S.

2.2.1 The Neutral Kaons

The strong eigenstates of the neutral kaons are K^0 and $\overline{K^0}$, but the observed physical (decay) states of the neutral kaons are called K-long (K_L) and K-short (K_S).

K_S and K_L have almost identical masses, but very different lifetimes. The mass of the kaons is $m_{K^0} = m_L \simeq m_S = (497.67 \pm 0.03)$ MeV/c^2 and the difference is $\Delta m_K \equiv m_L - m_S$, is $(3.489 \pm 0.008) \times 10^{-12}$ MeV/c^2. The lifetimes of K_L and K_S are $\tau_L = (5.17 \pm 0.08) \times 10^{-8}$ s, and $\tau_S = (8.935 \pm 0.008) \times 10^{-11}$ s respectively. The main decay modes of K_S and K_L are listed in table 2.1.

The relationship between the physical states K_L and K_S and the strong eigenstates K^0 and $\overline{K^0}$ is described in the following section.

2.3 Particle – Antiparticle Mixing

In this section we consider the mixing of the lightest neutral kaons K^0 and $\overline{K^0}$. This formalism can also be applied to the lightest neutral B-mesons, (B^0,$\overline{B^0}$) and ($B_s^0, \overline{B_s^0}$) and to the lightest neutral charmed mesons ($D^0, \overline{D^0}$).

K^0 and $\overline{K^0}$ are the antiparticles of each other so they may be related by **CP** and **CPT** transformations:

$$\begin{aligned} \mathbf{CP}\,|K^0\rangle &= -|\overline{K^0}\rangle & \mathbf{CP}\,|\overline{K^0}\rangle &= -|K^0\rangle \\ \mathbf{CPT}\,|K^0\rangle &= -\langle\overline{K^0}| & \mathbf{CPT}\,|\overline{K^0}\rangle &= -\langle K^0| \end{aligned} \tag{2.2}$$

where we have implicitly chosen a phase convention for the **CP** and **CPT** transformations.

Using these relations, the **CP** eigenstates of the neutral kaon system can be defined

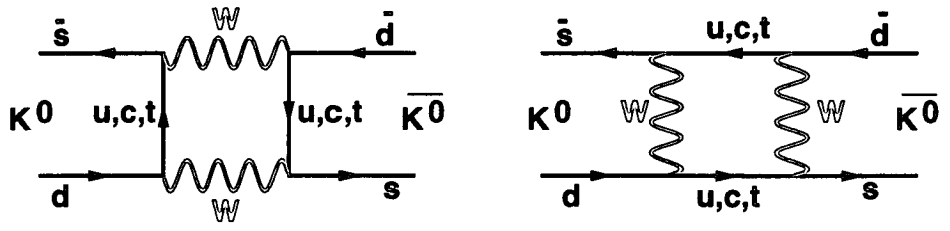

Figure 2.1: The box diagrams describing the $\Delta S = 2$ process of $K^0 \leftrightarrow \overline{K^0}$ mixing.

as:

$$\begin{aligned} |K_1\rangle &= \sqrt{\tfrac{1}{2}}\left(|K^0\rangle - |\overline{K^0}\rangle\right) \qquad \mathbf{CP}\,|K_1\rangle = +1\,|K_1\rangle \\ |K_2\rangle &= \sqrt{\tfrac{1}{2}}\left(|K^0\rangle + |\overline{K^0}\rangle\right) \qquad \mathbf{CP}\,|K_2\rangle = -1\,|K_2\rangle \end{aligned} \tag{2.3}$$

$|K_1\rangle$ and $|K_2\rangle$ are referred to as the **CP** even and **CP** odd eigenstates of the neutral kaon system.

The two kaons K^0 and $\overline{K^0}$ are distinct in the presence of the strong force. However as the weak interaction does not conserve strangeness, K^0 and $\overline{K^0}$ are allowed to mix with each other, provided that the weak Hamiltonian allows both K^0 and $\overline{K^0}$ to decay into at least one common state. For example:

$$K^0 \leftrightarrow (2\pi, 3\pi) \leftrightarrow \overline{K^0}$$

$K^0 \leftrightarrow \overline{K^0}$ mixing is a $\Delta S = 2$ process as the strangeness changes by two units. This mixing is illustrated by the two 'box diagrams' shown in figure 2.1.

To investigate the interactions of the K^0 and $\overline{K^0}$ under the weak interaction, we consider the state $|\psi(t)\rangle$ which is a linear combination of the two kaons:

$$|\psi(t)\rangle = a(t)\,|K^0\rangle + a'(t)\,|\overline{K^0}\rangle \tag{2.4}$$

2.3.1 Evolution of the Kaons

The evolution of the state $|\psi(t)\rangle$ is governed by the Schrödinger equation:

$$i\frac{\partial}{\partial t}|\psi(t)\rangle = \mathcal{H}_{\text{eff}}|\psi(t)\rangle \tag{2.5}$$

$\mathcal{H}_{\text{eff}}$ is the part of the Hamiltonian that describes the strong and electromagnetic interactions of K^0 and $\overline{K^0}$ as well as their mixing and decay due to the weak force. The remaining part of the Hamiltonian (not included in $\mathcal{H}_{\text{eff}}$) describes the creation of decay products such as $|\pi\pi\rangle$ due to the weak force.

The matrix representation of $\mathcal{H}_{\text{eff}}$ is not Hermitian. However, like any matrix it may be written as the sum of a Hermitian matrix (M) and an anti-Hermitian matrix ($-i/2\,\Gamma$):

$$\mathcal{H}_{\text{eff}} = M - \frac{i}{2}\Gamma \tag{2.6}$$

M is the mass matrix. It represents the interactions of K^0 and $\overline{\mathrm{K}^0}$ due to the strong and electromagnetic interactions where strangeness is conserved and interactions due to the weak force where strangeness changes by two units. Γ is the decay matrix. It represents the decay of the kaons due to the weak interaction where strangeness changes by one unit.

The elements of these matrices can be written in terms of the transition amplitudes between the $|\mathrm{K}^0\rangle$ and $|\overline{\mathrm{K}^0}\rangle$ states:

$$\begin{aligned}
(\mathcal{H}_{\text{eff}})_{11} &= M_{11} - \tfrac{i}{2}\Gamma_{11} = \langle \mathrm{K}^0 \,|\, \mathcal{H}_{\text{eff}} \,|\, \mathrm{K}^0 \rangle \\
(\mathcal{H}_{\text{eff}})_{12} &= M_{12} - \tfrac{i}{2}\Gamma_{12} = \langle \overline{\mathrm{K}^0} \,|\, \mathcal{H}_{\text{eff}} \,|\, \mathrm{K}^0 \rangle \\
(\mathcal{H}_{\text{eff}})_{21} &= M_{21} - \tfrac{i}{2}\Gamma_{21} = \langle \mathrm{K}^0 \,|\, \mathcal{H}_{\text{eff}} \,|\, \overline{\mathrm{K}^0} \rangle \\
(\mathcal{H}_{\text{eff}})_{22} &= M_{22} - \tfrac{i}{2}\Gamma_{22} = \langle \overline{\mathrm{K}^0} \,|\, \mathcal{H}_{\text{eff}} \,|\, \overline{\mathrm{K}^0} \rangle
\end{aligned} \tag{2.7}$$

The real and imaginary parts of $(\mathcal{H}_{\text{eff}})_{11} = \langle \mathrm{K}^0 \,|\, \mathcal{H}_{\text{eff}} \,|\, \mathrm{K}^0 \rangle$ represent respectively the mass and decay width of K^0. Similarly $(\mathcal{H}_{\text{eff}})_{22}$ is related to the mass and decay width of $\overline{\mathrm{K}^0}$.

Due to the Hermiticity of the matrices M and Γ, the terms in the diagonal elements M_{11}, M_{22}, Γ_{11} and Γ_{22} are all real. The off-diagonal elements are related by: $M_{12} = M_{21}^*$ and $\Gamma_{12} = \Gamma_{21}^*$. Using these constraints $\mathcal{H}_{\text{eff}}$ can be written as:

$$\mathcal{H}_{\text{eff}} = \begin{pmatrix} M_{11} - \frac{i}{2}\Gamma_{11} & M_{12} - \frac{i}{2}\Gamma_{12} \\ M_{12}^* - \frac{i}{2}\Gamma_{12}^* & M_{22} - \frac{i}{2}\Gamma_{22} \end{pmatrix} \tag{2.8}$$

2.3.2 Constraints from CPT Conservation

If we assume that the interactions due to $\mathcal{H}_{\text{eff}}$ are invariant under a **CPT** transformation we can write:

$$\langle \mathrm{K}^0 | \, \mathcal{H}_{\text{eff}} \, | \mathrm{K}^0 \rangle = \langle \mathrm{K}^0 | \, \mathbf{1} \, \mathcal{H}_{\text{eff}} \, \mathbf{1} \, | \mathrm{K}^0 \rangle = \langle \mathrm{K}^0 | \, \mathbf{CPT}\,\mathbf{CPT}\,\mathcal{H}_{\text{eff}}\,\mathbf{CPT}\,\mathbf{CPT} \, | \mathrm{K}^0 \rangle \tag{2.9}$$

where we have inserted $(\mathbf{CPT})^2 = \mathbf{1}$, where $\mathbf{1}$ is the unit matrix.

Now **CPT** invariance implies that $(\mathbf{CPT}\,\mathcal{H}_{\text{eff}}\,\mathbf{CPT}) = \mathcal{H}_{\text{eff}}$. So the above equation becomes:

$$\langle \mathrm{K}^0 | \, \mathbf{CPT}\,\mathcal{H}_{\text{eff}}\,\mathbf{CPT} \, | \mathrm{K}^0 \rangle = \langle \overline{\mathrm{K}^0} | \, \mathcal{H}_{\text{eff}} \, | \overline{\mathrm{K}^0} \rangle \tag{2.10}$$

where we have used the relations in equation (2.2).

This implies $M_{11} = M_{22}$ and $\Gamma_{11} = \Gamma_{22}$. Physically this means the masses and decay rates of K^0 and $\overline{K^0}$ must be equal.

Defining M_0 as the mass and Γ_0 as the decay width of K^0 and $\overline{K^0}$ the Hamiltonian can now be written as:

$$\mathcal{H}_{\text{eff}} = \begin{pmatrix} M_0 - \frac{i}{2}\Gamma_0 & M_{12} - \frac{i}{2}\Gamma_{12} \\ M_{12}^* - \frac{i}{2}\Gamma_{12}^* & M_0 - \frac{i}{2}\Gamma_0 \end{pmatrix} \tag{2.11}$$

The eigenstates of this Hamiltonian are the physical states $|K_L\rangle$ and $|K_S\rangle$ with eigenvalues λ_L and λ_S. In terms of the strong eigenstates we have:

$$\begin{aligned} |K_S\rangle &= \frac{1}{\sqrt{|p|^2+|q|^2}}\left(p\,|K^0\rangle + q\,|\overline{K^0}\rangle\right) & \mathcal{H}_{\text{eff}}|K_S\rangle &= \lambda_S|K_L\rangle \\ |K_L\rangle &= \frac{1}{\sqrt{|p|^2+|q|^2}}\left(-q\,|K^0\rangle - p\,|\overline{K^0}\rangle\right) & \mathcal{H}_{\text{eff}}|K_L\rangle &= \lambda_L|K_L\rangle \end{aligned} \tag{2.12}$$

with p and q related by:

$$\frac{p}{q} = \sqrt{\frac{M_{12} - \frac{i}{2}\Gamma_{12}}{M_{12}^* - \frac{i}{2}\Gamma_{12}^*}} \tag{2.13}$$

The eigenvalues λ_L and λ_S are:

$$\begin{aligned} \lambda_S &= m_S - \tfrac{i}{2}\Gamma_S = M_0 - \tfrac{i}{2}\Gamma_0 - \sqrt{\left(M_{12} - \frac{i}{2}\Gamma_{12}\right)\left(M_{12}^* - \frac{i}{2}\Gamma_{12}^*\right)} \\ \lambda_L &= m_L - \tfrac{i}{2}\Gamma_L = M_0 - \tfrac{i}{2}\Gamma_0 + \sqrt{\left(M_{12} - \frac{i}{2}\Gamma_{12}\right)\left(M_{12}^* - \frac{i}{2}\Gamma_{12}^*\right)} \end{aligned} \tag{2.14}$$

The parameters m_L, m_S, Γ_L and Γ_S are all real and correspond to the masses and decay rates of the particles K_L and K_S.

Using equations (2.3) and (2.12), it is also possible to write the states $|K_L\rangle$ and $|K_S\rangle$ in terms of the **CP** eigenstates $|K_1\rangle$ and $|K_2\rangle$:

$$\begin{aligned} |K_S\rangle &= \frac{1}{\sqrt{2(|p|^2+|q|^2)}}\left((p+q)\,|K_1\rangle + (p-q)\,|K_2\rangle\right) \\ |K_L\rangle &= \frac{1}{\sqrt{2(|p|^2+|q|^2)}}\left((p-q)\,|K_1\rangle + (p+q)\,|K_2\rangle\right) \end{aligned} \tag{2.15}$$

In the kaon system, the amount of **CP** violation is small. It is conventional to define an asymmetry parameter $\bar{\epsilon} = (p-q)/(p+q)$. Then we can write:

$$\begin{aligned} |K_S\rangle &= \frac{1}{\sqrt{1+|\bar{\epsilon}|^2}}\left(|K_1\rangle + \bar{\epsilon}\,|K_2\rangle\right) = \frac{1}{N_K}\left[(1+\bar{\epsilon})\,|K^0\rangle - (1-\bar{\epsilon})\,|\overline{K^0}\rangle\right] \\ |K_L\rangle &= \frac{1}{\sqrt{1+|\bar{\epsilon}|^2}}\left(|K_2\rangle + \bar{\epsilon}\,|K_1\rangle\right) = \frac{1}{N_K}\left[(1+\bar{\epsilon})\,|K^0\rangle + (1-\bar{\epsilon})\,|\overline{K^0}\rangle\right] \end{aligned} \tag{2.16}$$

where $N_K = \sqrt{2(1+|\bar{\epsilon}|^2)}$.

2.3.3 CP Conservation

Now let us consider for a moment what happens if **CP** is conserved in addition to **CPT**.

Following the method of equations (2.9) and (2.10) and using the fact that $(\mathbf{CP})^2 = \mathbf{1}$:

$$\langle \overline{K^0} | \mathcal{H}_{\text{eff}} | K^0 \rangle = \langle K^0 | \mathbf{CP}\, \mathcal{H}_{\text{eff}}\, \mathbf{CP} | K^0 \rangle = \langle K^0 | \mathcal{H}_{\text{eff}} | \overline{K^0} \rangle \tag{2.17}$$

This means the elements M_{12} and Γ_{12} of $\mathcal{H}_{\text{eff}}$ have no relative phase.

Using equation (2.13), this implies that $|p/q| = 1$. If we choose a phase convention such that p and q are real then the asymmetry parameter $\overline{\epsilon}$ is 0. Using equation (2.16) the physical states can then be written as:

$$|K_S\rangle = |K_1\rangle \qquad |K_L\rangle = |K_2\rangle \tag{2.18}$$

Therefore if **CP** is conserved, the physical states are identical to the **CP** eigenstates. Or conversely, if the physical states are not identical to the **CP** eigenstates, **CP** is violated due to the mixing of the states $|K^0\rangle$ and $|\overline{K^0}\rangle$.

2.4 CP Violation in $K_L \to \pi\pi$ decays

To observe if **CP** is respected in the interactions of the neutral kaons we can look at the decay products of K_L and K_S.

The only purely hadronic decay modes of the neutral kaons are $\pi\pi$ and $\pi\pi\pi$. These states are **CP** eigenstates. The **CP** eigenvalue for these states from K^0 decays are:

$$\begin{array}{llll} \mathbf{CP}\,|\pi^+\pi^-\rangle = +1\,|\pi^+\pi^-\rangle & & \mathbf{CP}\,|\pi^0\pi^0\pi^0\rangle = -1\,|\pi^0\pi^0\pi^0\rangle \\ \mathbf{CP}\,|\pi^0\pi^0\rangle = +1\,|\pi^0\pi^0\rangle & & \mathbf{CP}\,|\pi^+\pi^-\pi^0\rangle = -(-1)^{L_{\pi^0}}\,|\pi^+\pi^-\pi^0\rangle \end{array} \tag{2.19}$$

In the $\pi^+\pi^-\pi^0$ final state, $L_{\pi^0} = 0$ is strongly favoured due to the small amount of energy released in the decay. In terms of the **CP** eignestates, the **CP** conserving decays are therefore $K_1 \to \pi\pi$ and predominantly $K_2 \to \pi\pi\pi$.

As shown in table 2.1, K_L is observed to decay to both 3 pion and 2 pion final states. This means that K_L can decay to both $\mathbf{CP} = +1$ and $\mathbf{CP} = -1$ final states, and therefore **CP** is not conserved.

There are two ways to explain how this **CP** violation takes place:

1. K_L has a component from both K_1 and K_2, and hence K_L is not a **CP** eigenstate. As discussed in section 2.3.3, this means that **CP** is violated due to the mixing of the kaons. In the kaon system **CP** violation in mixing is also called **indirect CP violation**.

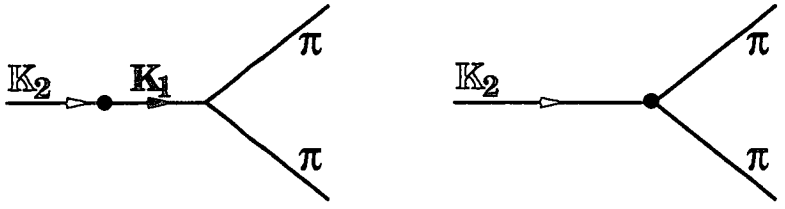

Figure 2.2: Illustration of the **CP** violating processes contributing to $K_L \to \pi\pi$. On the left, indirect **CP** violation: the K_2 part of K_L becomes a K_1 through mixing, before decaying to two pions. On the right, direct **CP** violation: the K_2 part of K_L decays *directly* to two pions.

2. **CP** symmetry is violated in the decay, *i.e.* the K_2 part of K_L can decay directly to 2 pions. In the kaon system **CP** violation in decay is also called **direct CP violation.**

These two possibilities are illustrated in figure 2.2. Actually both indirect and direct **CP** violation are involved in $K_L \to \pi\pi$ decays.

In the following section we will see how it is possible to disentangle these two types of **CP** violation through experimental observation. Also in sections 2.7 and 2.9 we will quantify the amount of indirect and direct **CP** violation in the kaon system.

2.5 Classification of CP Violation

It is possible to classify **CP** violation into three distinct types. To do this consider the decay of a pseudoscalar meson P^0 (such as a K^0 or B^0) into a final state f: $P^0 \to f$. The amplitude of this decay, A_f, can be expanded as

$$A_f = \sum_j A_j \, e^{i\phi_j} \, e^{i\delta_j} \tag{2.20}$$

The A_j terms are the magnitude of the decay from the weak Lagrangian. The $e^{i\phi}$ terms describe the phase shift due to the weak Lagrangian and the $e^{i\delta}$ terms describe the phase shift due to strong final state interactions.

The amplitude of the **CP** conjugate decay $\overline{A} \to \overline{f}$ is:

$$\overline{A}_{\overline{f}} = \sum_j A_j \, e^{-i\phi_j} \, e^{i\delta_j} \tag{2.21}$$

The sign of the phase shifts due to the weak decay change, but phase shifts due to the strong final state interactions are not affected by the **CP** transformation.

The three types of **CP** violation can now be defined as follows:

1. CP Violation in Mixing. This occurs if the weak eigenstates are not identical to the **CP** eigenstates, as discussed in section 2.3.3. In this case $|q/p| \neq 1$. This **CP** violation can be observed by looking at the decay rates of the weak eigenstates P_1 and P_2 into a final state f. We can define an asymmetry parameter, a:

$$a = \frac{\Gamma(P_1 \to f) - \Gamma(P_2 \to \overline{f})}{\Gamma(P_1 \to f) + \Gamma(P_2 \to \overline{f})} = \frac{1 - |p/q|^4}{1 + |p/q|^4} \tag{2.22}$$

For example the semi-leptonic decays of neutral kaons and B-mesons exhibit this asymmetry. A similar asymmetry is discussed in section 2.9.2, illustrating **CP** violation in mixing in neutral kaon decays.

2. CP Violation in Decay. This occurs if the amplitude of the decay $P^0 \to f$ is not equal to that of its **CP** conjugate decay: $\overline{P^0} \to \overline{f}$. Then $|A_f/\overline{A}_{\overline{f}}| \neq 1$. This can be observed in the decays of the P^0 and $\overline{P^0}$, again by looking at the asymmetry, a:

$$a = \frac{\Gamma(P^0 \to f) - \Gamma(\overline{P^0} \to \overline{f})}{\Gamma(P^0 \to f) + \Gamma(\overline{P^0} \to \overline{f})} = \frac{1 - |\overline{A}_{\overline{f}}/A_f|^2}{1 + |\overline{A}_{\overline{f}}/A_f|^2} \tag{2.23}$$

We can expand the $|\overline{A}_{\overline{f}}/A_f|$ term as:

$$\left|\frac{\overline{A}_{\overline{f}}}{A_f}\right| = \left|\frac{\sum_j A_j e^{-i(\phi_j + \delta_j)}}{\sum_j A_j e^{-i(\phi_j - \delta_j)}}\right| \tag{2.24}$$

This **CP** violation requires that the decay $P^0 \to f$ has a contribution from at least two weak processes. Only one contribution would give $|\overline{A}_{\overline{f}}/A_f| = 1$ and hence an asymmetry of 0. As an example consider a decay with two weak phases, assuming $A_2 \ll A_1$ gives

$$a = -2\frac{A_2}{A_1}\sin(\delta_2 - \delta_1)\sin(\phi_2 - \phi_1) \tag{2.25}$$

Therefore both the weak and the strong phases must be different.

As the asymmetry is observed by looking at the decays of the flavour eigenstates, this type of **CP** violation can also occur in the decays of charged mesons, which are also flavour eigenstates.

As discussed in section 2.9.5, the parameter $\mathcal{R}e\,\epsilon'$ is a measurement of this type of **CP** violation in the neutral kaon system.

3. CP Violation due to the Interference of Decays With and Without Mixing. This can occur if P^0 and $\overline{P^0}$ can decay to a common **CP** eigenstate f_{CP}. To classify this we define the parameter λ_f:

$$\lambda_f = \frac{q}{p}\frac{\overline{A}_{\overline{f}}}{A_f} \tag{2.26}$$

This parameter is independent of any phase convention [39]. **CP** violation occurs in interference if $|\lambda_f| = 1$ but $\mathcal{I}m\lambda_f \neq 0$. This can be observed by looking at the time dependent asymmetry in the decays of the decay states into common **CP** eigenstate $f_{\rm CP}$:

$$a = \frac{\Gamma(P_1(t) \to f_{\rm CP}) - \Gamma(P_2(t) \to f_{\rm CP})}{\Gamma(P_1(t) \to f_{\rm CP}) + \Gamma(P_2(t) \to f_{\rm CP})} = -\mathcal{I}m\lambda_{f_{\rm CP}} \sin(\Delta m t) \tag{2.27}$$

An example of this asymmetry is given later in section 2.6.3.

This classification of the types of **CP** violation will be used later when we discuss the phenomenology of $\mathrm{K} \to \pi\pi$ decays.

2.6 CP Violation in the Standard Model

In the Standard Model, **CP** violation is described in the electroweak sector by a single complex phase in the quark mixing matrix.

The interactions of quarks with the charged gauge bosons of the electroweak sector ($W^{\pm}$) are described by:

$$\mathcal{L} = -i\frac{g_W}{2\sqrt{2}} \sum_{i,j} \overline{u_i'}\, \gamma^{\mu}(1-\gamma^5)\, d_j'\, W_{\mu}^{+} + \text{hermitian conjugate} \tag{2.28}$$

where u_i' and and d_j' are weak eigenstates of the up-type and down-type quarks respectively. The subscripts $i, j = 1, 2, 3$ run over the three generations of quarks.

The mass eigenstates (u_i and d_j) can be written as a linear combination of the weak eigenstates as follows:

$$u_i = \sum_{i'=1}^{3} \tilde{U}_{ii'}\, u_{i'}' \qquad d_j = \sum_{j'=1}^{3} \tilde{V}_{jj'}\, d_{j'}' \tag{2.29}$$

The terms $\tilde{U}_{ii'}$ and $\tilde{V}_{jj'}$ are elements of 3×3 matrices.

Rewriting equation (2.28) in terms of the mass eigenstates of the quarks gives:

$$\mathcal{L} = -i\frac{g_W}{2\sqrt{2}} \sum_{i,j} \left(\tilde{V}_{jk}\tilde{U}_{ki}^{\dagger}\right) \overline{u_i}\, \gamma^{\mu}(1-\gamma^5)\, d_j\, W_{\mu}^{+} + \text{hermitian conjugate} \tag{2.30}$$

We can define the Cabibbo-Kobayashi-Maskawa (CKM) quark mixing matrix as $(V_{\rm CKM})_{ij} = (\tilde{V}_{jk}\tilde{U}_{ki}^{\dagger})$:

$$V_{\rm CKM} = \begin{pmatrix} V_{\rm ud} & V_{\rm us} & V_{\rm ub} \\ V_{\rm cd} & V_{\rm cs} & V_{\rm cb} \\ V_{\rm td} & V_{\rm ts} & V_{\rm tb} \end{pmatrix} \tag{2.31}$$

Field theory requires that this matrix is unitary ($V_{\rm CKM}V_{\rm CKM}^{\dagger} = 1$). In general a unitary 3×3 matrix has 3 real parameters and 6 phases. In the case of quark fields, only the relative phase between the fields can be observed. Five of these phases, ϕ, can be used to redefine the quark fields. This is equivalent to rephasing the CKM elements, *eg* $V_{\rm ud} \rightarrow V_{\rm ud}e^{i(\phi_{\rm d}-\phi_{\rm u})}$. This rephasing leaves only one observable phase in the CKM matrix.

It is this irremovable phase in the CKM matrix that allows possible **CP** violation. To see this consider again the coupling of the quarks to $W^{\pm}$ (equation (2.30)):

$$V_{ij}\,\overline{\mathrm{u}_i}\,\gamma^{\mu}(1-\gamma^5)\,\mathrm{d}_j\,W_{\mu}^{+} + V_{ij}^{*}\,\overline{\mathrm{d}_j}\,\gamma^{\mu}(1-\gamma^5)\,\mathrm{u}_i\,W_{\mu}^{-} \tag{2.32}$$

Under a **CP** transformation the terms in equation (2.32) transform as [39]:

$$\begin{aligned} W_{\mu}^{\pm} &\longrightarrow -(-1)^{\mu}\,W_{\mu}^{\mp} \\ \overline{\mathrm{u}_i}\,\gamma^{\mu}\,\mathrm{d}_j &\longrightarrow -(-1)^{\mu}\,\overline{\mathrm{d}_j}\,\gamma^{\mu}\,\mathrm{u}_i \\ \overline{\mathrm{u}_i}\,\gamma^{\mu}\,\gamma^5\,\mathrm{d}_j &\longrightarrow -(-1)^{\mu}\,\overline{\mathrm{d}_j}\,\gamma^{\mu}\,\gamma^5\,\mathrm{u}_i \end{aligned} \tag{2.33}$$

with similar terms for ($\mathrm{u} \leftrightarrow \mathrm{d}$). Therefore a **CP** transformation on equation (2.32) gives:

$$V_{ij}\,\overline{\mathrm{d}_j}\,\gamma^{\mu}(1-\gamma^5)\,\mathrm{u}_i\,W_{\mu}^{-} + V_{ij}^{*}\,\overline{\mathrm{u}_i}\,\gamma^{\mu}(1-\gamma^5)\,\mathrm{d}_j\,W_{\mu}^{+} \tag{2.34}$$

The two terms have effectively been interchanged with the exception of the CKM elements, V_{ij} and V_{ij}^{*}. Therefore **CP** is a good symmetry only if we could choose all of the CKM elements to be real.

There are three situations in which we can define all the CKM elements to be real:

1. Two quarks of the same charge have equal mass.
2. One of the three real parameters is 0 or $\frac{\pi}{2}$.
3. The single complex phase is 0 or π.

To summarise the last two conditions it is useful to define the Jarlskog **CP** parameter, J [44]:

$$\mathcal{I}m\left[V_{ij}\,V_{kl}\,V_{il}^{*}\,V_{kj}^{*}\right] = J\sum_{m,n=1}^{3}\epsilon_{ikm}\epsilon_{jln} \qquad \text{for any choice of } i,j,k,l = 1,2,3 \tag{2.35}$$

The conditions on the angles and phases for **CP** violation to occur can be summarised as: $J \neq 0$.

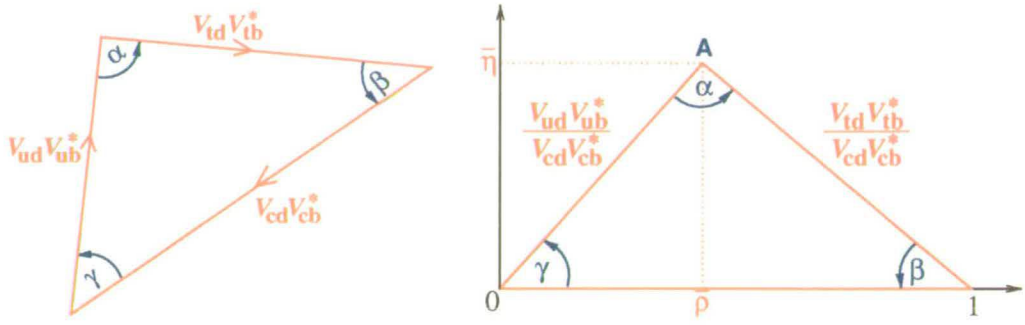

Figure 2.3: The Unitarity Triangle. The diagram on the left shows the unitary relation $V_{ud}V_{ub}^* + V_{cd}V_{cb}^* + V_{td}V_{tb}^* = 0$ in graphical form. On the right the sides of the triangle have been rescaled by $V_{cd}V_{cb}^*$.

2.6.1 The Unitarity Triangle(s)

The unitarity of the CKM matrix allows us to define relations between its elements. For example three commonly used relations are:

$$\begin{array}{ccccccc} V_{ud}V_{us}^* & + & V_{cd}V_{cs}^* & + & V_{td}V_{ts}^* & = & 0 \\ V_{us}V_{ub}^* & + & V_{cs}V_{cb}^* & + & V_{ts}V_{tb}^* & = & 0 \\ V_{ud}V_{ub}^* & + & V_{cd}V_{cb}^* & + & V_{td}V_{tb}^* & = & 0 \end{array} \tag{2.36}$$

These relations define the so-called *unitarity triangles* as they can be graphically represented by triangles in the complex plane. In total there are six unitarity triangles. Figure 2.3 shows the third relation graphically. The other two relations of equation (2.36) have two terms which are much larger than the third – pictorially they look more like lines than triangles. For this reason the triangle shown in figure 2.3 is known as *the* unitarity triangle. Any subsequent reference to the unitarity triangle refers to this triangle. It is conventional to rescale the sides of the unitarity triangle by normalising them to $V_{cd}V_{cb}^*$, so that one side has unit length and lies along the real axis.

Equation (2.35) can be used to show that all the unitarity triangles have an area of $|J|/2$ [39].

2.6.2 The Wolfenstein Parameterisation

It is useful to parameterise the CKM matrix in terms of its three real parameters and a complex phase. A popular choice is due to Wolfenstein [65]. The parameters are A, λ, ρ and η with $\lambda = |V_{us}| = 0.22$ used as an expansion parameter and $\tan^{-1}(\eta/\rho)$ representing the complex phase. To order λ^4 for the real part and to order λ^6 for the

imaginary part:

$$V_{\rm CKM} = \begin{pmatrix} 1-\frac{1}{2}\lambda^2 & \lambda & A\lambda^3\rho \\ -\lambda & 1-\frac{1}{2}\lambda^2 & A\lambda^2 \\ A\lambda^3[1-\overline{\rho}] & -A\lambda^2 & 1 \end{pmatrix} + i \begin{pmatrix} 0 & 0 & -A\lambda^3\eta \\ -A^2\lambda^5\eta & 0 & 0 \\ -A\lambda^3\overline{\eta} & -A\lambda^4\eta & 0 \end{pmatrix} \tag{2.37}$$

where

$$\overline{\rho} = \rho\left(1-\frac{\lambda^2}{2}\right) \qquad \overline{\eta} = \eta\left(1-\frac{\lambda^2}{2}\right) \tag{2.38}$$

Using this notation we can write the terms in the unitarity triangle (equation (2.36)) as:

$$\begin{aligned} V_{\rm ud}V_{\rm ub}^* &= A\lambda^3(\overline{\rho}+i\overline{\eta}) + \mathcal{O}(\lambda^7) \\ V_{\rm cd}V_{\rm cb}^* &= -A\lambda^3 + \mathcal{O}(\lambda^7) \\ V_{\rm td}V_{\rm tb}^* &= A\lambda^3(1-\overline{\rho}-i\overline{\eta}) + \mathcal{O}(\lambda^6) \end{aligned} \tag{2.39}$$

Then the sides of the triangle can be written as:

$$0{\rm A} \equiv -\frac{V_{\rm ud}V_{\rm ub}^*}{V_{\rm cd}V_{\rm cb}} = \overline{\rho}+i\overline{\eta} \qquad {\rm AB} \equiv -\frac{V_{\rm td}V_{\rm tb}^*}{V_{\rm cd}V_{\rm cb}} = 1-\overline{\rho}-i\overline{\eta} \tag{2.40}$$

We can also define the angles α, β and γ of the unitarity triangle as:

$$\alpha \equiv \arg\left[-\frac{V_{\rm td}V_{\rm tb}^*}{V_{\rm ud}V_{\rm ub}^*}\right] \qquad \beta \equiv \arg\left[-\frac{V_{\rm cd}V_{\rm cb}^*}{V_{\rm td}V_{\rm tb}^*}\right] \qquad \gamma \equiv \arg\left[-\frac{V_{\rm ud}V_{\rm ub}^*}{V_{\rm cd}V_{\rm cb}^*}\right] \tag{2.41}$$

2.6.3 B^0 Physics

It is the aim of current experiments in the B^0 system to measure the angles α, β and γ and the values of $|V_{\rm cb}|$ and $|V_{\rm ub}|$ in order to over-constrain the unitarity triangle and expose any discrepancies in the Standard Model picture of **CP** violation. The current best constraints on $\overline{\rho}$ and $\overline{\eta}$ are shown in figure 2.4. The method for extracting these **CP** violation parameters from B^0 and $\overline{B^0}$ decays can be found in [39].

As an example, the time-dependent asymmetry of the decays of B^0 and $\overline{B^0}$ into the **CP** $= -1$ eigenstate, $J/\psi\,K_S$, can be related to $\sin 2\beta$:

$$A(t) = \frac{\Gamma(B^0(t) \to J/\psi\,K_S) - \Gamma(\overline{B^0}(t) \to J/\psi\,K_S)}{\Gamma(B^0(t) \to J/\psi\,K_S) + \Gamma(\overline{B^0}(t) \to J/\psi\,K_S)} \simeq \sin(2\beta)\,\sin(\Delta m_B t) \tag{2.42}$$

where Δm_B is the mass difference between B^0 and $\overline{B^0}$. Comparing this asymmetry to equation (2.27), a non-zero measurement of $\sin 2\beta$ would be an observation of **CP** violation due to the interference of decays with and without mixing.

Currently there are three measurements of $\sin 2\beta$: $\sin 2\beta = 0.79^{+0.41}_{-0.44}$ from CDF [1], $0.45^{+0.44}_{-0.45}$ from Belle [3] and $\sin 2\beta = 0.12 \pm 0.37({\rm stat}) \pm 0.09({\rm syst})$ from BaBar [41]. The

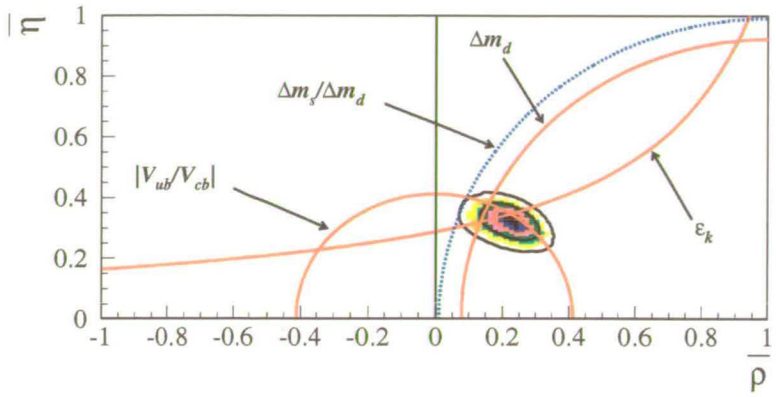

Figure 2.4: Current bounds on the Wolfenstein parameters $\overline{\eta}$ and $\overline{\rho}$, taken from [13].

prospects for improved measurements of $\sin 2\beta$ and other **CP** violation parameters in the B^0 system are very good: the BaBar experiment at the SLAC B-factory and the BELLE experiment at KEK2 will continue to take more data and the CDF and D0 experiments at the Tevatron will recommence data-taking in 2001, after a major upgrade of the detectors and accelerator.

2.7 Phenomenology of K → π π Decays

In order to quantify the amount of **CP** violation in the neutral kaon system it is useful to look at the decays of the K_L and K_S into the 2 pion states, $\pi^+\pi^-$ and $\pi^0\pi^0$.

In principle it is also possible to quantify the **CP** violation in the neutral kaon system by looking at the decays into 3 pions. However, experimental measurements of the 3 pion decays are difficult due to the small values of $BR(K_S \to 3\pi)$. Currently only $BR(K_S \to \pi^+\pi^-\pi^0) = (3.2^{+1.2}_{-1.0}) \times 10^{-7}$ [37] has been measured. $BR(K_S \to 3\pi^0)$ is expected to be the same order of magnitude.

Feynman diagrams for the decay $K \to \pi\pi$ are shown in figures 2.5 and 2.6. The value of strangeness changes by one unit in these decays, so they are referred to as $\Delta S = 1$ processes. To first order (at order G_F) strangeness changing processes only take place through charged current ($W^{\pm}$) interactions. These are illustrated in figure 2.5. At the next order, strangeness changing processes can take place through neutral current (Z^0, γ) interactions and gluon exchange, as illustrated by the penguin diagrams in figure 2.6. The upper two diagrams illustrate the neutral current interactions which contribute at order ${G_F}^2\alpha_{em}$. The lower diagram is the gluonic penguin which contributes at order ${G_F}^2\alpha_S$.

Pions form an isotriplet of $I = 1$, the third component of isospin is $I_3 = +1$ for a π^+,

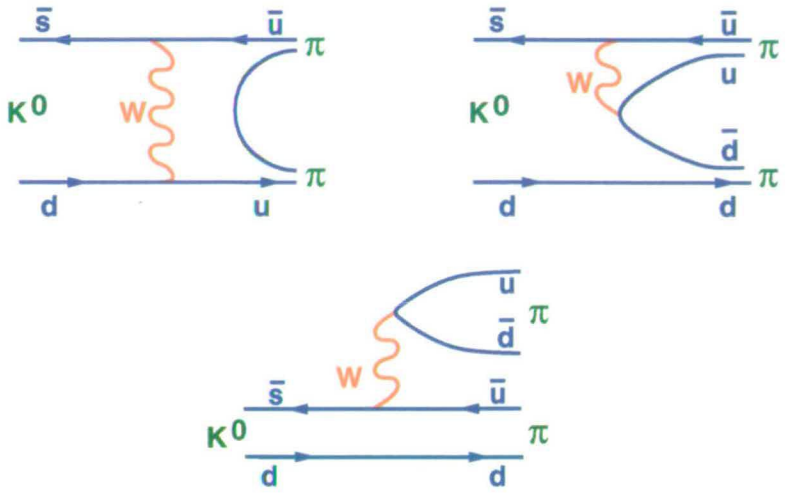

Figure 2.5: Feynman diagrams for first order contributions to $K \to \pi\pi$ decays.

$I_3 = 0$ for a π^0 and $I_3 = -1$ for a π^-. A combination of two pions can have either total isospin $I = 0$ or $I = 2$. An $I = 1$ final state is forbidden by Bose symmetry. The decomposition of the $\pi^+\pi^-$ and $\pi^0\pi^0$ states is as follows:

$$\begin{aligned} \langle \pi^+\pi^- | &= \sqrt{\tfrac{2}{3}}\, \langle (\pi\pi)_{I=0} | + \sqrt{\tfrac{1}{3}}\, \langle (\pi\pi)_{I=2} | \\ \langle \pi^0\pi^0 | &= -\sqrt{\tfrac{1}{3}}\, \langle (\pi\pi)_{I=0} | + \sqrt{\tfrac{2}{3}}\, \langle (\pi\pi)_{I=2} | \end{aligned} \tag{2.43}$$

There are therefore four transition amplitudes to describe neutral kaons decaying into a $\pi\pi$ pair of given isospin:

$$\begin{aligned} \mathcal{A}(\mathrm{K_S} \to (\pi\pi)_{I=0}) &= \langle (\pi\pi)_{I=0} \,|\, \mathcal{H} \,|\, \mathrm{K_S} \rangle \\ \mathcal{A}(\mathrm{K_L} \to (\pi\pi)_{I=0}) &= \langle (\pi\pi)_{I=0} \,|\, \mathcal{H} \,|\, \mathrm{K_L} \rangle \\ \mathcal{A}(\mathrm{K_S} \to (\pi\pi)_{I=2}) &= \langle (\pi\pi)_{I=2} \,|\, \mathcal{H} \,|\, \mathrm{K_S} \rangle \\ \mathcal{A}(\mathrm{K_L} \to (\pi\pi)_{I=2}) &= \langle (\pi\pi)_{I=2} \,|\, \mathcal{H} \,|\, \mathrm{K_L} \rangle \end{aligned} \tag{2.44}$$

Normalising to the dominant $\mathcal{A}(\mathrm{K_S} \to (\pi\pi)_{I=0})$ amplitude, we can define three complex numbers ϵ, ω and ϵ_2:

$$\epsilon \equiv \frac{\mathcal{A}(\mathrm{K_L} \to (\pi\pi)_{I=0})}{\mathcal{A}(\mathrm{K_S} \to (\pi\pi)_{I=0})} \tag{2.45}$$

$$\omega \equiv \frac{\mathcal{A}(\mathrm{K_S} \to (\pi\pi)_{I=2})}{\mathcal{A}(\mathrm{K_S} \to (\pi\pi)_{I=0})} \tag{2.46}$$

$$\epsilon_2 \equiv \frac{1}{\sqrt{2}} \frac{\mathcal{A}(\mathrm{K_L} \to (\pi\pi)_{I=2})}{\mathcal{A}(\mathrm{K_S} \to (\pi\pi)_{I=0})} \tag{2.47}$$

Instead of using ϵ_2 we choose to work with ϵ' which is defined as:

$$\epsilon' \equiv \epsilon_2 - \epsilon\,\omega/\sqrt{2} \tag{2.48}$$

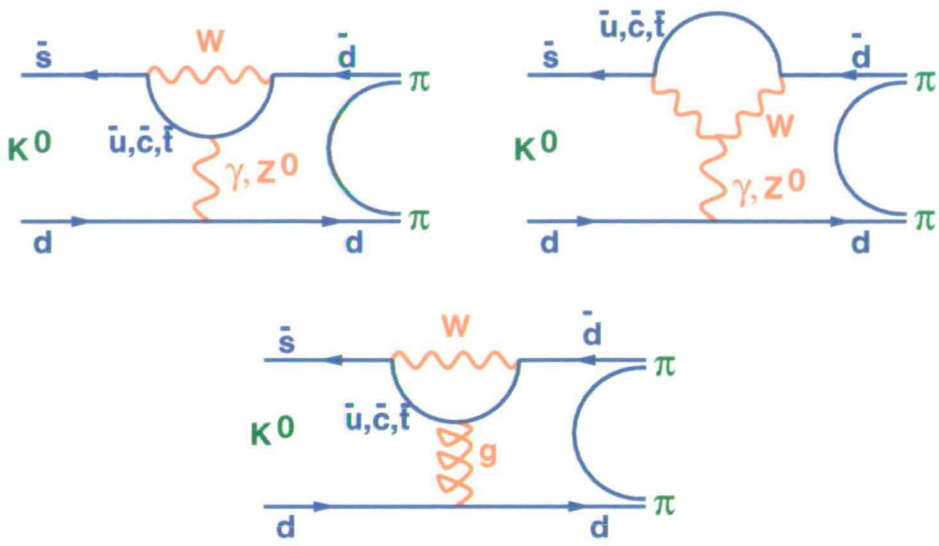

Figure 2.6: The three Penguin diagrams describing second order contributions to $\Delta S = 1$ decay $K \to \pi\pi$

We would like to relate the parameters ϵ, ω and ϵ' to the measurable quantities η_{00}, η_{+-} and δ:

$$\begin{aligned} \eta_{00} &= \frac{\mathcal{A}(K_L \to \pi^0\pi^0)}{\mathcal{A}(K_S \to \pi^0\pi^0)} = |\eta_{00}|\, e^{i\phi_{00}} = X(2.285 \pm 0.019) \times 10^{-3}\, e^{i\phi_{00}} \\ \eta_{+-} &= \frac{\mathcal{A}(K_L \to \pi^+\pi^-)}{\mathcal{A}(K_S \to \pi^+\pi^-)} = |\eta_{+-}|\, e^{i\phi_{+-}} = X(2.275 \pm 0.019) \times 10^{-3}\, e^{i\phi_{+-}} \end{aligned} \tag{2.49}$$

$$\delta = \frac{\Gamma(K_L \to \pi^-\ell^+\nu_\ell) - \Gamma(K_L \to \pi^+\ell^-\overline{\nu_\ell})}{\Gamma(K_L \to \pi^-\ell^+\nu_\ell) + \Gamma(K_L \to \pi^+\ell^-\overline{\nu_\ell})} = (3.27 \pm 0.12) \times 10^{-3} \tag{2.50}$$

The three quantities ϵ, ω and ϵ' are discussed in more detail in the following sections.

2.7.1 Notation

At this point, it is useful to introduce notation separating the weak and strong effects in the decay amplitudes of K^0 and $\overline{K^0}$, as discussed in section 2.5:

$$\mathcal{A}\left(K^0 \to (\pi\pi)_I\right) = A_I\, e^{i\delta_I} \qquad \mathcal{A}\left(\overline{K^0} \to (\pi\pi)_I\right) = A_I^*\, e^{i\delta_I} \tag{2.51}$$

Here the weak phases ϕ are included in the A_I, so A_0 and A_2 are the complex weak amplitudes. The δ_0 and δ_2 are the strong phases. Recall that as the strong phases come about from final state interactions between the pions, δ_0 and δ_2 do not change sign between K^0 and $\overline{K^0}$, whereas the weak phases do.

Since only the relative phases between the decay modes is observable, we are free to choose a phase convention where $\mathcal{I}mA_0 \ll \mathcal{R}eA_0$. This is known as the Wu-Yang phase convention [66] and we will use it where it is convenient to do so.

Two useful relations in terms of the A_I and δ_I may be derived. Using equation (2.16), we can write:

$$\begin{aligned}\mathcal{A}(\mathrm{K_S} \to (\pi\pi)_I) &= \frac{1}{N_\mathrm{K}}\left[(1+\bar{\epsilon})\,\mathcal{A}\left(\mathrm{K^0} \to (\pi\pi)_I\right) + (1-\bar{\epsilon})\,\mathcal{A}\left(\overline{\mathrm{K^0}} \to (\pi\pi)_I\right)\right] \\ &= \frac{2}{N_\mathrm{K}}\, e^{i\delta_I}\left[\mathcal{R}eA_I + i\,\bar{\epsilon}\,\mathcal{I}mA_I\right] \qquad \text{where } I = 0, 2 \end{aligned} \tag{2.52}$$

Likewise;

$$\mathcal{A}(\mathrm{K_L} \to (\pi\pi)_I) = \frac{2}{N_\mathrm{K}}\, e^{i\delta_I}\left[\bar{\epsilon}\,\mathcal{R}eA_I + i\,\mathcal{I}mA_I\right] \tag{2.53}$$

2.8 The $\Delta I = \frac{1}{2}$ Rule

The parameter ω defined in equation (2.46) is the ratio of the amplitudes of two isospin-breaking processes. These two processes are $\mathrm{K_S} \to (\pi\pi)_{I=0}$, where isospin changes by $\frac{1}{2}$, and $\mathrm{K_S} \to (\pi\pi)_{I=2}$, where isospin changes by $\frac{3}{2}$. Weak decays do not conserve the value of isospin, but it is observed that isospin symmetry is only broken minimally [49]. Hence we expect the $\Delta I = \frac{3}{2}$ transition to be suppressed with respect to the $\Delta I = \frac{1}{2}$ transition implying that ω will be small.

In terms of the notation introduced in equation (2.51) we can write:

$$\omega = e^{i(\delta_2-\delta_0)}\,\frac{\mathcal{R}eA_2 + i\,\bar{\epsilon}\,\mathcal{I}mA_2}{\mathcal{R}eA_0 + i\,\bar{\epsilon}\,\mathcal{I}mA_0} \simeq e^{i(\delta_2-\delta_0)}\,\frac{\mathcal{R}eA_2}{\mathcal{R}eA_0} \tag{2.54}$$

where we have made the approximation that $\bar{\epsilon}\,\mathcal{I}mA_I \ll \mathcal{R}eA_I$.

The magnitude of $|\omega|$ is measured to be 0.045 and the phase $(\delta_2 - \delta_0) = \arg(\omega)$ is measured to be $(-42 \pm 8)°$. Using equation (2.54) we see that $\mathcal{R}eA_2/\mathcal{R}eA_0 = 1/22.2$.

The smallness of ω means the decay of a neutral kaon to an $I = 2$ final state is suppressed by a factor of $\simeq 22$ compared to a decay into an $I = 0$ final state. This result is often referred to as the **$\Delta I = \frac{1}{2}$ rule** indicating that isospin symmetry is only minimally broken in $\mathrm{K} \to \pi\pi$ decays.

2.9 Indirect and Direct CP Violation

The parameters ϵ and ϵ' defined in equations (2.45) and (2.48) are ratios of the amplitudes of the **CP** violating decays $\mathrm{K_L} \to \pi\pi$ to the **CP** conserving decay $\mathrm{K_S} \to (\pi\pi)_{I=0}$. Therefore both ϵ and ϵ' measure **CP** violation in the neutral kaon system.

We have already seen in section 2.4, that there are two possible contributions to the process $K_L \to \pi\pi$: indirect **CP** violation, where the K_1 part of the K_L decays to two pions and direct **CP** violation where the K_2 part of the K_L decays directly to two pions. We will see below that ϵ is a measure of indirect **CP** violation and ϵ' is a measure of direct **CP** violation.

2.9.1 Expressions for ϵ and ϵ'

In this subsection we will derive some expressions for ϵ and ϵ'. In the following subsections we will use these expressions to investigate how the parameters may be measured, and what type of **CP** violation they measure.

η_{00} and η_{+-}. First we investigate the parameters η_{00} and η_{+-} defined in equation (2.49). η_{00} may be expanded as follows:

$$\begin{aligned}
\eta_{00} &= \frac{\mathcal{A}(K_L \to \pi^0\pi^0)}{\mathcal{A}(K_S \to \pi^0\pi^0)} \\
&= \frac{\sqrt{\frac{1}{3}}\mathcal{A}(K_L \to (\pi\pi)_{I=0}) - \sqrt{\frac{2}{3}}\mathcal{A}(K_L \to (\pi\pi)_{I=2})}{\sqrt{\frac{1}{3}}\mathcal{A}(K_S \to (\pi\pi)_{I=0}) - \sqrt{\frac{2}{3}}\mathcal{A}(K_S \to (\pi\pi)_{I=2})} \\
&= \epsilon - \frac{2\epsilon'}{1-\sqrt{2}\omega}
\end{aligned} \tag{2.55}$$

where we have used the definitions of ϵ, ω and ϵ' given in equations (2.45)–(2.48) and the isospin decomposition in equation (2.43). Similarly;

$$\begin{aligned}
\eta_{+-} &= \frac{\mathcal{A}(K_L \to \pi^+\pi^-)}{\mathcal{A}(K_S \to \pi^+\pi^-)} \\
&= \frac{\sqrt{\frac{2}{3}}\mathcal{A}(K_L \to (\pi\pi)_{I=0}) + \sqrt{\frac{1}{3}}\mathcal{A}(K_L \to (\pi\pi)_{I=2})}{\sqrt{\frac{2}{3}}\mathcal{A}(K_S \to (\pi\pi)_{I=0}) + \sqrt{\frac{1}{3}}\mathcal{A}(K_S \to (\pi\pi)_{I=2})} \\
&= \epsilon + \frac{\epsilon'}{1+\omega/\sqrt{2}}
\end{aligned} \tag{2.56}$$

Using the above equations we can write:

$$\epsilon \simeq \frac{1}{3}(\eta_{00} + 2\eta_{+-}) \qquad \epsilon' \simeq \frac{1}{3}(\eta_{00} - \eta_{+-}) \tag{2.57}$$

where we have neglected terms in $\epsilon'\omega$ in the first expression.

The definition of ϵ. The parameter ϵ is defined in equation (2.45). Using the relations in equations (2.52) and (2.53) we can write ϵ as:

$$\epsilon = \frac{\bar{\epsilon}\mathcal{R}eA_0 + i\mathcal{I}mA_0}{\mathcal{R}eA_0 + i\bar{\epsilon}\mathcal{I}mA_0} \simeq \bar{\epsilon} + i\frac{\mathcal{I}mA_0}{\mathcal{R}eA_0} = \bar{\epsilon} \tag{2.58}$$

where the Wu-Yang phase convention has been used in the last equality. The value of $\bar{\epsilon}$ depends on the phase convention, so $\bar{\epsilon}$ is not a physically meaningful parameter. However both $\mathcal{R}e\,\bar{\epsilon} \equiv \mathcal{R}e\,\epsilon$ and $\mathcal{I}m\,\epsilon$ are both meaningful parameters.

The λ_f parameter. In order to classify the type of **CP** violation involved in ϵ and ϵ', and also to further investigate ϵ' it is useful to use the notation introduced in section 2.5. First we introduce a λ_f parameter as defined in equation (2.26) for each of the final states, $(\pi\pi)_{I=0}$ and $(\pi\pi)_{I=2}$:

$$\lambda_I = \frac{p}{q}\frac{\mathcal{A}(\overline{\mathrm{K}^0} \to (\pi\pi)_I)}{\mathcal{A}(\mathrm{K}^0 \to (\pi\pi)_I)} = \frac{p}{q}\frac{A_I^* e^{i\delta_I}}{A_I e^{i\delta_I}} = \frac{p}{q}\,e^{-i\,2\phi_I} \tag{2.59}$$

where ϕ_I is the phase of A_I (cf equation (2.20)). Likewise we can define a λ_f for both the $\pi^0\pi^0$ and $\pi^+\pi^-$ final states:

$$\lambda_{00} = \frac{p}{q}\frac{\mathcal{A}(\overline{\mathrm{K}^0} \to \pi^0\pi^0)}{\mathcal{A}(\mathrm{K}^0 \to \pi^0\pi^0)} \qquad \lambda_{+-} = \frac{p}{q}\frac{\mathcal{A}(\overline{\mathrm{K}^0} \to \pi^+\pi^-)}{\mathcal{A}(\mathrm{K}^0 \to \pi^+\pi^-)} \tag{2.60}$$

We can write η_{00} and η_{+-} in terms of λ_{00} and λ_{+-}:

$$\eta_{00} = \frac{1-\lambda_{00}}{1+\lambda_{00}} \qquad \eta_{+-} = \frac{1-\lambda_{+-}}{1+\lambda_{+-}} \tag{2.61}$$

Using the isospin expansions in equation (2.43), it is possible to relate λ_{00} and λ_{+-} to λ_0, λ_2 and the A_I. Using the expressions for ϵ in equation (2.57), we obtain:

$$\epsilon = \frac{1-\lambda_0}{1+\lambda_0} \tag{2.62}$$

Similarly ϵ' is:

$$\begin{aligned} \epsilon' &= \frac{1}{2}\frac{\lambda_2 - \lambda_0}{1 + \sqrt{2}(A_2/A_0\, e^{i(\delta_2-\delta_0)} - A_0/A_2\, e^{-i(\delta_2-\delta_0)})} \\ &= \frac{1}{6}\,(\lambda_{00} - \lambda_{+-}) \end{aligned} \tag{2.63}$$

The first expression above can be simplified by making the approximations $A_2/A_0 \ll 1$ and $\lambda_0 \simeq 1$. As we will see below, $\epsilon \ll 1$ so equation (2.62) implies $\lambda_0 \simeq 1$. These approximations give:

$$\epsilon' \simeq \frac{-i}{\sqrt{2}}\left|\frac{A_2}{A_0}\right| e^{i(\delta_2-\delta_0)}\,\sin(\phi_2 - \phi_0) \tag{2.64}$$

2.9.2 Experimental Measurements of ϵ

The value of $\mathcal{R}e\,\epsilon$ can be related to the parameter δ in equation (2.50). In the Standard model, the semileptonic decay amplitudes of K^0 and $\overline{K^0}$ are equal:

$$|\mathcal{A}(K^0 \to \pi^+ \ell^- \overline{\nu_\ell})| = |\mathcal{A}(\overline{K^0} \to \pi^- \ell^+ \nu_\ell)| \tag{2.65}$$

So δ can be written as:

$$\delta = \frac{(1+\bar{\epsilon})^2 - (1-\bar{\epsilon})^2}{(1+\bar{\epsilon})^2 + (1-\bar{\epsilon})^2} = \frac{2\,\mathcal{R}e\,\bar{\epsilon}}{1+|\,\bar{\epsilon}\,|^2} \simeq 2\,\mathcal{R}e\,\bar{\epsilon} = 2\,\mathcal{R}e\,\epsilon \tag{2.66}$$

From the value in equation (2.50) we obtain $\mathcal{R}e\,\epsilon = (1.73 \pm 0.06) \times 10^{-3}$.

As discussed above, in order to obtain $|\epsilon|$ we can look at η_{00} and η_{+-}. From equations (2.55) and (2.56) above we obtain:

$$\begin{aligned} |\eta_{00}|^2 &\simeq |\epsilon|^2 - 4\,\mathcal{R}e(\epsilon\,\epsilon') + \frac{|\epsilon'|^2}{1 - 2\sqrt{2}\mathcal{R}e\,\omega} \\ |\eta_{+-}|^2 &\simeq |\epsilon|^2 + \mathcal{R}e(\epsilon\,\epsilon') + \frac{|\epsilon'|^2}{1 + \sqrt{2}\mathcal{R}e\,\omega} \end{aligned} \tag{2.67}$$

As the values of $|\eta_{00}|$ and $|\eta_{+-}|$ in equation (2.49), agree within errors we can deduce that $\epsilon' \ll \epsilon$. Without having to know the phase of η_{00} or η_{+-} we can write:

$$|\eta_{00}| \simeq |\eta_{+-}| \simeq |\epsilon| = (2.280 \pm 0.013) \times 10^{-3} \tag{2.68}$$

Comparing this to our previous result, $\mathcal{R}e\,\epsilon = 1.73 \times 10^{-3}$, gives $\arg(\epsilon) \simeq \pm\frac{\pi}{4}$. A more detailed analysis gives $\arg(\eta_{+-}) \simeq \arg(\epsilon) = (43.3 \pm 0.5)^\circ$ [37].

2.9.3 Interpretation of ϵ

From equations (2.62) and (2.45) we can see that ϵ only receives contributions from one weak decay amplitude, A_0. In section 2.5 it was shown that **CP** violation in decay requires contributions from at least two weak decay amplitudes. Therefore ϵ must measure indirect **CP** violation.

Recall the definition of $\bar{\epsilon} \equiv (p-q)/(p+q)$. A non-zero value of $\mathcal{R}e\,\epsilon = \mathcal{R}e\,\bar{\epsilon}$ means that $p/q \neq 1$. In section 2.5 it was shown that if $|p/q| \neq 1$ then **CP** violation in mixing is taking place. Therefore $\mathcal{R}e\,\epsilon$ is a measure of **CP** violation in mixing.

Also in section 2.5 **CP** violation due to the interference between decay with and without mixing was introduced. This may be observed in decays to a final **CP** eigenstate, f_{CP}. This type of **CP** violation occurs if the $\lambda_{f_{CP}}$ parameter satisfies $|\lambda_{f_{CP}}| = 1$ and $\mathcal{I}m\,\lambda_{f_{CP}} \neq 0$.

The imaginary part of ϵ, $\mathcal{I}m\,\epsilon$ measures $\mathcal{I}m\,\lambda_0$. The state $(\pi\pi)_{I=0}$ is a **CP** eigenstate, so **CP** violation due to interference could be observed in ϵ. As ϵ is small, from equation (2.62), we have $\lambda_0 \simeq 1 \Rightarrow |\lambda_0| \simeq 1$. Therefore $\mathcal{I}m\,\epsilon$ is a measure of **CP** violation due to interference.

2.9.4 Experimental Measurements of ϵ'

Experimentally, it is usually the ratio ϵ'/ϵ that is measured.

From equation (2.63) above the phase of ϵ' is:

$$\arg(\epsilon') = (\delta_2 - \delta_0) + \frac{\pi}{2} = (48 \pm 8)^\circ. \tag{2.69}$$

As the phase of ϵ and ϵ' are similar we expect that $\mathcal{I}m(\epsilon'/\epsilon) \simeq 0$, or $\mathcal{R}e(\epsilon'/\epsilon) \simeq \epsilon'/\epsilon$.

For future reference, we can derive an expression for ϵ'/ϵ. Using the definition of ϵ' in equation (2.48) we can write:

$$\begin{aligned} \frac{\epsilon'}{\epsilon} &= \frac{1}{\sqrt{2}}\left[\frac{\mathcal{A}(\mathrm{K_L} \to (\pi\pi)_{I=2})}{\mathcal{A}(\mathrm{K_L} \to (\pi\pi)_{I=0})} - \frac{\mathcal{A}(\mathrm{K_S} \to (\pi\pi)_{I=2})}{\mathcal{A}(\mathrm{K_S} \to (\pi\pi)_{I=0})}\right] \\ &= \frac{\omega}{\sqrt{2}|\epsilon|}\left[\frac{\mathcal{I}mA_2}{\mathcal{R}eA_2} - \frac{\mathcal{I}mA_0}{\mathcal{R}eA_0}\right] \end{aligned} \tag{2.70}$$

In order to measure ϵ'/ϵ we use a slightly different method from that implied by equation (2.57). We define the *double ratio* of decay rates, **R** as:

$$\mathbf{R} \equiv \left|\frac{\eta_{00}}{\eta_{+-}}\right|^2 = \frac{\Gamma(\mathrm{K_L} \to \pi^0\pi^0)/\Gamma(\mathrm{K_S} \to \pi^0\pi^0)}{\Gamma(\mathrm{K_L} \to \pi^+\pi^-)/\Gamma(\mathrm{K_S} \to \pi^+\pi^-)} \tag{2.71}$$

Using equations (2.55) and (2.56) we get:

$$\mathbf{R} \equiv \left|\frac{\eta_{00}}{\eta_{+-}}\right|^2 \simeq 1 - 6\,\mathcal{R}e\left(\frac{\epsilon'}{\epsilon}\right) \tag{2.72}$$

where we have neglected small terms in $(\epsilon'/\epsilon)^2$.

Therefore by measuring the double ratio (**R**) defined in equation (2.71) we can gain access to the parameter $\mathcal{R}e(\epsilon'/\epsilon)$. In this analysis the parameter $\mathcal{R}e(\epsilon'/\epsilon)$ is obtained by measuring **R**.

2.9.5 Interpretation of ϵ'

In order to interpret the **CP** violation measured by ϵ' the relevant expressions are equations (2.63) and (2.64):

$$\epsilon' = \frac{-i}{\sqrt{2}} \left|\frac{A_2}{A_0}\right| e^{i(\delta_2-\delta_0)} \sin(\phi_2 - \phi_0)$$
$$\epsilon' = \frac{1}{6}(\lambda_{00} - \lambda_{+-})$$

From these expressions it can be seen that ϵ' is sensitve to the difference in the phase of the amplitudes of two decays, $K^0 \to (\pi\pi)_{I=0}$ and $K^0 \to (\pi\pi)_{I=2}$.

In section 2.5 it was shown that **CP** violation in decay requires two different weak phases. If one decay amplitude was dominant, **CP** violation could be observed through the asymmetry (equation (2.25)):

$$a = -2\left|\frac{A_2}{A_1}\right| \sin(\delta_2 - \delta_1) \sin(\phi_2 - \phi_1)$$

Looking at the first expression above and substituting $1 \to 0$ we see that $\mathcal{R}e\,\epsilon' \propto a$. Therefore $\mathcal{R}e\,\epsilon'$ is a measurement of **CP** violation in decay.

Recall that **CP** violation due to the interference can be observed when the final state is a **CP** eigenstate. Both $\pi^0\pi^0$ and $\pi^+\pi^-$ are final **CP** eigenstates, so this type of **CP** violation could be observed in ϵ'.

In the second expression for ϵ' above we see that a non-zero measurement of $\mathcal{I}m\,\epsilon'$ implies that at least one of λ_{00} or λ_{+-} must be complex. As both λ_{00} and λ_{+-} are approximately 1 (see equation (2.61) and recall that both η_{00} and η_{+-} are small) $\mathcal{I}m\,\epsilon'$ measures **CP** violation due to the interference between decay with and without mixing.

From the above discussion, we see that ϵ' does not measure any effects due to $K^0 \leftrightarrow \overline{K^0}$ mixing. Therefore ϵ' is a measure of direct **CP** violation in the decay $K \to \pi\pi$.

2.10 Theoretical Estimates of $\mathcal{R}e(\epsilon'/\epsilon)$

The equation for ϵ'/ϵ given in equation (2.70) can be written as [54]:

$$\frac{\epsilon'}{\epsilon} = \mathcal{I}m\lambda_t \frac{G_F}{2|\epsilon|\mathcal{R}eA_0\,\omega}\left[\Pi_0 - \frac{1}{\omega}\Pi_2\right] \qquad \text{where } \lambda_t = -V_{ts}^* V_{td} \tag{2.73}$$

The Π_0 and Π_2 describe the amplitudes of the penguin diagrams shown in figure 2.6. Π_0 describes the QCD penguin operators, where the final $\pi\pi$ state has isospin, $I = 0$. Π_2 describes the electroweak penguin operators, where the final state has $I = 2$.

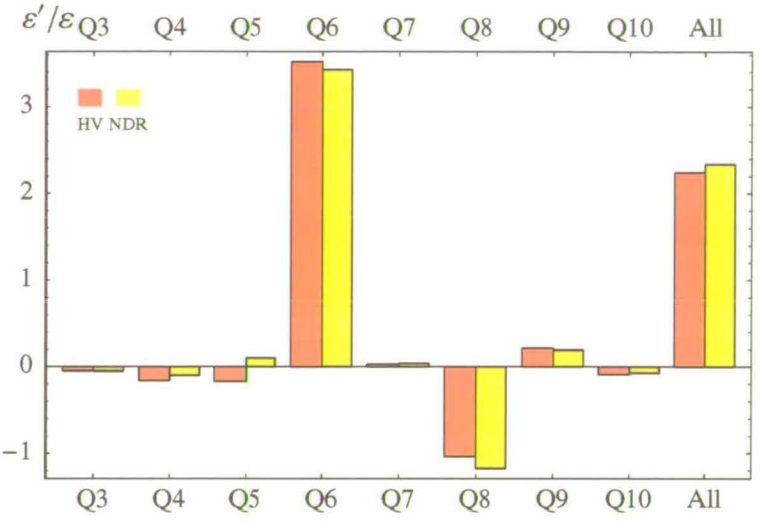

Figure 2.7: The estimations of the contributions of the $\langle Q_i \rangle$ to ϵ'/ϵ from the phenomenological analysis in reference [13]. The contributions from Q_6 and Q_8 dominate the result. The two different results were obtained using two different renormalisation schemes.

Both Π_0 and Π_2 can be expanded within the Operator Product Expansion as follows:

$$\begin{aligned} \Pi_0 &= \sum_{i=3}^{10} y_i \langle Q_i \rangle_0 \, (1-\Omega) \quad \simeq \quad y_6 \langle Q_6 \rangle_0 \, (1-\Omega) \\ \Pi_2 &= \sum_{i=7}^{10} y_i \langle Q_i \rangle_2 \quad \simeq \quad y_8 \langle Q_8 \rangle_2 \end{aligned} \tag{2.74}$$

The terms in these equations are detailed below.

- The y_i are Wilson coefficients that describe the short distance physics effects. They have been reliably calculated with pertubative–QCD techniques [16].
- $\Omega = 0.25 \pm 0.08$ [17] parameterises the isospin breaking effects.
- The $\langle Q_i \rangle_I \equiv \langle (\pi\pi)_I | \hat{Q}_i | \mathrm{K} \rangle$ for $i = 1$ to 10 are the local four-quark operators. The exact form of each of the $\hat{Q}_i$ can be found in [54]. These describe the long distance effects. Calculations of the $\langle Q_i \rangle_I$ require non-pertubative techniques which are discussed in more detail below.

Figure 2.7 shows one estimation of the contributions to ϵ'/ϵ from each of the $\langle Q_i \rangle$, $i = 3$ to 10. As indicated in equation (2.74), Π_0 and Π_2 are each dominated by one contribution known as $y_6 \langle Q_6 \rangle_0$ and $y_8 \langle Q_8 \rangle_2$ respectively. These can be parameterised

further:

$$\langle Q_6\rangle_0 = -4\sqrt{\frac{3}{2}}\left(\frac{m_{\mathrm{K}^0}}{m_{\mathrm{s}}(\mu)+m_{\mathrm{d}}(\mu)}\right)^2 \cdot (F_{\mathrm{K}}-F_\pi)\, B_6^{(1/2)}(\mu) \tag{2.75}$$

$$\langle Q_8\rangle_2 = \sqrt{3}\,F_\pi\left[\left(\frac{m_{\mathrm{K}^0}}{m_{\mathrm{s}}(\mu)+m_{\mathrm{d}}(\mu)}\right)^2 - \frac{1}{6}\left(m_{\mathrm{K}^0}^2-\mathrm{m}_\pi^2\right)\right] B_8^{(3/2)}(\mu) \tag{2.76}$$

The terms in these equations are:

- m_{K^0}, m_π, $F_{\mathrm{K}} = 160$ MeV, $F_\pi = 132$ MeV are the masses and decay constants of the K^0 and the π.
- μ is an arbitrary scale parameter, it is normally chosen in the range 1 to 2 GeV. The scale dependence of $\langle Q_6\rangle_0$ and $\langle Q_8\rangle_2$ is cancelled by the Wilson coefficients y_i of equation (2.74).
- $m_{\mathrm{d}}(\mu)$ and $m_{\mathrm{s}}(\mu)$ are the s and d quark masses at the scale μ.
- $B_8^{(3/2)}$ and $B_6^{(1/2)}$ are the hadronic *bag factors* for the $\Delta I = 3/2$ and $\Delta I = 1/2$ transitions. It is this set of bag factors that have to be calculated by non-pertubative methods.

There are three standard methods used to calculate the B-factors: Lattice gauge theory, $1/N_c$ expansion and the chiral perturbation theory.

1. Lattice gauge theory solves non-pertubative QCD on a discrete spacetime lattice. Currently lattice gauge methods calculate $\langle\pi|Q_i|\mathrm{K}\rangle$ and $\langle 0|Q_i|\mathrm{K}\rangle$ and relate them to $\langle(\pi\pi)_I|Q_i|\mathrm{K}\rangle$ via Chiral Perturbation Theory. The calculation of the $I = 0$ final state amplitudes proves to be difficult on the lattice so there are no current lattice results for $B_6^{(1/2)}$. The most recent lattice gauge theory estimates for ϵ'/ϵ are from the Rome group [21]. They rely on an 'educated guess' for $B_6^{(1/2)}$ of (1.0 ± 1.0). They quote two values for ϵ'/ϵ of $(3.6^{+6.7}_{-6.3})\times10^{-4}$ and $(6.7^{+9.2}_{-8.5})\times10^{-4}$ for two different renormalisation schemes.
2. The $1/N_c$ expansion is another QCD method. The expansion parameter is the inverse of the number of colours, $1/N_c = 1/3$. Using a mixture of phenomenology and a $1/N_c$ approach, the Münich group [17] find $B_6^{(1/2)} = (1.0 \pm 0.3)$ and $B_8^{(3/2)} = (0.8 \pm 0.2)$ with the constraint $B_6^{(1/2)} \geq B_8^{(3/2)}$. They quote $\epsilon'/\epsilon = (7.7^{+6.0}_{-3.5}) \times 10^{-4}$ and $\epsilon'/\epsilon = (5.2^{+4.6}_{-2.7}) \times 10^{-4}$ for two different renormalisation schemes.
3. Chiral perturbation theory calculates all the B-parameters in terms of three model parameters, which are determined from the measured values of $\mathcal{R}eA_0$ and $\mathcal{R}eA_2$. Currently corrections up to the third order ($\mathcal{O}(p^4)$) have been calculated. Using chiral perturbation theory the Trieste group [13], estimates $\epsilon'/\epsilon = (23 \pm 6) \times 10^{-4}$.

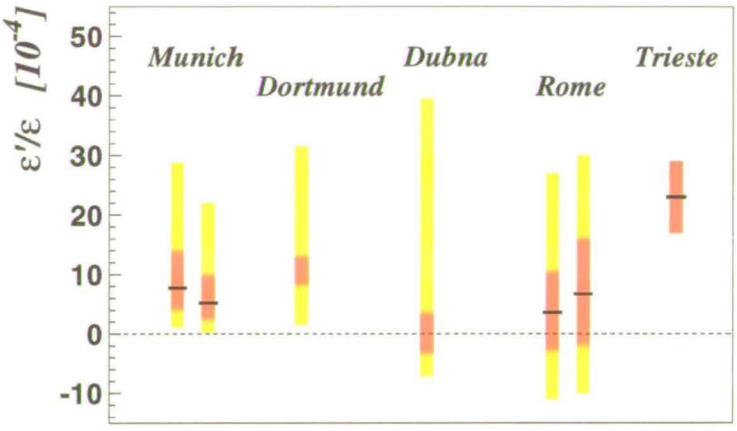

Figure 2.8: Recent theoretical estimates of ϵ'/ϵ in chronological order [17, 38, 11, 21, 13]. The red/dark-grey error bars correspond to a Gaussian treatment of the input parameters. The yellow/light-grey error bars correspond to a flat scanning of all the input parameters. The cross lines corresponds to the most favoured value. Where there are two different results from one group, these correspond to different renormalisation schemes.

A plot of these results is detailed in figure 2.8, along with other recent results [11, 38].

From the discussion above, it can been seen that the calculated value of $\mathcal{R}e(\epsilon'/\epsilon)$ depends on the mass of the strange quark at the scale μ and the CKM matrix parameter $\mathcal{I}m\lambda_t$. These two parameters still contain large experimental errors, and the measurement of $\mathcal{R}e(\epsilon'/\epsilon)$ could be used to constrain them. $\mathcal{R}e(\epsilon'/\epsilon)$ is also sensitive to new physics, which would appear as new contributions to the Wilson coefficients y_i.

There is still some disagreement about whether the theoretical predictions agree with the experimental results. All the results shown in figure 2.8 do agree with the experimental results, but in some cases only if all the input parameters they use are simultaneously near the extremes of their allowed ranges. Some authors (*eg* [21]) argue that this conspiracy of parameters is unnatural and new physics processes are needed to explain the experimentally measured value of ϵ'/ϵ. It is hoped that new techniques in Lattice QCD (and better experimental measurements of the other input parameters) will eventually allow more accurate calculations of Π_0 and Π_2 to be made. This may finally settle the debate as to whether the experimental value of ϵ'/ϵ can be accommodated within the Standard Model.

Chapter 3

The NA48 Experiment

3.1 Introduction and motivation

The NA48 experiment is a fixed target experiment at the CERN Super Proton Synchrotron accelerator.

The aim of the NA48 experiment is to measure $\mathcal{R}e(\epsilon'/\epsilon)$ to an accuracy of 2×10^{-4}. As shown in chapter 2, $\mathcal{R}e(\epsilon'/\epsilon)$ can be measured through the double ratio of decay widths, $\mathbf{R}$:

$$\mathbf{R} \equiv \frac{\Gamma(\mathrm{K_L} \to \pi^0\pi^0)/\Gamma(\mathrm{K_S} \to \pi^0\pi^0)}{\Gamma(\mathrm{K_L} \to \pi^+\pi^-)/\Gamma(\mathrm{K_S} \to \pi^+\pi^-)} = 1 - 6\,\mathcal{R}e(\epsilon'/\epsilon) \tag{3.1}$$

In order to measure $\mathcal{R}e(\epsilon'/\epsilon)$ to the required accuracy, the key features of the NA48 experiment are:

- A detector system that is able to detect and differentiate between the main $\mathrm{K_S}$ and $\mathrm{K_L}$ decay products (see table 2.1): $\pi^\pm$, $e^\pm$, $\mu^\pm$ and γ's (from the almost instantaneous electromagnetic decay $\pi^0 \to \gamma\gamma$).

- The collection of large numbers of $\mathrm{K_L}$ and $\mathrm{K_S}$ decays. To achieve a statistical error on $\mathcal{R}e(\epsilon'/\epsilon)$ of $\simeq 1 \times 10^{-4}$, the statistical error on $\mathbf{R}$, $\sigma_{\mathbf{R}}$, must be $\simeq 6 \times 10^{-4}$. Assuming Poisson statistics and linear error propagation $\sigma_{\mathbf{R}}$ is given by:

$$\left(\frac{\sigma_{\mathbf{R}}}{\mathbf{R}}\right)^2 = \frac{1}{N_S^{+-}} + \frac{1}{N_S^{00}} + \frac{1}{N_L^{+-}} + \frac{1}{N_L^{00}} \simeq (6 \times 10^{-4})^2$$

  where the N's are the numbers of each decay mode collected. As $\mathbf{R} \simeq 1$, around 10^7 events of each decay mode needs to be collected. In particular, due to the small branching ratio of $\mathrm{K_L}$ into $\pi^+\pi^-$ and $\pi^0\pi^0$ (see table 2.1) around 10^{10}

K_L decays will need to be collected. This requires high-intensity neutral kaon beams.

- The simultaneous collection of both K_L and K_S decays from the same fiducial volume and over the same energy range, with a similar energy spectrum of the kaon decays. This reduces systematic errors from time, position and energy-dependent effects.

This Chapter describes how these aims are met in the NA48 experiment.

3.2 Overview

The standard NA48 coordinate system is a right-handed Cartesian system, with the z-axis pointing along the direction of the K_L beam and the y-axis pointing vertically upwards. The origin is on the axis of the K_L beam with $z = 0$ defined as the end of the K_S target.

Figure 3.1 shows the layout of the NA48 experiments beamline and detector.

The NA48 experiment uses two simultaneous beams of neutral kaons to collect statistics for all four $\mathcal{R}e(\epsilon'/\epsilon)$ decay modes at the same time. The beams are created by two targets placed 240 m (K_L target) and 122 m (K_S target) upstream of the electromagnetic calorimeter. All protons directed onto the K_S target pass through a proton tagging detector which records the time of the proton hits. Both beams are cleaned and collimated before entering the common decay region.

To detect the products of the neutral kaon decays, the NA48 detector has the following components:

- Anti-K_L and K_S detectors (AKL, AKS). These identify decays which happen outside the fiducial region so they can be rejected from the analysis. The AKS detector is also used to define the detector's energy scale.
- A magnetic spectrometer (DCH). This measures the trajectories and momenta of charged particles. It is used primarily to detect $K^0 \to \pi^+\pi^-$ decays. The information can also be used to partially reconstruct the background decays: $K_L \to \pi^\pm e^\mp \nu_e$ (Ke3) and $K_L \to \pi^\pm \mu^\mp \nu_\mu$ (Kμ3).
- A charged hodoscope (CHOD). This measures the time of charged particles and provides an input for the $K^0 \to \pi^+\pi^-$ trigger.
- A liquid krypton electromagnetic calorimeter (LKR). This measures the positions, energies and times of photons from $\pi^0 \to \gamma\gamma$ decays which are used in

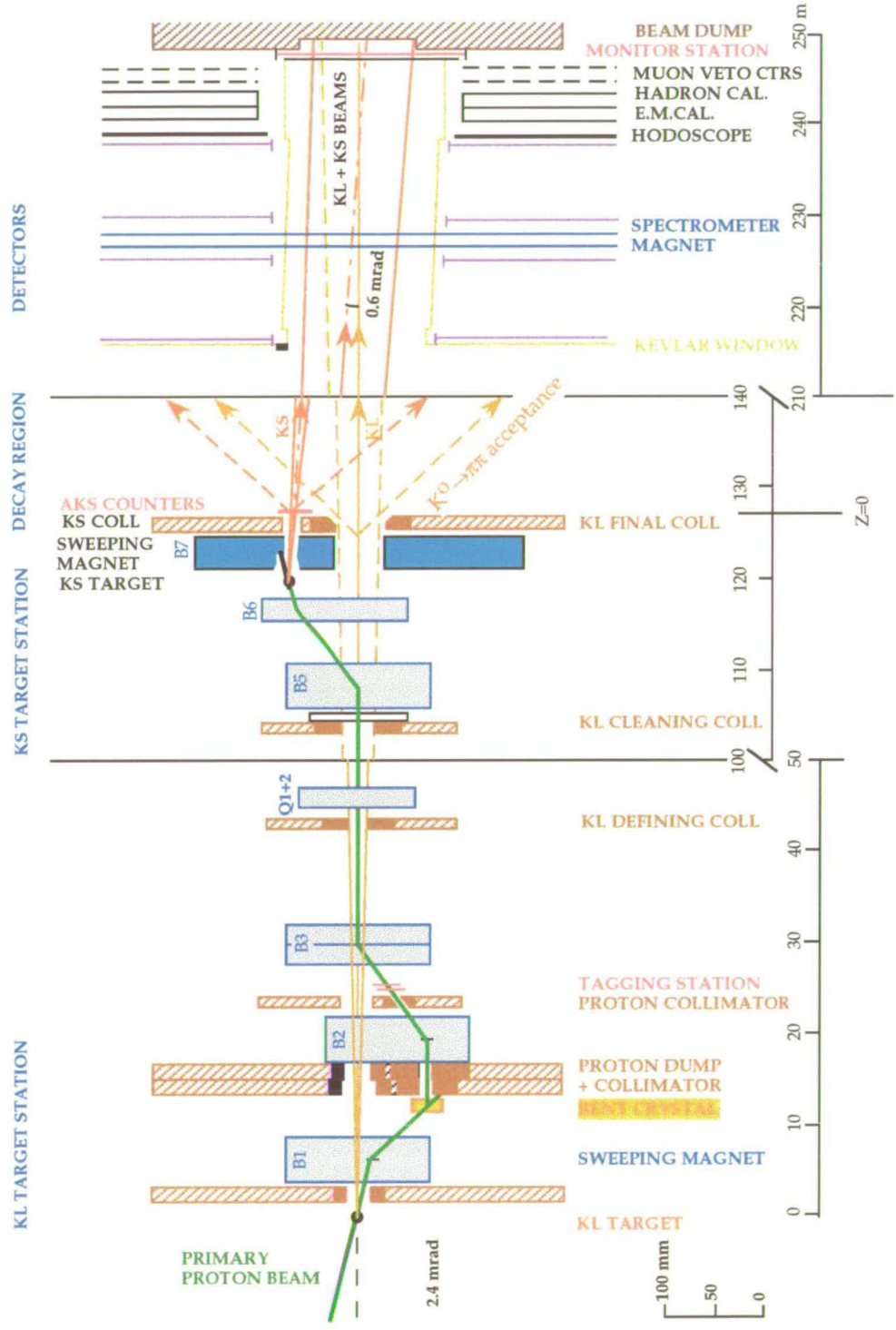

Figure 3.1: A schematic layout of the NA48 experiment. Note that the diagram shows 3 separate sections along the beam direction. Rectangles labelled B are dipole (bending) magnets and those labelled Q are quadruple (focusing) magnets.

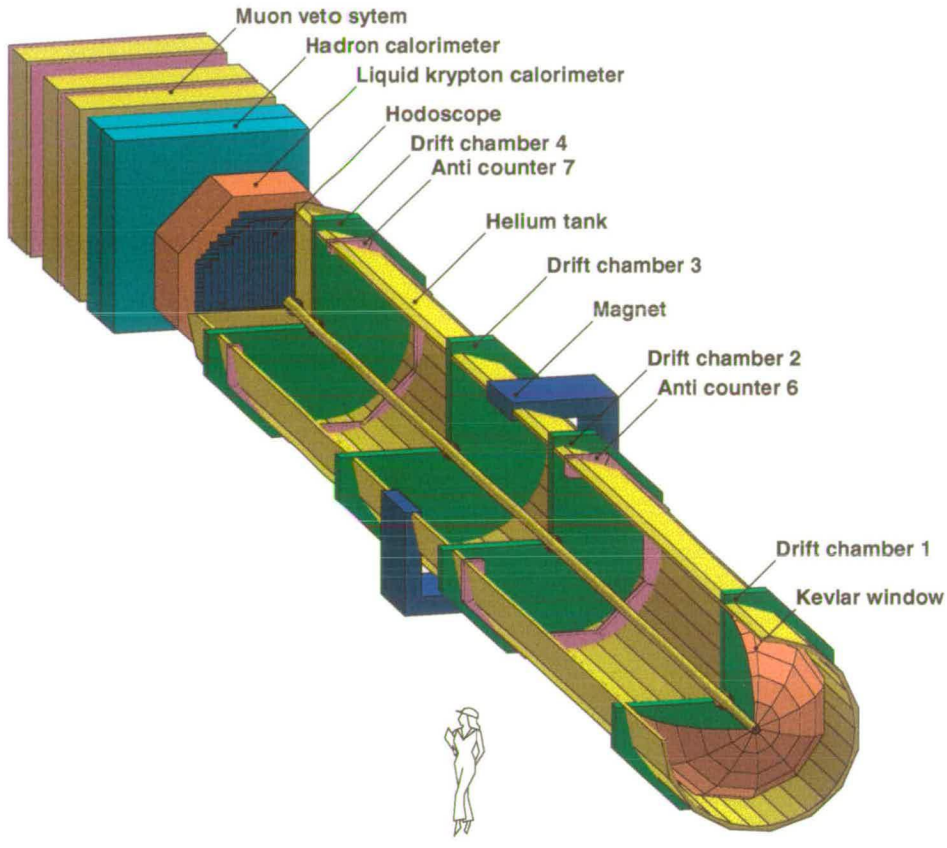

Figure 3.2: A GEANT generated picture of the NA48 Detector.

the reconstruction of $K^0 \rightarrow \pi^0\pi^0$ decays. It can also be used, along with track information from the DCH, to identify electrons from background $K_L \rightarrow \pi^{\pm}e^{\mp}\nu_e$ decays.

- A hadronic calorimeter (HAC). This detects showers from charged pions and is used in conjunction with the LKR to calculate the total hadronic energy of an event, providing an input for the $\pi^+\pi^-$ trigger.
- A muon veto system (MUV) to detect muons. This information is used to reject $K_L \rightarrow \pi^{\pm}\mu^{\mp}\nu_\mu$ decays.

Figure 3.2 shows the layout of these subdetector systems.

3.3 The Simultaneous K_L and K_S Beams

The NA48 beamlines are shown in figure 3.1.

As K_L and K_S mesons have very different mean decay lengths ($\lambda_S = 5.9$ m and $\lambda_L = 3480$ m at a typical kaon energy of $E_K = 110$ GeV) the NA48 experiment uses two neutral kaon beams. The K_L beam is produced along the z axis, 240 m upstream of the LKR. The K_S beam is produced 122 m upstream of the LKR at a height of $y = 72$ mm above the K_L beam axis. The K_S and K_L beams converge at an angle of 0.6 mrad and meet spatially at the front face of the LKR. The longer path length for the K_L beam ensures that all of the K_S component of that beam has decayed away by the beginning of the fiducial region. In the K_S beam there is a small contribution from K_L decays, corresponding to about 0.4 % of the decays in the fiducial region.

The nearly-collinear double beam geometry gives a large overlap in the spatial decay region for both K_L and K_S decays. The position of the targets with respect to the proton beam is tuned such that the energy spectrum of the observed kaon decays is as similar as possible for both beams over the canonical kaon energy range of $70 < E_K < 170$ GeV.

3.3.1 The SPS

The two NA48 beams are created by directing proton beams onto Beryllium targets. The initial source of protons is the CERN Super Proton Synchrotron (SPS) accelerator. The SPS is a circular accelerator with a circumference of 7 km which accelerates protons to 450 GeV/c. The beam therefore has a natural period of $7\ \text{km}/c = 23\ \mu\text{s}$.

The cycle of the SPS accelerator is 14.4 s. During this period the SPS receives protons at 14 GeV/c from the CERN proton synchrotron and accelerates them to 450 GeV/c. These protons fill 10/11 of the circumference of the SPS. A 200 MHz RF (Radio Frequency) system is used to artificially increase the longitudinal momentum spread of the beam, the σ of the momentum spread is 450 MeV/c. This allows the protons to spread around all of the ring. The RF system is switched off before the protons are extracted.

NA48 receives protons from the SPS during the *slow extraction* phase of the SPS. The slow extraction takes 2.38 s during which a burst, or spill, of protons are transferred to the NA48 targets. The primary proton beam to NA48 is nominally 1.5×10^{12} protons per burst.

3.3.2 The K_L Beam

The K_L beam is produced by directing the primary proton beam onto a cylindrical beryllium target. The target is 0.2 cm in diameter and 40 cm long, corresponding to 1 proton interaction length. The target is positioned such that the proton beam is incident at an angle of 4.2 mrad. This angle is chosen so that the flux of neutrons in the

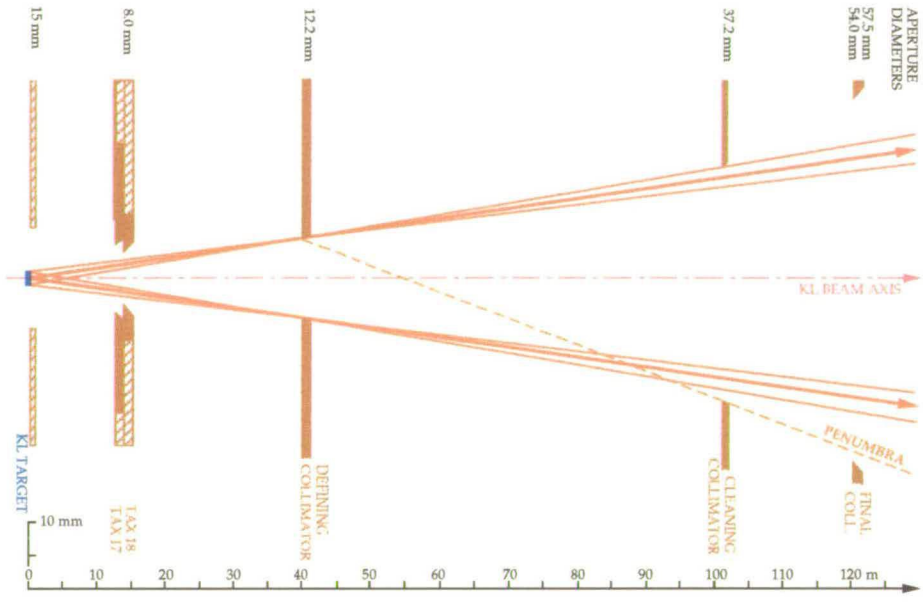

Figure 3.3: The positions and apertures of the defining, cleaning and final collimators in the K_L beam.

kaon beam is reduced by a factor of approximately 4 compared to a zero production angle [4].

One neutral kaon is produced for approximately every 10^5 protons hitting the target. The emerging beam from the target also contains strange baryons, muons, charged pions, protons, neutrons and photons. The beam is cleaned of charged particles by a dipole sweeping magnet (magnet B1 in figure 3.1), which also deflects the non-interacting protons.

The K_L beam is collimated in three successive stages by defining, cleaning and final collimators placed respectively 40 m, 100 m and 125 m downstream of the K_L target, as shown in figure 3.3.

The resulting beam has a divergence of ± 0.15 mrad and has a flux of around 2×10^7 K_L particles per burst.

3.3.3 The Bent Crystal

Protons which do not interact in the K_L target are swept away from the K_L beamline by the sweeping magnet. A small fraction of these protons are redirected towards the K_L beamline by a bent silicon mono-crystal, placed 10 m downstream of the K_L target.

Figure 3.4 shows a schematic diagram of the crystal including all the relevant dimensions.

When this proton beam hits the crystal 5×10^{-5} of the protons emerging from the K_L target become trapped between the crystallographic planes and undergo channelling, producing a clean, well-collimated beam of protons. The crystal has been mechanically bent so that the trapped protons are deflected.

The use of a crystal is advantageous over a magnet for a number of reasons:

- The crystal is only 6 cm long, but has an bending power equivalent to a 14.4 Tm magnet, which would be ordinarily over 5 m in length.
- The protons are bent without cancelling the effects of the sweeping magnet. A bending magnet would have increased the flux of muons in the emerging beam by an order of magnitude.
- The crystal is not selective about the longitudinal momentum of the protons it deflects. This means the secondary proton beam emerging from the crystal has an almost identical momentum spectrum to that of the primary proton beam.
- The crystal defines the emittance of the proton beam in both the horizontal and vertical direction.
- The crystal reduces the flux of the proton beam by 5×10^{-5}.

The crystal is mounted on a goniometer to allow fine tuning of the beam to take place.

3.3.4 The K_S Beam

The emerging secondary beam of protons from the bent crystal contains $\sim 3 \times 10^7$ protons per burst. This beam is then transported to a point 72 mm above the K_L beam axis where the K_S target is situated. The K_S target is identical to the K_L target, but is arranged so that the angle of incidence of the incoming protons is 2.4 mrad. This angle is chosen so that the resulting momentum spectra of the kaons which decay in the fiducial volume is similar for both the K_S and K_L beams [4, 8].

A sweeping magnet clears the beam of charged particles and the beam is collimated so that it points towards the centre of the LKR. The final edge of the K_S collimator is at the same z-position as the final K_L collimator. The resulting beam has a divergence of ± 0.375 mrad and a flux of around 2×10^2 K_S particles per burst.

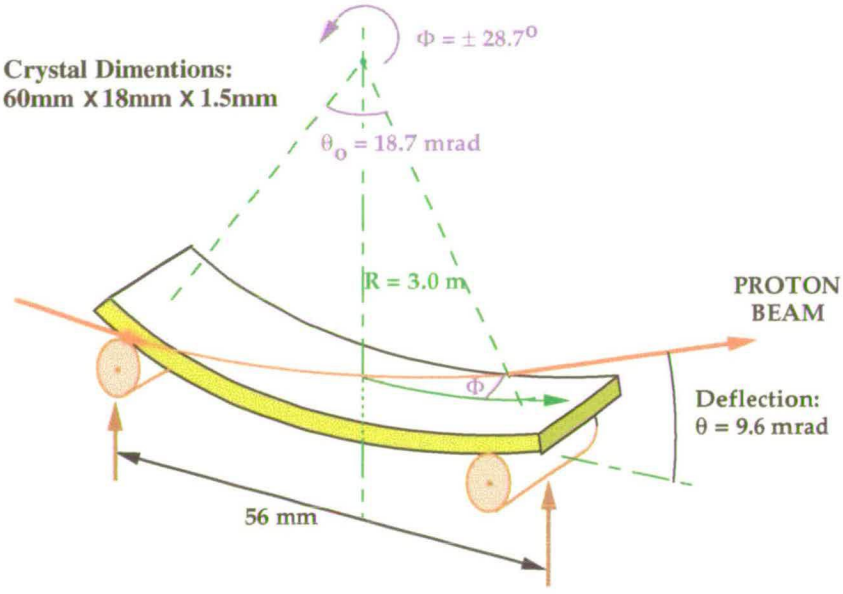

Figure 3.4: A diagram of the bent silicon crystal, showing the crystal's dimensions and the path of protons. The two cylindrical rollers shown maintain the radius of the crystal's arc at 3 m.

3.3.5 Beam Monitors

Information about the beam intensities is recorded by the Beam Counter and the K_S-monitor.

The Beam Counter is placed directly behind the beam dump, at the very end of the experiment. It measures the profile and intensity of the K_L and K_S beams. The beam counter consists of one horizontal and one vertical plane each made of 24 scintillating fiber bundles. Due to the relative intensity of the two beams, the activity in the beam counters is dominated by K_L beam. Figure 3.5 shows the profile of the beams as measured by the Beam Counter.

The K_S-monitor is placed along side to the K_S target. It monitors the K_S beam intensity by counting particles emitted from the K_S target perpendicular to the beam direction. It consists of four plastic scintillators arranged parallel to the K_S target.

The beam monitors are used to make random triggers to study accidental activity in the K_L and K_S beams (see section 7.11.1). Activity in the beam counters is downscaled and the trigger is issued after 69 μs (3 times the SPS period). This ensures that random triggers are taken in proportion to the instantaneous beam intensity.

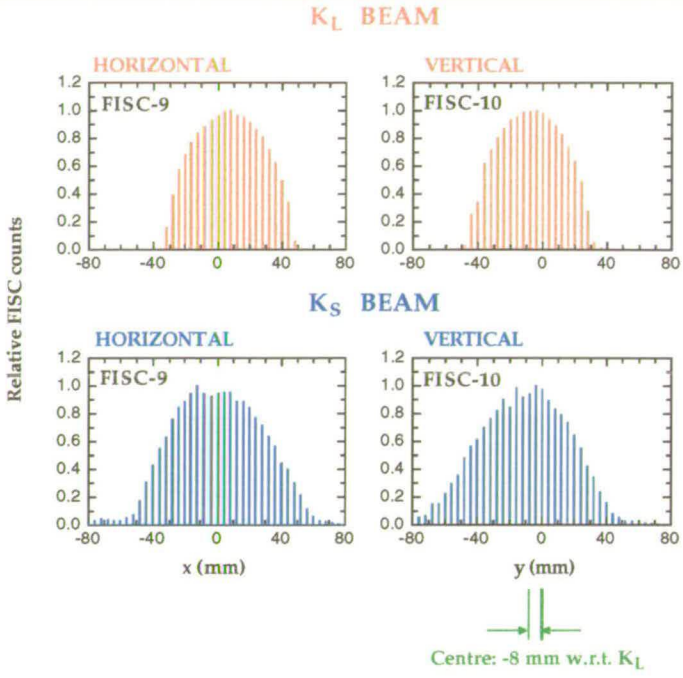

Figure 3.5: The profiles of the K_L and K_S beams as measured by the Beam Counter. It can be seen that the K_L beam is better defined than the K_S beam. This is because the distance from the target to the final collimator is longer for the K_L beam than for the K_S beam.

3.4 Proton Tagging

As the K_L and K_S beams coincide in space at the LKR where $\pi^0\pi^0$ decays are detected, a time of flight method is used to distinguish decays from the K_L and K_S beams. All of the protons being transported to the K_S target travel through the proton tagging detector which records the time of the proton hits. The time of the hits in the tagger can then be compared to the time of the decay products downstream in the detectors. The time for $\pi^+\pi^-$ events comes from the charged hodoscope and the LKR is used for the time of $\pi^0\pi^0$ events.

As discussed in section 6.2, the time of the proton hits is compared to the event times in the detector. After subtracting an appropriate time offset, if there is a proton hit within a small time window around the event time the decay is tagged as K_S, otherwise the decay is tagged as K_L. In this analysis a time window of $[-2, +2]$ ns is used for the tagging procedure. Figure 3.6 illustrates this procedure.

If the tagger is inefficient, or if the scintillators are mis-aligned, a proton may fail to be detected. This will cause a K_S decay to be incorrectly identified as a K_L decay. This effect is known as tagging inefficiency. Accidental hits in the tagger will cause K_L decays to be wrongly labelled as K_S decays. This effect is called tagging dilution.

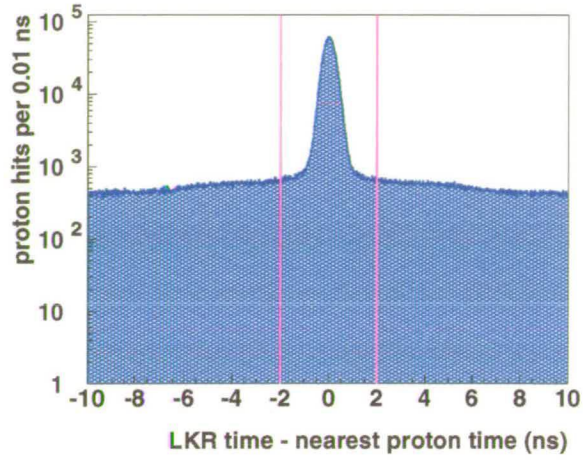

Figure 3.6: Time difference between the LKR and the nearest proton in the proton tagger for $K \rightarrow \pi^0\pi^0$ decays. A time offset has been applied to the distribution to centre the distribution at zero. The events within the lines at -2 ns and $+2$ ns are identified as coming from the K_S beamline.

These two effects are discussed in detail in sections 6.2.1 and 7.1.

3.4.1 The Proton Tagger

The proton tagger is illustrated in figure 3.7. It is designed to cope with the $\sim 10^7$ Hz rate of protons and the high radiation dose of 1 Gy per proton burst.

The tagger is composed of 2 interleaved, orthogonal ladders each containing 12 narrow strips of scintillation foil. The width of each foil is matched to the beam profile such that each foil sees approximately the same rate of incident protons. Each foil can be moved horizontally and vertically to ensure optimal alignment with the proton beam. To avoid proton detection inefficiencies, the foils overlap slightly. At both ends of the array there are anticounters to identify halo particles. Special trigger counters are placed at the front and the back of the tagger for efficiency studies.

The photons from the scintillator are directed to photomultipliers through an 8 mm air gap and lightguides. In total, around 400 photoelectrons are produced per proton hit. The photomultipliers are read out with a 1 GHz Flash ADC (Analogue to Digital Converter) system.

During the proton spill, the average proton rate in the tagger is $\sim 10^7$ Hz. However, due to the spill structure, the instantaneous rate in the tagger can reach $\sim 3 \times 10^7$ Hz [43]. To resolve the time between two proton hits to 5 σ, the resolution of the tagger must be better than $(3 \times 10^7)^{-1}/5 \simeq 7$ ns. The time resolution of a single

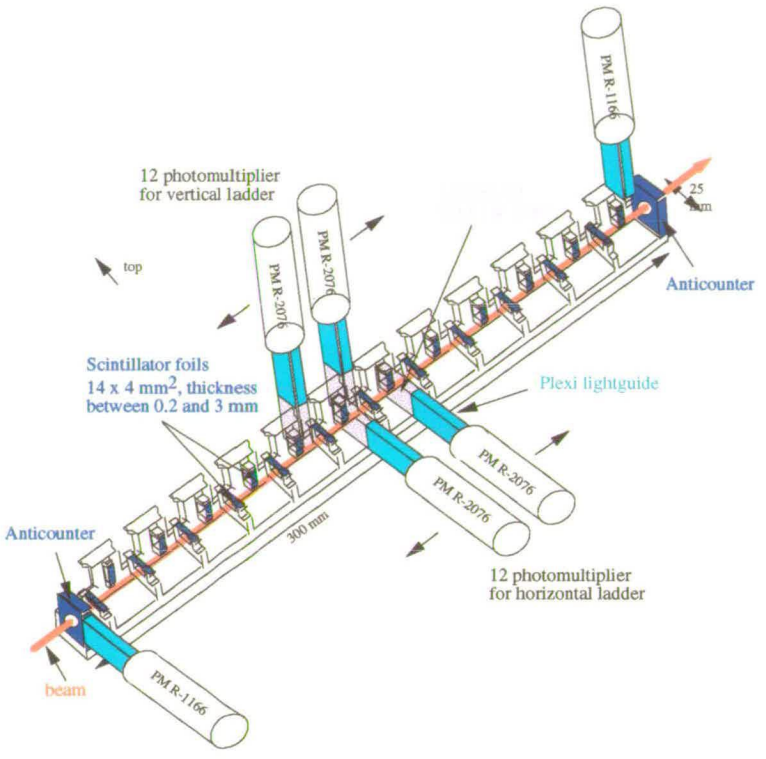

Figure 3.7: The proton tagging detector. The two ladders of scintillator foils are read out by photomultipliers.

proton should be as small as possible to allow a small time window for the tagging to be used. This will minimise the amount of tagging dilution (decays from the K_L beam that are identified as K_S decays by the tagging method).

The measured time resolution of a single proton hit is 120 ps and the double-pulse separation is 4 ns.

3.5 The Anti-K_S detector

The principle of the experiment requires that the four $\mathcal{R}e(\epsilon'/\epsilon)$ decay modes are selected from the same fiducial volume. As K_S decays have a steeply falling z-vertex distribution, resolution effects could cause a net migration of events into, or out of, the fiducial region. To avoid such effects, the Anti-K_S detector (AKS) provides a hardware definition of the beginning of the fiducial region. In contrast, K_L decays have an almost flat z-vertex distribution, therefore the counting of these decays is less sensitive to resolution effects.

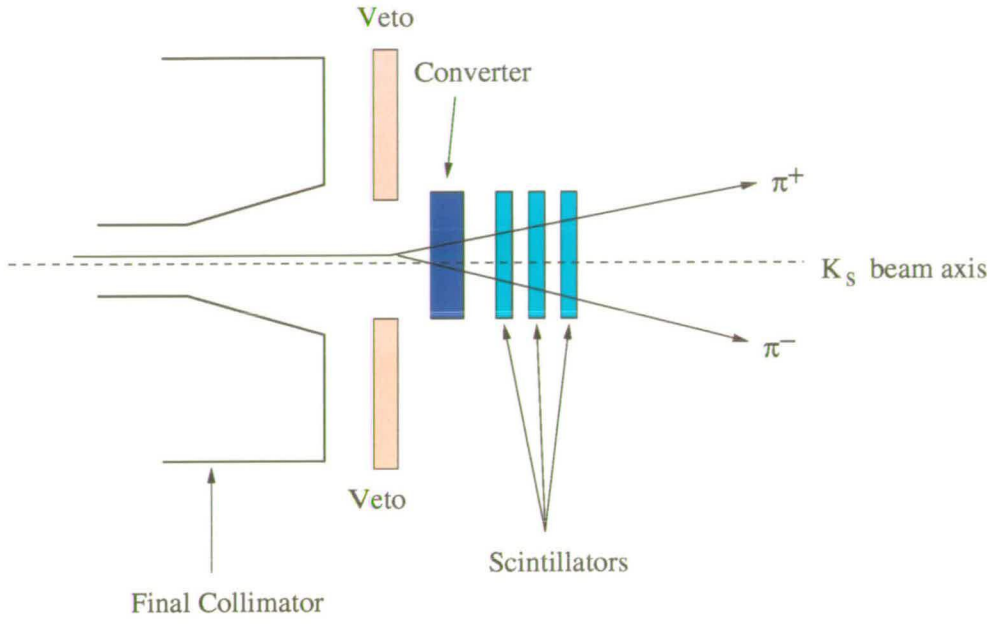

Figure 3.8: A schematic view of the AKS detector.

The AKS is placed directly behind the K_S collimator. It detects photons and charged particles from K_S decays occurring upstream of the AKS, allowing these decays to be vetoed from the analysis. As illustrated in figure 3.8, the AKS consists of an iridium crystal to convert photons from $K_S \to \pi^0\pi^0 \to 4\gamma$ decays into electrons, followed by an array of three scintillators to detect the electrons and charged pions from $K_S \to \pi^+\pi^-$ decays. The central scintillator is used as the veto. The other two scintillators are used for efficiency measurements.

The AKS detector is used also in the analysis of the energy scale of the detectors. The reconstructed z-vertex position of a decay is a function of the energy of the decay products. As K_S decays upstream of the AKS are rejected, the minimum reconstructed z-vertex position of K_S decays should therefore be z_{AKS}. (The effect is, obviously, smeared due to the finite resolution of the measurement.) Any disagreement can be used to calculate corrections to the energies measured in the detectors. This procedure is discussed in detail in section 7.14.

The probability of conversion in the crystal is measured to be $(99.964 \pm 0.003)\%$ [14]. The efficiency of the central scintillator is measured to be $(99.97 \pm 0.01)\%$ for detecting both $\pi^\pm$ and $e^\pm$.

3.6 The Decay Region

The decay region of the NA48 experiment starts at the z position of the AKS detector, $z = 6.09$ m. It is contained in a cylindrical steel tank which is evacuated to a pressure of $< 3 \times 10^{-5}$ mbar. The vacuum vessel is terminated at $z = 96$ m by a 0.9 mm thick Kevlar window. It is followed by a Helium tank, which is held at atmospheric pressure, containing the spectrometer. The kaon beams continue in a 16 cm diameter evacuated carbon fiber tube to the beam monitor and beam dump which are downstream of the subdetectors. The vacuum is terminated as the drift chambers are not strong enough to withstand the pressure difference that would be caused by a vacuum. Helium is chosen to fill the tank in order to minimise multiple scattering effects.

The vacuum tube and the helium tank are surrounded by anticounters (AKL) which are designed to detect decay products which would escape the acceptance of the spectrometer or the LKR. There are seven anticounters which form a cone in space. Each anticounter consists of an octagonal ring of scintillator, preceded by 35 mm of iron which is used to convert photons. The AKL are not used in this analysis.

3.7 The Spectrometer

The momenta and vertex positions of charged particles from K^0 decays are measured by the magnetic spectrometer. The spectrometer is placed in the helium tank at the end of the decay volume. It consists of 4 drift chambers and a dipole magnet positioned between the second and third chambers. The field integral between these two chambers is 0.83 Tm, corresponding to a change in transverse momentum of 257 MeV/c. This is commensurate with the maximum transverse momentum of a $K^0 \to \pi^+\pi^-$ decay. This field is uniform to within 6%, which allows a fast online calculation of the track momentum in the Level 2 $\pi^+\pi^-$ trigger (see section 4.3).

3.7.1 The Drift Chambers

The structure of the drift chambers is illustrated in figure 3.9. Each drift chamber contains eight planes of 256 sense wires, spaced 10 mm apart. Each of the sense wires is surrounded by 4 potential wires. The planes of wires are orientated at 0°, 90°, −45° and +45°, known as the x, y, u and v views respectively. Each view has two planes of wires which are staggered. In chamber 3 only the x and y views are read-out.

Each drift chamber is filled with a 50% Argon–50% Ethane mixture. The position resolution of a single eight plane drift chamber is 90 μm.

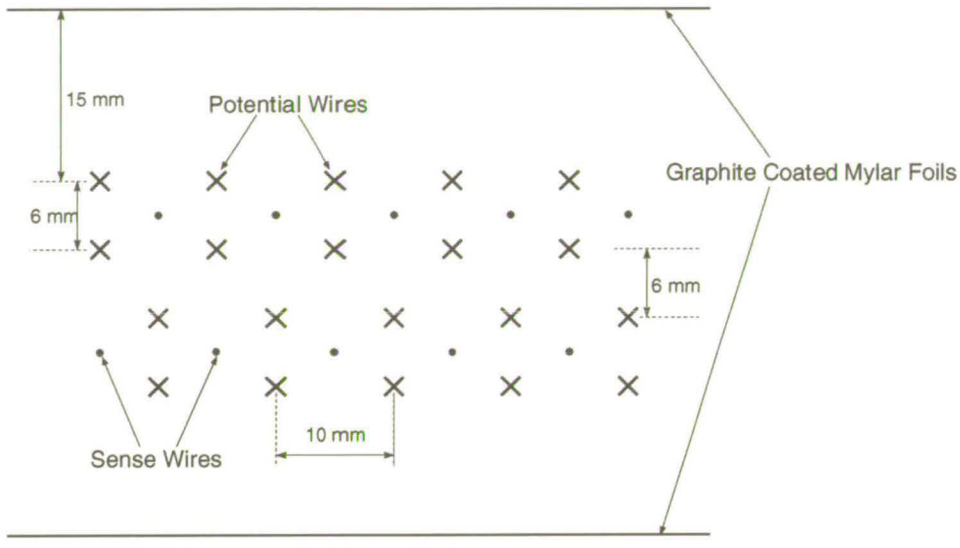

Figure 3.9: The internal structure of the drift chambers. The diagram shows a small section of one view of one drift chamber. Each view consists of two planes of 256 sense wires, with each sense wires surrounded by four potential wires. The two planes of sense wires are staggered.

3.7.2 Performance of the Spectrometer

The momentum resolution of the spectrometer is:

$$\left(\frac{\sigma_p}{p}\right) = 0.005 \oplus 0.00009 \times p \qquad \text{for } p \text{ measured in GeV/c} \tag{3.2}$$

The first term is due to multiple scattering effects in the helium and the second term comes from the position resolution in the drift chambers. At a typical $\pi^{\pm}$ momentum of 50 GeV/c, $\sigma_p/p = 0.66\%$ with the terms from position resolution and multiple scattering contributing about equally.

The resulting resolution on the position of a charged decay vertex is 50 cm in the z-direction and 2 mm in the x and y directions. Since the beams are separated vertically by around 60 mm in the decay region, a clean identification of $K_L \to \pi^+\pi^-$ and $K_S \to \pi^+\pi^-$ decays is possible. This information is used as a cross check of the tagging method.

3.7.3 Drift Chamber Readout

The Drift Chamber Readout system [5] is the link between the drift chamber wires and the PC Farm, where data for triggered events is collected.

Signals from the drift chamber wires are amplified and first sent to a TDC (Time to Digital Converter) card. There are a total of 28 TDC cards: one for each plane of wires that is read out. Each card contains a TDC chip and a FIFO (First In First Out) memory. The TDC cards record which sense wires were hit and the times of these hits. This information is temporarily stored in the FIFO memory before being sent to a 'Ring card' which stores this data for 200 μs. The data stored in the Ring cards can be read by either the Level 2 Charged Trigger system (see section 4.3) or sent to the PC Farm (see section 4.4.1).

The time taken to read out data from the Ring cards is proportional to the total number of wire hits. To keep this time low, if a plane has more than 8 wire hits in the previous 100 ns the FIFO memory on the appropriate TDC card is reset. When a memory reset occurs, the data residing in the FIFO is lost. If this happens, an additional 'overflow word' is added to the data by the TDC card.

In principle, events with high wire hit multiplicity are not candidates for $K^0 \to \pi^+\pi^-$ decays. So the loss of these high multiplicity events should not affect the analysis of $\mathcal{R}e(\epsilon'/\epsilon)$. However, in practice, around 16% of $K^0 \to \pi^+\pi^-$ are influenced by the loss of the data due to the memory reset. These effects are discussed in detail in section 6.4.7.

3.8 The Charged Hodoscope

The charged hodoscope (CHOD) is used to define the times of charged events. This time can be compared with information from the proton tagger to decide whether the event came from the K_L or K_S beamline. As with the tagger, the event time resolution from the charged hodoscope should be as small as possible. This allows a small time window to be used to distinguish events from the K_L or K_S beamline. This minimises the effects of misidentifying K_L decays as K_S. The time resolution of the CHOD for $\pi^+\pi^-$ events is measured to be 300 ps. The hodoscope signals are also used as a basis for the $\pi^+\pi^-$ trigger.

The hodoscope is placed directly behind the helium tank of the spectrometer, before the LKR calorimeter. As illustrated in figure 3.10, it consists of a plane of 64 vertical half-strips of scintillator, followed by a second plane of 64 horizontal half-strips. Each of the strips are read out at one end by a photomultiplier. The second plane is placed as close to the LKR as possible (80 cm from the first plane) to allow differentiation between the forward-going particles and those backscattering from the LKR.

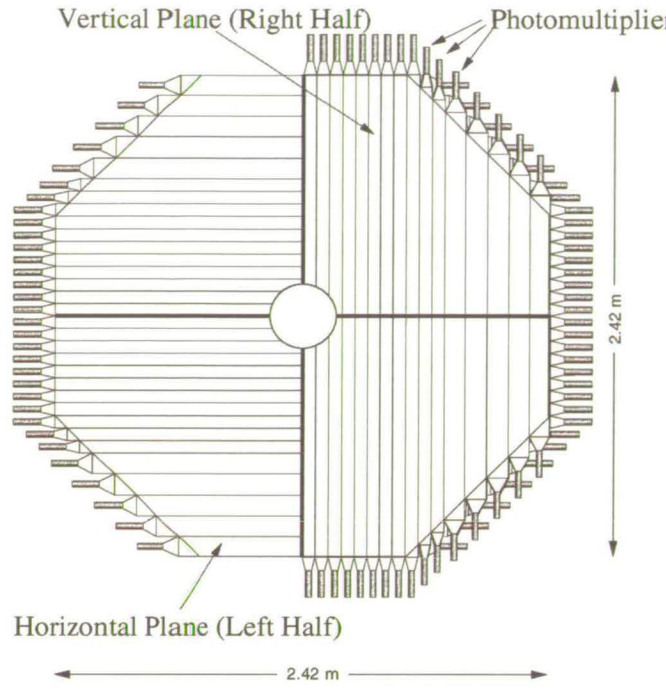

Figure 3.10: The scintillator strips in the charged hodoscope.

3.9 The Electromagnetic Calorimeter

Information from the Electromagnetic Calorimeter is used to reconstruct $K^0 \rightarrow \pi^0\pi^0 \rightarrow 4\gamma$ decays. The LKR provides measurements of the energy and x and y positions of photons and electrons. It is also used for differentiating between charged pions and electrons from $K_L \rightarrow \pi^{\pm}e^{\mp}\nu_e$ decays.

3.9.1 LKR Design Aims

In order to measure $\mathcal{R}e(\epsilon'/\epsilon)$ with a systematic error of $\lesssim 2 \times 10^{-4}$, the calorimeter must have a fast and stable response to cope with the high event rate. To keep the background from $K_L \rightarrow 3\pi^0$ decays to less than 0.1% the invariant mass of photon pairs needs to be well measured. The design aims of the calorimeter were for an energy resolution of 1% and x and y positions resolution of 1 mm for photons above 20 GeV. The time resolution of a photon must be better than 0.5 ns, in order to provide an accurate event time to distinguish between events from the K_L and K_S beamlines. In addition the energy scale of the calorimeter must be known to an accuracy of 10^{-4}.

Liquid krypton is chosen as the active medium as it has an interaction length (X_0) of 4.7 cm, allowing a compact detector to be built. Liquid krypton is also able to cope

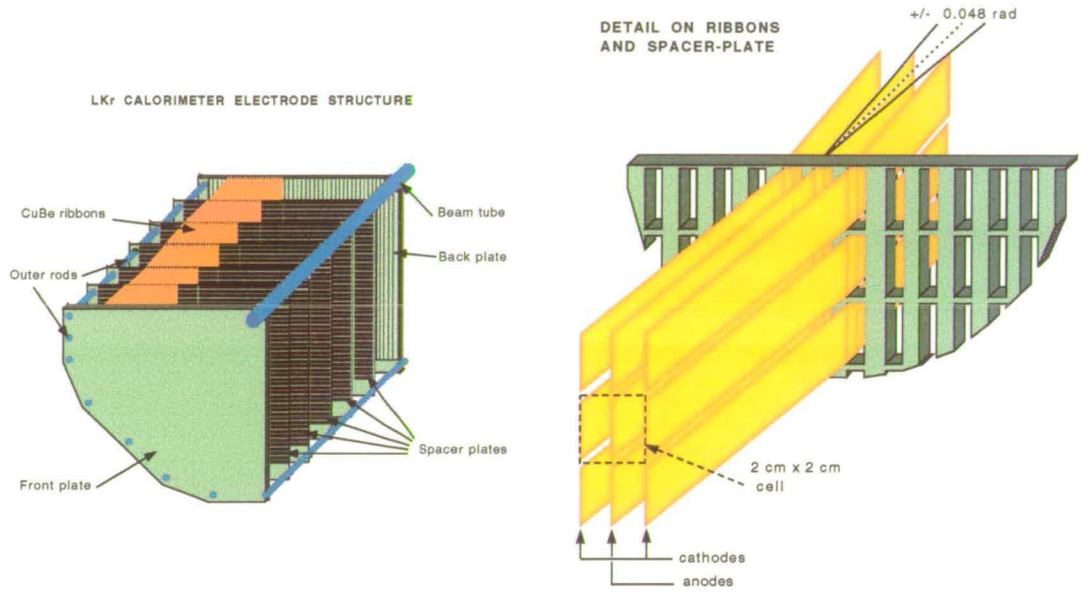

Figure 3.11: Left: the internal structure of one quadrant of the LKR. The beam is incident on the front face of the calorimeter, shown on the lower left of the diagram. Right: the definition of a single readout cell in terms of the electrodes.

with the high radiation dose without significant deterioration of performance.

3.9.2 Cryogenics and the LKR readout cells

The 9 m^3 of liquid krypton is placed in a cryostat and kept at its boiling point of 121 K. Evaporated krypton is filtered, cooled and returned to the vessel. The lifetime of an electron in the Krypton is 40 μs, which is comfortably larger than the typical drift time across the electrodes of 0.5 μs.

The LKR is divided into 13248 readout cells each defined by three Cu-Be electrodes, as shown in figure 3.11. The cells are 2×2 cm^2, approximately $\frac{1}{2}X_0$, in the x and y directions, and 127 cm long in the z direction: equivalent to 27 X_0 or 2 nuclear interaction lengths. The geometry of the cells is projective, *i.e.* the cells point towards the average K_S decay position. A voltage of 5 kV is applied to each of the electrodes.

The longitudinal design of the cells means that only a few are important in any one event. Showers from incident photons and electrons develop almost parallel to the electrodes, and up to 35% of the energy of a single shower can be within one cell. The energy of the clusters is reconstructed using the expected shower profile in the calorimeter. Therefore to measure accurately the energy of a shower, the transverse size of the cells must be accurately known. To measure the energy scale of the calorimeter to 1 part in 10^4, the size of the cells must be correct to an accuracy

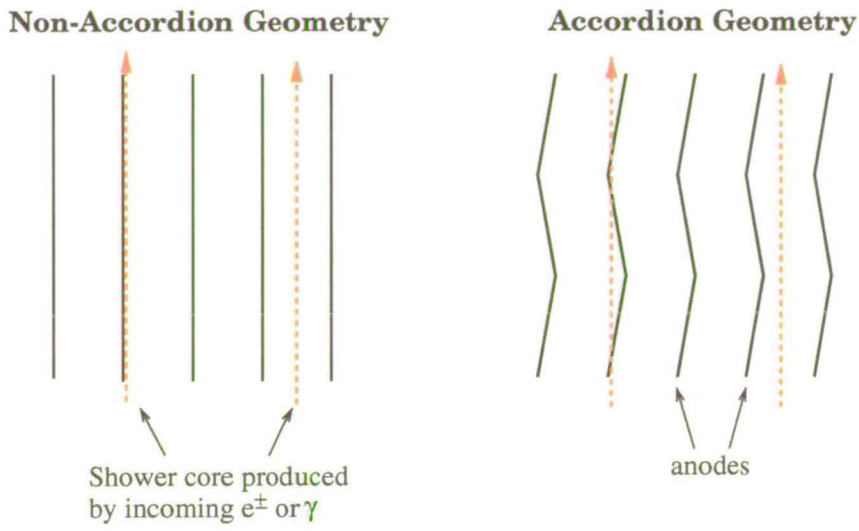

Figure 3.12: The effect of the accordion geometry of the LKR cells.

of 50 μm.

To ensure the size of the cells in the transverse directions, each of the electrodes is stretched between five accurately machined spacer plates and the front and back plates of the calorimeter. The spacer plates also apply a zig-zag, or accordion, geometry to the cells. This reduces the free length of the electrodes in the LKR from their total length of 125 cm to 20 cm, (the distance between the spacer plates). The angle applied to the electrodes by the spacer plates is 48 mrad.

Another advantage of the zig-zag geometry is that it reduces effects due to the impact position of the particle. The incoming particle produces a shower of electrons and positrons, which in turn cause the ionisation of the Krypton atoms. The electric field in the calorimeter causes these ionisation electrons to drift towards the anodes where a current is induced. (The drift velocity of the Krypton ions is much lower than that of the electrons and does not appreciably contribute to the induced current.) The current induced varies non-linearly with the distance between the core of the shower and the anode. In particular, the response of the calorimeter is diminished when the shower core is very close to the anode. As illustrate in figure 3.12, the zig-zag shape of the electrodes does not allow a shower core to remain critically close to the anodes as the shower develops through the detector. This means the calorimeter response is less sensitive to the impact position of the incoming particle. The residual correction to the energy due to the impact position of the particle is $\pm 0.5\%$, which is applied offline.

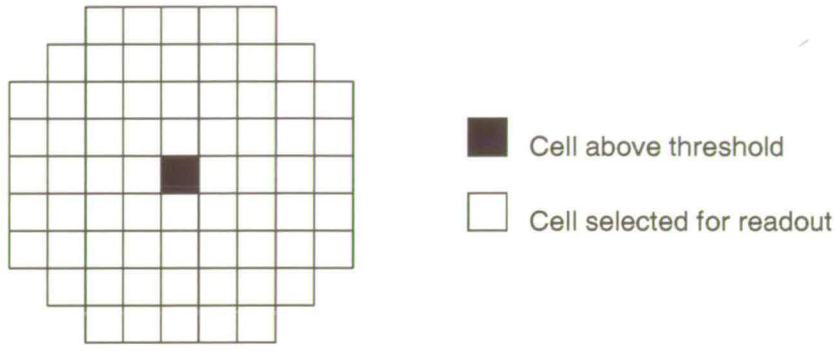

Figure 3.13: The Data Concentrator algorithm for a single cell above threshold. Sixty-Nine cells are selected for read out.

3.9.3 Readout of the LKR

The LKR Readout system processes the currents created by the showers in each of the readout cells and digitises the signal. If a trigger is issued for that event, these signals are read by the data concentrator which sends the data to the PC Farm.

In order to achieve a good time resolution, only the initial current from each cell is read out. The current is read out by charge preamplifiers placed directly on the back of the detector. The signal is amplified and sent to one of the 246 Calorimeter Pipeline Digitiser Modules (CPD). The CPD digitises the signal in a 40 MHz Flash ADC (FADC). To allow a large range of energies to be read out accurately, the FADC has a 4-bit gain switching algorithm. This means the FADC can choose to digitise the signal according to one of four different algorithms, or gains. Each of the gains is optimised for a different sub-energy range. The gain is chosen dynamically from the pulse height information. The chosen gain and the digitised signal are stored in a buffer to be read by the data concentrator if a trigger is issued for that event.

Analogue summed signals of the calorimeter information are also produced in the CPD's for the neutral trigger system. This is described in detail in section 4.2.1.

3.9.4 The Data Concentrator

There are 13248 readout cells in the calorimeter but only a few contain interesting information at any one time. To reduce the data volume from the LKR the data concentrator identifies the interesting cells in each event. The data concentrator identifies cells with energies above a predefined threshold. Cells around these cells are selected to be read out, as illustrated in figure 3.13. For a typical photon shower there are several cells above threshold and around 100 cells are read out.

3.9.5 The Performance of the LKR

The calibration of the LKR is determined using two methods: η runs and Ke3 decays.

Special η runs were taken four times during the 1998 run. During an η run the K_L beamline is used to transport a 75 GeV/c π^- beam to a 3.5 cm polythene target. The target is placed at either $z = z_{AKS}$ or $z = 1500$ cm. Charge exchange processes cause π^0 and η particles to be produced in the target. The instantaneous decays $\eta \to 2\gamma$ and $\eta \to 3\pi^0 \to 6\gamma$ are used to calculate the calibration factors.

During normal $\mathcal{R}e(\epsilon'/\epsilon)$ data-taking, $K_L \to \pi^\pm e^\mp \nu_e$ decays are recorded. All of the electron's energy is deposited in the calorimeter. The measurement of the electron's energy can be compared to the momentum measured in the spectrometer to calculate any corrections needed. Both methods were used to calculate cell-by-cell correction factors, and also to determine the overall energy scale of the LKR. The application of these corrections to the data is described in more detail in section 7.14.

After the calibration factors have been applied, the energy resolution was measured to be:

$$\frac{\sigma(E)}{E} = \frac{0.032}{\sqrt{E}} \oplus \frac{0.1 \text{ GeV}}{E} \oplus 0.005 \qquad \text{for } E \text{ measured in GeV} \tag{3.3}$$

The first term is the stochastic term, which is due to the number of ionisation electrons produced at a given energy. The second term is due to electronic noise and the last term is due to the uncertainty in the calibration factors. The energy resolution of a typical 25 GeV photon from a $K^0 \to \pi^0\pi^0 \to 4\gamma$ decay is 1%, with the three terms contributing with the same order of magnitude.

After these corrections are applied any residual energy scale correction can be determined by fitting the reconstructed z position of the AKS, as described in sections 3.5 and 7.14.

The position resolution of photon clusters is better than 1.3 mm in the x and y directions for photon energies above 20 GeV. Combining the energy and position measurements gives a reconstructed z-vertex resolution of $\sigma_z \simeq 60$ cm for $\pi^0\pi^0$ decays.

The time resolution of a single photon cluster of 20 GeV or more is better than 300 ps. The time resolution of a $\pi^0\pi^0$ decay is 260 ps.

During the 1998 run around 50 of the calorimeter cells had either faulty preamplifiers or no voltage was applied to the electrodes. Events where the shower maximum is in or near one of these dead cells are excluded from the analysis offline.

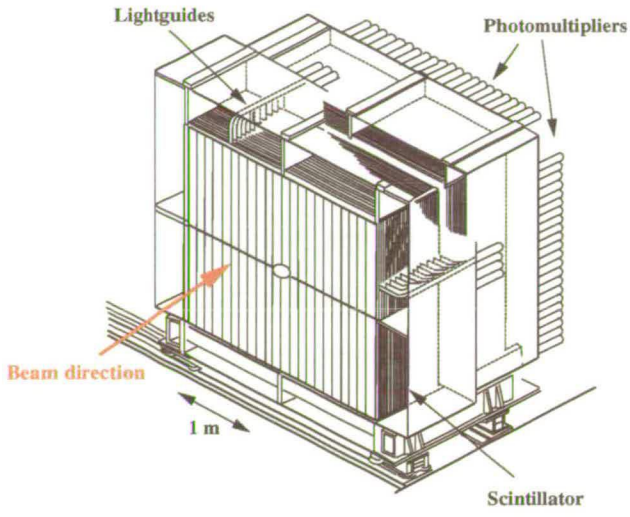

Figure 3.14: The Hadronic Calorimeter.

3.9.6 The Neutral Hodoscope

The Neutral Hodoscope (NHOD) is used to provide an independent trigger for $\pi^0\pi^0$ events. It also gives an independent time measurement for $\pi^0\pi^0$ events, which can be used to cross check the time from the LKR. It is made of 32 bundles of scintillating fiber counters, installed inside the LKR at $\sim 9.5\ X_0$, where the shower profile reaches its maximum. For photons of 15 GeV or greater the time resolution of the NHOD is better than 300 ps.

3.10 The Hadronic Calorimeter

The Hadronic Calorimeter (HAC) is a secondary calorimeter used to detect the remaining energy in $\pi^+\pi^-$ decays. The HAC is illustrated in figure 3.14. It is an iron-scintillator sandwich calorimeter divided into front and back modules. The HAC has a total of 6.7 nuclear interaction lengths. Each module is made of 23 planes of iron and 24 planes of scintillator which are divided into 44 half-strips per plane. The strips are alternately horizontally and vertically orientated. Photomultipliers collect the light from the scintillator strips in such a way that the readout is projective, *i.e.* signals from strips in the same position and orientation are sent to the same photomultiplier. Four CPD's (identical to those described for the readout of the LKR) are used to digitise the signals. The sum of the signals is sent to the Level 1 trigger to determine the hadronic contribution to the total energy.

3.11 The Muon Veto

The Muon Veto detector (MUV) is used to veto $K_L \to \pi^{\pm}\mu^{\mp}\nu_{\mu}$ decays. It is also used to give a positive muon trigger for rare decays, such as $K_L \to \mu^+\mu^-\gamma$.

The MUV consists of three planes of scintillator each preceded by 80 cm of iron. The final scintillator plane is followed by 40 cm of iron. The first two planes have 11 strips of scintillator in the horizontal and vertical directions respectively. Plane three has 6 strips of scintillator in the vertical direction. The scintillators overlap slightly to avoid any inefficiencies. The scintillators are read out by photomultipliers at both ends of each strip. Planes one and two are used to define the muon trigger. Plane three is used in conjunction with the HAC for efficiency studies.

A problem with the MUV has been the age of the scintillator, which was first used in the NA31 experiment in 1985. At the end of the 1998 run the scintillator in planes one and two of the MUV was replaced. The new scintillator gives around 40 photoelectrons per strip per muon, compared to only 3 or 4 in the old scintillator. The result is that the time resolution of the MUV improved from 700 ps during the 1998 run to 350 ps during the 1999 run.

Chapter 4

Triggers and Data Acquisition

The trigger and data acquisition systems of the NA48 experiment are designed to cope with high event rates. The trigger consists of two stages which reduce the rate from about 2 million events per burst in the subdetectors to about 17,000 events to be read out. A PC Farm is used to collect the data from the subdetectors and build them into complete events. The data is then processed by the Level 3 program which carries out an online reconstruction of the data. The Level 3 program also filters this reconstructed data and several output streams are written to tape.

This chapter describes the trigger and data acquisition systems of the NA48 experiment, with special emphasis on the triggering, acquisition and reconstruction of $K^0 \to \pi^0\pi^0$ and $K^0 \to \pi^+\pi^-$ events.

4.1 The trigger architecture

A schematic overview of the NA48 trigger system is shown in figure 4.1.

The NA48 trigger system is designed to cope with the high event rate, to have negligible dead time and to avoid biases in the collection of the four $\mathcal{R}e(\epsilon'/\epsilon)$ decay modes. The trigger system has two stages, Level 1 and Level 2, which reduce the number of events to be read out to around 17,000 per burst. This number is limited by the amount of information that can be sent from the LKR to the PC farm.

The NA48 trigger system is asynchronous, trigger signals may be sent or received at any time. Time information is used to connect the data from the subdetectors. A universal 40 MHz clock is distributed to all the subsystems, except the tagger, to provide a reference time. Due to its higher rate of activity the proton tagger has a 960 MHz clock which is in phase with the 40 MHz clock.

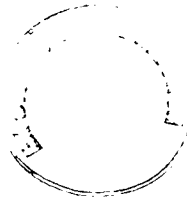

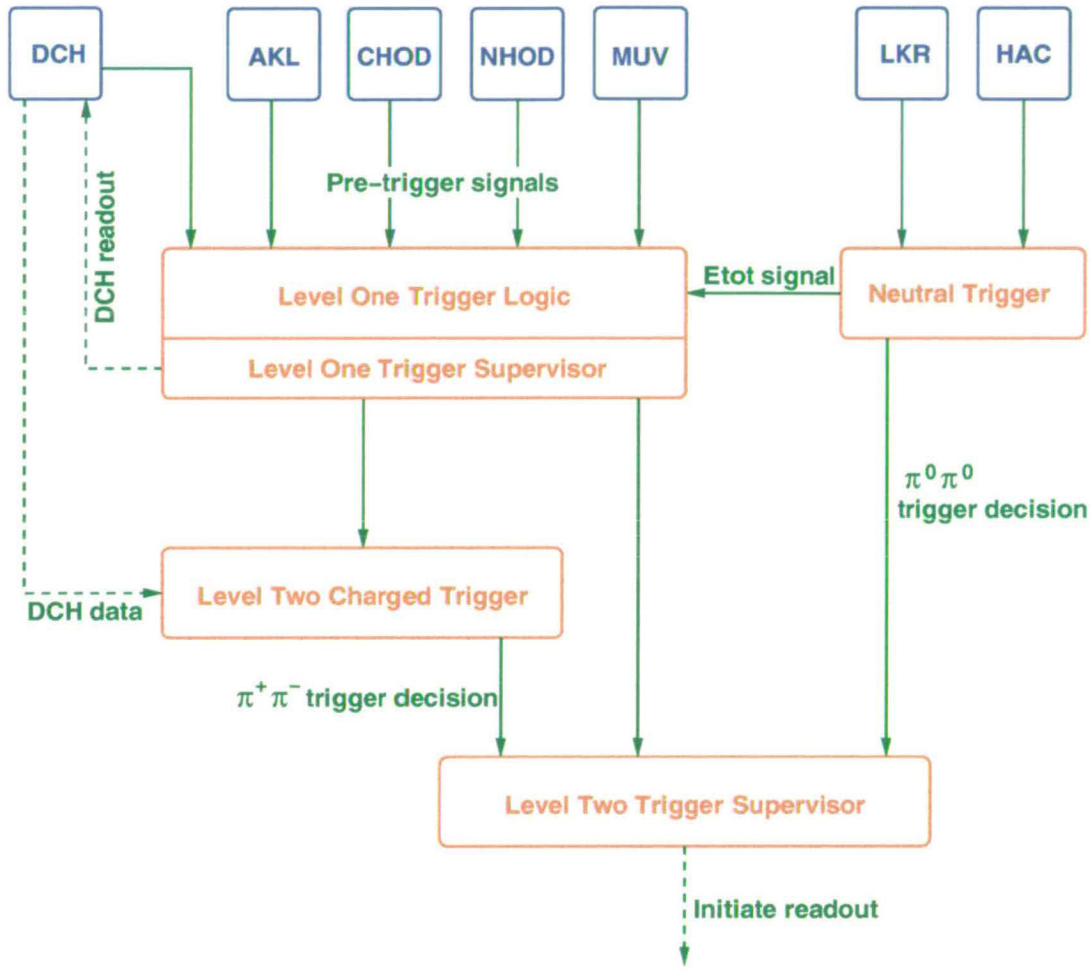

Figure 4.1: A simplified schema of the NA48 Level 1 and Level 2 Trigger Systems.

All the trigger information is collected by the Trigger Supervisors. The Level One Trigger Supervisor (L1TS) collects pre-trigger signals from various subsystems: the drift chambers, the Anti-K_L detectors, the charged and neutral hodoscopes, the muon veto and the neutral trigger system. The main signals from these systems are detailed in table 4.1. These asynchronous signals are read into the L1TS every 25 ns. The L1TS decides whether a trigger condition has been fulfilled. Positive Level 1 trigger decisions are sent to the Level 2 Trigger Supervisor (L2TS). The L2TS also receives information from the Level 2 Charged Trigger and the Neutral Trigger system. If the Level 2 Trigger conditions are satisfied the L2TS generates a timestamp for the event and issues a request for the event to be read out.

Dedicated triggers are defined for $K^0 \to \pi^0\pi^0$ and $K^0 \to \pi^+\pi^-$ decays. The $\pi^0\pi^0$ trigger decision, described in section 4.2.1, is made by the Neutral Trigger system using information from the calorimeters. The $\pi^+\pi^-$ trigger decision is described in

Sub-system	Signal	Description
AKL	AKL	activity in any of the AKL counters
DCH	2 track	2 tracks in drift chamber 1
DCH	4 track	4 tracks in drift chamber 1
CHOD	Q_X	activity in diagonally opposite quadrants of the Charged Hodoscope
NHOD	NHOD	activity in any two quadrants of the Neutral Hodoscope
Neutral Trigger	E_{TOT}	energy sum of LKR and HAC > 30 GeV
MUV	1μ	1 hit in both MUV planes 1 & 2
MUV	2μ	2 hits in either MUV planes 1 or 2, plus 1 hit in the other plane

Table 4.1: The main pre-trigger signals sent to the level one trigger supervisor.

section 4.3. If the event satisfies the Level 1 $\pi^+\pi^-$ conditions the Level 2 Charged trigger makes a final $\pi^+\pi^-$ trigger decision using the wire hit information from the drift chambers.

Downscaled 'minimum-bias' triggers are taken concurrently in order to investigate the efficiency of the $\pi^0\pi^0$ and $\pi^+\pi^-$ triggers. The NHOD trigger, described in table 4.1, is used as a minimum-bias trigger for $\pi^0\pi^0$ events. The pre-trigger signals: E_{TOT}, 2 track and Q_X are used as the minimum-bias triggers for $\pi^+\pi^-$ events. These signals are described in more detail in sections 4.2.2 and 4.3.

Special triggers can also be defined to investigate rare kaon decays such as $K_L \to \pi^+\pi^-e^+e^-$ and $K_L \to \mu^+\mu^-\gamma$.

In total around 17,000 positive trigger decisions are made every burst. Around 11,000 of these are $K^0 \to \pi^0\pi^0$ and $K^0 \to \pi^+\pi^-$ triggers. The remaining 6,000 are made up of minimum-bias triggers, rare decay triggers, triggers for calibration data and random triggers (as described in section 3.3.5).

4.2 The Neutral Trigger System

The main purpose of the neutral trigger system [26, 10] is to provides a trigger for $\pi^0\pi^0$ decays. It also provides a total energy trigger (E_{TOT}) which is used in the Level 1 $\pi^+\pi^-$ trigger.

The dead-time of the neutral trigger system is kept low by employing a fully pipelined trigger which makes a decision every 25 ns. There are 128 stages of the pipeline which

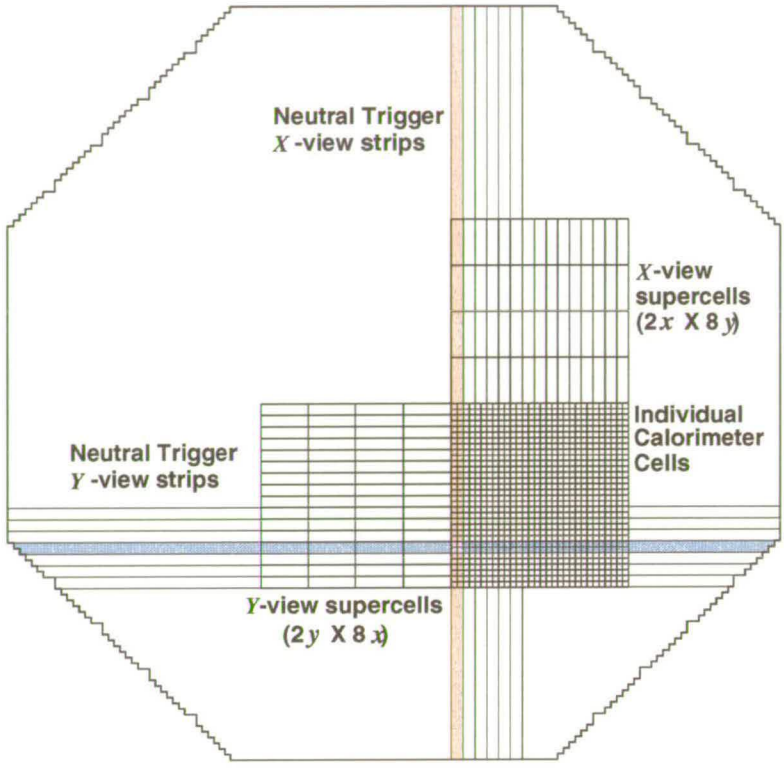

Figure 4.2: Illustration of the summing procedure for defining the projective strips of the LKR. One strip in each view is shaded for clarity

make a calculation and pass the information to the next stage of the pipeline. The decision of the Neutral Trigger System arrives at the L2TS after a fixed delay of 3.2 μs after the event.

4.2.1 The $\pi^0\pi^0$ Trigger

In order to calculate physical quantities quickly, the calorimeter information from the individual cells is first summed into projective strips.

Sixty-four horizontal and sixty-four vertical strips are used, each 4 cm wide. The procedure for summing the cells into the strips is illustrated in figure 4.2. First, the individual calorimeter cells are added together to make 2×8 supercells. This is done individually for both projections. The pedestals (background electronic noise) are subtracted from the supercells. Second, the supercells are added to make 64 strips in both the X and Y views; each strip is two cells wide. Only regions of the LKR near energy depositions (photon candidates) are allowed to contribute to the sums, thus reducing the noise level. The final results of the summing are 12-bit energy sums, E_i^x

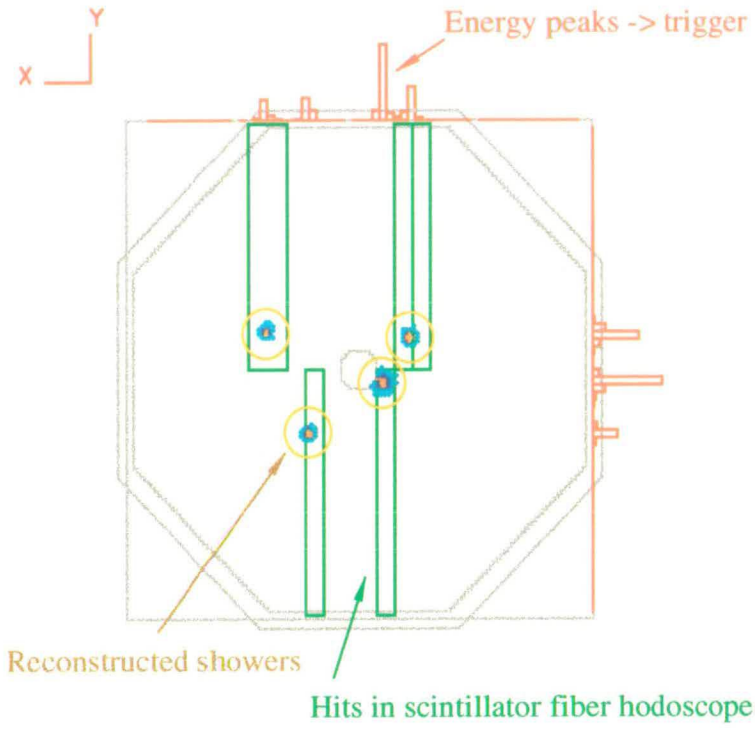

Figure 4.3: An online plot of a $K^0 \to \pi^0\pi^0 \to 4\gamma$ event. The four γ clusters are circled. The energy in the neutral trigger projective strips are shown along the top and right-hand side of the diagram. In this example, there are 4 peaks in the X-view and 3 peaks in the Y-view.

and E_i^y, for each of the strips ($i = 1, 64$) in each projection (X and Y).

The energies of the strips E_i^x and E_i^y are used to calculate the moments, $m_{n,x}$ and $m_{n,y}$, according to the formulae:

$$\begin{array}{lllll} m_{0,x} & = & \sum_{i=1}^{64} E_i^x & m_{0,y} & = & \sum_{i=1}^{64} E_i^y \\ m_{1,x} & = & \sum_{i=1}^{64} E_i^x (i-32) & m_{1,y} & = & \sum_{i=1}^{64} E_i^y (i-32) \\ m_{2,x} & = & \sum_{i=1}^{64} E_i^x (i-32)^2 & m_{2,y} & = & \sum_{i=1}^{64} E_i^y (i-32)^2 \end{array} \qquad (4.1)$$

Here $i = 1, 64$ labels the number of the strip, from the bottom to the top of the calorimeter for the X-projection and from the right to the left of the calorimeter for the Y-projection. In both projections $i = 32$ labels the central strip.

These moments are used in the calculation of physical quantities: the total energy in the LKR, E_{LKR}, the centre of gravity, r_{cog}, and the distance of the kaon decay vertex from the front face of the calorimeter, d_{vertex}:

$$E_{\mathrm{LKR}} = \frac{1}{2}(m_{0,x} + m_{0,y}) \qquad (4.2)$$

Quantity	Trigger Cut	Analysis Cut
Kaon energy, E_{LKR}	≥ 50 GeV	≥ 70 GeV
r_{cog}	≤ 15 cm	< 10 cm
Kaon lifetime from AKS	$< 6\ \tau_{\mathrm{K_S}}$	$< 3.5\ \tau_{\mathrm{K_S}}$
peaks in x-projection	≤ 5	4 γ clusters
peaks in y-projection	≤ 5	

Table 4.2: The 1998 online cuts used in the Neutral Trigger for the $\pi^0\pi^0$ trigger. The offline cuts made in this analysis are shown for comparison.

$$r_{\mathrm{cog}} = \frac{\sqrt{(m_{1,x})^2 + (m_{1,y})^2}}{E_{\mathrm{LKR}}} \tag{4.3}$$

$$(d_{\mathrm{vertex}})^2 = \frac{E_{\mathrm{LKR}}\,(m_{2,x} + m_{2,y}) - (m_{1,x})^2 - (m_{1,y})^2}{m^2_{\mathrm{K^0}}} \tag{4.4}$$

The distance d_{vertex} is then used to estimate the lifetime of the kaon from the AKS position in units of $\tau_{\mathrm{K_S}}$:

$$\frac{c\tau}{c\tau_{\mathrm{K_S}}} = \frac{(z_{\mathrm{LKR}} - z_{\mathrm{AKS}}) - d_{\mathrm{vertex}}}{E_{\mathrm{LKR}} \cdot c\tau_{\mathrm{K_S}}/m_{\mathrm{K^0}}} \tag{4.5}$$

The trigger also uses the number of 'peaks' in the LKR energy distribution to make its decision. A 'peak' is a local energy maximum in the projective strips. A photon hit in the calorimeter will cause a peak in both the X and Y views, as shown in figure 4.3. Clusters may overlap in the projections, so a good $\pi^0\pi^0$ event should have ≤ 4 peaks in both the X and Y views. More formally, a peak is found on strip i when the following conditions are met:

$$E_{i-1} < E_i \quad , \quad E_i \geq E_{i+1} \tag{4.6}$$

A $\pi^0\pi^0$ trigger is issued if the conditions in table 4.2 are met. Around 5000 $\pi^0\pi^0$ trigger are issued per burst.

4.2.2 The $\mathsf{E_{TOT}}$ signal

The Neutral Trigger also calculates the total energy in both the LKR and the HAC for use in the Level 1 $\pi^+\pi^-$ trigger. The neutral trigger system also receives analogue sum information from the HAC readout. This is added to E_{LKR} (equation (4.2)) to calculate the total energy. An $\mathsf{E_{TOT}}$ signal is issued if the calculated total energy is greater than 30 GeV. The $\mathsf{E_{TOT}}$ signal is used in the Level 1 $\pi^+\pi^-$ trigger.

Quantity		Cut Value
vertex cuts	closest distance of approach	< 5 cm
	opening angle	< 15 mrad
	z-position from K_S target	$1 < z < 48$ m
mass cut, $m_{\pi^+\pi^-}$		$> 0.95\ m_{K^0}$
lifetime from K_S target, τ		$< 4.5\ \tau_{K_S}$

Table 4.3: Cuts applied by the Level 2 Charged Trigger.

4.3 The $\pi^+\pi^-$ Trigger

The $\pi^+\pi^-$ trigger [22, 29] is made in two stages. The Level 1 $\pi^+\pi^-$ trigger (L1$\pi\pi$) requires a coincidence of three pre-trigger signals:

1. The E_{TOT} signal from the neutral trigger, as described in section 4.2.2.
2. The 2 track drift chamber multiplicity signal [6]. This is based upon the number of wire hits in both planes of each view (x, y, u and v) of drift chamber 1. If two tracks have passed through the chamber there should be 2 hits in each plane of wires, or equivalently 4 hits in each view. To account for possibly inefficiencies, the 2 track signal is issued if at least 3 views each find 3 or more hits.
3. The Q_X signal from the charged hodoscope. The Q_X signal is issued if there is a coincidence of hits in diagonally opposite quadrants of the charged hodoscope. To avoid inefficiencies, the definition of the quadrants for the trigger are extended to include the two adjacent counters of the neighbouring quadrant. A hit in either plane (horizontal or vertical) of the quadrant is sufficient.
   This Q_X signal rejects some of the background from three-body decays such as Ke3, Kμ3 and $K_L \to \pi^+\pi^-\pi^0$, since the two charged particles from these decays may hit adjacent quadrants of the detector.

The L1TS requires the coincidence $E_{TOT} \cdot 2\,\text{track} \cdot Q_X$ to issue a L1$\pi\pi$ trigger. This particular coincidence is chosen as it allows all of the $K \to \pi^+\pi^-$ decays to be selected whilst keeping the instantaneous rate to the Level 2 Charged Trigger at less than 150 kHz, which is the maximum rate it can accept. Around 180,000 L1$\pi\pi$ triggers are issued during each 2.2 s proton burst.

If a L1$\pi\pi$ trigger is issued by the L1TS, a request is sent to the Level 2 Charged Trigger, also known as the Massbox. The Massbox uses information from chambers 1, 2 & 4 to make a decision. It performs the following tasks:

- The coordinates and times of the hits in each view (x, y, u and v) of each

chamber are calculated.

- Using the coordinates and time information from chambers 1 and 2 all possible tracks are constructed.
- For each set of two tracks, the decay vertex is reconstructed. Sets of tracks that do not satisfy the vertex cuts shown in table 4.3 are rejected.
- Taking into account the field in the magnet, the impact positions of the track pairs in chamber 4 are calculated. If extrapolated tracks match to the calculated coordinates in chamber 4, the invariant $\pi^+\pi^-$ mass, $m_{\pi^+\pi^-}$, and kaon lifetime from the K_S target are calculated. The mass resolution achieved is around 5 MeV/c^2. If these quantities pass the cuts shown in table 4.3, the event is flagged as a $\pi^+\pi^-$ trigger.

The decision of the Massbox is sent to the L2TS.

The Massbox achieves a rejection power of around 35, the resulting rate of $\pi^+\pi^-$ triggers is around 5500 per burst. The average time for the Massbox to make its decision is 69 μs. About 0.5% of events cannot be processed within the limit of 102.5 μs. In this case a "Massbox doesn't know" signal is sent to the L2TS and the event is kept.

If the Massbox receives more L1$\pi\pi$ requests than it can process in a given period of time, the Massbox sends a signal (L1off) to the L1TS which disables further L1$\pi\pi$ requests. The L1off signal is removed as soon as the Massbox is able to process more requests. This effect is known as Charged Trigger Deadtime as the Massbox cannot make decisions about L1$\pi\pi$ triggers issued during this time. The Charged Trigger Deadtime accounts for up to 5% of the time during a burst.

The Massbox can also make triggers for rare decays such as a four track trigger for $K_L \to \pi^+\pi^-e^+e^-$.

4.4 Data Acquisition

An overview of the NA48 Data Acquisition is given in figure 4.4. If a trigger is issued by the Trigger Supervisor, the subdetectors send data for that event to the PC farm. The PC farm builds the subdetector data into complete events and sends it to the CERN computing centre where the data is processed and stored.

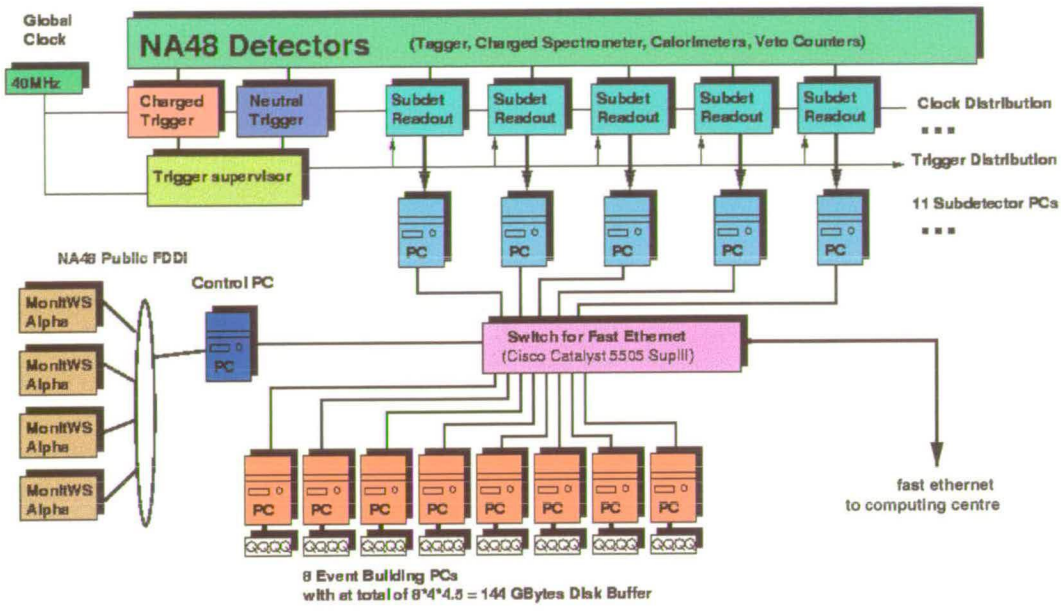

Figure 4.4: The NA48 data acquisition system.

4.4.1 Subdetector Read Out

The data from each of the subdetector systems is digitized at the clock frequency of 40 MHz and stored in ring buffers: each of the buffers is at least 200 μs deep.

If a positive trigger decision has been made, the Level 2 Trigger Supervisor issues a readout request containing the event number, the time stamp and the trigger code of the event. The readout request must be issued within 200 μs of the event, otherwise the event information will be lost. The minimum time between L2TS readout requests is 20 μs, the time it takes to read out one event. When a readout request is received by a subdetector, the event information is selected from the buffer based on the time stamp information. Information in a $[-400, +400]$ ns window around the trigger time stamp is sent to a dedicated PC, known as a subdetector PC. The subdetector PCs form part of the PC farm.

4.4.2 The PC Farm

The PC farm consists of 11 subdetector PCs (SDPCs), 8 event building PCs (EBPCs) and a control PC, each running Linux. As explained in the previous section, the subdetector PCs store the subdetector data which has been collected from the ring buffers. The event building PCs rearrange the data and send it to the CERN comput-

ing center. The control PC issues instructions to the SDPCs and EBPCs and monitors the PC farm processes.

The transfer of information between the PCs is enabled by a fully connected, fast ethernet switch. Each PC can send and receive information to and from the switch at a rate of 200 Mbit/s.

During the SPS burst, the SDPCs store the subdetector data. At the end of the burst this data is checked and partitioned into eight blocks. Each data block is sent to one of the eight EBPCs via the switch. The partitioning is carried out so that all the information from one event is given to the same EBPC. The data on the EBPCs are arranged into complete events: each complete event contains information from each of the subdetectors.

The complete events are then sent, via the switch and a 7 km fast ethernet link, to the CERN computing centre. The data is placed on a Meiko Computing Surface 2 parallel processing computer (CS2). Here the events are assembled into a burst file, which contains all the events from the SPS burst in chronological order.

4.5 The Level 3 Trigger

The final stage of online data processing is the reconstruction of the data and the selection of the reconstructed events by the Level 3 Trigger.

The Level 3 Trigger and Real Time Reconstruction (L3/RTR) is implemented entirely in software and run on the CS2 computer.

For events with $\pi^0\pi^0$ or $\pi^+\pi^-$ triggers, the L3/RTR program first executes the LKR and DCH reconstructions, as described in sections 4.6.1 and 4.6.2, using the best available calibration constants. These events are then filtered by the Neutral or Charged Filter, as described below. If an event is selected by the Filters, the reconstruction of the data from the other subdetectors is carried out and the event is saved to tape. A small fraction of events that do not satisfy the filter conditions are also saved to tape.

The Neutral Filter. Events with a $\pi^0\pi^0$ trigger are filtered by the Neutral Filter. To be selected, the total reconstructed energy in the LKR must be over 50 GeV. The number of clusters with 2 GeV or over, within a 12.5 ns window, has to be between 4 and 25. The radius of the centre of gravity (defined in equation (6.6)) must be less that 15 cm, and the lifetime of the reconstructed kaon from the AKS position less than 6 τ_{K_S}. To reject background from $K_L \to 3\pi^0$, the ellipse number of the event (equation (6.11)) must be smaller than 20.

The Charged Filter. Events with a $\pi^+\pi^-$ trigger are filtered using the Charged Filter. For an event to be selected, there must be at least two reconstructed tracks with a closest distance of approach of less than 5 cm. The radius of the centre of gravity (defined in equation (6.7)) must be less than 15 cm. The reconstructed invariant $\pi^+\pi^-$ mass must satisfy $|m_{\pi^+\pi^-} - m_{\mathrm{K}^0}| \leq 20$ MeV/c^2. The reconstructed lifetime of the kaon from the AKS position must be less than 5 $\tau_{\mathrm{K_S}}$. To reject background from $\mathrm{K_L} \to \pi^\pm e^\mp \nu_e$ events, a requirement is made on tracks from $\mathrm{K_L}$ decays that the ratio of the tracks' energy in the LKR, to their momenta (E_{LKR}/p) must be less than 0.95.

Events with other triggers are also reconstructed, filtered, and if selected, saved to tape. These filters are described in detail in [28].

4.5.1 Data Formats and Post-Run Reprocessing

The events are saved to tape in two formats: Compact and Raw. The Raw data format contains the unreconstructed subdetector information. The Compact data format contains a selection of reconstructed quantities and is used for physics analysis. Due to the large data volume of the NA48 experiment, there is also a SuperCompact data format, which contains the subset of the Compact variables relevant for the measurement of $\mathcal{R}e(\epsilon'/\epsilon)$. The Compact data set is filtered and those events suitable for the $\mathcal{R}e(\epsilon'/\epsilon)$ analysis are written in SuperCompact format.

After the 1998 data-taking period was complete, the Raw data set was reprocessed by running the reconstruction program using updated values of the calibration constants.

The data used in this analysis is from the post-run reprocessing in SuperCompact format.

4.6 Data Reconstruction

The analysis of $\mathrm{K}^0 \to \pi^0\pi^0$ decays uses the reconstructed LKR data. The analysis of the $\mathrm{K}^0 \to \pi^+\pi^-$ decays uses the reconstructed DCH and LKR data, as well as information from the Charged Hodoscope and the Muon Veto. Reconstruction of the data from these subdetectors is described below.

4.6.1 Reconstruction of the LKR calorimeter data

The aim of the LKR reconstruction [61] is to calculate the energies, positions, times and sizes of the clusters due to the particle hits. A particle hit in the calorimeter is known as a 'cluster'. The program is designed to take into account overlapping

clusters and dead cells within the calorimeter.

The starting point for the neutral reconstruction is the signals from the calorimeter cells. Cells with energies greater than 0.2 GeV are designated as candidate seed cells for clusters. If such a cell is higher in energy than the eight surrounding cells, and is greater than a cut defined by the average energy of the eight surrounding cells ($E_{\text{seed}} > 0.18\ \text{GeV} + 1.8 \cdot E_{\text{ave}}$) then a 'cluster' is said to have been found.

The next stage of the reconstruction loops over all the clusters. Cells within 11 cm of the seed cell are allowed to contribute to the energy of the cluster. If a cell can belong to two or more clusters, the energy of the cell is apportioned between clusters according to the expected shower profile. The shower profile was estimated using a GEANT [68] simulation of showers in the calorimeter. At this stage corrections are made for the energy loss due to the hole for the beam pipe, residual effects due to the zig-zag electrode structure (see section 3.9.2) and for the overall energy scale of the calorimeter (see section 3.9.5).

The position of a cluster is computed as the barycentre of the energy distribution in a 3×3 box of cells centred on the cluster seed cell. The cluster sizes in the x and y directions are computed using the RMS of the energy distribution in a 5×5 cell box around the seed cell. Likewise, the time of the cluster hits is calculated as the energy-weighted time average of the cells in 5×5 box centred on the seed cell.

Each set of four clusters is considered as a candidate for a $\mathrm{K}^0 \to \pi^0\pi^0 \to 4\,\gamma$ event. Using the positions and energies of the clusters, the following quantities are calculated for each $\mathrm{K}^0 \to \pi^0\pi^0$ candidate:

1. The kaon energy, which is defined as the sum of the energies of the 4 clusters:

$$E_{\mathrm{K}} = \sum_{i=1}^{4} E_{\gamma^i} \tag{4.7}$$

2. The distance from the calorimeter to the decay vertex, $d = z_{\text{LKR}} - z_{\text{decay}}$:

$$d^2 = \sum_{i=1}^{4} \sum_{j=i+1}^{4} \frac{E_{\gamma^i}\, E_{\gamma^j}\, \mathbf{r}_{ij}^2}{m_{\mathrm{K}}^2} \tag{4.8}$$

   where $\mathbf{r}_{ij}$ is the distance between the clusters i and j in the calorimeter.

3. The invariant mass of each of the possible photon pairs:

$$(m_{\gamma^1\gamma^2})^2 = \frac{E_{\gamma^1}\, E_{\gamma^2}\, \mathbf{r}_{12}^2}{d^2} \tag{4.9}$$

   For each set of 4 photons, there are three possible combinations of the photon pairing. As a first approximation, the best pairing is chosen by minimising:

$$\chi_m^2 = (m_{\gamma^i\gamma^j} - m_{\pi^0})^2 + (m_{\gamma^k\gamma^l} - m_{\pi^0})^2 \tag{4.10}$$

4. The time of the $K^0 \rightarrow \pi^0\pi^0$ event is the energy weighted average of the individual cluster times.

4.6.2 Reconstruction of the drift chamber data

The drift chamber reconstruction [19] reconstructs particle tracks from hits in the drift chambers. It calculates the charge, momenta, and the positions and times of the track hits in the drift chambers. The reconstruction is made in two stages. The first stage uses only the wire hit information to reconstruct the tracks. The second stage uses the drift time information to improve the resolution and to resolve any left-right ambiguities. From the reconstructed tracks the momenta, decay vertex and track times can be calculated.

The first step of the reconstruction algorithm is to form 'mini-tracks' between chambers 1 and 2. A mini-track is formed by joining clusters of wire hits in chambers 1 and 2 by a straight line. The mini-tracks must be consistent with the path of a decay product from either the K_L or K_S beam. The directions of these mini-tracks are used to estimate y-position of the track hits in chamber 4. (The y-position can be most accurately estimated at this stage as there is almost no deflection in this direction due to the magnetic field.)

Clusters of wire hits in chamber 4 are grouped together into 'spacepoints'. A spacepoint is a set of 3 or 4 clusters where the x and y-view positions agree with the u and v-view positions. If a spacepoint agrees with an estimated y-position within 4 cm, then a 'track' is said to have been found.

In the second stage the reconstructed tracks are compared with the times of the wire hits. This information is used to refine the cluster information into the positions of spacepoints in each of the chambers 1, 2 and 4. A quality variable is assigned to each track and those of poor quality are rejected. Tracks are also rejected if the reconstructed spacepoints in the chambers are inconsistent with the wire hit information.

The track momentum is calculated using the curvature of the track trajectory and an accurate map of the magnetic field. If the closest distance of approach between track pairs is less than 5 cm, then the tracks are said to come from a common decay vertex. The position of the vertex is defined as the mid-point between the two tracks at their closest distance of approach.

Each decay vertex with oppositely charged tracks is considered as a candidate for a $K^0 \rightarrow \pi^+\pi^-$ event. The energy of the kaon for this decay is calculated using the opening angle θ between the two tracks and the energies of the two tracks, assuming

they were charged pions:

$$E_{\mathrm{K}} = \frac{\sqrt{R\,(m_{\mathrm{K}}^2 - m_{\pi^\pm}^2 R)}}{\theta} \quad \text{where} \quad R = \frac{(E_+ + E_-)^2}{E_+\,E_-} \tag{4.11}$$

A derivation of this formula may be found in [56]. This definition is used in preference to more usual formula $E_{\mathrm{K}} = E_+ + E_-$ as it reduces the effects from uncertainties in magnetic field and multiple scattering on the measurement of E_{K}.

4.6.3 Reconstruction of the Charged Hodoscope Data

The Charged Hodoscope defines the event time of a $\pi^+\pi^-$ event [50]. Reconstructed tracks from a common vertex are used to calculate the positions of charged particle hits in the hodoscope. These positions are used to identify whether the hodoscope hits belong to the track pair, and to correct the times for the signal propagation in the scintillator. The corrected times of the hodoscope hits belonging to the vertex are averaged to define the event time.

4.6.4 Reconstruction of the Muon Veto Data

The MUV reconstruction identifies which charged particles are muons [32, 33]. A search is made for hits in the MUV scintillator in regions around the projected impact points of the reconstructed tracks. If a hit is found in both planes 1 and 2, then the track is identified as a muon. The time of the muon hit is calculated as the average of the two hits, corrected for the propagation time of the photons in the scintillator and the time for the muon to travel between the scintillator planes.

Chapter 5

$\mathcal{R}e(\epsilon'/\epsilon)$ Analysis Strategy

This chapter describes the analysis strategy and the data used to measure $\mathcal{R}e(\epsilon'/\epsilon)$. The techniques of K_L event weighting and energy binning are discussed and expressions for fitting the result and calculating errors are presented.

5.1 The Double Ratio

As shown in chapter 2, $\mathcal{R}e(\epsilon'/\epsilon)$ can be accessed by measuring the *double ratio* of decay rates, **R**:

$$\mathbf{R} \equiv \frac{\Gamma(K_L \to \pi^0\pi^0)/\Gamma(K_S \to \pi^0\pi^0)}{\Gamma(K_L \to \pi^+\pi^-)/\Gamma(K_S \to \pi^+\pi^-)} \simeq 1 - 6\,\mathcal{R}e\left(\frac{\epsilon'}{\epsilon}\right) \tag{5.1}$$

Each of the decay rates Γ can be expanded further. As an example, the decay rate for $K_L \to \pi^0\pi^0$ can be expressed in terms of measurable quantities:

$$\Gamma(K_L \to \pi^0\pi^0) = (\Phi_L\, \epsilon_L^{00}\, a_L^{00}\, \tau_L)^{-1} N(K_L \to \pi^0\pi^0) \tag{5.2}$$

Here Φ_L represents the integrated flux of the K_L beam, ϵ_L^{00} represents the efficiency of the triggers and subdetector systems to detect a $K_L \to \pi^0\pi^0$ decay and a_L^{00} represents the geometric acceptance of the detector for a $K_L \to \pi^0\pi^0$ decay and τ_L is the lifetime of K_L. $N(K_L \to \pi^0\pi^0)$ is the number of $\pi^0\pi^0$ decays observed from the K_L beamline. Similar expansions can be made for the other decay modes.

As data is collected simultaneously for all four $\mathcal{R}e(\epsilon'/\epsilon)$ decay modes, many of these quantities cancel. The beam fluxes Φ_L and Φ_S vary with time, but as the data is collected simultaneously both these quantities cancel from **R**. To a first approximation, the efficiency for detecting a decay depends only on the decay type, hence $\epsilon_L^{00} = \epsilon_S^{00}$ and $\epsilon_L^{+-} = \epsilon_S^{+-}$.

The geometric acceptance (a) for a particular decay mode depends on the geometry of the detector and its illumination by the decay products. The distribution of the decay products within the detector depends on both the energy of the kaon and the position of its decay vertex. The K_L and K_S beams are designed to be nearly collinear and converge at the detector. Therefore the ratio of the acceptances a_L/a_S is largely insensitive to the detector geometry and depends mainly on the kaon energy and the longitudinal decay vertex, or equivalently the kaon lifetime.

To reduce the effects on $\mathbf{R}$ from the ratio a_L/a_S only those decays occurring within a certain lifetime and energy range are counted. For this analysis, decays with kaon energies between 70 and 170 GeV and lifetimes between 0 and 3.5 K_S lifetimes (as measured from the AKS position) are used. As discussed in section 3.5, the AKS detector is used to define $t_K = 0$ for K_S decays. For K_L decay $t_K = 0$ is defined offline using $z_{decay} = z_{AKS}$.

Within this fiducial range, the distributions of K_L and K_S events is still very different, due to their very different lifetimes and different energy spectra. In order to reduce effects from the lifetime difference, the K_L events are *weighted* in such a way that the distribution of the decay vertex for weighted K_L decays is the same as that for (unweighted) K_S decays. This procedure is discussed further in section 5.3. To reduce effects arising from the variation of the energy spectra, the analysis is performed in bins of kaon energy. The size of the bins is chosen so effects due to variation within one bin can be neglected. The energy binning and its implications for the analysis are discussed further in section 5.4.

After the weighting procedure and energy binning, to a first approximation, the acceptance for a given decay mode is independent of the beam, *i.e.* $a_L^{00} = a_S^{00}$ and $a_L^{+-} = a_S^{+-}$.

The kaon decay products $\pi^\pm$ and π^0 can themselves decay. The neutral pions decay almost instantaneously, 98.8% of the time to 2 photons. In this analysis the $\pi^0\pi^0$ are selected by looking for $\pi^0\pi^0 \to 4\gamma$ decays. Charged pions have a lifetime of 7.8 m/c and decay almost 100% of the time to $\mu\nu_\mu$. At a typical $\pi^\pm$ energy of 50 GeV, around 5% of charged pions decay before reaching the detector. For a decay at a given kaon energy and decay position, the fraction of $\pi^\pm$ which decay in flight is equal for K_L and K_S decays. Therefore by using energy binning and weighting, the effect from $\pi^\pm$ decays in flight cancels in the measurement of $\mathbf{R}$.

Using the cancellations discussed above, it is possible to make an approximation for the double ratio in a given energy bin i, called $\mathbf{R}_{raw,i}$:

$$\mathbf{R}_{raw,i} = \frac{N_W(K_L \to \pi^0\pi^0 \to 4\gamma)/N(K_S \to \pi^0\pi^0 \to 4\gamma)}{N_W(K_L \to \pi^+\pi^-)/N(K_S \to \pi^+\pi^-)} \tag{5.3}$$

The W subscript on the numbers of the K_L decays indicates that these numbers are

the sum of the weights. The fitted value of $\mathbf{R}_{\text{raw}}$ over all of the energy bins is then obtained using the method described in section 5.4.1 of this chapter.

In order to determine $\mathbf{R}_{\text{raw}}$, one only needs to:

1. Select $K^0 \to \pi^0\pi^0 \to 4\gamma$ decays.
2. Select $K^0 \to \pi^+\pi^-$ decays.
3. Determine if the kaon came from the K_L or K_S beamline. This procedure is known as tagging, as it uses the proton tagging detector described in section 3.4.1.
4. Calculate the energy of the kaons and the weights for the K_L decays.

Chapter 6 describes the methods for selecting $K^0 \to \pi^0\pi^0 \to 4\gamma$ and $K^0 \to \pi^+\pi^-$ decays, and the tagging procedure.

To calculate the true value of $\mathbf{R}$, as defined in equation (5.1), corrections are calculated and applied to $\mathbf{R}_{\text{raw}}$ to account for various effects. These corrections account for:

- Miscounting in the selection of the $K^0 \to \pi^0\pi^0 \to 4\gamma$ or $K^0 \to \pi^+\pi^-$ decays. This can be due to background decays, accidental activity in the detector or due to kaon scattering off material in the beam line.
- Mistagging effects where a decay from the K_L beamline is mis-identified as a decay from the K_S beamline, or vice-versa.
- Differences in the acceptance and efficiency for detecting each of the decay modes.

It is worth noting that many of these corrections are *a priori small* because what affects $\mathbf{R}$ is not absolute effects, because only the difference between the $\pi^+\pi^-$ and the $\pi^0\pi^0$ decays, or between the weighted K_L and K_S events, as appropriate, has an effect on the value of $\mathbf{R}$. The calculations of these corrections and their effect on $\mathbf{R}_{\text{raw}}$ are described in detail in chapter 7.

5.2 The 1998 Run

The data used in this analysis was taken during the 1998 run, which included 122 days of active data taking between May and September 1998. The experiment received protons from the SPS accelerator at the nominal proton intensity of 1.5×10^{12} protons per burst. The total amount of data collected in 1998 was 68.5 TeraBytes.

Special data taking conditions were used for short periods during the run. K_S runs were taken where only the beam from the K_S target was used. This data is used to study the identification of K_S decays using the tagger (see section 7.4). η runs, as described in section 3.9.5, were taken to study the detector's response to different energies.

After the processing of the data was complete, all of the data was analysed to investigate the performance of the sub-detectors and the trigger systems. If one or more of the subsystems was deemed to have been operating unsatisfactorily for a period of time, data from this period was excluded from the data set used to determine $\mathcal{R}e(\epsilon'/\epsilon)$.

5.3 K_L Event Weighting

As discussed in section 5.1, a weight is applied to K_L events to reduce effects due to the different decay distributions of K_L and K_S beams. The weight applied depends on the kaon lifetime (t) and the kaon energy (E_K). The weight is defined such that the distribution of decay vertices is the same for $K_S \rightarrow 2\pi$ and weighted $K_L \rightarrow 2\pi$ decays.

The weight (w_i) for an event i is defined as the ratio of the decay distributions ($F(t, E_K)$) of kaons to 2 pions from each of the two targets:

$$w_i = \frac{F(t_S, E_K)}{F(t_L, E_K)} \tag{5.4}$$

Here t_S is the reconstructed kaon lifetime in event i, based on the hypothesis the kaon came from the K_S target. Similarly t_L is the reconstructed kaon lifetime in event i based on the hypothesis the kaon came from the K_L target. E_K is the kaon energy in event i.

The decay distribution $F(t, E_K)$ (where $t = t_S$ or t_L) is, up to normalisation factors, the probability density for $K \rightarrow 2\pi$ decays from the point of kaon production, *i.e.* from one of the targets. This distribution is the same for both targets, it depends only on the lifetime of the kaon from the target (t) and the kaon energy (E_K). The function $F(t, E_K)$ is derived in the following subsection.

The weight w_i is normalised such that $w_i = 1.0$ for a kaon that decays at the z-position of the AKS converter. Figure 5.1 illustrates the weighting function over the range 70 to 170 GeV and 0 to 3.5 K_S lifetimes used in this analysis.

K_L event weighting results in a factor of 1.4 loss in statistical power when using a lifetime range of 0 to 3.5 K_S lifetimes. However the dominant error on $\mathcal{R}e(\epsilon'/\epsilon)$ is from systematic effects and K_L event weighting greatly reduces many systematic uncertainties. Therefore the loss in statistical power caused by the event weighting is justified.

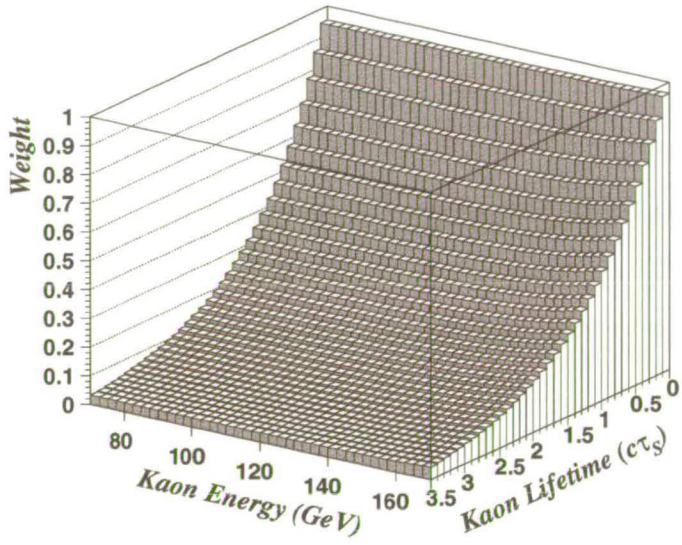

Figure 5.1: The weighting function for K_L decays. The weighting function is exponential as a function of kaon lifetime, as it essentially gives K_L decays the same decay distribution as K_S decays.

5.3.1 Kaon Decay Distribution

The amplitudes of K_L and K_S decays a two pions final states are:

$$A_S^{2\pi}(t) = \mathcal{A}(K_S \to 2\pi) = A_S(0)\, e^{-(1/2\tau_S + i m_S)t} \tag{5.5}$$

$$A_L^{2\pi}(t) = \mathcal{A}(K_L \to 2\pi) = A_L(0)\, |\eta| e^{i\phi}\, e^{-(1/2\tau_L + i m_L)t} \tag{5.6}$$

The terms used in the above equations are:

- $A_S(0)$ and $A_L(0)$ are the amplitudes for all decay modes at $t = 0$.
- $|\eta| \simeq |\eta_{00}| \simeq |\eta_{+-}| = 2.28 \times 10^{-3}$, as defined in equation (2.49), is the ratio of the decay amplitudes of K_S and K_L to two pions.
- $\phi = \arg(\eta) = 43.48°$ is the phase of η.
- τ_S, τ_L, m_S and m_L are the lifetimes and masses of K_S and K_L respectively.

In the targets kaons are produced in their strong eigenstates: K^0 and $\overline{K^0}$. Using equation (2.16), K^0 and $\overline{K^0}$ can be written as:

$$|K^0\rangle = \frac{1+|\epsilon|^2}{\sqrt{2}\,(1+\epsilon)}\Big(|K_L\rangle + |K_S\rangle\Big) \qquad |\overline{K^0}\rangle = \frac{1+|\epsilon|^2}{\sqrt{2}\,(1-\epsilon)}\Big(|K_L\rangle - |K_S\rangle\Big) \tag{5.7}$$

The decay rate of initially pure K^0 or $\overline{K^0}$ into two pions can then be found using equation (5.6) and setting $A_L(0) = A_S(0) = 1/\sqrt{2}$:

$$\begin{aligned}\Gamma\left(K^0 / \overline{K^0} \to 2\pi\right) &= \left(A_L^{2\pi}(t) \pm A_S^{2\pi}(t)\right)\left(A_L^{2\pi}(t)^* \pm A_S^{2\pi}(t)^*\right) \\ &\simeq \frac{1}{2\,(1 \pm \epsilon)^2}\left[e^{-t/\tau_S} + |\eta|^2 e^{-t/\tau_L} \pm 2|\eta|\cos(\Delta m t + \phi)\, e^{-(t/2\tau_S + t/2\tau_L)}\right]\end{aligned} \tag{5.8}$$

where $\Delta m = m_L - m_S = 3.489 \times 10^{-12}$ MeV/c^2 is the mass difference between K_L and K_S.

Now let us consider the distribution of $K \to 2\pi$ decays from a target. Both K^0 and $\overline{K^0}$ are produced in the targets. The decay distribution is therefore a weighted sum of the decay distribution of pure K^0 and $\overline{K^0}$ decays. If N_{K^0} K^0 and $N_{\overline{K^0}}$ $\overline{K^0}$ are produced in the target with energy E_K, the decay distribution for $K \to 2\pi$ decays from the target is:

$$\begin{aligned}F(t, E_K) &\equiv N_{K^0}\,\Gamma(K^0 \to 2\pi) + N_{\overline{K^0}}\,\Gamma(\overline{K^0} \to 2\pi) \\ &= \frac{1}{2}\,(N_{K^0} + N_{\overline{K^0}})\, e^{-t/\tau_S} + \frac{1}{2}\,(N_{K^0} + N_{\overline{K^0}})\,|\eta|^2\, e^{-t/\tau_L} + \\ &\quad (N_{K^0} - N_{\overline{K^0}})\,|\eta|\,\cos(\Delta m t + \phi)\, e^{-(t/2\tau_S + t/2\tau_L)} + \mathcal{O}(\epsilon^2)\end{aligned} \tag{5.9}$$

where t is the reconstucted lifetime of the kaon from the target.

The exact number of K^0's and $\overline{K^0}$'s produced in either target is unknown. Dividing through by the total number of kaons produced $(N_{K^0} + N_{\overline{K^0}})$ gives:

$$F(t, E_K) \propto e^{-t/\tau_S} + |\eta|^2 e^{-t/\tau_L} + 2\,D(E_K)\,|\eta|\,\cos(\Delta m t + \phi)\, e^{-(t/2\tau_S + t/2\tau_L)} \tag{5.10}$$

where we have introduced the parameter D which parameterises the production asymmetry in the target as a function of the kaon energy E_K. For a given kaon energy:

$$D(E_K) \equiv \frac{(N_{K^0} - N_{\overline{K^0}})}{(N_{K^0} + N_{\overline{K^0}})} \tag{5.11}$$

This function has been measured by the NA31 collaboration [12] who used identical targets to those used in NA48. The value of D varies from around 0.2 at $E_K = 70$ GeV to around 0.4 at $E_K = 170$ GeV.

5.4 Energy Binning

The analysis of **R** is performed in bins of kaon energy. The binning minimises the sensitivity of **R** to the differences in the observed decay spectra of K_L and K_S. As discussed in section 3.3, the orientation of the targets is chosen so that the decay spectra are as similar as possible over the energy range 70 to 170 GeV. These spectra

are not accurately known, but it is estimated that the spectra differ by up to 10% over this range [8]. A bin size of 5 GeV is chosen. This ensures that the difference in the geometric acceptance between K_L and K_S (for a given decay mode) can be kept to less than 10^{-4} in each energy bin [56]. The effects of the energy binning are discussed further in section 7.15.3.

5.4.1 Fitting the Double Ratio

Performing the analysis in 20 kaon energy bins is equivalent to making 20 independent measurements of the double ratio, $\mathbf{R}_i$. To calculate the global value of $\mathbf{R}$ an unbiased logarithmic estimator is used, known as the log-$\mathbf{R}$ estimator.

To see why a logarithmic estimator is unbiased consider the error of the ratio a/b:

$$\sigma\left(\frac{a}{b}\right) = \left|\frac{a}{b}\right| \sqrt{\frac{\sigma^2(a)}{a^2} + \frac{\sigma^2(b)}{b^2}} \tag{5.12}$$

Therefore the error on the ratio is proportional to the magnitude of the ratio itself. In contrast the error on the logarithm of the ratio, $\log(a/b)$, is:

$$\sigma\left(\log\frac{a}{b}\right) = \sqrt{\frac{\sigma^2(a)}{a^2} + \frac{\sigma^2(b)}{b^2}} \tag{5.13}$$

which is independent of a/b.

The estimator used in this analysis to obtain $\mathbf{R}$ is based on the logarithm, L_i of $\mathbf{R}_i$.

$$L_i \equiv \log(\mathbf{R}_i) = \log(N_L^{00})_i - \log(N_S^{00})_i - \log(N_L^{+-})_i + \log(N_S^{+-})_i \tag{5.14}$$

The N_i are the numbers of decays in each energy bin i. In the case of K_L events, the N_i are therefore the sum of the weights of each of the events. The error on L_i can be defined by:

$$\sigma_{L_i} = \sqrt{\frac{\sigma^2(N_L^{00})_i}{(N_L^{00})_i^2} + \frac{\sigma^2(N_S^{00})_i}{(N_S^{00})_i^2} + \frac{\sigma^2(N_L^{+-})_i}{(N_L^{+-})_i^2} + \frac{\sigma^2(N_S^{+-})_i}{(N_S^{+-})_i^2}} \tag{5.15}$$

The individual errors $\sigma(N)$ on the number of events are discussed in the following section.

The log-$\mathbf{R}$ estimator is defined in terms of the L_i and the errors σ_{L_i}:

$$\log(\mathbf{R}) \equiv \overline{L} = \frac{\sum_i (L_i/\sigma_{L_i}^2)}{\sum_i 1/\sigma_{L_i}^2} \tag{5.16}$$

The error on $\overline{L}$ is:

$$\sigma(\overline{L}) = \left(\sum_i \frac{1}{\sigma_{L_i}^2}\right)^{-1/2} \tag{5.17}$$

5.5 Error and Efficiency Formulae

In this section the formulae used to calculate statistical errors and efficiencies are presented. These formulae are used in the calculation of $\mathbf{R}$ and in the investigation of systematic effects.

The sum of the weights of N events, $N_W = \sum_{i=1}^{N} w_i$, is used in the calculation of $\mathbf{R}_{\text{raw}}$ and in the investigation of the systematic effects.

The uncertainty on N_W is:

$$\sigma(N_W) = \sqrt{\left(\sum_{i=1}^{N} w_i^2\right)} \tag{5.18}$$

In the case of unweighted events ($w_i = 1$ for all i) the uncertainty becomes the usual Possion formula $\sigma(N) = \sqrt{N}$.

The efficiency of some systems (for example the triggers systems) are used to investigate systematic effects.

Efficiencies are calculated from a set of control events which are subject to a set of selection criteria. Defining N_W as the sum of the weights of the selected events and M_W as the sum of the weights of the events not selected, then $N_W + M_W$ is the sum of the weights of the total number of events in the control sample. Using these quantities the efficiency of the system may be defined as:

$$\epsilon = \frac{N_W}{N_W + M_W} \tag{5.19}$$

The uncertainty on the efficiency is:

$$\sigma(\epsilon) = \sqrt{\frac{M_W^2\ \sigma(N_W)^2 + N_W^2\ \sigma(M_W)^2}{(N_W + M_W)^4}} \tag{5.20}$$

For unweighted events this formula reduces to

$$\sigma(\epsilon) = \sqrt{\frac{\epsilon\,(1-\epsilon)}{N+M}} \tag{5.21}$$

where N is the number of events passing the selection criteria and M is the number of events failing the selection criteria.

Chapter 6

Event Selection

6.1 Introduction

The aim of the event selection is to count the number of events in each of the four $\mathcal{R}e(\epsilon'/\epsilon)$ decay modes:

$$K_L \to \pi^0\pi^0 \to 4\gamma \quad K_S \to \pi^0\pi^0 \to 4\gamma \quad K_L \to \pi^+\pi^- \quad K_S \to \pi^+\pi^-$$

As discussed in the previous chapter, this involves selecting $K^0 \to \pi^0\pi^0 \to 4\gamma$ and $K^0 \to \pi^+\pi^-$ events, and determining whether the kaon was from the K_L or K_S beamline. These selections are made by using reconstructed quantities such as the energies, positions and times of clusters or tracks in the detectors. The reconstruction of these quantities has been described in section 4.6.

This chapter begins with a description of the tagging procedure which establishes which beamline the decay came from. The criteria applied for selecting $K^0 \to \pi^+\pi^-$ and $K^0 \to \pi^0\pi^0 \to 4\gamma$ events are discussed.

6.1.1 Time Offsets

A time offset has been applied to all the reconstructed time information, such that the relative time distribution between any two detectors is centred at zero. Therefore when any times are compared as part of the selection criteria, it means that the times are effectively being compared after taking into account the time of flight of the particle(s) between the two subdetectors.

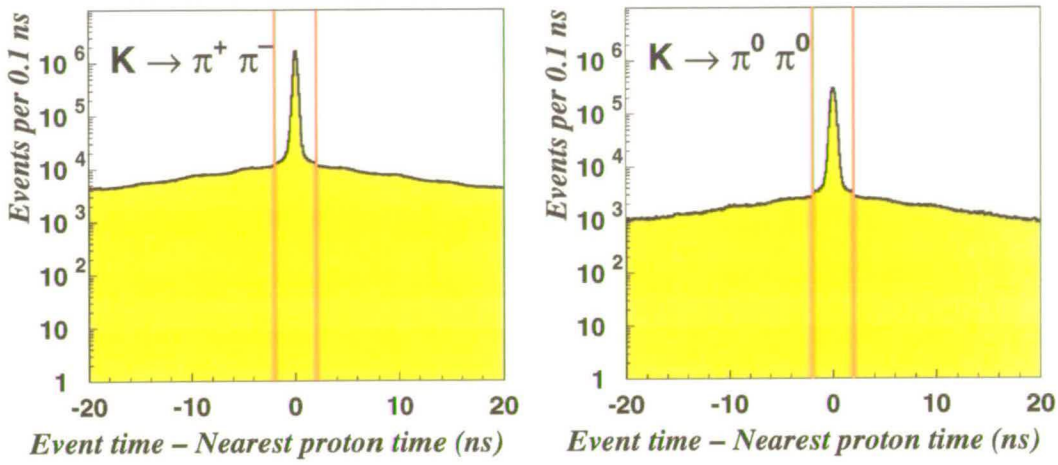

Figure 6.1: The time difference between the event time and the time of the nearest proton for all selected $K^0 \to \pi^+\pi^-$ and $K^0 \to \pi^0\pi^0$ decays. As described in section 6.1.1 a time offset has been applied to centre the distribution at 0. Events in the ± 2 ns coincidence band shown are tagged as K_S decays, and events outside this range are tagged as K_L decays.

6.2 Proton Tagging

The purpose of proton tagging is to determine from which of the beamlines a decay was from.

The tagging procedure is based on a time of flight method to distinguish whether the event came from the K_L or K_S beamline. As described in section 3.4, the proton tagging detector records the time of all protons in transport to the K_S target. The times of the protons in the tagger (t_{proton}) can be compared to the reconstructed event times in the detector (t_{event}). After subtracting a time offset corresponding to the time of flight between tagger and the detector, the distribution ($t_{\text{event}} - t_{\text{proton}}$) for K_S events should be centred around 0, see figure 6.1.

A ± 2 ns window is chosen to identify events as K_S. All decays within this window are identified as K_S events, all other decays are identified as K_L events. When this procedure is used to determine K_L or K_S, it is usual to say that an event is *tagged* as a K_L or a K_S decay.

6.2.1 Tagging Dilution

It is possible to cross check the tagging method for $K^0 \to \pi^+\pi^-$ decays using the reconstructed decay vertex position. The K_L and K_S targets are vertically displaced

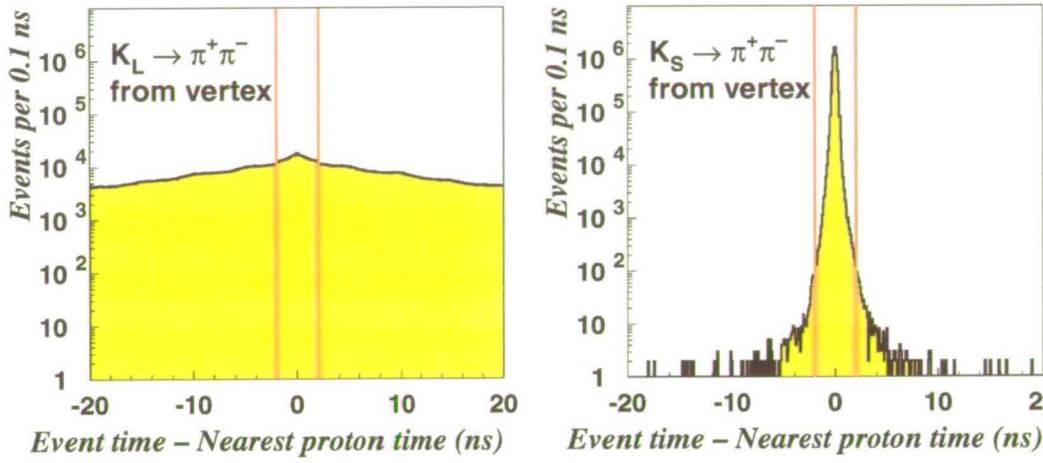

Figure 6.2: Tagging distributions for $K_L \to \pi^+\pi^-$ and $K_S \to \pi^+\pi^-$ events, in which the vertex position has been used to distinguish K_L from K_S. Events within the lines at ± 2 ns are tagged as K_S events, all other events are tagged as K_L events.

by 7 cm and both beams converge at the position of the LKR.

Figure 6.2 shows the time difference separately for $K_L \to \pi^+\pi^-$ and $K_S \to \pi^+\pi^-$ events using the vertex position to separate K_L and K_S, as described in the following paragraph. It can be seen that the tagging method can misidentify events from both the K_L and K_S beamlines. Those events which are misidentified by the tagging procedure are referred to as *mis-tagged* events.

The y and z positions of the decay vertices for $K^0 \to \pi^+\pi^-$ decays are shown in figure 6.3. The distribution of these vertices allows decays from the K_L and K_S targets to be unambiguously identified. Decays where the y-position (y_{decay}) of the decay vertex satisfies $y_{\text{decay}} > 4.2 \cdot (1 - z_{\text{decay}}/z_{\text{LKR}})$ are from the K_S target, the other decays are from the K_L target.

When K_S events are mis-tagged as K_L, the effect is known as *tagging inefficiency*. As shown in figure 6.2, very few $K_S \to \pi^+\pi^-$ events are outwith the ± 2 ns window and therefore tagging inefficiency is small. The consequences of tagging inefficiency on the measurement of the double ratio, **R**, are discussed in section 7.4.

When K_L decays are mis-tagged as K_S decays the effect is called *tagging dilution*. Tagging dilution can be parameterised by α_{LS}:

$$\alpha_{LS} = \frac{\text{Number of events tagged as } K_S \text{ from the } K_L \text{ beam}}{\text{Number of events from the } K_L \text{ beam}} \tag{6.1}$$

α_{LS} is independent of the lifetime selection made on the events, therefore α_{LS} may be defined using unweighted events.

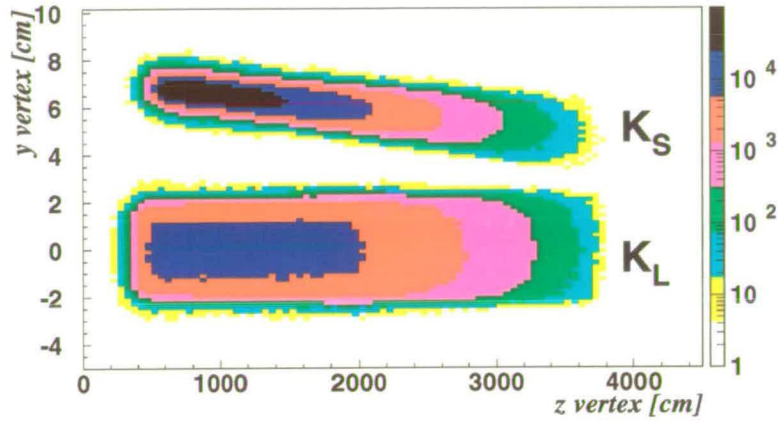

Figure 6.3: The y and z positions of the decay vertex for all $K^0 \to \pi^+\pi^-$ decays. As indicated, the two branches of the distribution can be identified as decays from the K_S beamline (above) and decays from the K_L beamline (below).

Using the definition of α_{LS} above, the corrected number of events from the K_L or K_S beams can be written as:

$$N_L^{beam} = \frac{1}{(1-\alpha_{LS})} N_L^{tag} \quad (6.2)$$

$$N_S^{beam} = N_S^{tag} - \frac{\alpha_{LS}}{(1-\alpha_{LS})} N_L^{tag} \quad (6.3)$$

The value of α_{LS} can be measured directly for $\pi^+\pi^-$ decays. Using the selection of $K^0 \to \pi^+\pi^-$ events described in this chapter, *except* for the requirement on the kaon lifetime $t_K > 0$:

$$\alpha_{LS}^{+-} = \frac{586113}{5300501} = (11.058 \pm 0.014)\% \quad (6.4)$$

It is not possible to measure α_{LS} directly for $\pi^0\pi^0$ decays. However as the value of α_{LS} is primarily a function of the rate of protons in the tagger, it is expected that: $\alpha_{LS}^{00} \simeq \alpha_{LS}^{+-}$. Therefore, to first approximation, the effect of tagging dilution cancels in the double ratio, **R**.

In section 7.3 the difference in the tagging dilution between the charged and neutral modes and its effect on the measurement of **R** will be discussed. Effects due to the tagging inefficiency, which has been ignored in the above discussion, will be discussed in section 7.3.3.

6.3 Event Selection Criteria

$K^0 \to \pi^+\pi^-$ and $K^0 \to \pi^0\pi^0 \to 4\gamma$ events are selected from events that pass the Charged and Neutral Filters described in section 4.5. A $K^0 \to \pi^+\pi^-$ candidate event

must contain 2 oppositely charged tracks which have a closest distance of approach (CDA) of less than 3 cm. A $K^0 \to \pi^0\pi^0 \to 4\gamma$ candidate event must contain 4 reconstructed energy clusters in the LKR. In the event selection procedure additional selection criteria or 'cuts' are applied to these candidate events.

In general, data is rejected for one of the following reasons:

- To ensure the decay came from the fiducial volume.
- To ensure that the decay products would hit every appropriate subdetector.
- To maintain the principle of simultaneous data taking.
- To reject background events.
- To minimise the systematic uncertainty on **R**.

As a general principle the cuts used to select $K^0 \to \pi^+\pi^-$ and $K^0 \to \pi^0\pi^0 \to 4\gamma$ decays should be as symmetric as possible between K_L and K_S. Where it is possible, the same selection criteria are applied to the charged and neutral decay modes.

The following sections first describe selection cuts that are applied to all events, followed by the selection cuts specific to the charged and neutral decay modes. The selection cuts are summarised in tables 6.3, 6.4 and 6.5 at the end of this chapter.

6.4 Common Event Selection

This section discusses selection criteria which are applied to both the $K^0 \to \pi^+\pi^-$ and $K^0 \to \pi^0\pi^0$ candidate events.

As discussed in section 5.1, all four $\mathcal{R}e(\epsilon'/\epsilon)$ decay modes must be collected from the same fiducial volume. In this analysis, the fiducial volume is defined in terms of the energy of the kaon (E_K) and the lifetime of the kaon from the AKS counter (t_K). All events must satisfy $70 < E_K/\text{GeV} < 170$ and $0 < t_K/\tau_S < 3.5$. Additional cuts are applied to define the active volume of the detectors, remove events from the 'halo' surrounding the K_S beam, and to effectively symmetrize the data taking conditions for the $\pi^0\pi^0$ and $\pi^+\pi^-$ events.

6.4.1 Kaon Energy Selection

The reconstructed energies of the kaon for the neutral and charged decay modes are defined in equations (4.7) and (4.11) respectively. The energy range of 70 to 170 GeV is the experiment's design value. For example: the LKR is designed to have a linear

response for photons from kaon decays in this energy range and the relative angles of the K_L and K_S targets are chosen so that the decay spectra are similar over the range 70 to 170 GeV.

6.4.2 Kaon Lifetime Selection

The lifetime of a kaon from the AKS position in units of τ_S is given by:

$$\frac{t_K}{\tau_S} = \frac{(z_{decay} - z_{AKS})\, m_{K^0}}{p_K\, \tau_S} \tag{6.5}$$

It should be noted that the definition of z_{AKS} is slightly different for $\pi^0\pi^0$ and $\pi^+\pi^-$ decays. Photons from $\pi^0 \rightarrow 2\gamma$ decays are converted in the AKS crystal, therefore the $\pi^0\pi^0$ decays are vetoed from the AKS crystal position. Charged pions are detected in the AKS scintillator counter and therefore $\pi^+\pi^-$ decays are vetoed from the AKS counter position. The AKS crystal and counter are 2.1 cm apart. Another point to note is that the weight w_i applied to a K_L event is normalised to $w_i = 1$ at the AKS crystal. This means that a $K_L \rightarrow \pi^+\pi^-$ event will always have a weight of less than 1.

The selection on the kaon lifetime is $t_K < 3.5\,\tau_S$ for both K_L and K_S events. For K_L events a cut $z_{decay} > z_{AKS}$ (equivalent to $t_K > 0$) is made. To reject K_S events that decay upstream of the AKS position, no activity is allowed in the AKS detector within ± 3 ns of the reconstructed event time.

K_S decays have a steeply falling lifetime distribution. Therefore selecting K_S events with a $z_{decay} > z_{AKS}$ cut could cause a net migration of events into, or out of, the true fiducial volume. Instead the AKS detector is used to provide a hardware definition of the beginning of the fiducial volume for events in the K_S beamline.

Such a detector in the K_L beamline would cause regeneration of K_S particles in the K_L beam. As K_L decays have an almost flat lifetime distribution they are much less sensitive to resolution effects. Therefore to make the lifetime selection of $t_K > 0$, events tagged as K_L must satisfy $z_{decay} > z_{AKS}$.

The $z_{decay} > z_{AKS}$ cut is applied to all events *tagged as* K_L. However, as discussed in section 6.2.1, around 11% of the events from the K_L beamline are incorrectly identified as K_S events. These mis-tagged events are not subject to the $z_{decay} > z_{AKS}$ cut and therefore events mis-tagged as K_S with $t_K < 0$ remain in the event samples. Figure 6.4 shows the vertex distribution of tagged $K_S \rightarrow \pi^+\pi^-$ and $K_S \rightarrow \pi^0\pi^0$ decays. The mis-tagged events are visible in both the $\pi^+\pi^-$ and $\pi^0\pi^0$ samples with $(z_{decay} - z_{AKS}) \lesssim -150$ cm.

It can be seen in figure 6.4 that the minimum decay vertex position is different for the $\pi^+\pi^-$ and $\pi^0\pi^0$ decays: around 4 m and 8 m respectively before the AKS position.

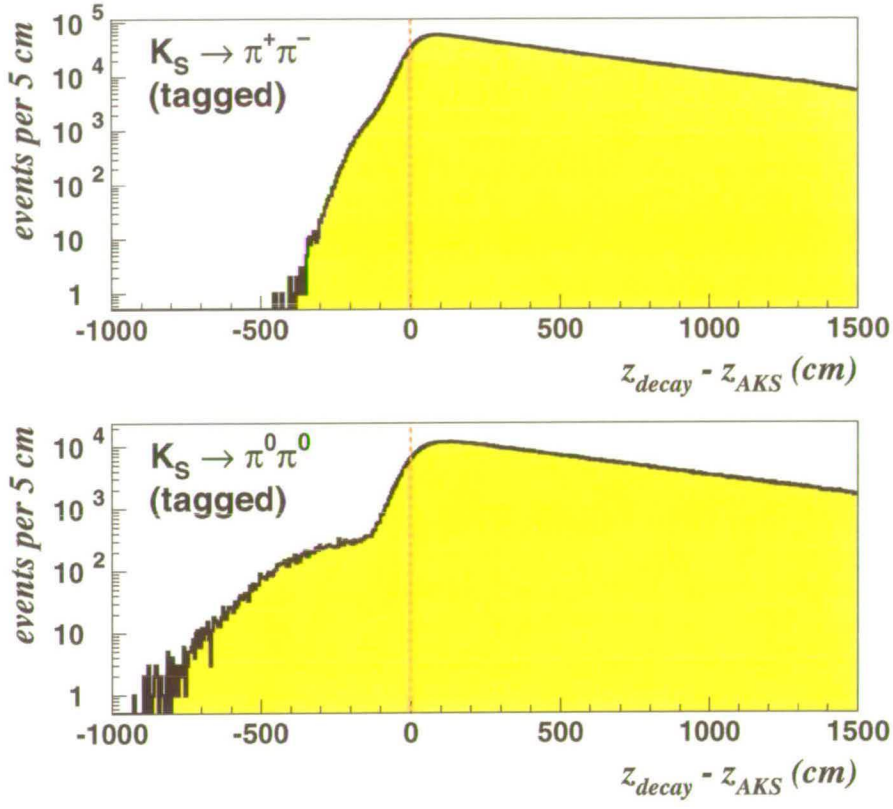

Figure 6.4: The z-positions of the decay vertex for tagged K_S decays to both $\pi^+\pi^-$ and $\pi^0\pi^0$ final states. Events where a decay occurs in the K_S beamline upstream of the AKS have been rejected. In the $\pi^0\pi^0$ distribution there is a clear contribution from K_L decays mis-tagged as K_S, visible below -150 cm. In the $\pi^+\pi^-$ distribution there is also a small contribution from K_L decays mis-tagged as K_S.

Referring to figure 3.1 (which shows the layout of the NA48 experiment) and remembering that these decays are actually from the K_L beamline, it can be seen that these $\pi^0\pi^0$ decays occur upstream of the final K_L collimator at the position of the dipole magnet B6. If a kaon were to decay to $\pi^+\pi^-$ at this position, the decay products would be deflected by the magnet and therefore would not reach the detector.

This difference in the minimum decay vertex position, means that the relative contribution from mis-tagged events is different in the charged and neutral decays modes. Therefore the amount of mis-tagged events will not cancel in **R**. To reduce this effect on **R** an additional selection criteria is made on events tagged as K_S, that the position of the decay vertex can be no further from the AKS position than 2 m, *i.e.* $(z_{\text{decay}} - z_{\text{AKS}}) > -2$ m.

The residual effect on the double ratio from the mis-tagged events in the K_S samples

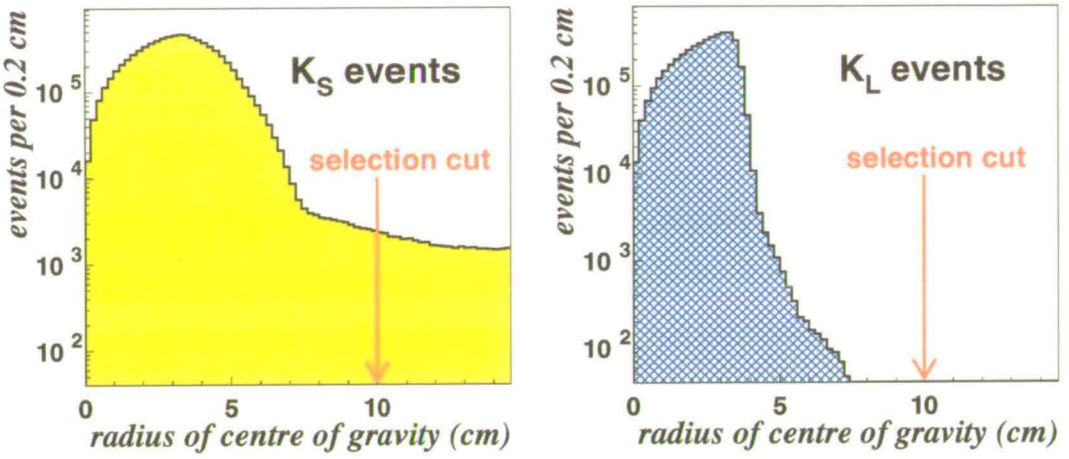

Figure 6.5: The centre of gravity distributions for $K^0 \to \pi^+\pi^-$ events.

is discussed in section 7.3.

6.4.3 Detector Active Volume

In order for an event to be fully reconstructed, all decay products must hit the active regions of the detector. For $\pi^0\pi^0$ candidate events cuts are applied to the reconstructed positions of the photon clusters in the LKR $(x_{\gamma^i}, y_{\gamma^i})$. For $\pi^+\pi^-$ candidate events the reconstructed positions of the tracks in the drift chambers $(x^{\pm}, y^{\pm})$ are used to estimate the impact positions of the tracks in the LKR, and cuts are made on these positions.

The active volume of the LKR is defined as an annulus from a radius between 15 cm to 110 cm around the centre of the beampipe. Dead cells within the calorimeter (see section 3.9.5) may cause the energy of the clusters to be mis-reconstructed. Therefore if the position of a cluster or a track in the LKR is within 2 cm of a dead cell, the event is rejected.

The selection of $K^0 \to \pi^+\pi^-$ events also uses information from the drift chambers and the muon veto system. Therefore cuts are also made on the position of the tracks in these detectors (see table 6.4 for details).

6.4.4 Centre of Gravity Selection

The centre of gravity is the energy weighted position of the event in the LKR. It corresponds to the impact position of the kaon in the detector. For a $K^0 \to \pi^0\pi^0 \to 4\,\gamma$

event the x and y positions and the radius (r) of the centre of gravity are defined as:

$$r_{\rm cog} = \sqrt{x_{\rm cog}^2 + y_{\rm cog}^2} \quad \text{with} \quad x_{\rm cog} = \frac{\sum_{i=1}^{4}(E_{\gamma^i}\, x_{\gamma^i})}{\sum_{i=1}^{4} E_{\gamma^i}}, \quad y_{\rm cog} = \frac{\sum_{i=1}^{4}(E_{\gamma^i}\, y_{\gamma^i})}{\sum_{i=1}^{4} E_{\gamma^i}} \tag{6.6}$$

The equivalent quantity for a $K^0 \to \pi^+\pi^-$ event is the momentum weighted position of the event at the LKR position. The positions of the tracks at the LKR $(x'_\pm, y'_\pm)$ are calculated as if there was no deflection by the magnetic field. Then the centre of gravity can be defined by:

$$x_{\rm cog} = \frac{p_+\, x'_+ + p_-\, x'_-}{p_+ + p_-}, \quad y_{\rm cog} = \frac{p_+\, y'_+ + p_-\, y'_-}{p_+ + p_-} \tag{6.7}$$

Here $p_\pm$ are the magnitudes of the track momenta. The distributions of $r_{\rm cog}$ for events from the K_L and K_S beams are shown in figure 6.5.

The difference in the distributions of $r_{\rm cog}$ between the K_L and K_S beams is a reflection of the beam geometry. The distance from the target to the final collimator is much longer for the K_L beam than for the K_S beam. Therefore the K_L beam is much better defined than the K_S beam, resulting in a smaller spread of $r_{\rm cog}$ values for K_L events.

The K_S beam also has a surrounding 'halo' of kaons, which appear in figure 6.5 as events with $r_{\rm cog} \gtrsim 8$ cm. This halo is due to scattering in the K_S collimator and the AKS crystal [24]. To reject events in the K_S beam halo events must satisfy $r_{\rm cog} < 10$ cm for all four $\mathcal{R}e(\epsilon'/\epsilon)$ decay modes.

As K_L and K_S exhibit very different $r_{\rm cog}$ distributions, this cut is essentially asymmetric between K_L and K_S decays. Therefore it is preferable to make the cut symmetric between the $\pi^+\pi^-$ and $\pi^0\pi^0$ distributions. The cut is made at 10 cm to be well within the flatter halo region of the $r_{\rm cog}$ distribution, to avoid any bias from the different resolutions of the $r_{\rm cog}$ distributions between the charged and neutral decay modes.

6.4.5 Deadtime Effects

In order to maintain the principle of simultaneous data taking, any time interval in which one of the decay modes could not be recorded are also excluded from the analysis of the other modes. There are two such effects in the 1998 data set: charged trigger deadtime (see section 4.3) and drift chamber overflow conditions (see section 3.7.3). Both of these effects prevent $\pi^+\pi^-$ events from being fully recorded.

6.4.6 Charged Trigger Deadtime

During periods of charged trigger deadtime no decisions can be made about issuing new $\pi^+\pi^-$ triggers, therefore any $\pi^+\pi^-$ events which occur during this time are lost.

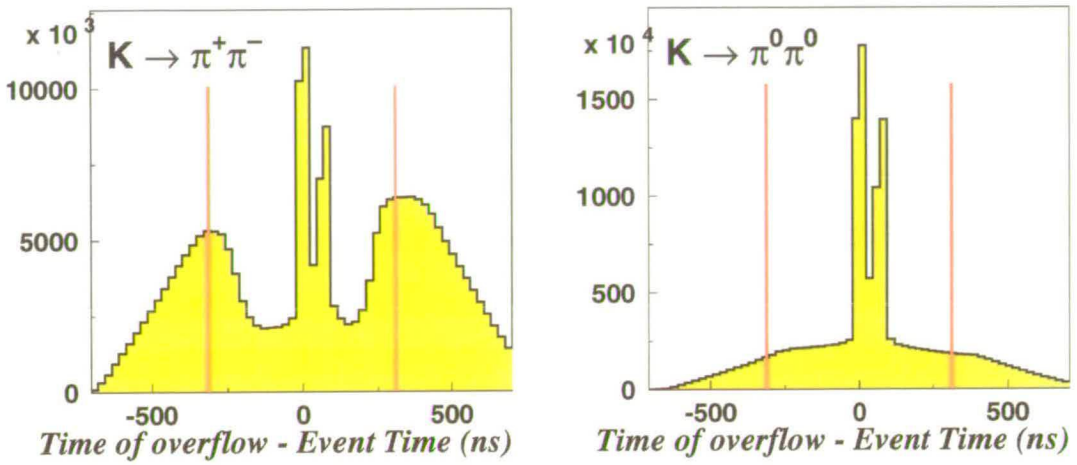

Figure 6.6: Time of an overflow condition with respect to the event time for $\pi^+\pi^-$ and $\pi^0\pi^0$ candidate events.

When this condition occurs a 'L1off' signal is recorded. It is found that $(4.05 \pm 0.02)\%$ of $\pi^0\pi^0$ events contain the 'L1off' signal. These events are excluded from the analysis, in order to symmetrize the effect of the charged trigger deadtime between $\pi^+\pi^-$ and $\pi^0\pi^0$ events.

6.4.7 Drift Chamber Overflow Conditions

A drift chamber overflow condition occurs when there are more than 8 hits in a single drift chamber plane within a period of 100 ns. In this case the memory in the readout is reset, and information about the activity in that drift chamber plane may be lost. This may cause the tracks and vertices to be mis-reconstructed.

Figure 6.6 shows the time of an overflow condition with respect to the event time for $\pi^+\pi^-$ and $\pi^0\pi^0$ events. Both distributions show a peak around 0, corresponding to events that themselves cause an overflow condition. In the $\pi^+\pi^-$ distribution there is a reduction in the number of events around the time of an overflow. This is due to events that cannot be reconstructed as information has been lost due to the memory reset. As the reconstruction of $\pi^0\pi^0$ events does not use information from the drift chambers, there is no similar loss of events around the time of an overflow for neutral decays.

To symmetrize the data taking conditions for $\pi^+\pi^-$ and $\pi^0\pi^0$ events, and to reject any $\pi^+\pi^-$ events that may be mis-reconstructed, any $\pi^+\pi^-$ and $\pi^0\pi^0$ events which have an overflow condition within ± 312.5 ns of the event time are rejected from the analysis. The fraction of events in each $\mathcal{R}e(\epsilon'/\epsilon)$ decay mode rejected by this requirement is shown in table 6.1.

	$\pi^0\pi^0$	$\pi^+\pi^-$
K_L	$(24.052 \pm 0.041)\%$	$(16.152 \pm 0.013)\%$
K_S	$(24.799 \pm 0.012)\%$	$(16.312 \pm 0.004)\%$

Table 6.1: The fraction of events lost in each of the $\mathcal{R}e(\epsilon'/\epsilon)$ decay modes due to the nearby presence of a drift chamber overflow condition. The K_L events are weighted.

It is currently not fully understood why so many events have a high drift chamber hit multiplicity thus causing an overflow condition. It is observed that some of the drift chamber planes have a significantly higher fraction of overflow conditions than others. Therefore there is speculation that some fraction of the overflow condition could be caused by noise effects which could vary from plane to plane. The large fraction of overflow conditions observed in time with $\pi^0\pi^0$ events suggests that photon conversions, $\gamma \rightarrow e^+e^-$, caused by material in the beam line (for example: the collimators, the Kevlar window or the beampipe) may also cause the high hit multiplicities.

6.5 Charged Event Selection

In addition to the common event selection cuts described in the previous section, additional selection criteria are applied to the $K^0 \rightarrow \pi^+\pi^-$ events to reduce the contribution from background decays and to reduce systematic effects. All the cuts used to select $K^0 \rightarrow \pi^+\pi^-$ decays are summarised in table 6.4 at the end of this chapter.

6.5.1 Backgrounds

Any decay mode containing two oppositely charged tracks from a common vertex can act as a background to $K^0 \rightarrow \pi^+\pi^-$ decays. From table 2.1 it can be seen that the decays $K_L \rightarrow \pi^\pm e^\mp \nu_e$, $K_L \rightarrow \pi^\pm \mu^\mp \nu_\mu$ and $K_L \rightarrow \pi^+\pi^-\pi^0$ are therefore potential backgrounds for $K^0 \rightarrow \pi^+\pi^-$ events. In the K_S beam, there is also a possible source of background from Λ baryons, which are produced in the target. Λ baryons have a lifetime of $c\tau = 7.89$ cm, which is comparable with that of K_S. The main charged decay mode of the Λ is $\Lambda \rightarrow p\pi^-$ with a branching ratio of 64%.

These backgrounds are identified and rejected as follows:

- **$K_L \rightarrow \pi^\pm e^\mp \nu_e$ background.** Electrons can be identified using the shower of electromagnetic energy that they deposit in the LKR. Any cluster in the calorimeter that is within 4 cm of a track's projected impact position is considered to be produced by the same particle. As the LKR is 27 radiation lengths

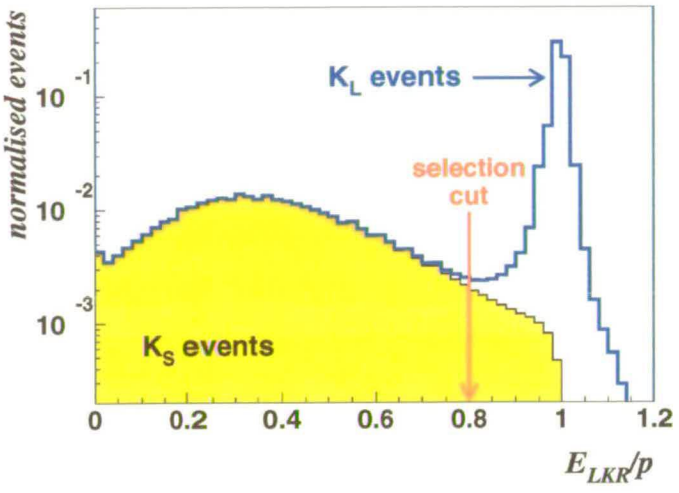

Figure 6.7: The E_{LKR}/p distribution of tracks. The excess of events in the $\mathrm{K_L}$ sample around $E_{\mathrm{LKR}}/p = 1$ is due to electrons from $\mathrm{K_L} \to \pi^{\pm}e^{\mp}\nu_e$ decays. All of the events in the $\mathrm{K_S}$ sample are $\pi^+\pi^-$ as $\mathrm{K_S}$ has no other charged decay modes. Events where at least one track has $E_{\mathrm{LKR}}/p > 0.8$ are rejected to reduce this background in the $\mathrm{K}^0 \to \pi^+\pi^-$ sample.

long, an electron should deposit all of its energy in the LKR. Therefore the ratio of the cluster energy to the track momentum (E_{LKR}/p) for an electron should be close to 1. A plot of E_{LKR}/p for tracks from $\mathrm{K}^0 \to \pi^+\pi^-$ events is shown in figure 6.7. Events where either of the tracks has $E_{\mathrm{LKR}}/p > 0.8$ are rejected. $\mathrm{K_S} \to \pi^+\pi^-$ are free of Ke3 background and can be used to study the impact of the E_{LKR}/p cut. The cut on E_{LKR}/p rejects around 5% of $\mathrm{K_S} \to \pi^+\pi^-$ events which would otherwise have been accepted.

- **$\mathrm{K_L} \to \pi^{\pm}\mu^{\mp}\nu_\mu$ background.** As described in section 4.6.4, a track is identified as a muon if there are associated hits in both planes 1 and 2 of the MUV. All events where a muon hit is reconstructed within ± 4 ns of the event time are rejected.

- **$\mathrm{K_L} \to \pi^+\pi^-\pi^0$ background.** As the π^0 carries away momentum, the reconstructed mass of the $\pi^+\pi^-$ pairs from $\pi^+\pi^-\pi^0$ decays is always much smaller than m_{K^0}. Therefore $\mathrm{K_L} \to \pi^+\pi^-\pi^0$ decays are rejected by the cut on the invariant $\pi^+\pi^-$ mass described below.

- **Λ background.** As described in the following section $\Lambda \to p\pi$ decays are rejected by the cut on momentum asymmetry, A.

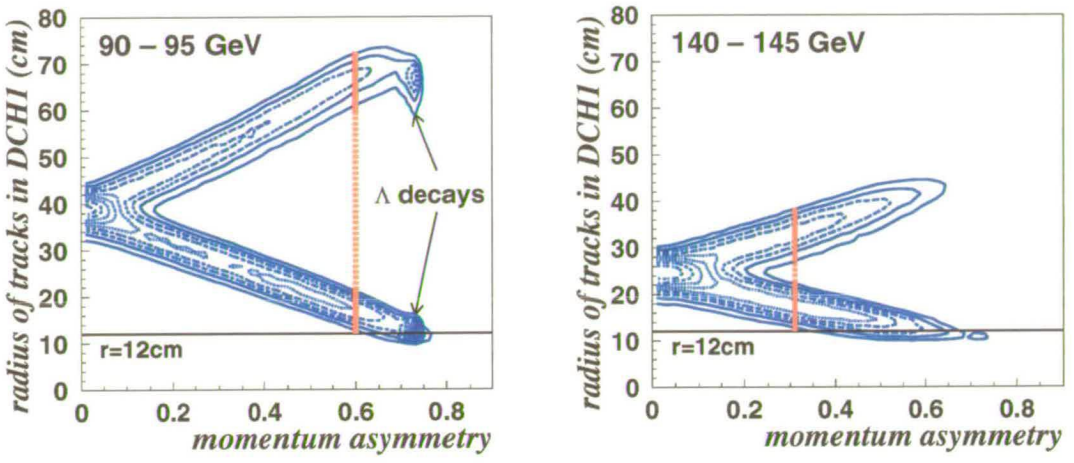

Figure 6.8: The radii of tracks in the first drift chamber versus the momentum asymmetry (A) for two kaon energy ranges. There are two radii plotted for each event. The vertical lines illustrate the value of the cut on A for that kaon energy. In the left hand plot the Λ decays are clearly visible with $A \simeq 0.74$.

6.5.2 Momentum Asymmetry

The momentum asymmetry (A) of a track pair is defined in terms of the magnitude of the momenta of the two tracks:

$$A = \left| \frac{|p_+| - |p_-|}{|p_+| + |p_-|} \right| \tag{6.8}$$

For a given kaon energy, the momentum asymmetry is essentially a measure of the positions of the tracks in the first drift chamber. Figure 6.8 shows the radial positions of the tracks in DCH1 versus A. A cut is made on A to be commensurate with the minimum allowed radius in DCH1 of 12 cm. Events are selected if they satisfy: $A < 0.62$ and $A < 1.08 - 0.0052 \cdot E_K/\text{GeV}$.

The most significant geometrical effect on the measurement of $\mathbf{R}$ is the separation of the K_L and K_S beams at the first drift chamber. The cut on the momentum asymmetry removes events with one track near the beam pipe from the $\pi^+\pi^-$ sample. This reduces the systematic error applied to $\mathbf{R}$ due to the correction for the geometrical acceptance (see section 7.15.3).

Background from Λ and $\overline{\Lambda}$ decays are also rejected by the cut on momentum asymmetry. $\Lambda \rightarrow p\pi^-$ decays have very little allowed phase space, resulting in a narrow band of allowed values around $A = 0.74$.

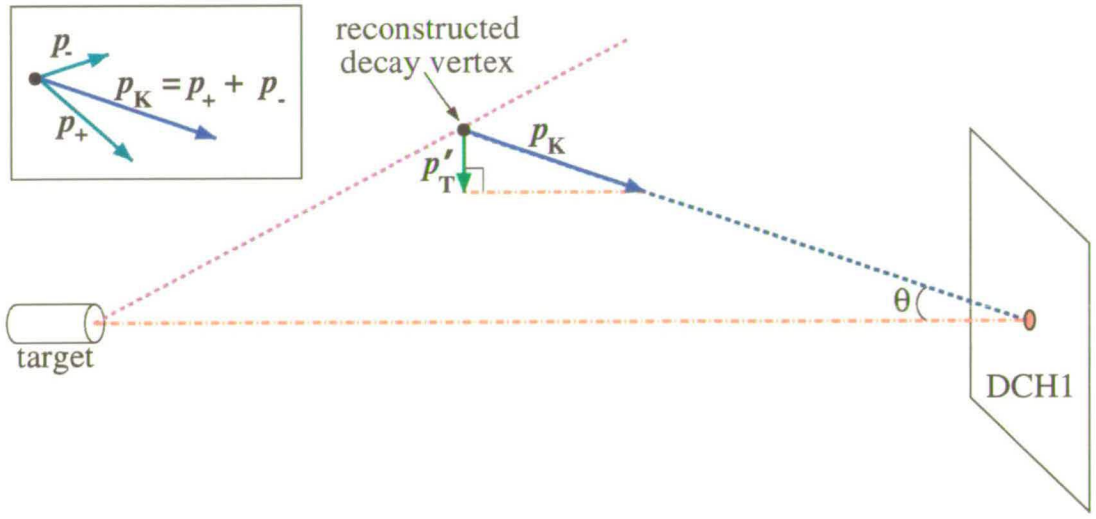

Figure 6.9: The definition of the transverse momentum variable p'_{T}. p'_{T} is defined with respect to two quantities: the kaon momentum vector $\overrightarrow{p_{\mathrm{K}}} = \overrightarrow{p_+} + \overrightarrow{p_-}$ (shown in the inset) and axis between the target and the projected impact point of the kaon in the first drift chamber, which is illustrated as the (red) horizontal dashed line.

6.5.3 Definition of the Signal Region

Two variables are used to define the signal region for the charged decay modes: the invariant $\pi^+\pi^-$ mass of the track pair and p'^2_{T}, which is a modified transverse momentum variable.

Figure 6.9 illustrates the definition of the transverse momentum variable p'_{T}, which is defined as:

$$p'^2_{\mathrm{T}} \equiv (\overrightarrow{p_+} + \overrightarrow{p_-})^2 \cdot \sin^2\theta \tag{6.9}$$

where θ is the angle between the measured vector $\overrightarrow{p_{\mathrm{K}}} = \overrightarrow{p_+} + \overrightarrow{p_-}$ and the axis from the centre of the target to the projected impact position of the kaon in DCH 1, as illustrated in figure 6.9. The $\mathrm{K_L}$ or $\mathrm{K_S}$ target is chosen according to the decay vertex position (see figure 6.3).

For a two body decay the angle θ should be small, as the reconstructed momentum vector $\overrightarrow{p_{\mathrm{K}}}$ will be almost parallel to the target–drift chamber axis. Therefore p'^2_{T} is small for these events. A plot of p'^2_{T} for $\mathrm{K_L}$ and $\mathrm{K_S}$ events is shown in figure 6.10. It can be seen that the resolution of p'^2_{T} is almost the same for events from each of the two targets.

In the case of background three body decays, Ke3, Kμ3 and $\mathrm{K_L} \to \pi^+\pi^-\pi^0$ ($\overrightarrow{p_+} + \overrightarrow{p_-}$) is not equal to the kaon momentum, as the neutrino or neutral pion also carries momentum. Therefore θ and hence p'^2_{T} can be large. In figure 6.10 the events in

the tail of the K_L distribution are due to background Ke3 and Kμ3 decays. (The $K_L \to \pi^+\pi^-\pi^0$ events are rejected by the cut on $m_{\pi^+\pi^-}$.) To reject background from these decays, only events with $p_T'^2 < 200$ (MeV/c)^2 are selected.

A plot of the invariant $\pi^+\pi^-$ mass for K_L and K_S events is shown in figure 6.11. The resolution (σ_m) of $m_{\pi^+\pi^-}$ varies with the energy of the parent kaon (E_K). Figure 6.12 shows a Gaussian fit to the $m_{\pi^+\pi^-}$ mass peak for two kaon energy ranges. Figure 6.13 shows the values of σ_m over the full kaon energy range. A linear fit to σ_m gives:

$$\sigma_m = 0.00161 + 8.342 \times 10^{-6} \cdot E_K/\text{GeV} \tag{6.10}$$

The cut made to select $K^0 \to \pi^+\pi^-$ decays is $|m_{\pi^+\pi^-} - m_{K^0}| < 3\sigma_m$. The resulting signal region is illustrated in figure 6.13.

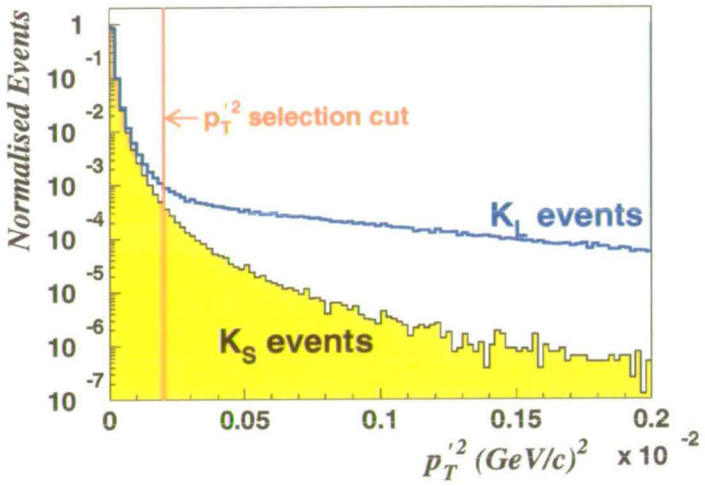

Figure 6.10: The $p_T'^2$ distribution for K_L and K_S events, as distinguished by the decay vertex position. In the K_L sample, most of the events in tail of the $p_T'^2$ distribution are from semileptonic three body decays.

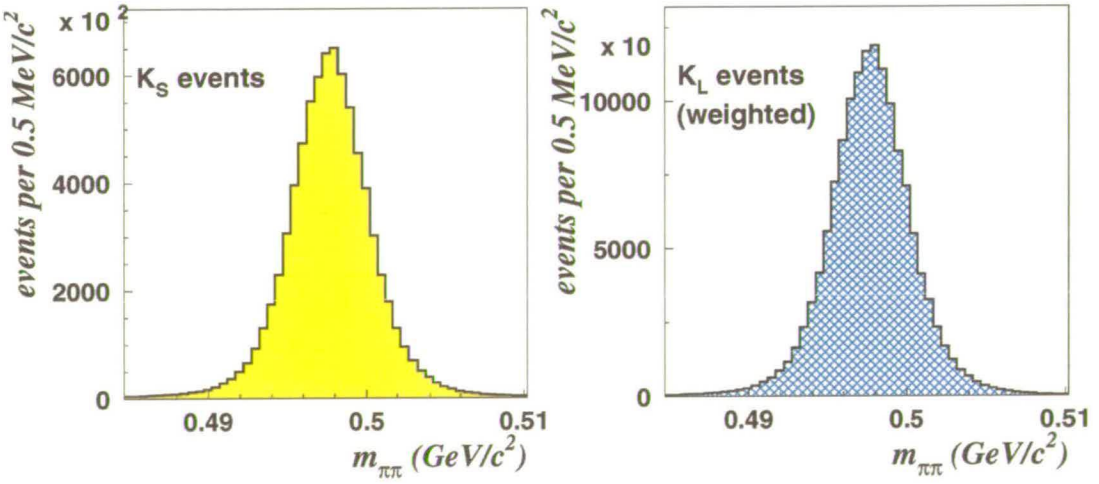

Figure 6.11: The invariant mass $m_{\pi^+\pi^-}$ for all selected K_L and K_S events. (K_L and K_S have been separated using the position of the decay vertex.)

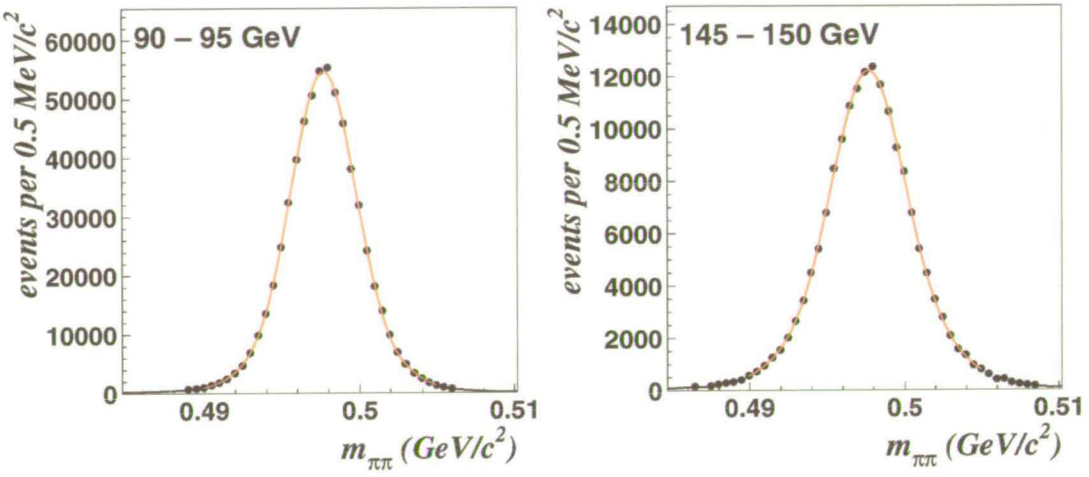

Figure 6.12: Fits of the $m_{\pi^+\pi^-}$ distribution from $K_S \rightarrow \pi^+\pi^-$ for two kaon energy ranges. The width of the distribution increases with higher values of the kaon energy.

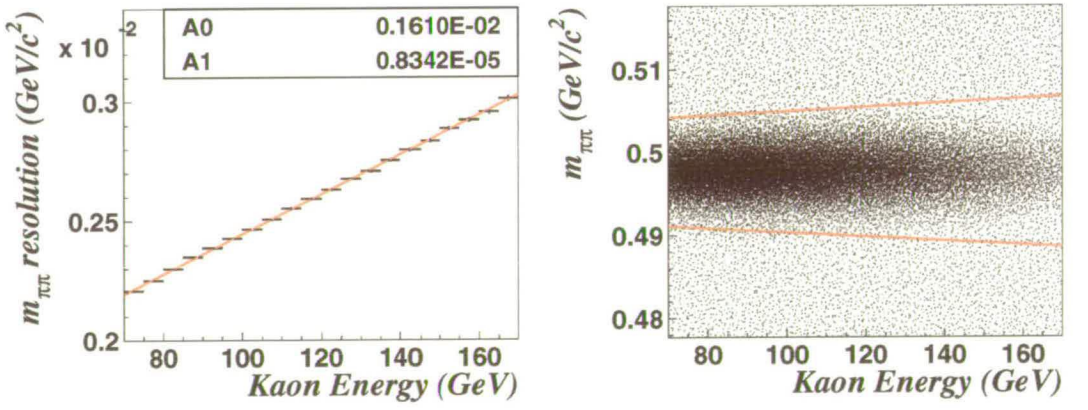

Figure 6.13: Kaon energy dependence of the resolution of $m_{\pi^+\pi^-}$, σ_m. A cut is made at $3\sigma_m$ around the nominal kaon mass to define the signal region.

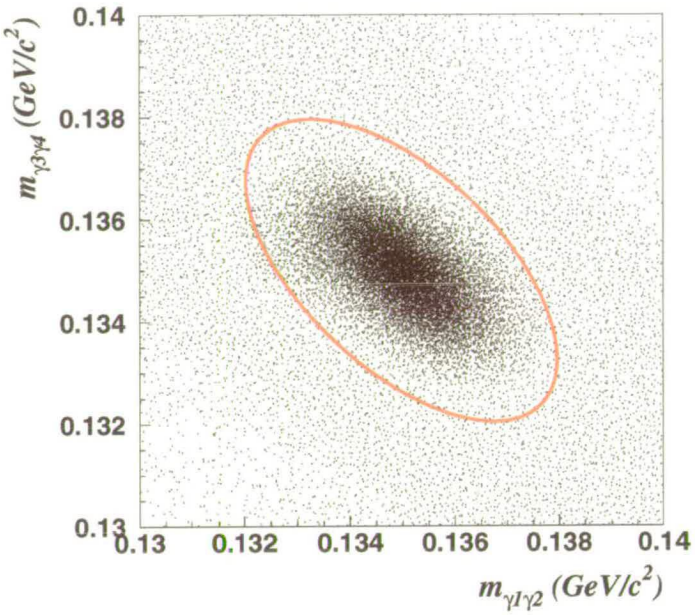

Figure 6.14: The invariant masses ($m_{\gamma^1\gamma^2}$ and $m_{\gamma^3\gamma^4}$) of the selected photon pairs for $K_S \to \pi^0\pi^0 \to 4\gamma$ candidate events. The pairings of the photons have been made using the R_{ellipse} variable defined in equation (6.11). The ellipse represents a typical position of the $R_{\text{ellipse}} = 1.5$ selection cut.

6.6 Neutral Event Selection

In addition to the common event selection cuts described in section 6.4 above, cuts are applied to the $K^0 \to \pi^0\pi^0$ candidate events to select data which are well understood (thus minimising the systematic uncertainties due to the LKR response) and to reject background from $K_L \to 3\pi^0$ decays.

Only four clusters in the energy range $3 < E_{\gamma^i}/\text{GeV} < 100$ are allowed to contribute to a $K^0 \to \pi^0\pi^0 \to 4\gamma$ event. The times of the clusters must be within ± 5 ns of the mean of the cluster times. The distance between each of the four clusters (r_{ij}) must be at least 10 cm. The cut on r_{ij} rejects events where photon showers may have overlapped. These events are rejected as the response of the calorimeter to overlapping showers is not fully understood. No additional clusters of more than 1.5 GeV are allowed within 3 ns of the event time. The cut on the allowed energies of the clusters coincides with the range of energies for which the response of the calorimeter is well understood. This cut on the additional clusters removes background from $K_L \to 3\pi^0$ events, whilst keeping genuine $K^0 \to \pi^0\pi^0 \to 4\gamma$ events in which one of the photon showers has fluctuated, resulting in more than one cluster for that photon being reconstructed.

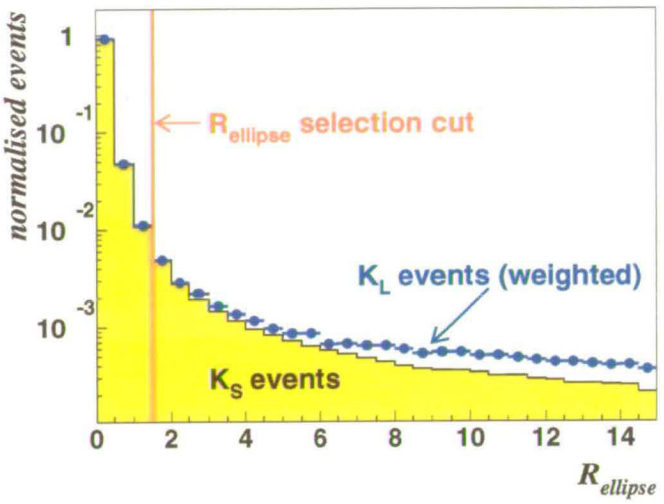

Figure 6.15: The distribution of the R_{ellipse} variable for K_S and K_L events.

Using the kaon mass as a constraint, the longitudinal position of the decay vertex and the photon pair masses are calculated using equations (4.8) and (4.9). There are three possible pairings of the photon masses. After selecting the best mass pairings, a plot of the photon pair masses $m_{\gamma^1\gamma^2}$ versus $m_{\gamma^3\gamma^4}$ (figure 6.14) exhibits an elliptical shape. This shape comes about because the reconstructed mass pairs are not independent because the kaon mass has been used as a constraint.

A selection variable, called R_{ellipse}, is defined to take account of the elliptical distribution:

$$R_{\text{ellipse}} = \left(\frac{(m_{\gamma^1\gamma^2} + m_{\gamma^3\gamma^4})/2 - m_{\pi^0}}{3\,\sigma_+} \right)^2 + \left(\frac{(m_{\gamma^1\gamma^2} - m_{\gamma^3\gamma^4})/2}{3\,\sigma_-} \right)^2 \qquad (6.11)$$

where σ_+ and σ_- are the resolutions of the distributions $(m_{\gamma^1\gamma^2} + m_{\gamma^3\gamma^4})/2$ and $(m_{\gamma^1\gamma^2} - m_{\gamma^3\gamma^4})/2$ as a function of the energy of the least energetic photon. Typically $\sigma_+ = 0.42$ MeV/c^2 and $\sigma_- = 0.83$ MeV/c^2.

The selected mass pairings used in this analysis are chosen by minimising the R_{ellipse} variable. A plot of the R_{ellipse} distribution for K_L and K_S events is shown in figure 6.15. Constant values of the R_{ellipse} variable are ellipses on the plot of $m_{\gamma^1\gamma^2}$ versus $m_{\gamma^3\gamma^4}$. As illustrated in figures 6.14 and 6.15, events are selected if $R_{\text{ellipse}} < 1.5$.

The events in the tail of the R_{ellipse} distributions ($R_{\text{ellipse}} \gtrsim 1.5$) are from two main sources: the mis-reconstruction of the cluster energies and background from $K_L \to 3\,\pi^0$ events. As stated above the response of the calorimeter to overlapping showers is not completely understood. The reconstructed cluster energies may be influenced by a nearby cluster (even after selecting events where $r_{ij} > 10$ cm).

Decay mode	Unweighted	Weighted
$K_L \to \pi^0\pi^0 \to 4\gamma$	1019455	287656.7
$K_S \to \pi^0\pi^0 \to 4\gamma$	1939096	
$K_L \to \pi^+\pi^-$	4334423	1217409.9
$K_S \to \pi^+\pi^-$	8039283	

Table 6.2: The number of events in each of the four $\mathcal{R}e(\epsilon'/\epsilon)$ decay modes.

6.7 The Raw Double Ratio

After selecting events using the selection criteria discussed in this chapter, the number of events in each mode are shown in table 6.2. The number of events in each decay in the kaon energy bins are shown in figure 6.16.

Figure 6.17 shows the raw values of the double ratio (equation (5.3)) in each energy bin. These values can be combined using the log-**R** estimator of equation (5.16) giving:

$$\mathbf{R}_{\text{raw}} = 0.98746 \pm 0.00170 \tag{6.12}$$

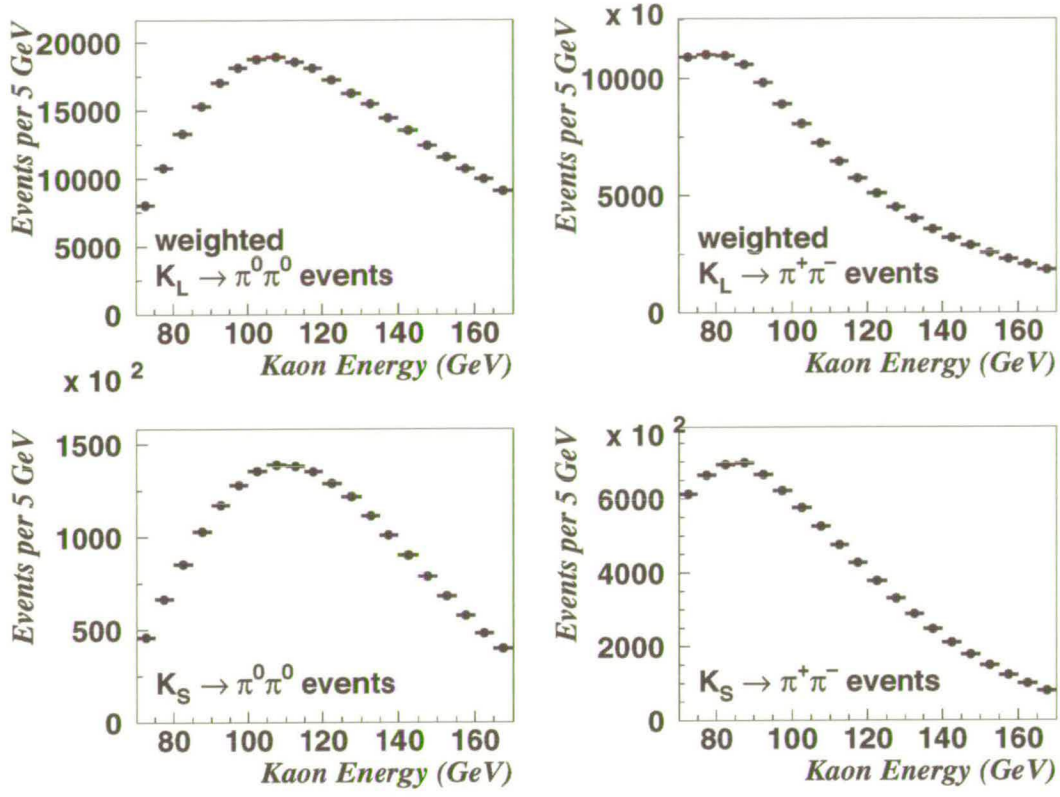

Figure 6.16: The numbers of events for the four $\mathcal{R}e(\epsilon'/\epsilon)$ decay modes in 5 GeV energy bins. These distributions show the spectra of the four modes.

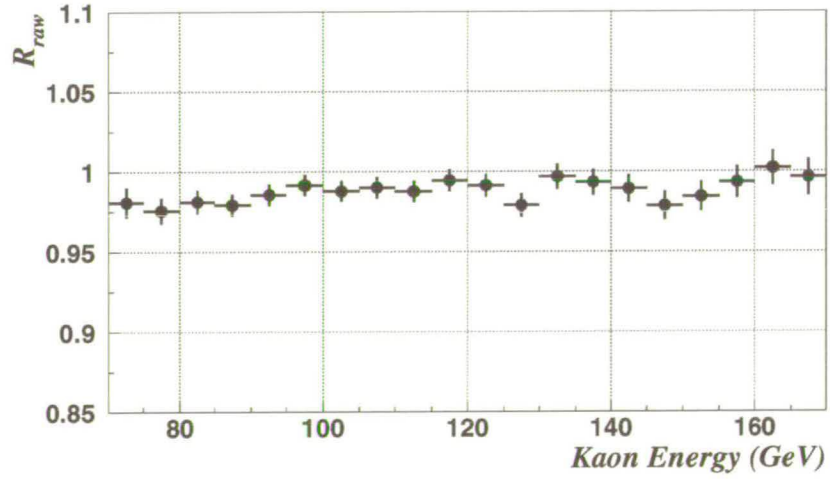

Figure 6.17: The raw value of the double ratio in bins of kaon energy.

Cut Variable	Cut Value
Kaon energy	$70\ \text{GeV} < E_K < 170\ \text{GeV}$
Kaon lifetime	$t_K < 3.5\ \tau_S$ for all events
	$z_{decay} > z_{AKS}$ for K_L events
	$(z_{decay} - z_{AKS}) > -2$ m for K_S events
AKS hits	no hit in AKS counter within ± 3 ns of the event time
Centre of Gravity	$r_{cog} < 10$ cm
LKR	$15\ \text{cm} < \sqrt{x_{LKR}^2 + y_{LKR}^2} < 110\ \text{cm}$
LKR dead cells	no cluster or track within 2 cm
Massbox Dead Time	no L1off signal
Overflow condition	no overflow within ± 312.5 ns of the event time

Table 6.3: Summary of the event selection criteria applied to both the $K^0 \to \pi^0\pi^0$ and $K^0 \to \pi^+\pi^-$ candidate events.

Cut Variable	Cut Value
Fiducial Cuts	$r_{track} > 12$ cm at DCH1, 2 & 4
	$x_{track}, y_{track} > 12.5$ cm at MUV
Track momentum	$\lvert p_{track}\rvert > 10\ \text{GeV/c}$
Decay Vertex	CDA < 3 cm
E_{LKR}/p	$E_{LKR}/p < 0.8$ for both tracks
MUV hits	No hit within ± 4 ns of the event time.
Momentum Asymmetry, A	$A < 0.62$ and $A < 1.08 - 0.00052 \cdot E_K/\text{GeV}$
Transverse momentum, $p_T'^2$	$p_T'^2 < 200\ \text{MeV}^2/\text{c}^2$
Invariant $\pi^+\pi^-$ mass	$\lvert m_{\pi^+\pi^-} - m_{K^0}\rvert < 3\sigma_m$
	with $\sigma_m = 0.00161 + 8.342 \times 10^{-6} \cdot E_K/\text{GeV}$

Table 6.4: Summary of the criteria used to select $K^0 \to \pi^+\pi^-$ events.

Cut Variable	Cut Value
Cluster energies	$3\ \text{GeV} < E_{\gamma^i} < 100\ \text{GeV}$
Number of clusters	4 clusters with $3\ \text{GeV} < E_{\gamma^i} < 100\ \text{GeV}$
	No additional clusters with $E_{\gamma^i} > 1.5$ GeV within 3 ns of the mean cluster time
Cluster times	Within ± 5 ns of the mean cluster time
Cluster separation	$r_{ij} > 10$ cm for all pairs
$R_{ellipse}$	$R_{ellipse} < 1.5$

Table 6.5: Summary of the criteria used to select $K^0 \to \pi^0\pi^0$ events.

Chapter 7

Corrections to the Double Ratio

This chapter discusses the corrections that have to be applied to the raw double ratio presented in the previous chapter. Corrections have to be applied to correct $\mathbf{R}$ for tagging effects, the efficiencies of the triggers, background decays, the scattering of the K_L beam, accidental activity, the energy scale of the detector and the acceptance of the detector and the selection cuts.

Where it is appropriate, the correction to $\mathbf{R}$ for a given effect is calculated and applied in every kaon energy bin. After each successive correction is applied, the log-$\mathbf{R}$ estimator (equation (5.16)) is then used to recalculate $\mathbf{R}$. The difference between the value of $\mathbf{R}$ before and after the correction ($\Delta\mathbf{R}$) is then considered to be the correction to the double ratio for the effect being considered. For clarity, the final correction for each of the effects being considered appears in a box.

The values of $\Delta\mathbf{R}$ are summarised in table 7.5 at the end of the chapter. Finally the sum of the $\Delta\mathbf{R}$ values is applied to $\mathbf{R}_{\mathrm{raw}}$ and the final, corrected, value of the double ratio is presented.

7.1 Tagging Corrections

Proton tagging is used to distinguish decays from the K_L and K_S beamlines. As discussed in section 6.2.1, both K_L and K_S events can be misidentified by the tagging procedure.

If the tagger is misaligned or inefficient, a K_S decay may be mistagged as a K_L decay. This is known as tagging inefficiency and can be parameterised by α_{SL}:

$$\alpha_{SL} = \frac{\text{Number of events tagged as } K_L \text{ from the } K_S \text{ beam}}{\text{Number of events from the } K_S \text{ beam}} \tag{7.1}$$

Accidental protons in the tagger cause K_L events to be mistagged as K_S decays. This is known as tagging dilution and can be parameterised by α_{LS} as defined in equation (6.1).

Using α_{LS} and α_{SL} it is possible to relate the numbers of tagged events to the actual numbers of events from the K_L and K_S beamlines:

$$N_S^{tag} = (1-\alpha_{SL})\,N_S^{beam} + \alpha_{LS}\,N_L^{beam} \quad (7.2)$$

$$N_L^{tag} = (1-\alpha_{LS})\,N_L^{beam} + \alpha_{SL}\,N_S^{beam} \quad (7.3)$$

Rearranging these expressions gives:

$$N_L^{beam} = \frac{1-\alpha_{SL}}{1-\alpha_{LS}-\alpha_{SL}}N_L^{tag} - \frac{\alpha_{SL}}{1-\alpha_{LS}-\alpha_{SL}}N_S^{tag} \quad (7.4)$$

$$N_S^{beam} = \frac{1-\alpha_{LS}}{1-\alpha_{LS}-\alpha_{SL}}N_S^{tag} - \frac{\alpha_{LS}}{1-\alpha_{LS}-\alpha_{SL}}N_L^{tag} \quad (7.5)$$

Setting $\alpha_{SL} \equiv 0$ in the above expressions gives back equations (6.2) and (6.3), where the effect of tagging inefficiency was ignored.

The values of α_{LS} and α_{SL} may be different for $\pi^0\pi^0$ and $\pi^+\pi^-$ decays. The tagging procedure uses the time difference between the protons in the tagger and the event time in the detectors to distinguish K_L and K_S decays. Different detectors are used to determine the event times of $\pi^0\pi^0$ and $\pi^+\pi^-$ decays: the LKR for $\pi^0\pi^0$ decays and the charged hodoscope for $\pi^+\pi^-$ decays. Therefore the amount of mistagging and tagging inefficiency can be different between the two decay modes.

The corrections applied to $\mathbf{R}$ for tagging effects are evaluated in three stages:

- First the values of α_{LS} and α_{SL} in the charged mode are calculated. Equations (7.4) and (7.5) are then used with these values of α_{LS} and α_{SL} to correct the numbers of events of each decay mode, and $\mathbf{R}$ is re-evaluated.
- Second the dilution difference ($\Delta\alpha_{LS} = \alpha_{LS}^{00} - \alpha_{LS}^{+-}$) between the neutral and charged modes is calculated and a correction to $\mathbf{R}$ due to this difference is made.
- Lastly the tagging inefficiency difference ($\Delta\alpha_{SL} = \alpha_{SL}^{00} - \alpha_{SL}^{+-}$) is estimated and again a correction to $\mathbf{R}$ is made.

7.2 Dilution and Tagging Inefficiency in $\pi^+\pi^-$ decays

As discussed in section 6.2.1, the beams can be cleanly separated in $\pi^+\pi^-$ decays by the y-position of the decay vertex (see figure 6.3). Using the definitions of α_{LS} and

α_{LS} in equations (6.1) and (7.1) respectively:

$$\alpha_{LS}^{+-} = \frac{586113}{5300501} = (11.058 \pm 0.014)\% \quad (7.6)$$

$$\alpha_{SL}^{+-} = \frac{1414}{7211425} = (1.96 \pm 0.05) \times 10^{-4} \quad (7.7)$$

These values of α_{LS} and α_{SL} are used in equations (7.4) and (7.5) to correct the tagged numbers of events in each kaon energy bin. The resulting correction to the value of **R** is:

$$\boxed{\Delta \mathbf{R} = (+15.1 \pm 3.6) \times 10^{-4}} \quad (7.8)$$

7.3 Tagging Dilution Difference

The tagging dilution (α_{LS}) is essentially the probability that an event from the K_L beamline has at least one proton hit in the tagger, during the tagging window $[-2, +2]$ ns. The value of α_{LS} is therefore a function of the rate of protons in the tagger. The rate of protons may also be investigated using protons in the sidebands of the tagging distribution. A quantity β_{tag} is defined as the probability that a K_L event (as identified by tagging) has at least one proton hit in a window of ± 2 ns in the sidebands.

7.3.1 Probability in the Sidebands

Figures 7.1 show the difference between the event time and *all* protons in the tagger, for events identified as K_L by the tagging procedure. The rate of protons shows a 200 MHz structure, which is the RF frequency of the SPS accelerator. As the tagging window $[-2, +2]$ ns is centred on a peak of this structure, the measurement of β_{tag} also uses windows of ± 2 ns centred on the structure.

Figure 7.2 shows the probability β_{tag} of having at least one proton in a ± 2 ns window for K_L events. To calculate the average value of β_{tag}, the windows centred at $-30, -25, -20$ and -15 ns from the event time are used. The other windows are not used as they are either too close to the edge of the tagger readout window, or too close to 0.

The average values of β_{tag} from the chosen time windows (see figure 7.2) are:

$$\beta_{tag}^{00} = (10.530 \pm 0.015)\% \qquad \beta_{tag}^{+-} = (10.474 \pm 0.007)\% \quad (7.9)$$

It is clear that α_{LS} and β_{tag} do not measure the same value. This is because β_{tag} is defined for K_L events as identified by tagging, whereas α_{LS} is defined for *all* K_L

events, including those which are identified as K_S by the tagging procedure. Therefore a method must be found to relate the values of β_{tag} and α_{LS}.

A parameter, W, may be defined as the difference between β_{tag} and α_{LS}:

$$W \equiv \alpha_{LS} - \beta_{tag} \tag{7.10}$$

Therefore the difference in the tagging dilutions ($\Delta\alpha_{LS}$) can be written as:

$$\Delta\alpha_{LS} \equiv \Delta\beta_{tag} + \Delta W \quad \text{with} \quad \Delta W \equiv W^{00} - W^{+-} \tag{7.11}$$

Using the results of equations (7.7) and (7.9) we obtain:

$$\Delta\beta_{tag} \equiv \beta_{tag}^{00} - \beta_{tag}^{+-} = (5.5 \pm 1.6) \times 10^{-4} \tag{7.12}$$

$$W^{+-} = \alpha_{LS}^{+-} - \beta_{tag}^{+-} = (58.3 \pm 1.5) \times 10^{-4} \tag{7.13}$$

The remaining unknown quantity W^{00} is considered in the following subsection.

7.3.2 The calculation of W^{00}

Unlike in the $\pi^+\pi^-$ mode, W^{00} cannot be calculated directly. Instead W^{00} is approximated by the equivalent quantity in $K_L \to 3\pi^0$ decays: W^{000}. As the event time of both $\pi^0\pi^0$ and $3\pi^0$ events are measured by the LKR, it is expected that $W^{000} \simeq W^{00}$.

It is possible to calculate directly a value for α_{LS}^{000} (and hence W^{000}) as the branching ratio of the decay $K_S \to 3\pi^0$ is expected to be $\mathcal{O}(10^{-7})$ and can therefore be ignored in this analysis The small number of $K_L \to 3\pi^0$ decays from the K_S beamline can be calculated and corrected for.

An independent analysis of $K_L \to 3\pi^0$ decays [23] gives:

$$\alpha_{LS}^{000} = (11.110 \pm 0.009)\% \qquad \beta_{tag}^{000} = (10.519 \pm 0.005)\% \tag{7.14}$$

$$W^{00} \simeq W^{000} \equiv \alpha_{LS}^{000} - \beta_{tag}^{000} = (59.1 \pm 1.0) \times 10^{-4} \tag{7.15}$$

Using this result and that of equation (7.13), the value of ΔW is:

$$\Delta W \equiv W^{00} - W^{+-} = (0.8 \pm 1.8) \times 10^{-4} \tag{7.16}$$

7.3.3 Correction to R from the Tagging Dilution Difference

Using equation (7.11) and the results in equations (7.12) and (7.16):

$$\begin{aligned} \Delta\alpha_{LS} &= \Delta\beta_{tag} + \Delta W \\ &= (5.5 \pm 1.6) \times 10^{-4} + (0.8 \pm 1.8) \times 10^{-4} \\ &= (6.3 \pm 2.2) \times 10^{-4} \end{aligned} \tag{7.17}$$

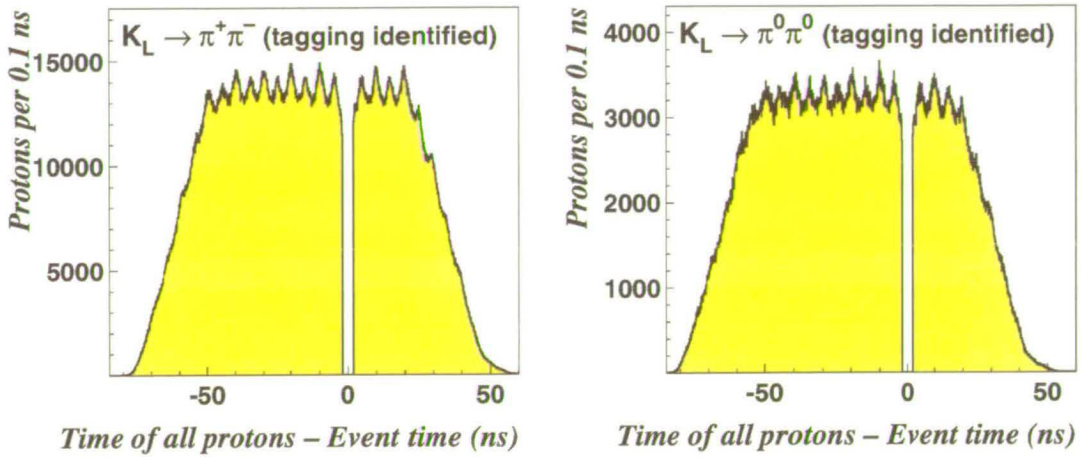

Figure 7.1: The time difference between *all* protons in the tagger and the event time for events identified as K_L by the tagging procedure. By definition there are no protons within ± 2 ns of the event time. The clearly visible 200 MHz structure is due to the RF acceleration of the protons in the SPS accelerator.

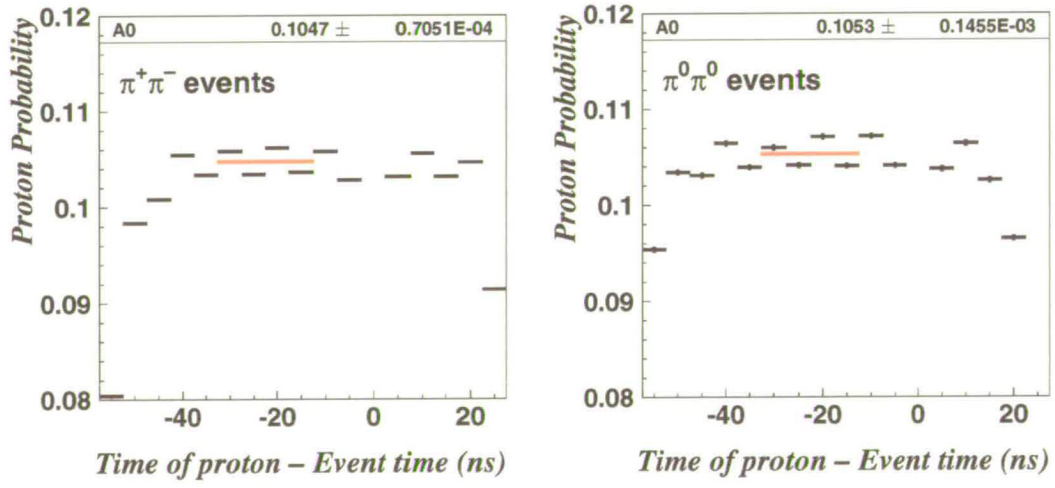

Figure 7.2: The probability (β_{tag}) of finding at least one proton in ± 2 ns windows for events identified as K_L by the tagging. Note that the probability in the tagging window is by definition zero, as the probability is for events *tagged* as K_L. The windows centred at $-30, -25, -20$ and -15 ns are used to define the average value of β_{tag}. The result is shown at the top of each graph.

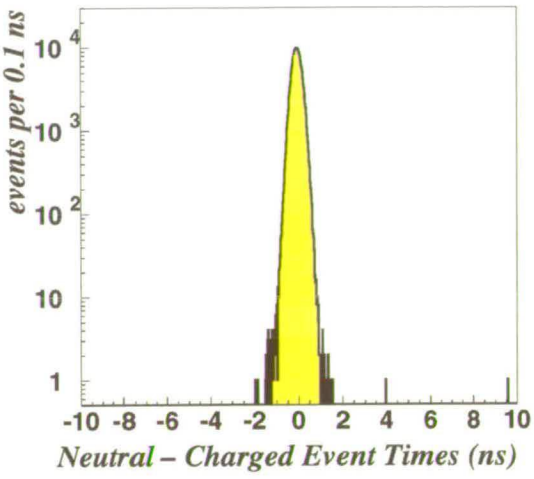

Figure 7.3: The difference between the event time reconstructed by the LKR and the Charged Hodoscope for events with a photon conversion: $\gamma \rightarrow e^+e^-$.

The calculated value of $\alpha_{LS}^{00} = \alpha_{LS}^{+-} + \Delta\alpha_{LS}$ is used to corrected the number of events in the $\pi^0\pi^0$ decay modes. The resulting correction to **R** is:

$$\boxed{\Delta\mathbf{R} = (+12.0 \pm 4.3) \times 10^{-4}} \tag{7.18}$$

7.4 Tagging Inefficiency Difference

The tagger inefficiency (α_{SL}) measures the amount of K_S decays misidentified as K_L decays by the tagging procedure. In the charged decay mode $\alpha_{SL}^{+-} = (1.96 \pm 0.05) \times 10^{-4}$ is measured directly using the position of the decay vertex to separate K_L and K_S decays.

There are two methods that can be used to estimate a value for α_{SL}^{00}. The first is a direct measurement, distinguishing $K_S \rightarrow \pi^0\pi^0$ decay by a method other than the tagger. The second is a measurement of the difference in mistagging probability ($\Delta\alpha_{SL}$) by looking at events where both the LKR and the Charged Hodoscope make a measurement of the event time.

Three different data sets have been studied to estimate a value for $\Delta\alpha_{SL}$ [48]:

- **K_S only runs.** As described in section 5.2, for some periods of data taking, protons were directed only to the K_S target. Therefore all decays in these periods are from the K_S beamline allowing a direct measurement of both α_{SL}^{+-} and α_{SL}^{00}. The difference in tagging inefficiency is measured to be $\Delta\alpha_{SL} = (-0.11 \pm 0.49) \times 10^{-4}$ in K_S only runs.

- **π^0 Dalitz decays.** Electron tracks from π^0 Dalitz decays can be used to reconstruct the decay vertex of $K^0 \to \pi^0\pi^0 \to \gamma e^+e^-\gamma\gamma$ decays. The y-position of the vertex can be used to distinguish decays from the K_L and K_S beamlines, allowing a direct measurement of α_{SL}^{00}. Unfortunately this measurement is limited by poor statistics. The result is $\alpha_{SL}^{00} = (3.0^{+5.0}_{-2.5}) \times 10^{-4}$, which is consistent with $\Delta\alpha_{SL} = 0$.

- **Photon conversions.** Photons from both $K^0 \to \pi^0\pi^0 \to 4\gamma$ and $K_L \to 3\pi^0 \to 6\gamma$ decays can convert into a e^+e^- pair when they pass through some material in the detector. Most photon conversions take place at the Kevlar Window. For these decays the event time is reconstructed by both the Charged Hodoscope and the LKR. Figure 7.3 shows the difference between these reconstructed times. From this study it is estimated that $\Delta\alpha_{SL} < 1 \times 10^{-4}$.

All of these studies are consistent with a value of $\Delta\alpha_{SL} = 0$, *i.e.* the tagging inefficiency in both the charged and neutral decays modes is small. The error on this measurement of $\Delta\alpha_{SL}$ is estimated to be 0.5×10^{-4}.

The correction on **R** due to the difference in tagging efficiency is calculated to be:

$$\boxed{\Delta\mathbf{R} = (0 \pm 3) \times 10^{-4}} \tag{7.19}$$

7.5 Trigger Efficiencies

If the trigger systems that are used to collect the $K^0 \to \pi^+\pi^-$ and $K^0 \to \pi^0\pi^0 \to 4\gamma$ decays are inefficient, they may prevent some of the decays being recorded. If the inefficiency depends on the energy of the kaon, or is asymmetric between K_L and K_S decays, it may bias the measured value of **R**.

For the purpose of measuring trigger efficiencies, so called 'minimum-bias' triggers are taken concurrently with the dedicated $\pi^+\pi^-$ and $\pi^0\pi^0$ triggers. Events taken with the minimum-bias triggers can be used as control events in the measurement of the efficiencies of the dedicated triggers. As the name suggests, minimum-bias triggers require only a minimum amount of activity in the detector, and are therefore much looser conditions than the dedicated triggers. This means that the rate of the minimum-bias triggers is very high. For example the NHOD signal (as defined in table 4.1) is used to measure the efficiency of the $\pi^0\pi^0$ trigger. The rate of this signal is around 75,000 triggers per burst. The minimum bias triggers are therefore prescaled, *i.e.* only a small fraction of these triggers are sent to the Level 2 Trigger Supervisor to prompt the readout of the subdetectors.

The efficiency of a particular trigger signal may be investigated by looking for $\pi^+\pi^-$ or $\pi^0\pi^0$ events that have been collected using a control trigger. If one of these events

was also selected by the dedicated $\pi^+\pi^-$ or $\pi^0\pi^0$ trigger, it is called an efficient event, otherwise the event is an inefficient event. The efficiency of the trigger signal (ϵ) is then given by equation (5.19):

$$\epsilon = \frac{N_W}{N_W + M_W} \tag{7.20}$$

where N_W is the sum of the weights of the efficient events and M_W is the sum of the weights of the inefficient events. The error on this quantity is given by equation (5.20).

7.6 Charged Trigger Efficiency

As described in section 4.3, the trigger for $K^0 \to \pi^+\pi^-$ events is made in two stages. The level 1 condition is that the event must have three pre-trigger signals: Q_X, E_{TOT} and 2 track. The Level 1 Trigger Supervisor (L1TS) reads in these signals and determines whether they are in coincidence. If a positive level 1 decision is made, the Level 2 Charged Trigger (also called the Massbox) makes the final trigger decision using information from the drift chambers. There are therefore three contributions to the $\pi^+\pi^-$ trigger efficiency:

1. The efficiency that a selected $K^0 \to \pi^+\pi^-$ event has the 3 pre-trigger signals: Q_X, E_{TOT} and 2 track.
2. The efficiency of the L1TS to make a coincidence of these pre-trigger signals. An inefficiency could arise if the three signals do not arrive at the L1TS at the same time.
3. The efficiency of the Massbox to issue a $\pi^+\pi^-$ trigger for a $K^0 \to \pi^+\pi^-$ event, given the Level 1 decision.

In order to take into account the coincidence efficiency (item 2. above) the E_{TOT} and 2 track signals are defined to be efficient only if they arrive at the L1TS at the same time as a Q_X signal.

7.6.1 The Pre-Trigger Signals

The efficiency of the Q_X trigger signal for $K^0 \to \pi^+\pi^-$ decays is measured using the coincidence $E_{TOT} \cdot$ 2 track as a control trigger. The results are shown in table 7.1 (as inefficiencies) for K_S and weighted K_L decays.

The efficiency that a selected $K^0 \to \pi^+\pi^-$ decay has a E_{TOT} or 2 track signal at the same time as a Q_X signal has been measured independently using prescaled Q_X triggers

Signal		Inefficiency
E_{TOT}	K_S	$(51.5 \pm 2.9) \times 10^{-4}$
	K_L	$(44.0 \pm 4.4) \times 10^{-4}$
2 track	K_S	$< 0.4 \times 10^{-4}$
	K_L	$< 0.4 \times 10^{-4}$
Q_X	K_S	$(5.2 \pm 0.8) \times 10^{-4}$
	K_L	$(5.6 \pm 1.6) \times 10^{-4}$

Table 7.1: The efficiencies of the Q_X, E_{TOT} and 2 track signals for $\pi^+\pi^-$ events. The K_L results use weighted events. The efficiencies of the E_{TOT} and 2 track signals are measured with respect to the time of the Q_X signal.

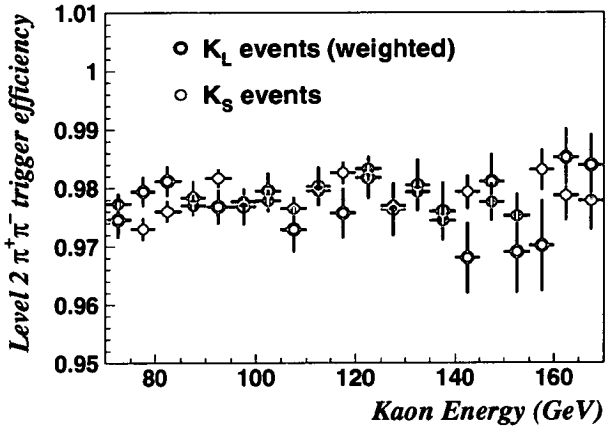

Figure 7.4: The efficiency of the Level 2 Charged Trigger in bins of Kaon energy. The efficiency is similar for both K_L and K_S decays and is independent of the Kaon energy.

as a control trigger [53]. Again the results are shown in table 7.1 for K_S and weighted K_L decays.

The efficiencies of the Q_X and 2 track trigger are very high and symmetric for K_S and weighted K_L events. Therefore no correction is applied to **R** for these signals.

The efficiency of the E_{TOT} signal for $K^0 \to \pi^+\pi^-$ decays, however, is only around 99.5%. Additionally, the efficiencies show around a 1σ difference between K_S and weighted K_L events. The E_{TOT} efficiency has been calculated in each bin of kaon energy. The resulting correction to **R** for the efficiency of the E_{TOT} signal is:

$$\Delta \mathbf{R} = (+5.8 \pm 5.3) \times 10^{-4} \tag{7.21}$$

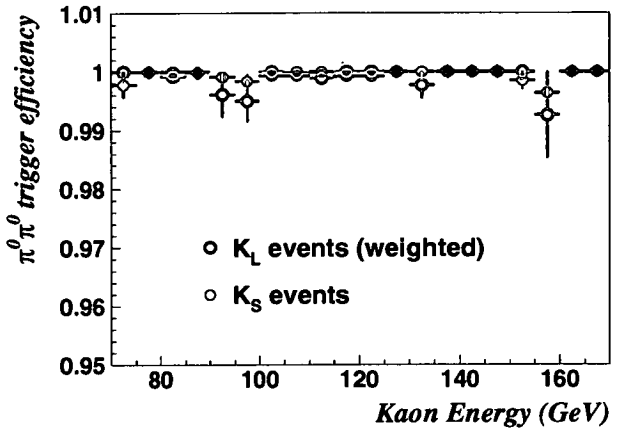

Figure 7.5: The efficiency of the $\pi^0\pi^0$ in bins of Kaon energy.

7.6.2 Massbox Inefficiency

The efficiency of the Massbox is measured using the Level 1 $\pi^+\pi^-$ trigger: $Q_X \cdot E_{TOT} \cdot$ 2 track as the control trigger. The measured efficiencies are $(97.80 \pm 0.05)\%$ for K_S events and $(97.75 \pm 0.08)\%$ for weighted K_L events. The Massbox efficiency is shown in figure 7.4 in bins of kaon energy. The resulting correction to **R** for the difference in Massbox efficiency between K_S and weighted K_L events is:

$$\Delta \mathbf{R} = (-8.0 \pm 10.7) \times 10^{-4} \tag{7.22}$$

The large uncertainty on this correction is due to the number of prescaled minimum bias events used to measure the correction.

7.6.3 Charged Trigger Correction

Combining the values of the corrections in equations (7.21) and (7.22) above, the total correction to **R** for the charged trigger efficiency is:

$$\boxed{\Delta \mathbf{R} = (-2.2 \pm 12.0) \times 10^{-4}} \tag{7.23}$$

7.7 Neutral Trigger Efficiency

The efficiency of the $\pi^0\pi^0$ trigger is measured using the NHOD signal as the control trigger (see table 4.1). The measured efficiencies are $(99.90 \pm 0.05)\%$ for weighted K_L events and $(99.94 \pm 0.02)\%$ for K_S events. The efficiency of the triggers in kaon energy

bins is shown in figure 7.5. It can be seen that there is no systematic dependence of the trigger efficiency on the kaon energy.

As the $\pi^0\pi^0$ trigger efficiency is very high, and no difference is found between weighted K_L and K_S events (within errors), no correction is applied to **R** for the $\pi^0\pi^0$ trigger efficiency.

7.8 Charged Background

As discussed in section 6.5.1, the main sources of background to $K^0 \to \pi^+\pi^-$ events are from the semileptonic decays $K_L \to \pi^\pm\mu^\mp\nu_\mu$ and $K_L \to \pi^\pm e^\mp\nu_e$ ($K\mu3$ and Ke3). There is no significant background in $K_S \to \pi^+\pi^-$ decays. The aim of the charged background analysis is to determine the number of $K\mu3$ and Ke3 decays remaining in the $K_L \to \pi^+\pi^-$ sample, and to correct the value of **R** appropriately.

The analysis is performed by investigating the distribution of events with respect to two variables. The invariant mass of two tracks, assuming that they were both charged pions ($m_{\pi^+\pi^-}$) and the transverse momentum variable $p_T'^2$ as defined in equation (6.9).

Figure 7.6 shows the distributions of selected $K_L \to \pi^+\pi^-$ and $K_S \to \pi^+\pi^-$ events in the $(m_{\pi^+\pi^-}, p_T'^2)$ plane, before the final cuts on $m_{\pi^+\pi^-}$ and $p_T'^2$ have been made. Figure 7.7 shows the same distributions for Ke3 and $K\mu3$ events.

The Ke3 and $K\mu3$ samples are selected from the same data set as $K^0 \to \pi^+\pi^-$ decays. Almost identical selection criteria are used to select these samples (see table 6.4), with the following exceptions:

- Ke3 events must have one track that satisfies $E_{LKR}/p > 0.95$ (to be compatible with an electron) and the other track must satisfy $E_{LKR}/p < 0.8$ (charged pion).
- $K\mu3$ events must have one (and only one) track compatible with a reconstructed muon in the MUV (see section 4.6.4).

In this analysis *control regions* are defined in the $(m_{\pi^+\pi^-}, p_T'^2)$ plane, away from the signal region: $p_T'^2 < 200$ (MeV/c)^2, $|m_{\pi^+\pi^-} - m_{K^0}| < 3\sigma_m$. In the control regions, it is assumed that the events in the $K_L \to \pi^+\pi^-$ sample can be attributed to a sum of Ke3 and $K\mu3$ events, and a small residual contribution from true $\pi^+\pi^-$ decays.

In choosing the control regions care must be taken to avoid the regions where $m_{\pi^+\pi^-}$ is too close to m_{K^0}. As will be discussed in section 7.9, some good $\pi^+\pi^-$ events are found with $p_T'^2 \gg 200$ (MeV/c)^2. This effect is investigated independently of the charged background analysis.

Two different methods are used to determine the amount of Ke3 and Kμ3 events in the control regions:

1. A fitting method. The shape of the $(m_{\pi^+\pi^-}, p_T'^2)$ distributions of Ke3 and Kμ3 in a control region is fitted to the distribution of events in the $K_L \to \pi^+\pi^-$ sample. This determines the number of Ke3 and Kμ3 decays in the control region.

2. A counting method. This uses two control regions. The relative proportion of Ke3 and Kμ3 decays in the control regions are calculated.

The numbers of Ke3 and Kμ3 events in the signal region are then found by making an extrapolation from the control region to the signal region.

Both of the methods are described in more detail below. Figures 7.8 and 7.9 illustrate the control regions used in these two methods.

7.8.1 The Charged Background Fitting Method

The Charged Background Fitting Method investigates the shape of the distribution of events in $m_{\pi^+\pi^-}$ and $p_T'^2$. Figures 7.10 and 7.11 show the distributions of the $K_L \to \pi^+\pi^-$, Ke3 and Kμ3 samples in $m_{\pi^+\pi^-}$ and $p_T'^2$ in the defined control region.

A CERN library routine, HMCMLL [7], is used to perform a log likelihood fit. The HMCMLL routine fits the Ke3 and Kμ3 distributions to the K_L distribution in this control region. Figure 7.12 shows the results of the HMCMLL routine.

An extrapolation factor (α) may be defined for the both the Ke3 and Kμ3 using the pure event samples (figure 7.7):

$$\alpha = \frac{\text{Number of events in the signal region}}{\text{Number of events in the control region}} \tag{7.24}$$

The result obtained in the control region can then be extrapolated to the signal region.

Due to a lack of statistics in the control regions, the fit cannot be reliably made in each bin of kaon energy. However, the amount of Ke3 and Kμ3 fitted in the control region does not show a significant variation with kaon energy. Therefore the fit is made using all the events in the energy range $70 < E_K/\text{GeV} < 170$. On the other hand, the extrapolation factors do vary significantly over the kaon energy range. Therefore these factors are calculated and applied in each kaon energy bin. Both the fit and the extrapolation are made using weighted events.

The number of Ke3 and Kμ3 events found (normalised to the number of $K_L \to \pi^+\pi^-$ events) is shown in figure 7.13. In total (1475 ± 62) Ke3 and (1115 ± 185) Kμ3 decays are found in the $K_L \to \pi^+\pi^-$ signal region. After correcting for tagging effects, there

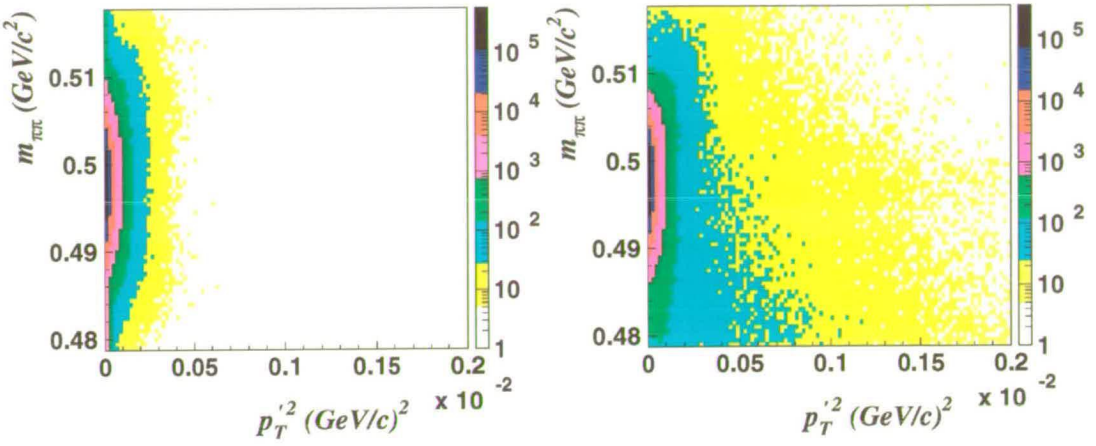

Figure 7.6: The distribution of $\pi^+\pi^-$ events in the $(m_{\pi^+\pi^-}, p_{\mathrm{T}}^{\prime 2})$ plane. The density of events is plotted on a logarithmic scale. The plot on the left shows decays from the $\mathrm{K_S}$ beamline, and decays from the $\mathrm{K_L}$ beamline are shown on the right. It is clear that the $\mathrm{K_L}$ sample contains contributions from other decays at high values of $p_{\mathrm{T}}^{\prime 2}$.

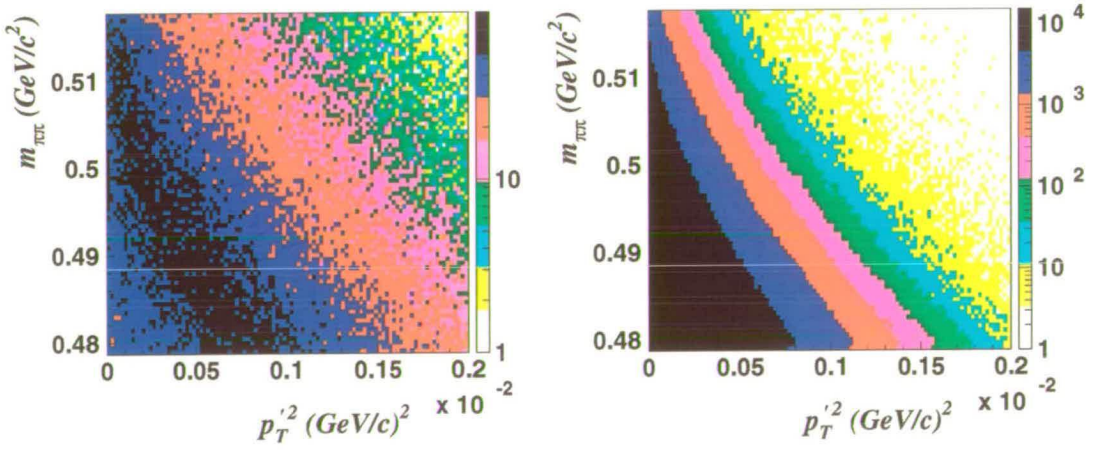

Figure 7.7: The distribution of Ke3 (left) and Kμ3 (right) events in the $(m_{\pi^+\pi^-}, p_{\mathrm{T}}^{\prime 2})$ plane.

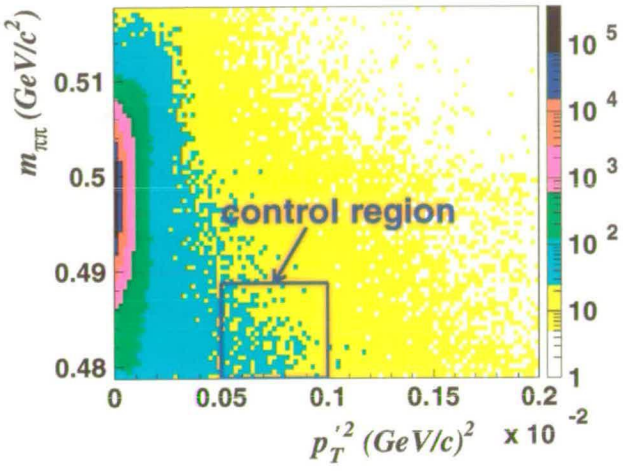

Figure 7.8: Definition of the control region for the charged background fitting method.

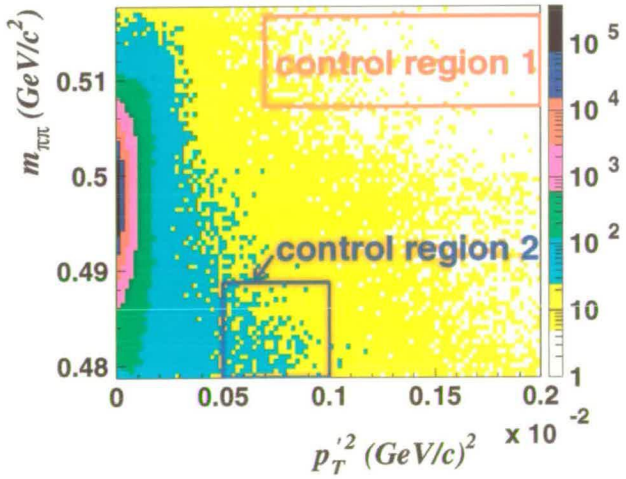

Figure 7.9: Definition of the control regions for the charged background counting method.

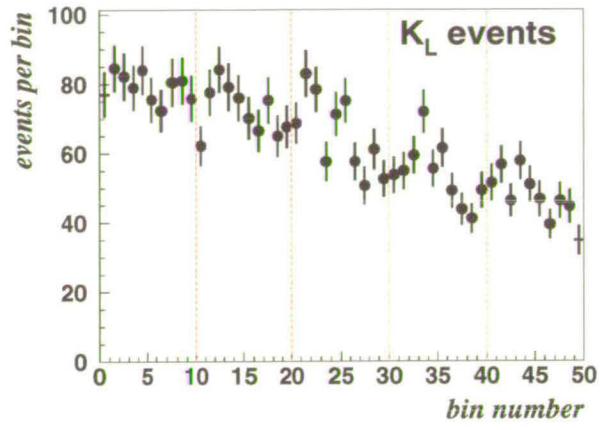

Figure 7.10: The distribution of $K_L \rightarrow \pi^+\pi^-$ events in the variables $m_{\pi^+\pi^-}$ and p'^2_T. The vertical lines demark different ranges of p'^2_T in the control region range of 500 $(MeV/c)^2$ to 1000 $(MeV/c)^2$. Within each p'^2_T range, events are plotted in bins of $m_{\pi^+\pi^-}$, where $m_{\pi^+\pi^-}$ ranges from 0.4787 GeV/c^2 to 0.4887 GeV/c^2.

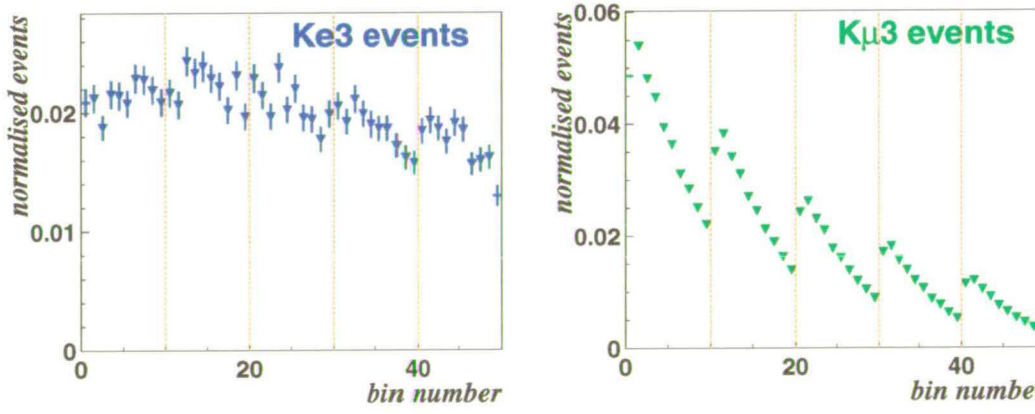

Figure 7.11: The distribution of Ke3 events (left) and Kμ3 events (right) in $m_{\pi^+\pi^-}$ and p'^2_T. The binning is as described for the above graph.

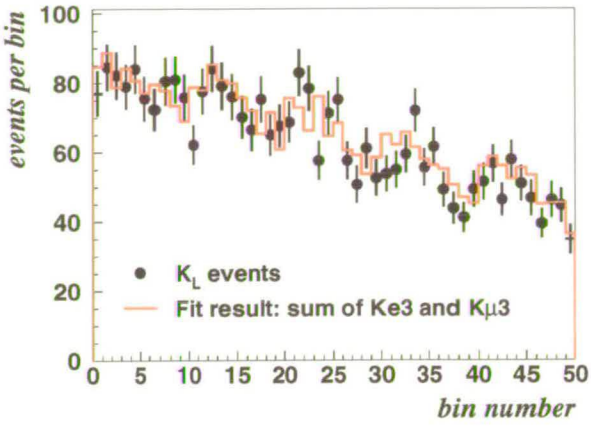

Figure 7.12: The result of the charged background fitting method. The black points are the distribution of $K_L \to \pi^+\pi^-$ events, as shown in figure 7.11. The solid line is the result of the best fit of Ke3 and Kμ3 events, as shown in figure 7.10. The resulting fit returned from the HMCMLL routine is $(82 \pm 2)\%$ of the Ke3 distribution plus $(18 \pm 1)\%$ of the Kμ3 distribution.

are 1368023 weighted $K_L \to \pi^+\pi^-$ events in the signal region. The amount of charged background is therefore $(18.9 \pm 1.4) \times 10^{-4}$.

7.8.2 The Charged Background Counting Method

A second method of determining the charged background has been used as a cross-check.

Figure 7.9 defines two control regions in the $(m_{\pi^+\pi^-}, p_T'^2)$ plane. It is assumed for both the control regions i, that the number of events in the $K_L \to \pi^+\pi^-$ sample has three contributions: Ke3 decays, Kμ3 decays, and a small residue of $\pi^+\pi^-$ decays. This can be expressed as:

$$N_L^i = N_{\pi e\nu}^i + N_{\pi\mu\nu}^i + N_{\pi^+\pi^-}^i \tag{7.25}$$

$N_{\pi^+\pi^-}^i$ is determined by an appropriate scaling of the number of events in the same control region of the $K_S \to \pi^+\pi^-$ sample. Subtracting this contribution from N_L^i gives:

$$N'^i_L = N_{\pi e\nu}^i + N_{\pi\mu\nu}^i \tag{7.26}$$

Again, extrapolation factors are defined between the signal region (sig) and the control regions (i) for both Ke3 and Kμ3 decays:

$$\alpha_{\pi e\nu}^i = \frac{M_{\pi e\nu}^{\text{sig}}}{M_{\pi e\nu}^i} \qquad \alpha_{\pi\mu\nu}^i = \frac{M_{\pi\mu\nu}^{\text{sig}}}{M_{\pi\mu\nu}^i} \tag{7.27}$$

Here the M's are the number of events for the pure Ke3/Kμ3 samples (figure 7.7).

The number of background decays ($N^{\rm sig}_{\pi e\nu}$, $N^{\rm sig}_{\pi\mu\nu}$) in the signal region of the $K_L \to \pi^+\pi^-$ sample is independent of the control region. Therefore we have:

$$\begin{array}{rcccl} N^{\rm sig}_{\pi e\nu} & = & \alpha^1_{\pi e\nu} \cdot N^1_{\pi e\nu} & = & \alpha^2_{\pi e\nu} \cdot N^2_{\pi e\nu} \\ N^{\rm sig}_{\pi\mu\nu} & = & \alpha^1_{\pi\mu\nu} \cdot N^1_{\pi\mu\nu} & = & \alpha^2_{\pi\mu\nu} \cdot N^2_{\pi\mu\nu} \end{array} \tag{7.28}$$

Rearranging the expressions in equations (7.26), (7.27) and (7.28) gives:

$$N^{\rm sig}_{\pi\mu\nu} = \frac{M^{\rm sig}_{\pi\mu\nu} \cdot (M^1_{\pi e\nu} \cdot N'^2_{\rm L} - M^2_{\pi e\nu} \cdot N'^1_{\rm L})}{M^1_{\pi e\nu} \cdot M^2_{\pi\mu\nu} - M^2_{\pi e\nu} \cdot M^1_{\pi\mu\nu}} \tag{7.29}$$

$$N^{\rm sig}_{\pi e\nu} = \frac{M^{\rm sig}_{\pi e\nu} \cdot (M^1_{\pi\mu\nu} \cdot N'^2_{\rm L} - M^2_{\pi\mu\nu} \cdot N'^1_{\rm L})}{M^1_{\pi e\nu} \cdot M^2_{\pi\mu\nu} - M^2_{\pi e\nu} \cdot M^1_{\pi\mu\nu}} \tag{7.30}$$

As with the fitting method, the number of background decays is calculated using weighted events.

The results are:

$$N^{\rm sig}_{\pi\mu\nu} = (1171 \pm 166) \qquad N^{\rm sig}_{\pi e\nu} = (1397 \pm 44) \tag{7.31}$$

Normalising to the number of $K_L \to \pi^+\pi^-$ decays in the signal region, the charged background found by the counting method is therefore $(18.8 \pm 1.3) \times 10^{-4}$, in agreement with the previous method.

7.8.3 Charged Background Correction to R

Figure 7.13 shows the total amount of background in the $K_L \to \pi^+\pi^-$ sample. Using different control regions, it is found that the amount of background calculated can vary as much as $\pm 3 \times 10^{-4}$ from the values presented here. Therefore an additional error is added to the correction for the charged background.

The number of background decays is subtracted in each kaon energy bin and **R** is recalculated. The resulting correction to **R** for the charged background is:

$$\boxed{\Delta\mathbf{R} = (+18.5 \pm 3.0) \times 10^{-4}} \tag{7.32}$$

7.9 Beam Scattering

In the K_L sample of charged events, some genuine $K^0 \to \pi^+\pi^-$ events are observed with values of p'^2_T much larger than the cut value of 200 (MeV/c)^2. Figure 7.14 shows

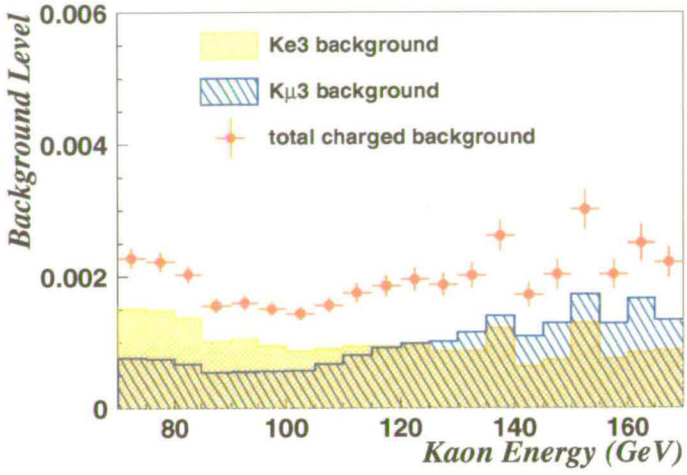

Figure 7.13: The amount of charged background in each kaon energy bin.

the distribution of $m_{\pi^+\pi^-}$ for events with $p_T'^2 > 200$ (MeV/c)^2 from both the K_L and K_S beams. It can be seen that there is a substantial contribution from real $K^0 \to \pi^+\pi^-$ decays in the K_L sample.

An extrapolation is made to calculate the x and y positions of the kaon producing these events at the z-positions of the final and cleaning collimators in the K_L beam. (For reference: figure 3.3 shows the positions and diameters of the collimators in the K_L beam.) The events in the sidebands of the mass distribution are used to subtract the background to these genuine $K^0 \to \pi^+\pi^-$ events (see the text for figure 7.15). Figure 7.15 and figure 7.16 show the radial positions of these events in the final and cleaning collimators. Figure 7.16 also shows the distribution of the reconstructed lifetime of these events.

These events form a peak around $r = (2.83 \pm 0.01)$ cm at the final collimator and $r = (1.83 \pm 0.04)$ cm at the cleaning collimator. The actual radii of the collimators are $2.70 - 2.86$ cm for the final collimator and 1.86 cm for the cleaning collimator. The reconstructed lifetime of these events is $t_K = (0.97 \pm 0.09)\ \tau_S$.

The $K^0 \to \pi^+\pi^-$ events found at high values of $p_T'^2$ are therefore K_S decays. They are produced by regeneration on the cleaning and final collimators in the K_L beam.

Due to the cut on $p_T'^2$ applied to $\pi^+\pi^-$ candidate events, these regenerated kaon events are not included in the final $\pi^+\pi^-$ event samples. However no similar cut can be defined for $\pi^0\pi^0$ events. Therefore a small fraction of selected $K_L \to \pi^0\pi^0$ events are due to regenerated kaons. This fraction of events is estimated using $K^0 \to \pi^+\pi^-$ decays, and subtracted from the $\pi^0\pi^0$ sample.

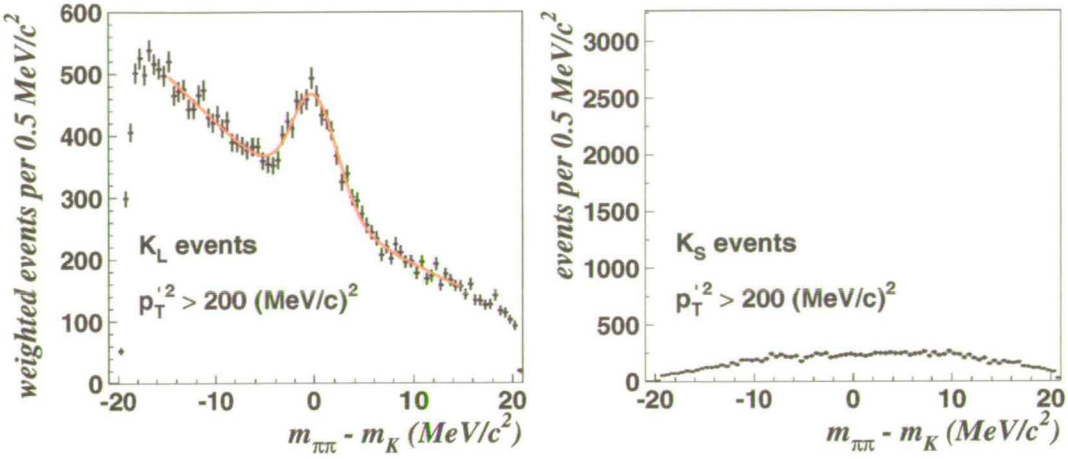

Figure 7.14: Events from the K_L and K_S beams with $p_T'^2 > 200$ (MeV/c)^2, *i.e.* events that do *not* pass the cut on $p_T'^2$. The vertical scale of the plots is proportional to the number of $\pi^+\pi^-$ events in the signal region. In the K_L sample there is a substantial contribution from genuine $K^0 \to \pi^+\pi^-$ decays.

For this analysis, an additional cut is applied to the $\pi^+\pi^-$ selection to reject additional activity in the LKR. This is the same cut that is made in the $\pi^0\pi^0$ selection (see table 6.5). Without making this cut the fraction of scattered events in the $K_L \to \pi^0\pi^0$ sample is overestimated. This is because when kaons are regenerated by scattering on the collimators, other particles (particularly photons) may be produced. If one of these photons is detected in the calorimeter the event would be rejected from the $\pi^0\pi^0$ sample by the cuts on additional activity.

Figure 7.17 shows the events from the K_L beam line, with $p_T'^2 > 200$ (MeV/c)^2, after rejecting events with additional clusters in the LKR. A fit has been made to the sum of a parabola and a Gaussian. The number of events in Gaussian is one of the fit parameters (labelled as 'Peak' in figure 7.17). In total there are (1256 ± 127) weighted events in the Gaussian. The number of weighted $K_L \to \pi^+\pi^-$ events in the signal region with no additional clusters is 1115240. The fraction of regenerated events in the $K_L \to \pi^0\pi^0$ sample is therefore $(11.3 \pm 1.1) \times 10^{-4}$.

Independent studies of regenerated events have been made using $\pi^0\pi^0$ events with high values of r_{cog} [18]. In these studies the fraction of regenerated events in the $K_L \to \pi^0\pi^0$ sample was estimated to be $(11 \pm 3) \times 10^{-4}$.

The method used to calculated this correction require large statistics, so this correction is not made in each kaon energy bin. However the effect of regeneration as a function of the kaon energy has been investigated, and the overall effect on the value of **R** remains unchanged.

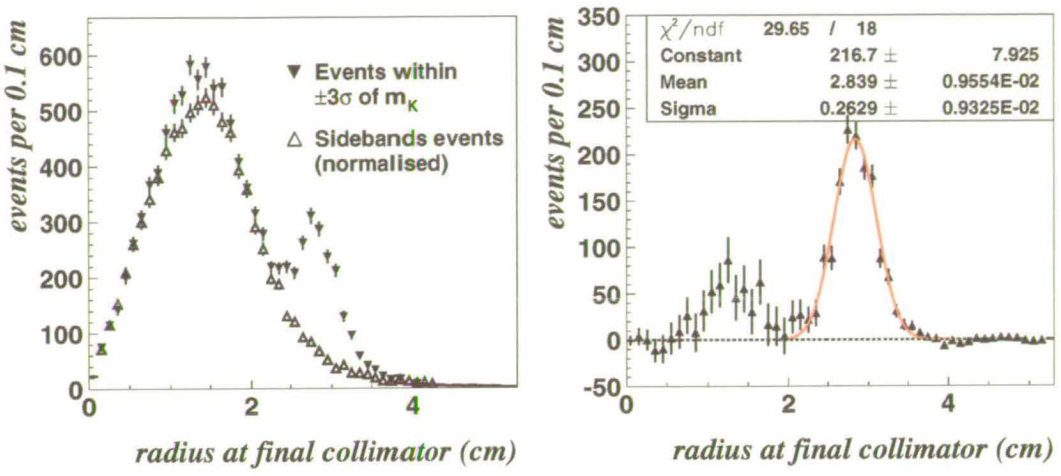

Figure 7.15: The extrapolated position of the kaon at the final K_L collimator, for K_L events with $p_T'^2 > 200$ (MeV/c)^2. The figure on the left shows the radii for two subsamples of the events in figure 7.14. The filled triangles are events within $\pm 3\sigma$ of m_{K^0}, and the open triangles are events from the sidebands. The figure on the right shows the difference between these two samples. The peak at 2.84 cm corresponds to kaons produced by regeneration in the final K_L collimator. The peak at around 1 cm is the shadow from kaons regenerated in the cleaning collimator.

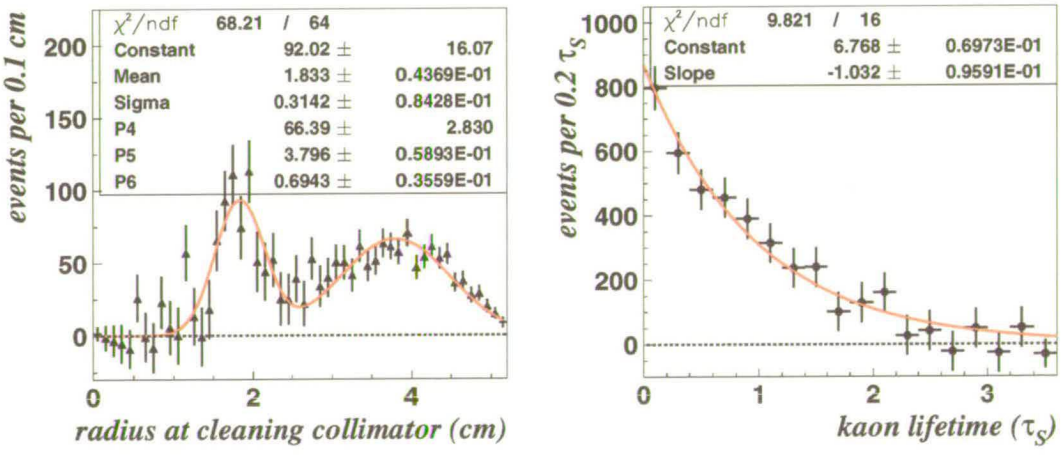

Figure 7.16: $K^0 \to \pi^+\pi^-$ events with $p_T'^2 > 200$ (MeV/c)^2. Left: the extrapolated position of the kaon at the cleaning K_L collimator. A peak is found around 1.83 cm, corresponding to kaons produced on this collimator. The secondary peak is due to kaons produced in the final collimator. Right: the reconstructed kaon lifetime of the regenerated kaons. This distribution has been fitted to an exponential function: $\exp(\text{Constant} + \text{Slope} * x)$. The lifetime of these events is $t_K = 1/(1.03 \pm 0.10)\ \tau_S = (0.97 \pm 0.09)\ \tau_S$.

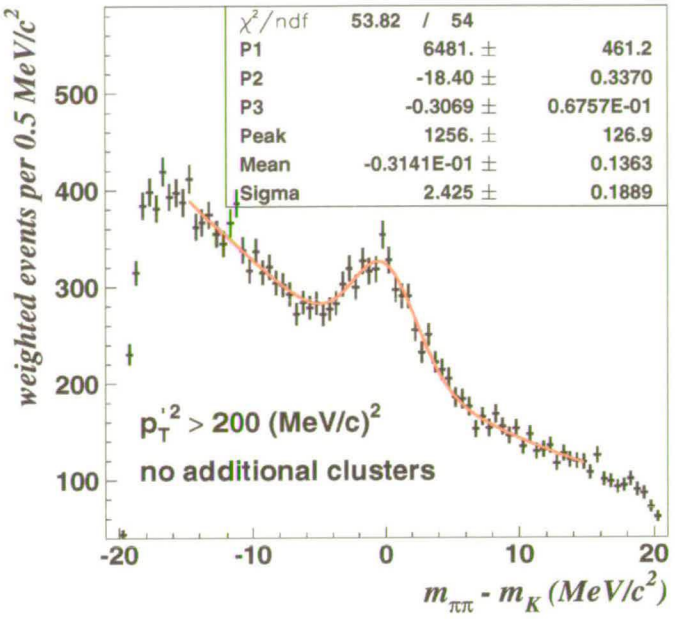

Figure 7.17: Events from the K_L beam with $p_T'^2 > 200$ $(MeV/c)^2$, after events with additional activity in the LKR have been rejected. The distribution has been fitted to the sum of a parabola and a Gaussian. The number of events in the Gaussian (labelled 'Peak') corresponds to the number of events produced by the collimator scattering.

The correction on **R** due to the regeneration on the collimators in the K_L beam is:

$$\boxed{\Delta\mathbf{R} = (-11.3 \pm 3.0) \times 10^{-4}} \tag{7.33}$$

7.10 Neutral Background

A $K_L \to 3\pi^0 \to 6\gamma$ decay may be misidentified as a $K_L \to \pi^0\pi^0$ decay if two of the photons do not hit the detector. There is no significant background for $K_S \to \pi^0\pi^0$ events.

To determine the amount of $K_L \to 3\pi^0$ events in the $K_L \to \pi^0\pi^0$ sample the $R_{ellipse}$ variable is used as defined in equation (6.11). Figure 6.15 in the previous chapter shows the distribution of $R_{ellipse}$ for K_L and K_S events.

The following procedure is used to determine the amount of background decays:

- The $R_{ellipse}$ distribution for $K_S \to \pi^0\pi^0$ events is corrected for the tagging dilution.

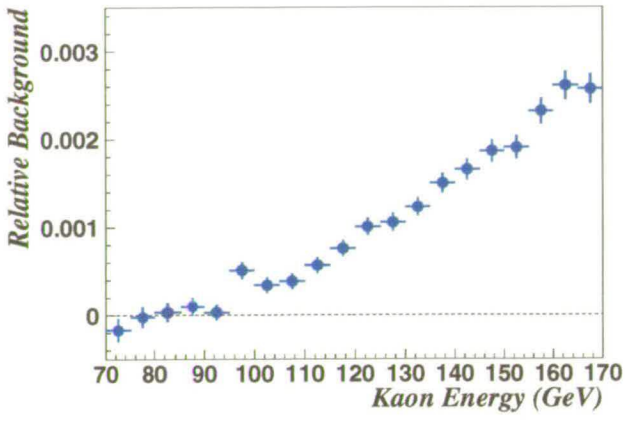

Figure 7.18: The amount of $K_L \to 3\pi^0$ background, relative to the amount of $K_L \to \pi^0\pi^0$, in each kaon energy bin.

- The distribution of $K_S \to \pi^0\pi^0$ events is normalised such that the number of decays in the signal region ($R_{\text{ellipse}} < 1.5$) is the same as for the weighted $K_L \to \pi^0\pi^0$ events.
- The difference between the normalised distributions in the control region ($4 < R_{\text{ellipse}} < 13$) are then considered to be from $K_L \to 3\pi^0$ decays.
- The difference is extrapolated to the signal region using an extrapolation factor of (1.2 ± 0.2) which was determined by a Monte Carlo sample of $K_L \to 3\pi^0$ events.

In total (264 ± 7) weighted $K_L \to 3\pi^0$ decays are found in 287651 weighted $K_L \to \pi^0\pi^0$ decays, corresponding to a background of $(9.2 \pm 1.5) \times 10^{-4}$.

Figure 7.18 shows the relative amount of $3\pi^0$ background subtracted in each kaon energy bin. It can be seen that the amount of background increases with energy. This is because $K_L \to 3\pi^0$ events with higher energy have a higher Lorentz boost. This means that these are more likely to have photons within the beam pipe at the LKR position, which are not detected. If two of the photons are not detected the $K_L \to 3\pi^0$ decay may be reconstructed as a $\pi^0\pi^0$ decay.

The number of weighted $K_L \to 3\pi^0$ is subtracted for the $K_L \to \pi^0\pi^0$ mode decays in each bin of kaon energy. If the number of $K_L \to 3\pi^0$ decays in a particular energy bin is calculated to be less than zero no events are subtracted.

The resulting correction to $\mathbf{R}$ for $3\pi^0$ background in $K_L \to \pi^0\pi^0$ decays is:

$$\boxed{\Delta\mathbf{R} = (-7.4 \pm 2.0) \times 10^{-4}} \tag{7.34}$$

7.11 Accidental Activity

Accidental activity occurs in the detector as a result of decays from the K_L and K_S beams. If another decay is concurrent with a $\pi^+\pi^-$ or $\pi^0\pi^0$ event, it may cause the event to be misreconstructed and rejected from the analysis. Due to the simultaneous nature of the beams, both K_L and K_S decays are sensitive to accidental activity from both beams. Therefore, as a first approximation, the measurement of **R** is independent of accidental activity. However there may be small residual effects from differences in instantaneous beam intensity and the small geometrical and kinematic differences between the two beams.

To study the effects of accidental activity, 'random events' are recorded in proportion to the instantaneous beam intensity (see section 3.3.5).

During the data reprocessing the random events are overlaid onto events with $\pi^0\pi^0$ or $\pi^+\pi^-$ triggers. All of the $\pi^0\pi^0$ events and a pre-selected 30% of $\pi^+\pi^-$ events were overlaid. The data with random events overlaid is equivalent to data taken with twice the beam intensity. The difference between the data with and without random events overlaid indicates the sensitivity of the measurement of **R** to accidental activity.

One problem with this method, is that the overlaid data is also equivalent to a doubling of detector noise. As was discussed in section 6.4.7, one of the reasons for the high number of drift chamber overflow conditions may be due to noise effects. In this analysis, random events that themselves contain an overflow condition, or cause an overflow condition are not considered. To study the effects of noise in more detail it is proposed to overlay random events onto Monte Carlo events, which are free of noise effects.

In this analysis the overlaid data is used to correct **R** for accidental activity which is proportional to the beam intensity. Then an additional error is added to **R** to account for noise and other effects which are not proportional to beam intensity.

7.11.1 Beam Related Activity

The accidental activity proportional to the beam intensity is studied by calculating the number of events selected by the analysis cuts, before and after the data is overlaid with random events.

There are four effects which change the number of events accepted:

1. **Losses**. If accidental particles are incident on the detector at the same time as a real $\pi^+\pi^-$ or $\pi^0\pi^0$ event, the original event may be misreconstructed, and rejected by one of the analysis cuts. This causes up to 8% of events to be rejected.

For $\pi^+\pi^-$ decays the main losses are due to muons which are reconstructed in time with the event. Other significant losses are due to the cuts on $E_{\rm LKR}/p$ and $m_{\pi^+\pi^-}$. For $\pi^0\pi^0$ decays the losses are due to additional clusters in the LKR which change the values of reconstructed quantities. The main losses are due to the cuts on kaon lifetime and $R_{\rm ellipse}$.

2. **Gains**. To a lesser extent (up to 1.6%), the accidental activity causes events to be added to the samples.

3. **Weight Shifts**. The accidental activity can cause the kaon lifetime to be misreconstructed. For K_L events this causes the weight of the event to change.

4. **$K_L \leftrightarrow K_S$ transitions**. Accidental activity may cause the reconstructed event time to change causing the tagger identification to change from K_L to K_S or vice-versa. This only happens to a very small number of events. As tagging effects are corrected separately, this effect is not taken into account here.

The change in the number of events in each decay mode can be written as [34]:

$$\delta = \frac{\Sigma_i(w_i')_{\rm gains} - \Sigma_i(w_i)_{\rm losses} + \Sigma_i(w_i' - w_i)_{\rm commons}}{\Sigma_i(w_i)_{\rm commons} + \Sigma_i(w_i)_{\rm losses}} \tag{7.35}$$

where w_i is the weight of the original event and w_i' is the weight of the event after the overlay. For K_S events the weights are all identically 1. The number of 'common' events is the number of events overlaid minus the losses.

Table 7.2 summarises the numbers of overlaid events used along with the numbers of events gained and lost in each mode. The correction to the measured value of **R** in a given energy bin is:

$$\frac{(1+\delta_S^{00})/(1+\delta_L^{00})}{(1+\delta_S^{+-})/(1+\delta_L^{+-})} \tag{7.36}$$

where δ is calculated for that energy bin.

The values of δ are calculated for each decay mode and in each energy bin. The resulting correction to **R** due to accidental activity is:

$$\Delta\mathbf{R} = (+0.8 \pm 6.5) \times 10^{-4} \tag{7.37}$$

This result confirms that the measurement of **R** is insensitive to accidental effects proportional to the beam intensity.

7.11.2 Noise Effects

The sensitivity of the measurement of **R** to noise effects cannot yet be reliably calculated. In order to estimate a limit of the noise effects on **R** the following pieces of information are considered:

mode	events	gains	losses	δ
$K_S \to \pi^0\pi^0$	2443584	15608	166028	$(-5.77 \pm 0.02)\%$
$K_L \to \pi^0\pi^0$	1273210	20932	99134	$(-5.69 \pm 0.04)\%$
$K_S \to \pi^+\pi^-$	1521615	1661	117247	$(-7.05 \pm 0.02)\%$
$K_L \to \pi^+\pi^-$	821956	1516	62938	$(-6.97 \pm 0.04)\%$

Table 7.2: The numbers of events gained and lost after the overlay of the random events.

- The differential effect of accidental activity between K_L and K_S decays is about 1% (see table 7.2).
- If the effect of the drift chamber overflow condition is considered, the difference in event losses between $\pi^+\pi^-$ and $\pi^0\pi^0$ events is $< 2.5\%$ [63].
- The detector noise does not change by more than a factor of 2 as a function of time.

These suggest that the effect of noise on the measurement of **R** is small. A conservative error on **R** has been estimated as a bound on these effects [63]:

$$\Delta\mathbf{R} < 10 \times 10^{-4} \tag{7.38}$$

7.11.3 Correction to R for Accidental Activity

The total correction applied to **R** for accidental and noise effects is the sum of the values in equations (7.37) and (7.38). The uncertainties are added in quadrature to give:

$$\boxed{\Delta\mathbf{R} = (+0.8 \pm 12.0) \times 10^{-4}} \tag{7.39}$$

7.12 Energy Scale

The energy scale of the detector measures the response of the detector to particles of different energies. Uncertainties in the knowledge of the energy scale of the drift chambers and the LKR limit the accuracy of the measurement of **R**.

Known quantities are first used to fix the energy scale of the drift chambers and the LKR. For the drift chambers the mass of the kaon is used and for the LKR the z-position of the AKS detector is used. Further studies are then made to investigate the stability of the detector response and limit the uncertainty on the value of **R**.

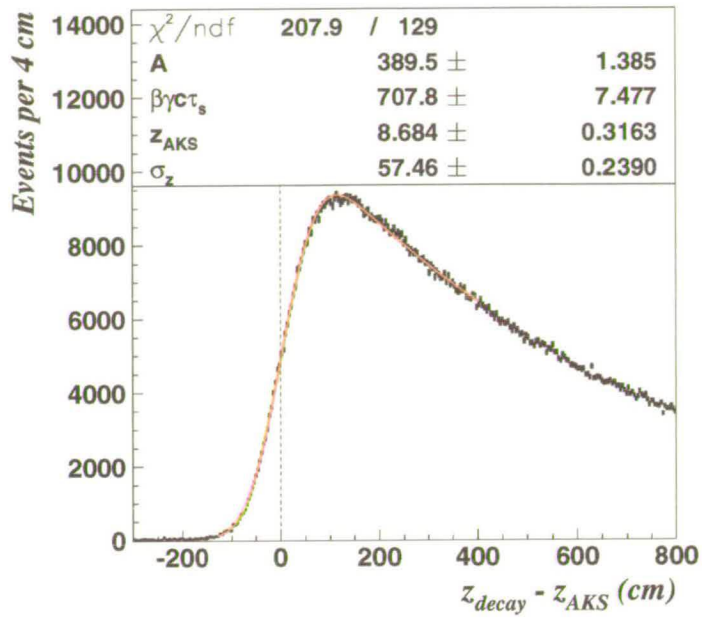

Figure 7.19: The z-position of the decay vertex for $K_S \to \pi^0\pi^0$ events *before* any energy-scale correction is applied. A correction has been made for tagging dilution effects. The histogram has been fitted to the function $f(z)$ in equation (7.42). The reconstructed position of the AKS detector is displaced 8.7 cm from its true position, due to the mismeasurement of the energies in the LKR. The resolution on the measurement of z_{decay} is $\sigma_z \simeq 60$ cm.

7.12.1 AKS Position Fitting

The position of the AKS detector (as described in section 3.5) can be used to investigate the response of the detector at different energies. For example for $K^0 \to \pi^0\pi^0 \to 4\gamma$ decays, the distance (d) of the decay vertex from the LKR, can be related to the energies of the photons measured using equation (4.8):

$$d^2 = \sum_{i=1}^{4} \sum_{j=i+1}^{4} \frac{E_{\gamma^i} E_{\gamma^j} \mathbf{r}_{ij}^2}{m_{\text{K}}^2} \tag{7.40}$$

The ratio of the true energy of the photons ($E_{\gamma^i}^{\text{true}}$) to the energy measured in the calorimeter ($E_{\gamma^i}^{\text{meas}}$) can then be related to the longitudinal distance scale:

$$\frac{E_{\gamma^i}^{\text{true}}}{E_{\gamma^i}^{\text{meas}}} = \frac{d^{\text{true}}}{d^{\text{meas}}} \tag{7.41}$$

Recall that the AKS detector is used to reject K_S events where the decay occurs upstream of the AKS position. Therefore the distribution of the longitudinal decay

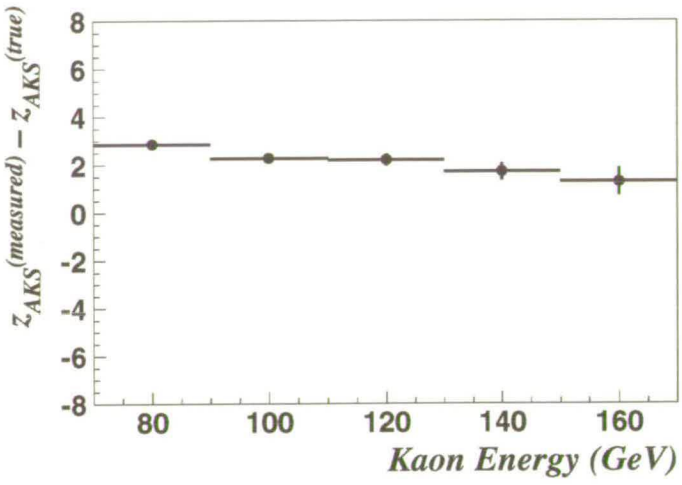

Figure 7.20: The reconstructed position of the AKS detector using $K^0 \to \pi^+\pi^-$ decays, after the corrections to the momenta discussed in the text have been applied.

vertex (z_{decay}) for $K_S \to \pi^0\pi^0$ events should be an exponential starting at $z_{\text{decay}} = z_{\text{AKS}}$, convoluted with the resolution of the measurement of z_{decay}. Assuming the resolution of the measurement of z_{decay} is Gaussian, the distribution of the decay vertices can be written as:

$$f(z_{\text{decay}}) = A \cdot \int_{z_{\text{AKS}}}^{\infty} \exp\left(\frac{z' - z_{\text{AKS}}}{\beta\gamma c\tau_S}\right) \cdot \exp\left(\frac{-(z_{\text{decay}} - z')^2}{2\sigma_z^2}\right) \mathrm{d}z' \qquad (7.42)$$

Figure 7.19 shows the fit of the above function to the distribution of the decay vertices for $K_S \to \pi^0\pi^0$ events. The fitted position of the AKS is at $z = (8.7 \pm 0.3)$ cm from the true position of the AKS counter. Using equation (7.41), the energy scale factor is:

$$E_{\gamma^i}^{\text{true}} / E_{\gamma^i}^{\text{meas}} = 1.00076 \pm 0.00003 \qquad (7.43)$$

where $d^{\text{true}} = (z_{\text{LKR}} - z_{\text{AKS}}) = 11501.0$ cm has been used as the true distance between the AKS crystal and the position of the shower maximum in the LKR.

In the charged decay mode the reconstructed position of the decay vertex also depends on the measured momenta of the pions. Therefore the AKS position fit may also be used to correct or check the measured momenta of tracks in the drift chambers.

7.13 Charged Energy Scale

The reconstructed momenta of tracks in the drift chambers are sensitive to three effects:

1. The magnetic field in the experiment. The reconstruction of the drift chamber data uses a map of the magnetic field which was taken before the 1998 run. Any difference between this mapping of the field and the actual field at the time of the data-taking will cause the momenta to be misreconstructed.

2. The transverse scale of the drift chambers, *i.e.* how accurately the x and y positions of the tracks have been measured. The data has been calibrated for the transverse scale using constants which were derived from a special data set taken with the spectrometer magnet turned off.

3. The longitudinal scale of the drift chambers, *i.e.* how accurately the longitudinal distances between the drift chamber planes are known.

The energy scale of the drift chambers is fixed by using the reconstructed mass of charged pions pairs ($m_{\pi^+\pi^-}$). The average reconstructed value of $m_{\pi^+\pi^-}$ should be the mass of the kaon, m_{K^0}.

In appendix A it is shown how the scale factor depends on the measured value of $m_{\pi^+\pi^-}$. In the 1998 data set, six separate periods were identified, each requiring a separate scale factor to correct the value of $m_{\pi^+\pi^-}$ [52]. Each of these periods can be identified with a change in the magnetic field conditions, for example when the magnetic field was reversed, or switched off for an η run.

After applying the corrections to the track momenta, the AKS position fit was made as a cross check. Figure 7.20 shows the fitted position of the AKS scintillator, with respect to its true position for $\mathrm{K}^0 \to \pi^+\pi^-$ decays. It can be seen that the position of the reconstructed position of the AKS detector depends on the kaon energy. As the effects of the magnetic field and the transverse scale of the drift chambers have been corrected, this effect is due to the uncertainty in the longitudinal scale of the drift chambers.

An independent calculation of the correction to $\mathbf{R}$ due to the uncertainty in the charged energy scale and the remaining effect of the longitudinal scale gave [30]:

$$\boxed{\Delta\mathbf{R} = (+2 \pm 2) \times 10^{-4}} \tag{7.44}$$

7.14 Neutral Energy Scale

The aim of the neutral energy scale analysis is to estimate the uncertainty on $\mathbf{R}$ due to the reconstruction of the photon energies in the LKR. There are two main classes of uncertainties affecting the measurement of the clusters energies in the LKR calorimeter:

Source	Uncertainty on $\mathbf{R}$ (10^{-4})
Energy/Distance scale	± 4
Non-Linear effects	± 5
Transverse scale	± 3
Reconstruction uncertainties	± 7
Total	± 10

Table 7.3: Uncertainties on $\mathbf{R}$ due to the response of the LKR.

1. The knowledge of the transverse and longitudinal scales. Equation 7.40 shows that the cluster energies depend on both transverse and longitudinal lengths: $\mathbf{r}_{ij}$ and d respectively.

2. The knowledge of how photons interact in the detector. The reconstruction program is modelled on a GEANT simulation of the detector. If the actual response of the calorimeter is different from the simulation, this could cause the energy of the cluster to be misreconstructed. This includes non-linear effects, which arise if the reconstructed energy of a cluster is not directly proportional to the true energy of the photon.

To investigate these effects, three techniques have been used:

- **Ke3 decays.** Ke3 decays are recorded at the same time as $\pi^+\pi^-$ and $\pi^0\pi^0$ decays. As $E_{\rm LKR}/p \simeq 1$ for electrons the measured value of the momentum p can be compared to the measured energy $E_{\rm LKR}$.

- **η runs.** As described in sections 3.9.5 and 5.2, η runs were taken periodically throughout the 1998 run. η mesons decay instantaneously and therefore the reconstructed decay vertex of the η decays should be the known target position. The decay modes of the η that were used for this analysis were $\eta \to \gamma\gamma$ and $\eta \to 3\pi^0 \to 6\gamma$

- **AKS position fit.** As described in detail in section 7.12.1 above.

The AKS position fit and the Ke3 data were used to derive corrections to the measured photon energies. These corrections have been applied during the data processing. All three techniques are used to investigate the residual uncertainties on $\mathbf{R}$. These uncertainties are summarised in table 7.3.

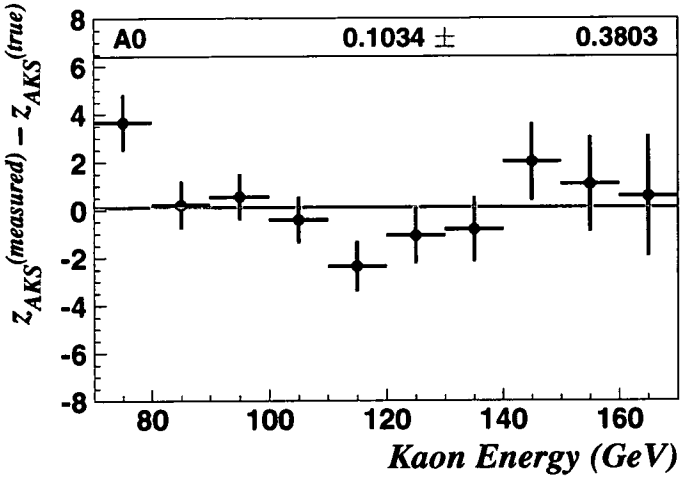

Figure 7.21: The reconstructed position of the AKS detector using $\pi^0\pi^0$ decays, after all the corrections to the energies discussed in the text have been applied. The residual variation of the fitted position of the AKS due to the uncertainty in the energy scale is approximately ±3 cm.

7.14.1 Linear Effects

Figure 7.21 shows the measured position of the AKS with respect to its true position, using the data with energy scale corrections applied. The variation of the fitted position is ±3 cm. An additional uncertainty in the distance $d^{\text{true}} = (z_{\text{LKR}} - z_{\text{AKS}})$ is from the uncertainty on the position of the shower maximum within the LKR which is known to ±2 cm. The total uncertainty of the energy scale (or equivalently on the longitudinal scale) is therefore $\pm 4 \times 10^{-4}$, corresponding to an uncertainty on **R** of $\pm 4 \times 10^{-4}$ [62].

The uncertainty of **R** due to the transverse scale is estimated to be $\pm 3 \times 10^{-4}$ [62].

7.14.2 Non-Linear Effects

Figure 7.22 shows the E_{LKR}/p distribution for electrons from Ke3 events. It can be seen that the value of E_{LKR}/p is not constant as a function of the electron energy. This implies that there is a non-linear relationship between the reconstructed energy of the cluster and the true energy of the photon. The observed variation of E_{LKR}/p has been used to correct the photon energies. After this correction has been applied, it is estimated that the total uncertainty on **R** due to non-linear effects is $\pm 5 \times 10^{-4}$ [62].

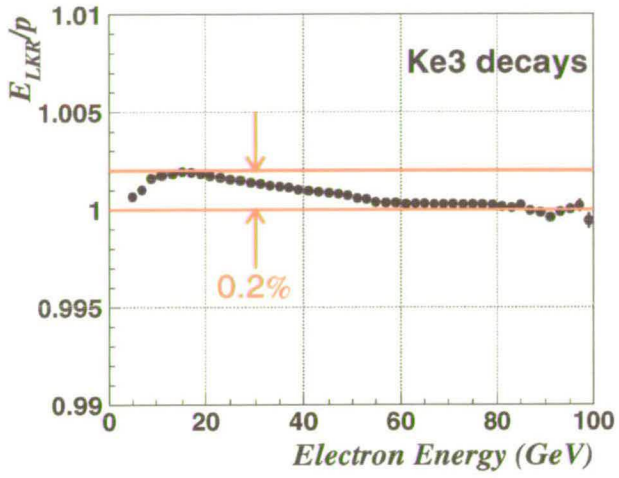

Figure 7.22: The E_{LKR}/p distribution for electrons from Ke3 decays. The distribution shows a variation of 0.2% over the energy range of the electrons.

7.14.3 Reconstruction Uncertainties

After applying the energy scale and non-linear correction discussed above, the response of the LKR calorimeter is still not fully understood. In particular the response of the calorimeter to overlapping clusters, the loss of energy due to the hole for the beam pipe and the tails of the energy response distribution.

The Ke3 data and the η data are used to investigate these effects. The analysis is described in detail in [62]. This analysis estimates that the uncertainty on **R** due to the reconstruction uncertainties is $\pm 7 \times 10^{-4}$.

7.14.4 Correction to R for the Neutral Energy Scale

Table 7.3 summarises all the uncertainties on **R** due to the LKR energy scale. These uncertainties are mainly independent as different data sets have been used to derive them. The uncertainties are therefore combined in quadrature. The total correction to **R** for the energy scale is:

$$\boxed{\Delta \mathbf{R} = (0 \pm 10) \times 10^{-4}} \tag{7.45}$$

7.15 Acceptance

As discussed in chapter 5, the effect of the geometrical acceptance and the efficiency of the selection cuts is, to first order, symmetric between $\mathrm{K_L}$ and $\mathrm{K_S}$ decays. However as

the geometry of the K_L and K_S beamlines is different, the geometrical acceptance of detector for a particular final state ($\pi^+\pi^-$ or $\pi^0\pi^0$) may vary for K_L and K_S decays. Additionally some of the selection cuts may not select K_L and K_S symmetrically. These effects may bias the measured value of **R**.

To calculate the effect of the detector acceptance and the selection cuts on the measurement of **R**, Monte Carlo samples of all four $\mathcal{R}e(\epsilon'/\epsilon)$ modes have been generated. The generation of the Monte Carlo samples is discussed further in the following subsection. The number of generated events can be used to calculate an input value of the double ratio, $\mathbf{R}_{MC}$. The Monte Carlo samples are analysed using the same selection cuts as the data, with a few important exceptions described below. The difference between the input value $\mathbf{R}_{MC}$ and the value for **R** calculated using the selected Monte Carlo events is then applied as a correction to **R**.

7.15.1 Monte Carlo

A Monte Carlo generation program has been written to generate simulated events in the NA48 experiment [58].

The momentum (p) of the kaons is generated according to the following differential formula, giving the number of kaons produced (N) per unit momentum and per unit solid angle:

$$\begin{aligned}\frac{\mathrm{d}^2N}{\mathrm{d}p\,\mathrm{d}\Omega} &= \frac{\eta p^2}{4p_0}\left[1.30\cdot\exp\left(-8.5\,\frac{p}{p_0}-3.0\,p^2\Theta^2\right)+4.35\cdot\exp\left(-13\,\frac{p}{p_0}-3.5\,p^2\Theta^2\right)\right] \\ &\quad\times\left[\exp\left(-4.2+0.0053\,p\right)+0.016\right] \qquad (7.46)\end{aligned}$$

Here $p_0 = 450$ GeV/c is the momentum of the SPS protons on the target and Θ is the angle at which the protons are incident on the target. $\Theta = 2.4$ mrad for the K_L target and $\Theta = 4.2$ mrad for the K_S target. This parameterisation is based on measurements recorded in [4] and adapted to agree with measurements made in 1995 using the NA48 apparatus [40]. The kaon decays are generated to include the effect of interference between the K^0 and $\overline{K^0}$ particles produced in the target.

The kaons are generated evenly over the surface of the targets. The direction and momentum of the generated kaons is used to select kaons that pass through the collimators. The kaons decay to either a $\pi^+\pi^-$ or $\pi^0\pi^0$ final state (as requested) at a position in accordance with an exponential decay distribution. Neutral pions decay either as $\pi^0 \to \gamma\gamma$ or $\pi^0 \to \gamma e^+e^-$. The charged pions may decay as $\pi^\pm \to \mu^\pm\nu_\mu$. Additionally the photons are allowed to convert: $\gamma \to e^+e^-$ whilst transversing a piece of material in the detector.

The decay products of the kaons are tracked through the detector using an accurate map of the magnetic field. The response of the subdetectors to the decay products is

modelled either using a parameterisation of the data, or using a GEANT simulation. The positions of the track hits in the drift chambers are simulated by using a smearing of the generated positions with a σ of 103 μm. The smearing function is based on a Gaussian distribution, but with non-Gaussian tails to take into account the effects of the particles scattering on the wires (or other material) in the chambers.

The response of the LKR is simulated using GEANT. An accurate description of the structure of the calorimeter including the vessel containing the calorimeter, the internal electrode structure and the spacer plates as well as the liquid krypton itself is used in the simulation. This information has been used to make a library of showers in the calorimeter for incident photons, electrons and charged pions of different energies. The Monte Carlo program selects showers from the library depending on the energy and type of particle incident on the LKR.

Finally the response of the Muon Veto detector is simulated for muons. The generated impact point of the muon is used to calculate the times at which the photons arrive at the photomultipliers. These times are smeared by a Gaussian function with a σ of 1.5 ns.

The tagger, the AKS and the trigger systems are not simulated. The corrections to $\mathbf{R}$ for these effects can be more accurately calculated using the data directly. The effect of accidental activity is not currently simulated in the Monte Carlo either.

Monte Carlo events are generated over the kaon momentum range 50 GeV $< p <$ 190 GeV and over the decay range of -210 cm $< z_{\text{decay}} <$ 4190 cm with respect to the AKS position. The Monte Carlo events are reconstructed using the standard reconstruction programs (as described in section 4.6). The events are then written into the SuperCompact data format.

7.15.2 The Acceptance of the Double Ratio

The Monte Carlo samples are analysed using the same selection cuts as the data with the following exceptions:

1. As the tagger is not simulated in the Monte Carlo, K_L and K_S decays are differentiated using the target the simulated decay originated from.

2. In order to simulate the effect of the AKS detector, K_S events are selected if the *true* position of the decay vertex is downstream of the AKS position. This is equivalent to simulating a fully efficient AKS detector. As with the data events, K_L Monte Carlo events are selected if the position of the *reconstructed* decay vertex (z_{decay}) satisfies $z_{\text{decay}} > z_{\text{AKS}}$.

3. There is no simulation of timing effects in the Monte Carlo, therefore all cuts

mode	acceptance
$K_S \to \pi^+\pi^-$	$(53.72 \pm 0.04)\%$
$K_L \to \pi^+\pi^-$	$(54.67 \pm 0.27)\%$
$K_S \to \pi^0\pi^0$	$(25.41 \pm 0.16)\%$
$K_L \to \pi^0\pi^0$	$(25.36 \pm 1.14)\%$

Table 7.4: The acceptance of the four $\mathcal{R}e(\epsilon'/\epsilon)$ decay modes over the energy range $70 < E_K/\text{GeV} < 170$ and the lifetime range $0 < t_K/\tau_S < 3.5$.

on time are ignored. The one exception to this is the cut used to reject muons. The time of the muon hits in the MUV is compared to the simulated event time of 0.

4. The cut on E_{LKR}/p is not made in the $\pi^+\pi^-$ selection. The simulation of the LKR response to hadronic particles is difficult. The distribution of E_{LKR}/p is intrinsically symmetric for both K_L and K_S decays, therefore omitting this cut does not bias the value of $\Delta\mathbf{R}$ being calculated.

The acceptance ($a(E_K)$) of a given decay mode in a given energy and lifetime range can be defined as:

$$a(E_K) = \frac{N_{MC}(E_K)\,(\text{accepted})}{N_{MC}(E_K)\,(\text{generated})} \tag{7.47}$$

where N_{MC}(accepted) is the number of Monte Carlo events that pass all the selection criteria (including the cuts on energy and lifetime), and N_{MC}(generated) is the number of Monte Carlo events generated in the energy and lifetime range. (In the case of K_L events, N_{MC} represents the sum of the weights of the events.)

Figure 7.23 shows the acceptance of the four $\mathcal{R}e(\epsilon'/\epsilon)$ decay modes in 5 GeV bins of kaon energy, over the lifetime range $0 < t_K/\tau_S < 3.5$. Table 7.4 gives the acceptances of the four $\mathcal{R}e(\epsilon'/\epsilon)$ decay modes integrated over kaon energy range $70 < E_K/\text{GeV} < 170$. It can be seen that the acceptance for $\pi^+\pi^-$ events is generally higher than for $\pi^0\pi^0$ events, and the acceptance is similar for K_L and K_S decays to the same final state.

The acceptance of the double ratio ($a_{\mathbf{R}}(E_K)$) in one kaon energy bin can be defined as:

$$a_{\mathbf{R}}(E_K) = \frac{a_L^{00}(E_K)/a_S^{00}(E_K)}{a_L^{+-}(E_K)/a_S^{+-}(E_K)} \tag{7.48}$$

Figure 7.23 shows the acceptance of the double ratio $\mathbf{R}$ in 5 GeV bins of kaon energy. These values are used to correct the measured values of $\mathbf{R}$. The resulting correction to the double ratio is:

$$\Delta\mathbf{R} = (+24.1 \pm 6.4) \times 10^{-4} \tag{7.49}$$

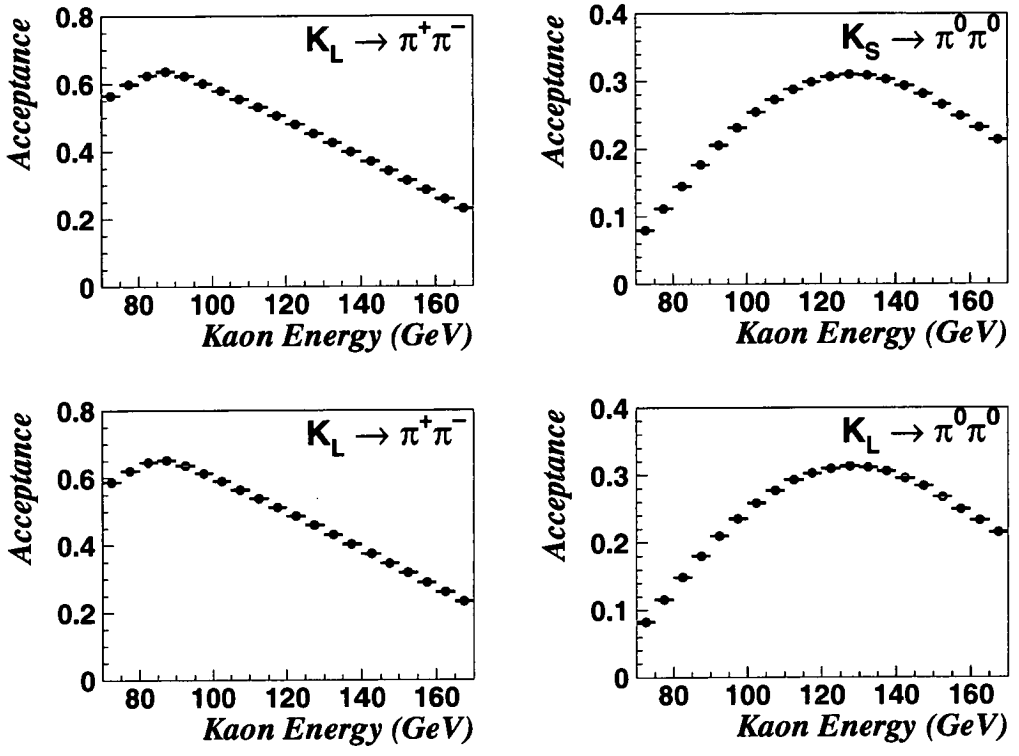

Figure 7.23: The acceptance of the four $\mathcal{R}e(\epsilon'/\epsilon)$ decay modes in 5 GeV energy bins.

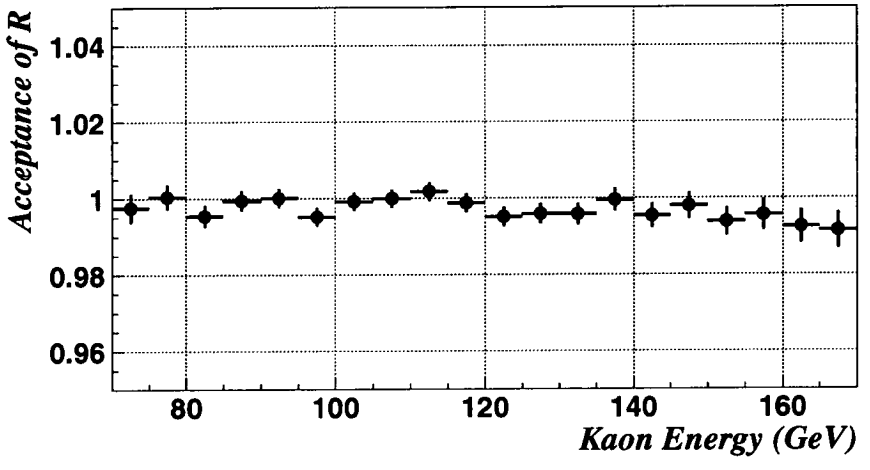

Figure 7.24: The acceptance of **R** in 5 GeV energy bins.

7.15.3 Comparison of Data and Monte Carlo Events

If the Monte Carlo events do not describe the data sufficiently well, the value of the acceptance correction in equation (7.49) may be incorrect. This is particularly true for effects that are not symmetric for K_L and K_S decays, such as the geometry of the beams.

Figures 7.25 to 7.31 on the following pages compare the distributions of selected variables of data to Monte Carlo. In each case the Monte Carlo events are represented by the filled area and the circles are the data. The numbers of Monte Carlo events have been normalised to the number of data events. All of the K_L events are weighted and the distributions have been corrected for tagging effects.

These comparisons are used to estimate the systematic uncertainty on **R** due to the acceptance correction. Two main sources of difference between the data and Monte Carlo are investigated:

1. The difference in the energy spectra between the data and the Monte Carlo.
2. The difference in distributions that depend on the geometry of the beams, such as the radial positions of particles in the sub-detectors and the centre of gravity.

Energy Spectra. Figures 7.25 and 7.26 compare the energy spectra of the kaons for the four decay modes. It can be seen that the spectra in the Monte Carlo differ from those of the data by up to 10%, over the range $70 < E_K/\text{GeV} < 170$. To measure $a(E_K)$ correctly the ratio of the spectra should be a constant. Therefore the Monte Carlo cannot be used to accurately calculate a over the total energy range of $70 < E_K/\text{GeV} < 170$. This is why the acceptance correction, and indeed the entire analysis, is calculated in 5 GeV energy bins.

The uncertainty ($\Delta a(E_K)$) on the calculated acceptance due to the difference of the energy spectra can be related to two quantities. The first is the variation of the acceptance as shown in figure 7.23. The second is the variation of the data energy spectra to the Monte Carlo energy spectra as shown in figure 7.26. In both cases, as the energy range is small, the variations can be considered to be linear. Parameterising the variation of the acceptance by α and variation of the ratio of the energy spectra to be β, the uncertainty on $a(E_K)$ is:

$$\frac{\Delta a(E_K)}{a(E_K)} = \alpha\beta\left(\frac{\Delta E_K}{12}\right)^2 \tag{7.50}$$

where $\Delta E_K = 5$ GeV is the width of the kaon energy bins used. For a detailed proof of this formula see [56].

As an estimate on the maximum uncertainty $\Delta a(E_K)$, two cases are considered:

1. The largest variation in the data–Monte Carlo ratio spectrum is for $K_S \to \pi^+\pi^-$ events with kaon energies around 150−170 GeV. Here the ratio changes by $\sim 6\%$ in 20 GeV corresponding to $\beta \simeq 0.003$ GeV^{-1}. In this range the value of α for the same decay mode is $\alpha \simeq 0.013$ GeV^{-1}. The corresponding uncertainty on $a(E_K)$ is therefore $\Delta a/a \simeq 7 \times 10^{-6}$.

2. The largest variation in the acceptance is for $K_S \to \pi^0\pi^0$ events with kaon energies in the range 70 − 90 GeV. In this range $\alpha \simeq 0.008$ GeV^{-1} and $\beta \simeq 0.002$ GeV^{-1} giving $\Delta a/a \simeq 3 \times 10^{-5}$.

Thus the acceptance, in each energy bin, for each decay mode is always known to $\lesssim 0.3 \times 10^{-4}$.

Geometrical Variables. Figures 7.27 to 7.31 on the following pages compare data and Monte Carlo events for quantities that are sensitive to the geometry of the experiment. The radial positions of the tracks and the photons in the detector depend strongly on the energy of the kaon. Therefore these distributions are compared in bins of kaon energy. In general, there is reasonable agreement between the data and the Monte Carlo events. The most noticeable difference is for the r_{cog} distributions of K_S events.

An independent study has been made to investigate the sensitivity of **R** to the description of the geometry for the Monte Carlo events [35, 64]. In this study the following effects were considered:

1. Re-weighting of the Monte Carlo events in the K_S beam halo, to correct the r_{cog} distributions.

2. Variation of the momentum asymmetry cut.

3. Variation of the cuts on the minimum radius of tracks in the drift chambers and the LKR.

Following the results of this study, an additional systematic error of $\pm 5 \times 10^{-4}$ is added to the acceptance correction, to account for the geometrical description of the experiment in the Monte Carlo program.

7.15.4 Correction to R for the Acceptance

Adding the systematic uncertainty to the correction in equation (7.49), gives a total correction to **R** for the geometric acceptance and the effect of the selection cuts of:

$$\boxed{\Delta \mathbf{R} = (+24.1 \pm 8.1) \times 10^{-4}} \tag{7.51}$$

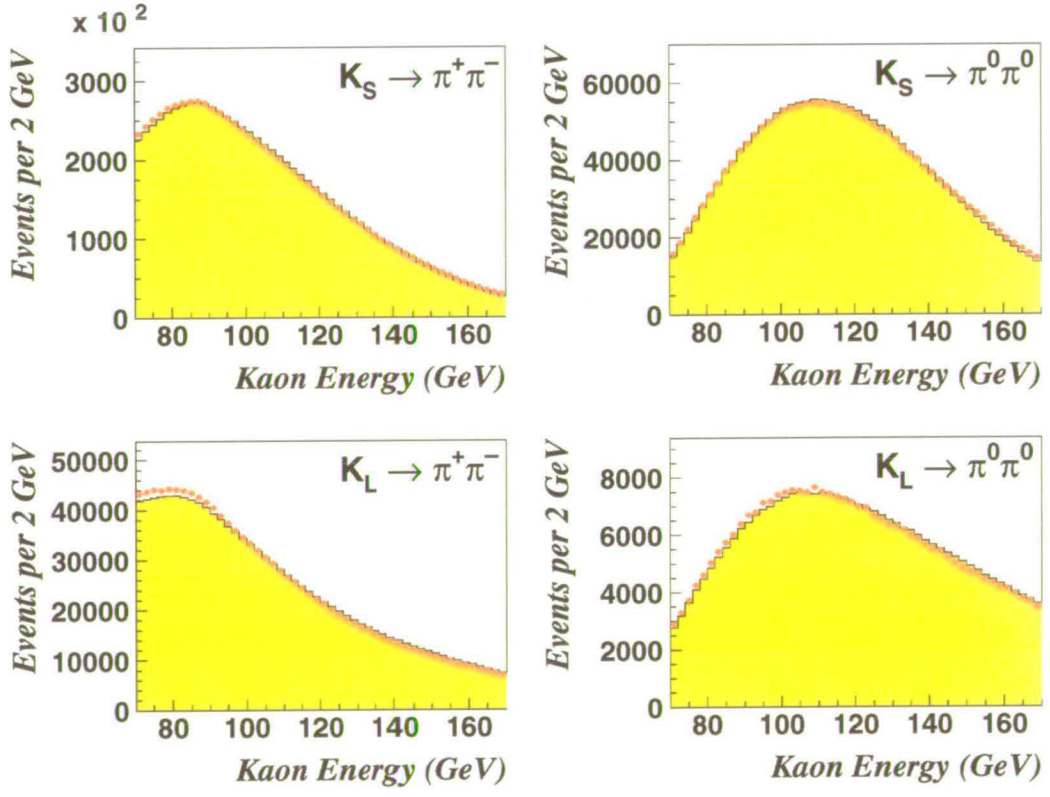

Figure 7.25: Comparison of the kaon energy spectra between data and Monte Carlo events. The data is shown as circles, and the Monte Carlo events are shown as the filled area. The K_L events are weighted and the number of Monte Carlo events is normalised to the number of data events in each decay mode.

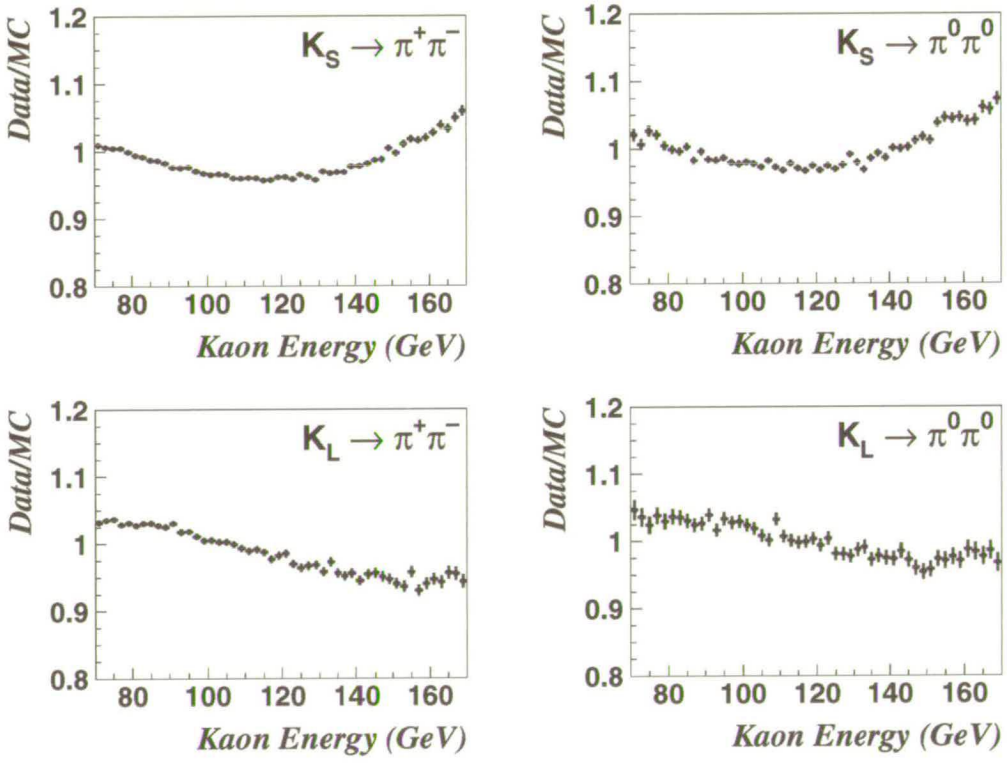

Figure 7.26: Ratio of the kaon energy spectra of data to those of Monte Carlo events.

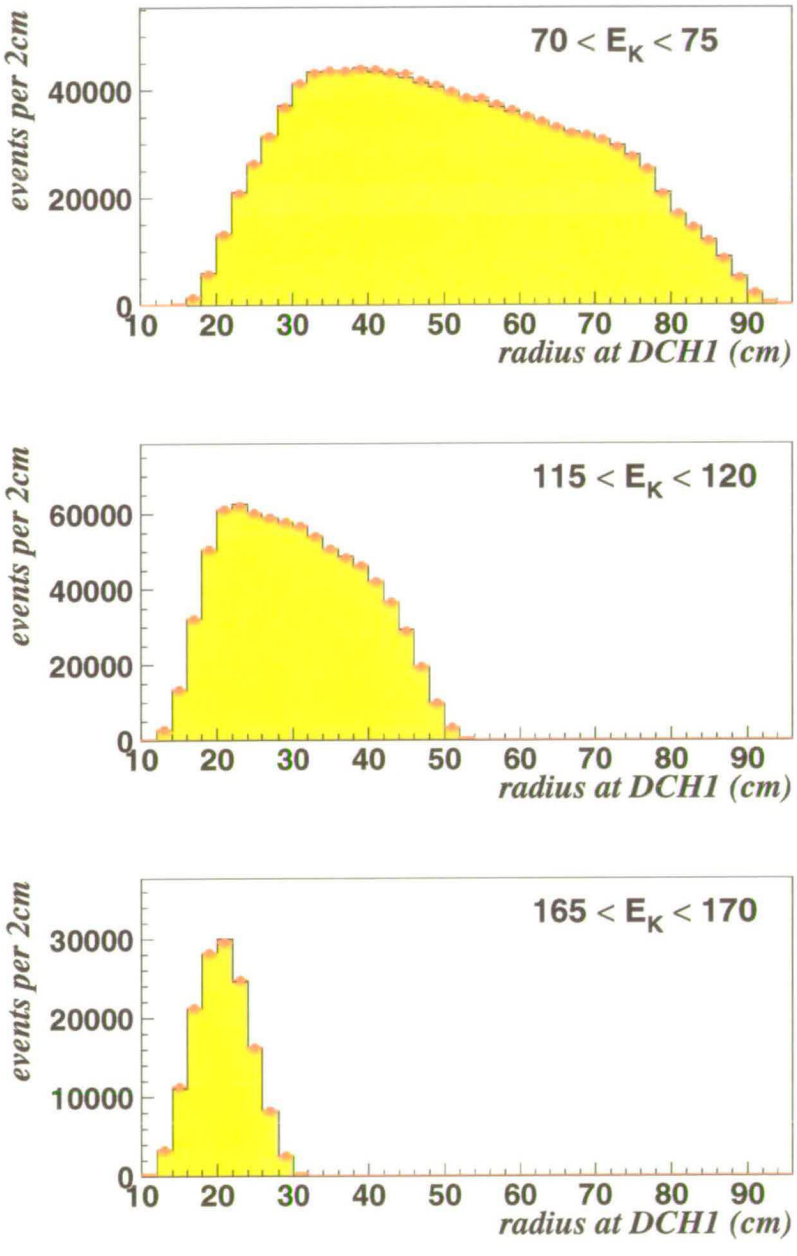

Figure 7.27: The radial position of the tracks in the first drift chamber for $K_S \to \pi^+\pi^-$ events.

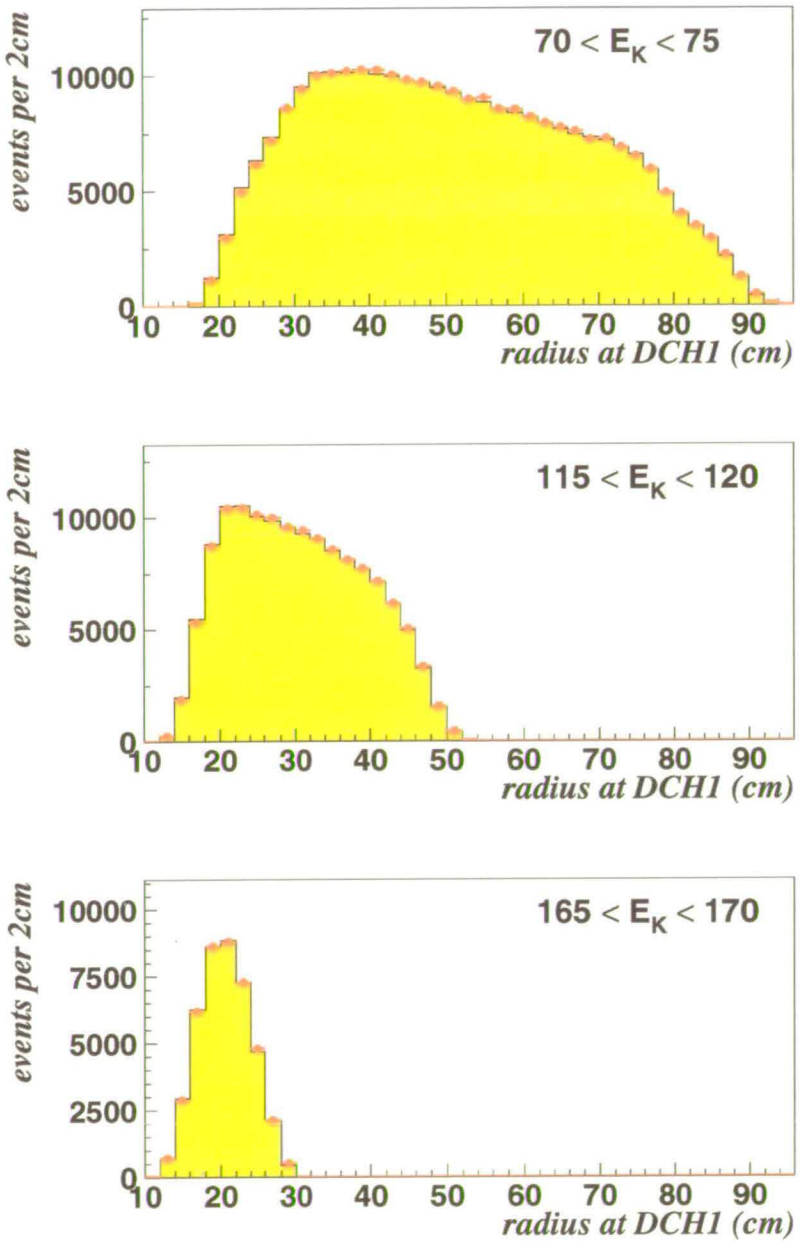

Figure 7.28: The radial position of tracks in the first drift chamber for $K_L \to \pi^+\pi^-$ events.

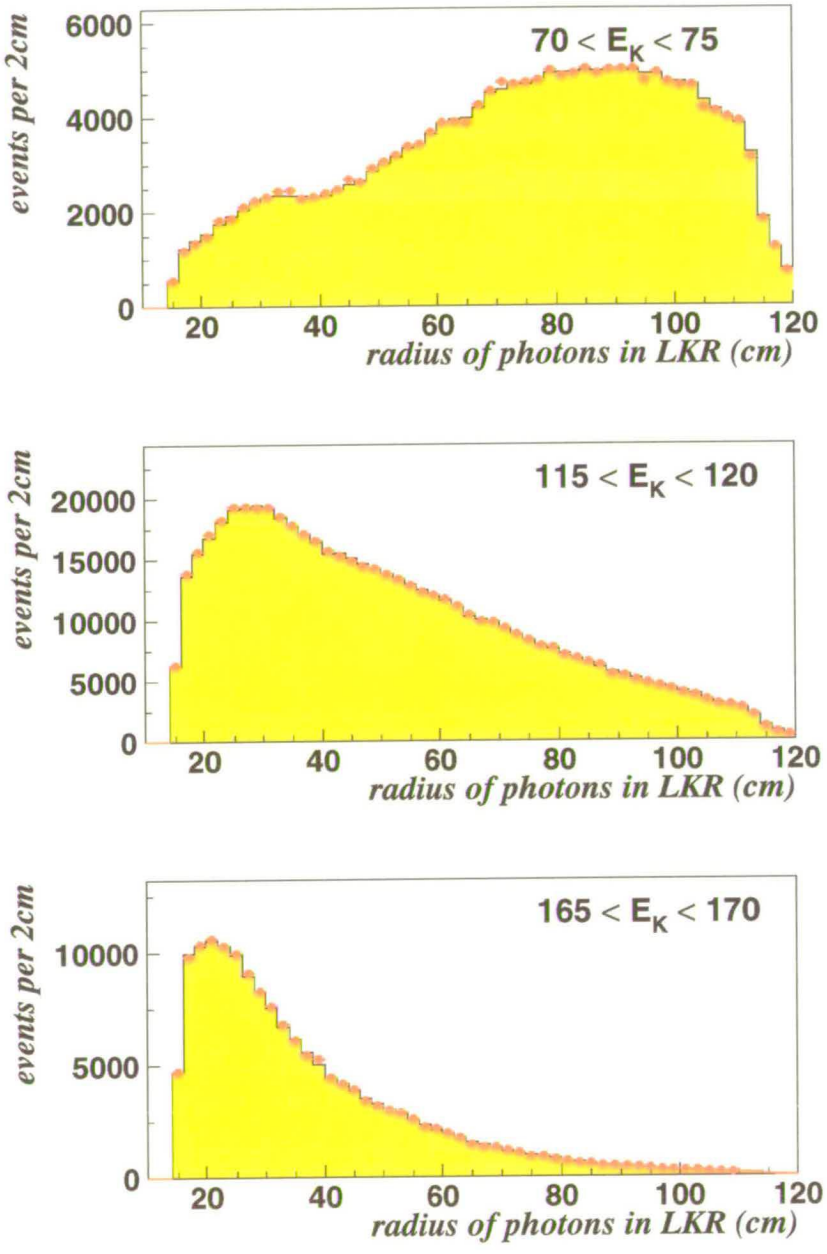

Figure 7.29: The radial position of clusters in the LKR from $K_S \to \pi^0\pi^0 \to 4\,\gamma$ events.

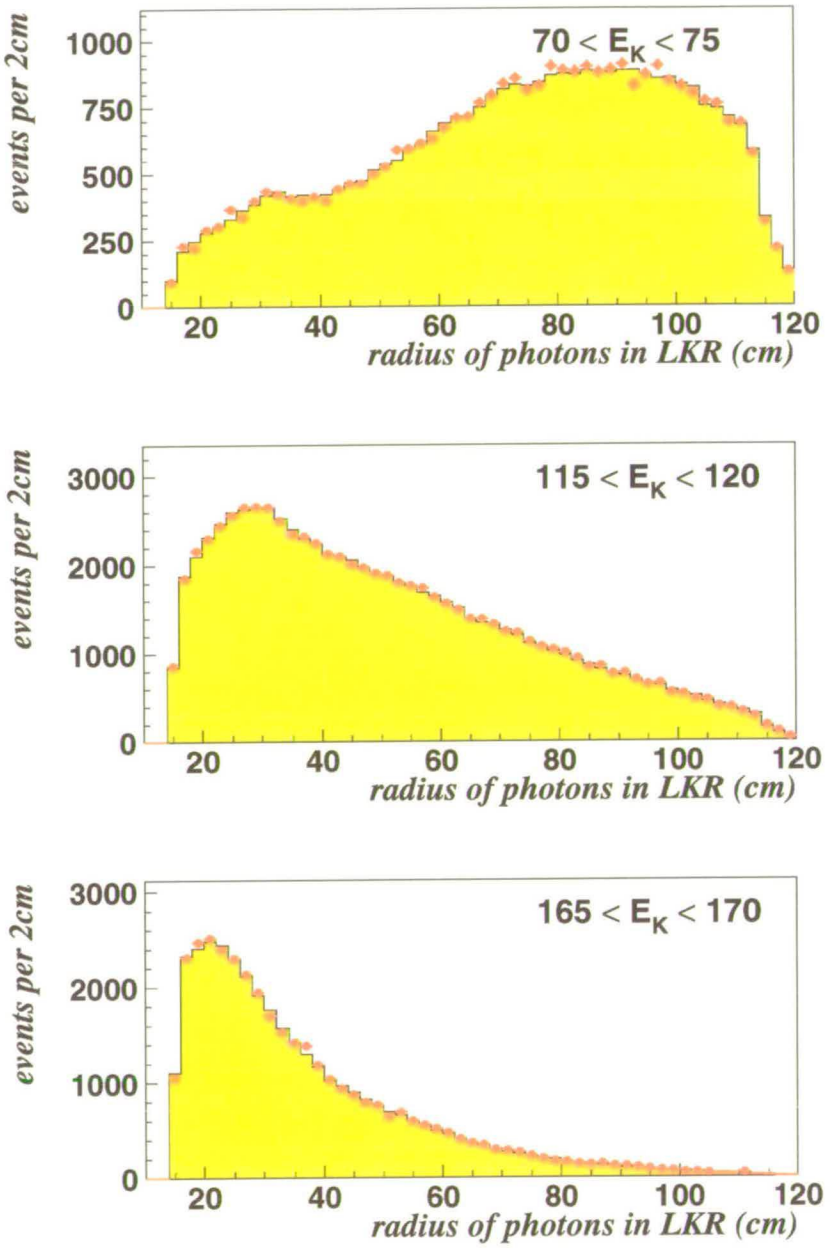

Figure 7.30: The radial position of clusters in the LKR from $K_L \to \pi^0\pi^0 \to 4\,\gamma$ events.

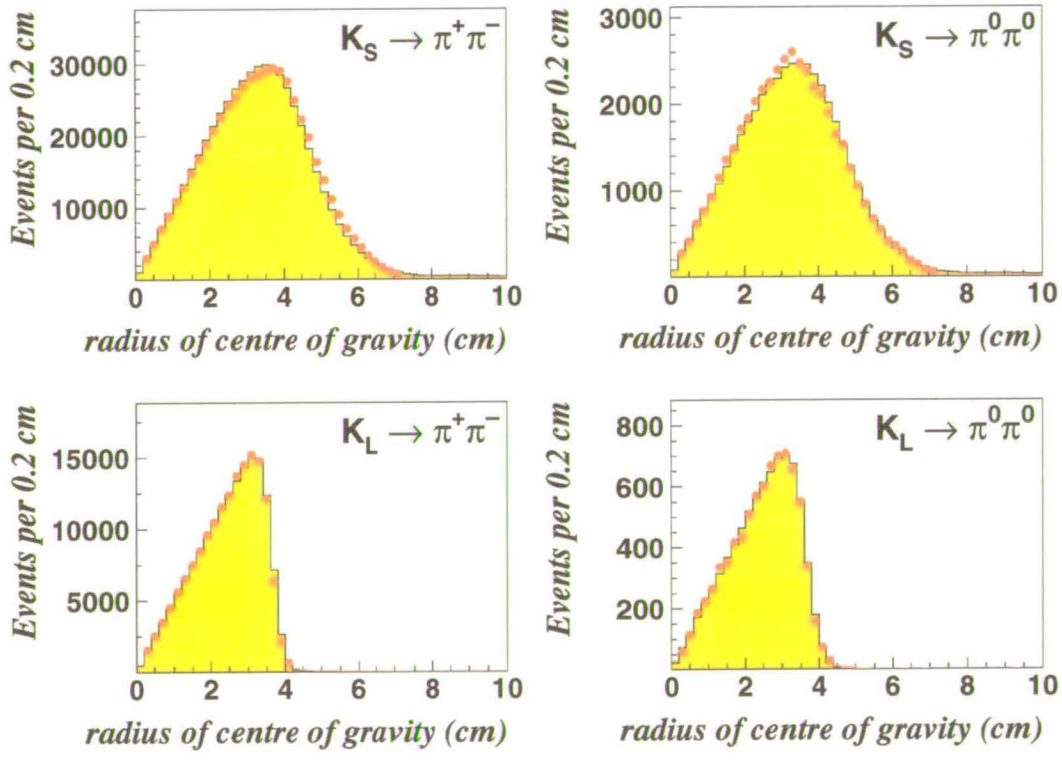

Figure 7.31: The distribution of $r_{\rm cog}$ for all four $\mathcal{R}e(\epsilon'/\epsilon)$ decay modes. The solid area is the Monte Carlo and the points are the data. The Monte Carlo does not describe the data well, particularly for K_S events in the range $2 < r_{\rm cog}/{\rm cm} < 5$ and K_L events in the range $3 < r_{\rm cog}/{\rm cm} < 4$.

Effect	Correction to $\mathbf{R}$ $[10^{-4}]$
Tagging dilution and efficiency	$+15 \pm 4$
Tagging dilution difference	$+10 \pm 4$
Tagging efficiency difference	0 ± 3
Charged trigger efficiency	-2 ± 12
Charged Background	$+18 \pm 3$
Beam Scattering	-11 ± 3
Neutral Background	-7 ± 2
Accidental Activity	$+1 \pm 12$
Charged Energy Scale	$+2 \pm 2$
Neutral Energy Scale	0 ± 10
Acceptance	$+24 \pm 8$
Total	$+51 \pm 22$

Table 7.5: Summary of all the corrections applied to $\mathbf{R}$. The last row shows the total correction to be applied to $\mathbf{R}_{\text{raw}}$. As the sources of the systematic corrections are independent, the individual errors have been added in quadrature to obtain the final systematic uncertainty on $\mathbf{R}$.

7.16 The Double Ratio after all Corrections

Table 7.5 summarises all the corrections applied to the double ratio, $\mathbf{R}$, as discussed in this chapter.

The 'raw' value of $\mathbf{R}$ given in equation (6.12) is:

$$\mathbf{R}_{\text{raw}} = 0.98746 \pm 0.00170 \tag{7.52}$$

From table 7.5, the total correction to be applied to $\mathbf{R}_{\text{raw}}$ is $(+51.6 \pm 22.1) \times 10^{-4}$. Therefore the final, corrected, value of $\mathbf{R}$ is:

$$\mathbf{R} = 0.99262 \pm 0.00170 \pm 0.00221 \tag{7.53}$$

where the first error is statistical (from the numbers of events) and the second error is systematic (from the corrections applied to $\mathbf{R}$).

Figure 7.32 shows the values of $\mathbf{R}$ in kaon energy bins after applying all the corrections discussed in this chapter. Fitting these points to a constant gives a χ^2 of 12.9 for 19 degrees of freedom. The distribution of points therefore indicates that the calculated value of $\mathbf{R}$ is independent of the kaon energy.

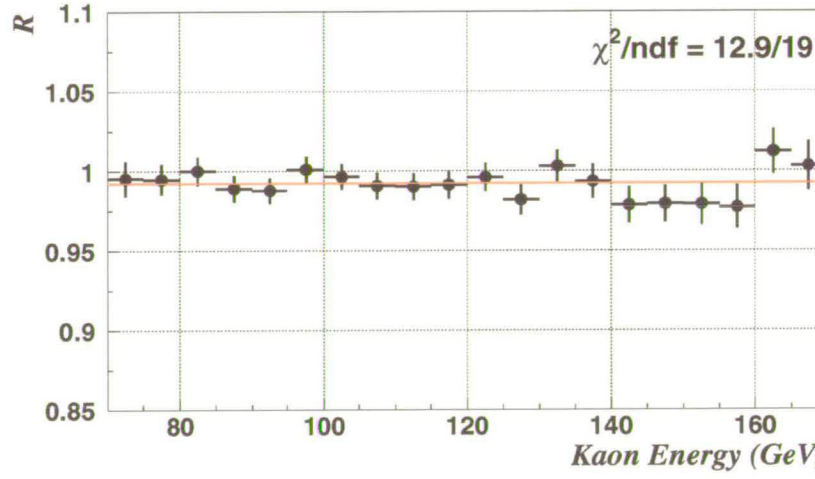

Figure 7.32: The value of **R** after all corrections.

Chapter 8

Result and Discussion

8.1 The Value of $\mathcal{R}e(\epsilon'/\epsilon)$

The double ratio **R** and the direct **CP** violation parameter $\mathcal{R}e(\epsilon'/\epsilon)$ are related by equation (2.72):

$$\mathbf{R} \simeq 1 - 6\,\mathcal{R}e\left(\frac{\epsilon'}{\epsilon}\right) \tag{8.1}$$

Using the corrected value of **R** presented in equation (7.53), the measured value of $\mathcal{R}e(\epsilon'/\epsilon)$ is:

$$\mathcal{R}e\left(\frac{\epsilon'}{\epsilon}\right) = (12.3 \pm 2.8 \pm 3.7) \times 10^{-4} \tag{8.2}$$

where the first error is statistical and the second error is due to systematic effects.

Combining the statistical and systematic errors in quadrature, this measurement of $\mathcal{R}e(\epsilon'/\epsilon)$ is 2.7 standard deviations above zero, and therefore indicates that direct **CP** violation takes place in the neutral kaon system.

8.2 Comparison with other Results

The measurement of $\mathcal{R}e(\epsilon'/\epsilon)$ presented above is shown in figure 8.1 with other recent measurements.

The NA31 and E731 measurements are the final results of the previous generation of experiments, which were announced in 1993. The result from NA31 at CERN was the first evidence for direct **CP** violation, whereas the result from E731 at FNAL is consistent with $\mathcal{R}e(\epsilon'/\epsilon) = 0$. The disagreement between these two results motivated the new generation of experiments: NA48 at CERN and KTeV at FNAL. The NA48 and KTeV results on figure 8.1 are the first results from these experiments which were

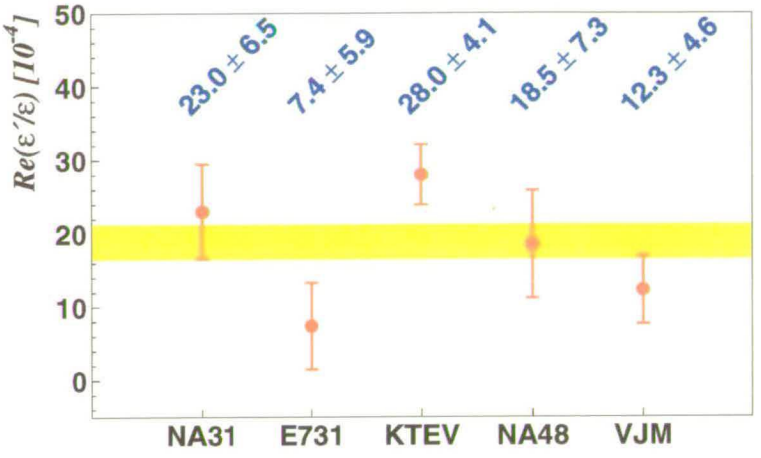

Figure 8.1: Recent measurements of $\mathcal{R}e(\epsilon'/\epsilon)$ [9, 31, 25, 2]. Where both a statistical and systematic error is given, these have been added in quadrature. The result presented in this thesis is labelled VJM. The yellow/light-grey band shows the $\pm 1\sigma$ allowed region of the average of these results.

announced in 1999. Both of these results are based on around $10 - 20\%$ of the total data set from these experiments.

The result presented in this thesis is based on around 30% of the total data set from NA48 and uses an independent data set with respect to the first NA48 result.

A weighted average of the five results gives $\mathcal{R}e(\epsilon'/\epsilon)_{\text{global}} = (18.9 \pm 2.4) \times 10^{-4}$ with a $\chi^2/\text{ndf} = 11.2/4$. The yellow/light-grey band on figure 8.1 shows the $\pm 1\sigma$ allowed region of this average. As the χ^2 per degree of freedom on the average is larger than 1, the approach proposed by the PDG [37] can be used to rescale the error by $(\chi^2/\text{ndf})^{1/2} = 1.7$, resulting in $\mathcal{R}e(\epsilon'/\epsilon)_{\text{global}} = (18.9 \pm 4.0) \times 10^{-4}$.

The experimental picture is now much clearer than it was in 1993. Direct **CP** violation in the neutral kaon system is now firmly established. However, due to the large variation in the measurements, it is too early to settle on an exact value for $\mathcal{R}e(\epsilon'/\epsilon)$. New, more precise results should be produced by both the KTeV and NA48 experiments in the future. The KLOE experiment at DAΦNE also intends to measure $\mathcal{R}e(\epsilon'/\epsilon)$ [60]. in contrast to the fixed target method employed by both KTeV and NA48, KLOE use a different experimental technique in which K_L and K_S pairs are produced by e^+e^- collisions at the Φ resonance.

The results of recent theoretical calculations of ϵ'/ϵ are shown in figure 2.8. Typically these calculations predict $\epsilon'/\epsilon \lesssim 10 \times 10^{-4}$, which is smaller than the experimental results. As discussed in section 2.10 there is an on-going discussion within the physics

community whether the experimental value of $\mathcal{R}e(\epsilon'/\epsilon)$ can be accommodated within the Standard Model or if new physics is needed. However, as the uncertainties on these calculations are large due to hadronic effects, it is probably too early to decide whether or not new physics has been discovered through the measurement of $\mathcal{R}e(\epsilon'/\epsilon)$.

In conclusion, direct **CP** violation in the neutral kaon system is now firmly established. Improvements in the theoretical calculations of ϵ'/ϵ and more precise measurements from KTeV, NA48 and KLOE should contribute to a better understanding of **CP** violation in the future.

Appendix A

Charged Energy Scale

The charged energy scale is investigated by using the reconstructed mass of the $\pi^+\pi^-$ pair, $m_{\pi^+\pi^-}$. For $K^0 \to \pi^+\pi^-$ events, the average value of $m_{\pi^+\pi^-}$ should be the kaon mass, m_{K^0}. We assume that any difference between the average value of $m_{\pi^+\pi^-}$ and m_{K^0} can be corrected by scaling of the measured momentum of the tracks by a linear factor $(1+a)$.

To calculate the value of a, consider the calculation of $m_{\pi^+\pi^-}$:

$$m^2_{\pi^+\pi^-} = E^2_K - p^2_K \quad \text{with} \quad E_K = E_+ + E_- \quad \text{and} \quad \overrightarrow{p_K} = \overrightarrow{p_+} + \overrightarrow{p_-} \tag{A.1}$$

where $\overrightarrow{p_\pm}$ are the momenta and $E_\pm$ are the energies of the two tracks.

The p^2_K term in the above equation can then be written as:

$$p^2_K = |p_+|^2 + |p_-|^2 + 2\,\overrightarrow{p_+} \cdot \overrightarrow{p_-} \tag{A.2}$$

Using $E^2_\pm = p^2_\pm + m^2_\pi$, we can write the E^2_K term as:

$$\begin{aligned} E^2_K &= |p_+|^2 + |p_-|^2 + 2\,m^2_\pi + 2\sqrt{p^2_+ p^2_- + m^2_\pi(p^2_+ + p^2_-) + m^4_\pi} \\ &\simeq |p_+|^2 + |p_-|^2 + 2\,|p_+|\,|p_-| + m^2_\pi\,R \end{aligned} \tag{A.3}$$

where we have used $p^2_\pm \gg m^2_\pi$ and defined R to be:

$$R = \left(2 + \frac{|p_+|}{|p_-|} + \frac{|p_-|}{|p_+|}\right) \tag{A.4}$$

Substituting the above results for p^2_K and E^2_K back into equation (A.1) gives:

$$m^2_{\pi^+\pi^-} = m^2_\pi\,R + 2\,|p_+|\,|p_-| - 2\,\overrightarrow{p_+} \cdot \overrightarrow{p_-} \tag{A.5}$$

After multiplying the momenta of the each of the tracks by the scale factor $(1+a)$ we have:

$$m'^2_{\pi^+\pi^-} = m^2_\pi\,R + (1+a)^2\,\{2\,|p_+|\,|p_-| - 2\,\overrightarrow{p_+} \cdot \overrightarrow{p_-}\} \tag{A.6}$$

We can denote the average value of $m_{\pi^+\pi^-}$ as $\langle m_{\pi^+\pi^-}\rangle$. As the number of events is large, the variance of the $m_{\pi^+\pi^-}$ can be neglected giving:

$$\langle m^2_{\pi^+\pi^-}\rangle = \langle m_{\pi^+\pi^-}\rangle^2 = m^2_\pi \langle R\rangle + \langle 2\,|p_+|\,|p_-| - 2\,\overrightarrow{p_+}\cdot\overrightarrow{p_-}\rangle \tag{A.7}$$

where $\langle\ \rangle$ around a quantity denotes using the mean value. Similarly for the corrected value of $m_{\pi^+\pi^-}$,

$$\langle m'^2_{\pi^+\pi^-}\rangle = \langle m'_{\pi^+\pi^-}\rangle^2 = m^2_{\mathrm{K}^0} = m^2_\pi \langle R\rangle + (1+a)^2\,\langle 2\,|p_+|\,|p_-| - 2\,\overrightarrow{p_+}\cdot\overrightarrow{p_-}\rangle \tag{A.8}$$

where we have used $\langle m'_{\pi^+\pi^-}\rangle = m_{\mathrm{K}^0}$, which is the constraint used to define the energy scale factor $(1+a)$.

Using equations (A.7) and (A.8) we can find the following relation for a:

$$(1+a)^2 = \frac{m^2_{\mathrm{K}^0} - m^2_\pi \langle R\rangle}{\langle m^2_{\pi^+\pi^-}\rangle - m^2_\pi \langle R\rangle} \tag{A.9}$$

A typical measured value of $\langle m_{\pi^+\pi^-}\rangle$ (before applying the energy scale correction) was 0.4970 GeV/c^2. The value of $\langle R\rangle$ is 4.449. The resulting value of the energy scale factor is therefore $(1+a) = 1.0016$, which is a correction of 0.16% on the measured values of $|p_\pm|$.

Bibliography

[1] T. Affolder *et al.*, The CDF Collaboration. *A Measurement of sin2β from* $B \to J/\psi K^0_S$ *with the CDF detector.* Phys. Rev. **D61**, 072005 (2000).

[2] A. Alavi-Harati *et al.*, The KTeV Collaboration. *Observation of Direct CP Violation in* $K_{S,L} \to \pi\pi$ *Decays.* Phys. Rev. Lett. **82**, 22 (1999).

[3] H. Aihara for the Belle Collaboration. *New Results from BELLE.* Talk at XXXth International Conference on High Energy Physics, 2000.

[4] H. Atherton *et al. Precise measurements of particle production by 400 GeV/c protons on beryllium targets.* CERN Yellow Report 80-07 (1980).

[5] I. Augustin, M. Bender, M. Holder, W. Otto, M. Roschangar and B. Schofer. *Readout of Wire Chambers in NA48.* NA48 Internal Note 94-33 (1994).

[6] I. Augustin, A. Gaponenko and M. Holder. *Performance of the Drift Chamber Multiplicity Trigger.* NA48 Internal Note 97-35 (1997).

[7] R. Barlow and C. Beeston. *Fitting using finite Monte Carlo samples.* Computer Physics Communications **77**, 219 (1993).

[8] G. D. Barr *et al.*, The NA48 Collaboration. *Proposal for a Precision Measurement of* $\frac{\epsilon'}{\epsilon}$ *in CP Violating* $\mathrm{K}^0 \to 2\pi$ *decays.* `CERN/SPSC/90-22` (1990).

[9] G. D. Barr *et al.*, The NA31 Collaboration. Physics Letters B**317**, 233 (1993).

[10] G. D. Barr *et al.*, The NA48 Collaboration. *The* $\mathrm{K}^0 \to \pi^0\pi^0$ *decay trigger for the NA48 experiment at CERN.* To be submitted to Nuclear Instruments and Methods.

[11] A. A. Bel'kov, G. Bohm, A. V. Lanyov and A. A. Moshkin. *Phenomenological analysis of* ϵ'/ϵ *within an effective chiral lagrangian approach at* $O(p^6)$. `hep-ph/9907335`

[12] I. Bertanaza *et al.* The NA31 Collaboration. *Measurement of the* $\mathrm{K_S}$ *mean lifetime from* $\pi^+\pi^-$ *and* $\pi^0\pi^0$ *decays using* $\mathrm{K_L}$ *to determine the acceptance.* Z. Phys. C **73**, 629 (1997).

[13] S. Bertolini, J. O. Eeg and M. Fabbrichesi. *An updated of ϵ'/ϵ in the Standard Model with hadronic matrix elements from the Chiral Quark Model.* hep-ph/0002234

[14] C. Biino, NA48 Collaboration Meeting, 17$^{\text{th}}$ February 2000.

[15] G. C. Branco, L. Lavoura and J. P. Silva. International Series of Monographs on Physics: *CP Violation.* Oxford University Press, 1999.

[16] G. Buchalla, A. J. Buras and M. E. Lautenbacher. *Weak decays beyond leading logarithms.* Rev. Mod. Phys. **68**, 1125 (1996).

[17] S. Bosch *et al. Standard Model Confronting New Results for ϵ'/ϵ.* hep-ph/9904408

[18] A. Ceccucci, NA48 Analysis Meeting, 17$^{\text{th}}$ February 2000.

[19] J. B. Chollet. *NA48 Drift Chamber Reconstruction Program.* NA48 Internal Documentation (1999).

[20] J. H. Christenson, J. W. Cronin, V. L. Fitch and R. Turlay. *Evidence of the 2π decay of the K_2^0 Meson.* Phys. Rev. Lett. **13**, 138 (1964).

[21] M. Ciuchini, E. Franco, L. Giusti, V. Lubicz and G. Martinelli. *Combined analysis of the unitarity triangle and CP violation in the Standard Model.* hep-ph/9910236

[22] P. Debu and R. Gränier de Cassagnac. *1997 Charged Trigger Efficiency.* NA48 Internal Note 98-08 (1998).

[23] R. Dosanjh and M. Lenti. *Tagging Dilution Difference in 1998 Data.* NA48 Internal Note 2000-6 (2000).

[24] J. Duclos and M. Porcu. K_S *Beam Halo and Momentum Distribution.* NA48 Internal Note 97-9 (1997).

[25] V. Fanti *et al.*, The NA48 Collaboration. *A new measurement of direct CP violation in two pion decays of the neutral kaon.* Phys. Lett. B**465**, 335 (1999).

[26] G. Fischer. *Implementation, calibration and performance analysis of a novel trigger system for $K^0 \to \pi^0\pi^0$ decays at the CERN NA48 CP-violation experiment.* PhD Thesis, University of Vienna, Austria, 1999.

[27] H. Fox. *A Measurement of Direct CP Violation with the NA48 detector.* PhD Thesis, Johannes-Gutenberg Universität Mainz, Germany, 2000.

[28] H. Fox, K. Holtz, L. Köpke, S. Schmidt and Y. Schue. *Filter Cuts and Configurations for Reprocessing in 1997 and 1998.* NA48 Internal Note 98-28 (1998).

[29] A. Formica. *1998 Charged Trigger Efficiency.* NA48 Internal Note 99-28 (1999).

[30] A. Formica, NA48 Analysis Meetings, 8$^{\text{th}}$ February and 17$^{\text{th}}$ February 2000.

[31] L. K. Gibbons *et al.*, The E731 Collaboration. Phys. Rev. Lett. **70**, 1203 (1993).

[32] T. J. Gershon. *Track Based Reconstruction of Muons.* NA48 Internal Note 98-25 (1998).

[33] T. J. Gershon. *Updates to the Muon Reconstruction.* NA48 Internal Note 99-01 (1999).

[34] B. Gorini. *Measurement of $Re(\epsilon'/\epsilon)$ using new calorimetry technique.* PhD Thesis, Scuola Normale Superiore Pisa, Italy, 1999.

[35] G. Graziani. *Measurement of direct CP violation with the NA48 experiment at CERN.* PhD Thesis, Università degli Studi di Firenze, Italy, 1999.

[36] G. Graziani, NA48 Analysis Meetings, 17$^{\text{th}}$ of February and 3$^{\text{rd}}$ May 2000.

[37] G. Groom *et al.*, The Particle Data Group. The European Physical Journal **C15**, 1 (2000).

[38] T. Hambye, G. O. Koehler, E. A. Paschos and P. H. Soldan. *Analysis of ϵ'/ϵ in the $1/N_c$ Expansion.* `hep-ph/9906434`

[39] P. E. Harrison and H. R. Quinn (Editors). *The BaBar Physics Book: Physics at an asymmetric B factory* (1998). `SLAC-R-504`

[40] B. Hay. *Determination of the Branching ratio $K_L \to \pi\mu\nu/K_L \to \pi e\nu$ and a study of $K_L \to \pi^+\pi^-\pi^0/K_L \to$ all charged.* PhD Thesis, The University of Edinburgh, 1996.

[41] D. Hitlin for The BaBar Collaboration. *New Results from BABAR.* Talk at XXXth International Conference on High Energy Physics, 2000.

[42] Q. Ho-Kim and Pham, X.-Y. *Elementary Particles and their Interactions.* Springer, 1998.

[43] L. Iconomidou-Fayard, NA48 Analysis Meeting, 24$^{\text{th}}$ August 1999.

[44] C. Jarlskog. Phys. Rev. Lett. **55**, 1039 (1985).

[45] M. Kobayashi and K. Maskawa. Prog. Theor. Phys. **49**, 282 (1972).

[46] L. Landau. *On the Conservation Laws for Weak Interactions.* Nuc. Phys. **3**, 127 (1957).

[47] T. D. Lee, R. Oehme and C. N. Yang. *Remarks on Possible Noninvariance under Time Reversal and Charge Conjugation.* Phys. Rev. **106**, 340 (1957).

[48] C. Lazzeroni and M. Lenti. *Tagging inefficiency in 98 data.* NA48 Internal Note 2000-1 (2000).

[49] T. D. Lee. *Particle Physics and Introduction to Field Theory.* Harwood Academic Press, 1981

[50] M. Lenti. *Charged event time reconstruction inefficiency in 98 data.* NA48 Internal Note 99-26 (1999).

[51] G. Lüders, Annuals of Physics, **2** (1957).

[52] V. Martin, NA48 Analysis Meeting, 19$^{\text{th}}$ January 2000.

[53] I. Mikulec, NA48 Analysis Meetings, 20$^{\text{th}}$ January and 17$^{\text{th}}$ February 2000.

[54] U. Nierste. *Theoretical status of* ϵ'/ϵ. `hep-ph/9910257`

[55] Y. Nir. *CP Violation In and Beyond the Standard Model:* Lectures given at the XXVII SLAC Summer Institute on Particle Physics, to appear in the proceedings. `hep-ph/9911321`

[56] H. L. C. Parsons. *A study of the CP Violation Parameter* $\frac{\epsilon'}{\epsilon}$. PhD Thesis, The University of Edinburgh, 1999.

[57] A. D. Sakharov. *Violation of CP Invariance, C Asymmetry and Baryon Asymmetry of the Universe.* JTEP Lett. **5**, 24 (1967).

[58] V. Schönharting. *NMC Users Guide.* NA48 Internal Note 96-17 (1996).

[59] M. Sozzi, NA48 Analysis Meeting, 5$^{\text{th}}$ May 2000.

[60] L. Tortora for the KLOE Collaboration. *The KLOE Detector and Physics Program.* Nucl. Phys. B (Proc. Suppl.) **78**, 157 (1999).

[61] G. Unal. *Reconstruction Program for the LKR.* NA48 Internal Note 98-01 (1998).

[62] G. Unal. *Neutral Energy Scale and Non linearities in 1998 Data.* NA48 Internal Note 2000-04 (2000).

[63] G. Unal, NA48 Analysis Meeting, 16$^{\text{th}}$ February 2000.

[64] G. Unal, NA48 Analysis Meeting, 17$^{\text{th}}$ February 2000.

[65] L. Wolfenstein. Phys. Rev. Lett. **51**, 1945 (1983).

[66] T. T. Wu and C. N. Yang. *Phenomenological Analysis of Violation of CP Invariance in decay of* K^0 *and* $\overline{\mathrm{K}^0}$. Phys. Rev. Lett. **13**, 380 (1964)

[67] C. S. Wu *et al. Experimental test of parity Conservation in β Decay.* Phys. Rev. **104**, 254 (1957).

[68] Application Software Group *GEANT: Detector Description and Simulation Tool.* `http://www.cern.ch/asdoc/geant_html3/geantall.html`